DE GRUYTER

MATHEMATICAL FLUID MECHANICS

ADVANCES IN CONVECTIVE INSTABILITIES AND INCOMPRESSIBLE FLUID FLOW

Edited by B. Mahanthesh

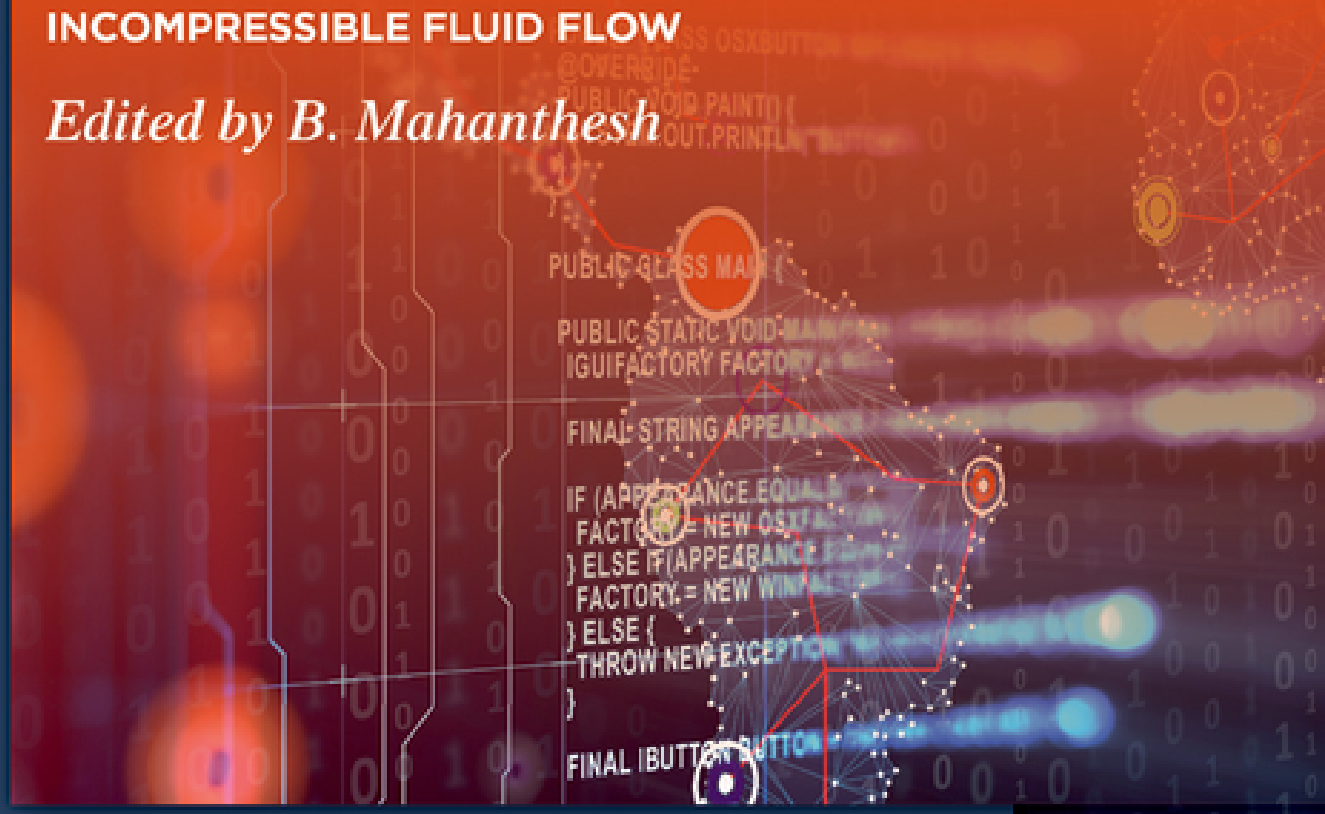

DE GRUYTER SERIES ON THE APPLICATIONS OF MATHEMATICS IN ENGINEERING AND INFORMATION SCIENCES

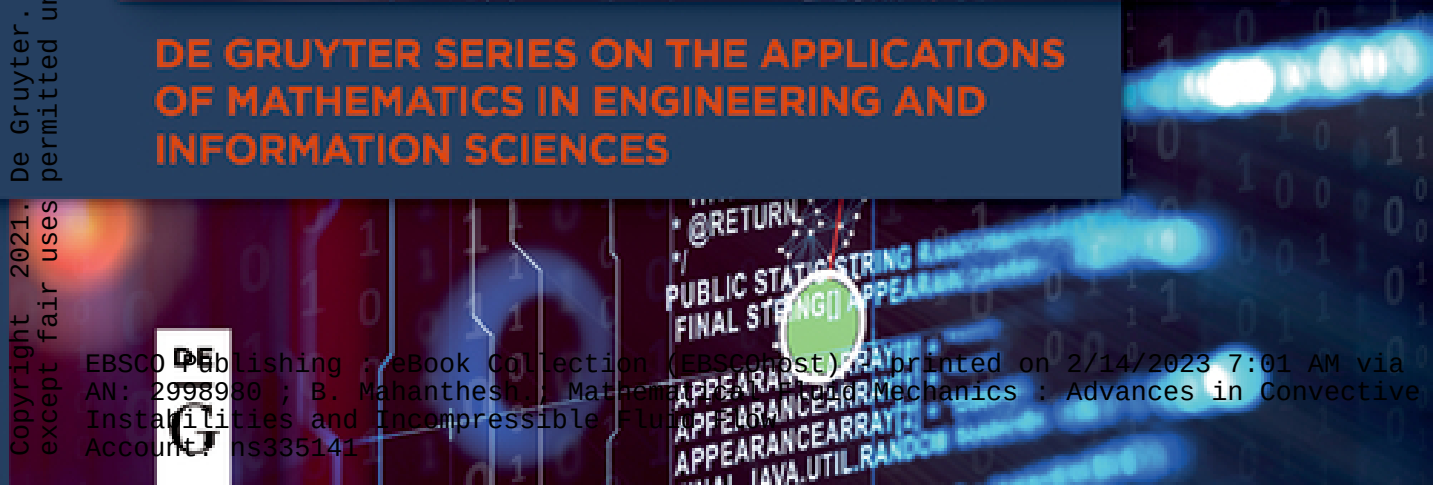

B. Mahanthesh (Ed.)
Mathematical Fluid Mechanics

De Gruyter Series on the Applications of Mathematics in Engineering and Information Sciences

Edited by
Mangey Ram

Volume 7

Mathematical Fluid Mechanics

Advances in Convective Instabilities and Incompressible Fluid Flow

Edited by
B. Mahanthesh

DE GRUYTER

Editor
Dr. B Mahanthesh
CHRIST (Deemed to be University)
Bangalore Central Campus,
Bhavani Nagar-560029, India
mahanthesh.b@christuniversity.in

ISBN 978-3-11-069603-5
e-ISBN (PDF) 978-3-11-069608-0
e-ISBN (EPUB) 978-3-11-069612-7
ISSN 2626-5427

Library of Congress Control Number: 2021936049

Bibliographic information published by the Deutsche Nationalbibliothek
The Deutsche Nationalbibliothek lists this publication in the Deutsche Nationalbibliografie; detailed bibliographic data are available on the Internet at http://dnb.dnb.de.

Cover image: MF3d/E+/Getty Images
Printing and binding: CPI books GmbH, Leck

www.degruyter.com

Contents

Foreword —— VII

P. G. Siddheshwar, B. N. Shivakumar
Analytical study of Küppers-Lortz instability in a Newtonian-Boussinesq liquid with rigid-isothermal boundaries —— 1

B. Mahanthesh
Quadratic radiation and quadratic Boussinesq approximation on hybrid nanoliquid flow —— 13

F. Mebarek-Oudina, A. Aissa
Convective heat transfer of magneto flow of Fe_3O_4-MWCNT/H_2O hybrid nanofluid in a porous space between two concentric cylinders —— 55

Taseer Muhammad, Hassan Waqas, B. Mahanthesh
Computational analysis of bioconvection in magnetized flow of thixotropic nanofluid with gyrotactic microorganisms —— 75

Md Faisal Md Basir, S.A. Shehzad, A. Rauf
On the features of Stefan blowing magnetized flow of bioconvected nanofluid through slip conditions —— 103

Mahesha Narayana, P. G. Siddheshwar, S. B. Ashoka
Computer-assisted successive linearization solution of the Darcy-Forchheimer-Brinkman flow through a rectangular channel —— 121

V. Ramachandramurthy, D. Uma, N. Kavitha
Linear and non-linear instability analysis of the onset of magnetoconvection in couple-stress fluids with thermorheological effect —— 143

J. Meghana, S. Pranesh
Two-component convection in micropolar fluid under time-dependent boundary concentration —— 163

Swaraj D. Lewis, Purushothama Chippar
A numerical study of metal hydride reactor embedded with helical coil heat exchanger —— 201

B. Mahanthesh, T. V. Joseph, K. Thriveni
Dynamics of non-Newtonian nanoliquid with quadratic thermal convection —— 223

List of contributors —— 249

Foreword

The book aims to include several substantial research topics in mathematical fluid mechanics that have enormous applications in engineering and applied sciences. This book should be a valuable resource for graduate students, academic researchers, and educators associated with areas of research or teaching, such as computational mathematics, mathematical modeling, fluid mechanics, nanofluid mechanics, and various branches of applied science. The book should also be of interest to general readers interested in gaining knowledge of recent trends in the applied mathematical sciences. The book consists of ten chapters, as follows.

Chapter 1 aims to use the single-term Galerkin approximation to study primary and secondary instabilities in the Rayleigh-Benard-Taylor convection in the case of rigid isothermal boundaries using Newtonian viscous fluid. The mathematical formulation of the model is presented using the conservation laws of mass, momentum and energy. The critical Rayleigh number and the number of critical waves are estimated for the primary instability. The Taylor critical number and the critical angle between the intersecting rolls are obtained for the secondary Kuppers-Lortz instability. A comparative analysis is also presented between the results of rigid isothermal limits with those of free isothermal limits.

Chapter 2 proposes a novel Rosseland quadratic approximation to study the radiative heat transport when the quadratic variation of the density temperature (QDT) is significant. For the first time, it proposes a quadratic Rosseland approximation. Mathematical modeling is performed with the help of the conservation laws of mass, momentum and energy. It uses the shooting method to examine the heat transfer characteristics of a hybrid nanoliquid over a vertical plate using a single-phase nanoliquid model. Hybrid nanoliquids are essential for reducing manufacturing and operating costs of microelectronics, nano electronics, pharmaceuticals, hybrid engines and fuel cells. It uses the response surface methodology to statistically analyze and optimize the heat transfer rate of hybrid nanoliquid. In addition, sensitivity analysis based on the multivariate quadratic regression model is also performed.

Chapter 3 deals with the magnetohydrodynamic (MHD) free convection of a hybrid nanofluid in the porous cavity using the control volume finite element method. MHD flow and heat transfer have various industrial and manufacturing applications, such as cooling underground power cables, nuclear reactors, geothermal energy extraction, plastic foil, and man-made fibers. Hybrid nanoparticles volume fraction, Hartmann number, Rayleigh number, Darcy number and porosity are the parameters **used** to control and visualize fluid flow through isotherms, flow lines,

https://doi.org/10.1515/9783110696080-203

and Nusselt mean number. It ends with extensive applications of hybrid nanoliquids.

Chapter 4 simulates the magnetohydrodynamic flow of a thixotropic nanoliquid that has mobile microorganisms with the aid of the Buongiorno model which leads to consider Brownian motion and thermophoretic diffusion. This chapter also deals with various external physical effects such as thermal radiation, heat generation and Joule dissipation. Similarity theory and the MATLAB solver were used to solve the nonlinear differential equations that model the problem. Numerical and graphical results are presented using various estimates of physical parameters.

Chapter 5 provides the numerical solution for the flow of magnetized bioconvected nanofluids induced by the movement of the slippery moving sheet with Stefan's blowing. The dominant expressions of the physical phenomenon are converted into dimensionless forms using the methodology of the Lie group. The Runge-Kutta-Fehlberg fourth and fifth order numerical scheme is used to present solutions of dimensionless expressions. The results of skin friction, heat transfer rate, temperature and velocity are discussed in detail.

Chapter 6 aims to solve the boundary layer problem describimg the fully developed Darcy-Forchheimer-Brinkman (DFB) flow through the freely compressed porous medium using the computer-aided successive linearization (SLM) method. The proposed method in this chapter, in general, has a quadratic convergence rate and is not sensitive to the initial solution unlike other numerical methods such as the shooting method. It concludes that the governing parameters have the least effect on the method, which means that the method converges even for large parameter values. This chapter also presents the applications of the Darcy-Forchheimer-Brinkman (DFB) model in frontier areas such as petroleum engineering, hydrogeology, reactor engineering, biology, medicine, etc.

The objective of Chapter 7 is to perform the linear and non-linear stability analysis of the Rayleigh-Benard convection for the couple-stress fluid with a thermorheological effect in the presence of an applied magnetic field. This chapter discusses the three important aspects of the convection control mechanism, namely, suspended particles, applied magnetic field, and variable viscosity. The Runge-Kutta method is used to solve the generalized Lorenz model.

Chapter 8 proposes to present the analytical solution of two-component convection in a micropolar fluid subjected to an imposed boundary concentration modulation. Two-component convection equations and associated mathematics are presented. The perturbation method is used to estimate the expression of the Rayleigh number and the correction Rayleigh number as a function of the parameters, frequency and

amplitude of the micropolar fluid. The effect of various parameters on heat and mass transport is studied by deriving the Ginzburg Landau equation from the sixth order Lorenz equations.

Chapter 9 proposes a comprehensive three-dimensional numerical model accounting for reaction kinetics and, heat and mass transfer for hydrogen charging and discharging in a LaNi5 based MH reactor. The model is compared with the experimental data, and the simulation results agree closely with the experimental data. In this chapter a detailed parametric study is carried out to optimize the operating conditions of the reactor and the geometry of the Helical Coil Heat Exchanger (HCHX) to improve the hydrogen charging and discharging rates. The effect of essential parameters such as supply/exit pressures, Heat Transfer Fluid (HTF) temperature, and helical coil pitch/turns on the thermal performance and sorption rate of the MH bed are analyzed systematically. It shows that increasing the inlet hydrogen pressure and reducing the HTF temperature significantly improves the charging rate.

Chapter 10 adopts the Response Surface Methodology to optimize the heat transfer rate of non-Newtonian Jeffrey nanoliquid flow driven by a flexible surface exposed to quadratic thermal radiation and Boussinesq's quadratic approximation. The Brownian motion and thermophoretic characteristics are also discussed here. The dimensionless distributions of velocity, temperature, nanoparticle concentration and heat transfer rate are simulated by solving the system of nonlinear differential equations using the finite difference-based routine. The importance of the different physical parameters of the problem was explored. In addition, a sensitivity analysis is also performed using the quadratic polynomial for the Nusselt number obtained from the central composite design.

The editor thanks the contributors for their timely contribution and cooperation during the revision and elaboration of the chapters. The reviewers deserve sincere thanks for their volunteer service in providing timely reports. The De Gruyter editorial team associated with this book project also deserves sincere thanks for their cooperation and support. The editor also wishes to thank his colleagues Dr. Fr. Joseph Varghese, and Dr. Siddhartha Bhattacharyya, for their support in publishing this book.

B. Mahanthesh
Bangalore, India
1st March 2021

Editor

Dr. B. Mahanthesh serves as an Assistant Professor of Mathematics at CHRIST (Deemed to be University), Bangalore Central Campus, Bangalore, India. He has to his credit over 110 research papers in reputed journals, and 2 book chapters so far. He has acted as resource person in different academic activities and delivered invited talks at national and international levels.

P. G. Siddheshwar, B. N. Shivakumar

Analytical study of Küppers-Lortz instability in a Newtonian-Boussinesq liquid with rigid-isothermal boundaries

Küppers-Lortz instability

Abstract: The paper deals with primary and secondary instabilities in Rayleigh-Bénard-Taylor convection in the case of rigid-isothermal boundaries. The single-term Galerkin approximation is used in obtaining estimates of the critical Rayleigh number and critical wave number for primary instability and critical Taylor number and critical angle between the intersecting rolls in the case of the Küppers-Lortz secondary instability. Comparison is made between the results of rigid isothermal boundaries with those of free isothermal boundaries.

Keywords: Lorenz model; Küppers-Lortz; Rigid boundaries; Isothermal; Rayleigh-Bénard; Newtonian liquid; Convection.

1 Introduction

The onset of convection is known to be delayed in the case of Rayleigh-Bénard-Taylor convection (RBTC) due to the Coriolis force and the same has been extensively examined by Chandrasekhar (5) for the case of both bounding surfaces that are (i) free, (ii) rigid and (iii) one bounding surface free and other rigid. Bhattacharjee (2) determined the Rayleigh number, critical wavenumber and frequency in rotating binary mixtures with both idealized and realistic boundary conditions. Siddheshwar and Sakshath (14) studied linear and non-linear stability analysis of RBTC. They have considered rigid boundaries in their study. More details on RBTC can be found in the book of Chandrasekhar (6).

An interesting secondary instability was discovered by Küppers and Lortz (10), who showed that in a rotating Rayleigh-Bénard system with stress-free, isothermal boundaries, if the rotation speed exceeds a critical value, the two-dimensional roll

P. G. Siddheshwar, Department of Mathematics, Bangalore University, Bengaluru-560 056, India, mathdrpgs@gmail.com

B. N. Shivakumar, Department of Mathematics, Bangalore University, Jnana Bharathi Campus Bengaluru-560 056, India

https://doi.org/10.1515/9783110696080-001

solutions are no longer stable against perturbations by rolls with a different axis. Bhattacharjee and McKane (1) predicted that the Küppers-Lortz (KL) instability occurs at a critical Taylor number of $Ta_c = 80\pi^4$ and critical angle of $tan\psi_c = 4/\sqrt{5}$. Zhong et al. (17) studied the KL-instability at a lower critical Taylor number. Bodenschatz et al. (3) discussed the KL-instability for the rotational problem, rotated about a vertical axis. They observed that the dominant mechanism of the instability involves the motion of boundaries between coherent regions of convection rolls of a given orientation. Ning and Ecke (11) showed that transition of KL-instability for rotating Rayleigh-Bénard convection occurs over a range of dimensionless rotation rates. Toral et al. (16) discussed the stabilization of the KL-instability in the Busse-Heikes dynamic model in terms of relaxational and non-relaxational dynamics. Rubio et al. (13) have studied the finite rotating thermal convection to get the onset of KL-like dynamics for the case of idealized boundary conditions. Rameshwar et al. (12) investigated onset of KL-instability by assuming stress free boundary conditions and found that $Ta_c = 2284$ and $\psi_c = 58.59$. Siddheshwar et al. (15) have investigated the effect of local thermal non-equilibrium on the onset of KL-instability in the rotating Brinkman-Bénard convection. They found that the critical Taylor number and angle between the rolls for the local thermal non-equilibrium case to be more compared to that of the local thermal equilibrium one.

Clune and Knobloch (7) have considered experimental boundary conditions for which they have determined the Ta_c and ψ_c of KL-instability to be 3003.04 and 59.7 respectively. Desaive et al. (8) made weakly non-linear analysis with rigid boundaries to derive the amplitude equation and used them to study the onset of the KL-instability. They found that KL-instability occurs at $Ta_c = 3003.04$ and $\psi_c = 59.7$. Kanchana et al. (9) investigated the effect of nanoparticles on the onset of KL-instability for the case of rigid isothermal boundaries. In the present paper we use a numerical method based on the Galerkin approximation and obtain an approximate value for both Ta_c and ψ_c in the case of rigid-isothermal boundaries.

2 Mathematical Formulation

Consider a Newtonian-Boussinesq liquid between infinite horizontal parallel plates distance h apart. The system is rotated about the z −axis with a constant angular velocity $\vec{\Omega}$. The upper and lower boundaries are maintained at constant temperatures T_0 and $T_0 + \Delta T$ respectively. The schematic of the same is shown in the Figure 1.

The governing equations describing the rotating Rayleigh-Bénard instability situation in a Newtonian-Boussinesq liquid are:

Continuity Equation

$$\nabla.\vec{q} = 0 \tag{1}$$

Momentum Equation

$$\rho_0 \frac{\partial \vec{q}}{\partial t} = -\nabla p + \mu \nabla^2 \vec{q} + \rho \vec{g} - 2\rho_0 (\vec{\Omega} \times \vec{q}), \tag{2}$$

Energy Equation

$$\frac{\partial T}{\partial t} + (\vec{q}.\nabla)T = \chi \nabla^2 T, \tag{3}$$

Equation of State

$$\rho = \rho_0[1 - \alpha(T - T_0)]. \tag{4}$$

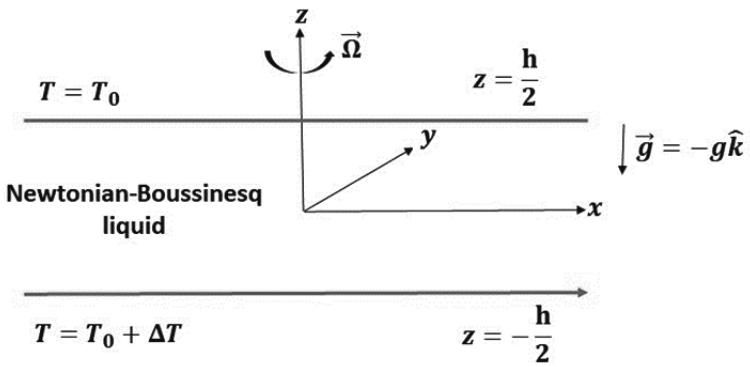

Fig. 1: Physical configuration of the Rayleigh-Bénard-Taylor convection problem.

Taking the velocity, temperature, density and pressure in the quiescent basic state as follows:

$$\left.\begin{array}{ll} \vec{q} = \vec{q}_b = (u_b, v_b, w_b) & = (0,0,0), \\ T(z) & = T_b(z), \\ \rho(z) & = \rho_b(z), \\ p(z) & = p_b(z), \end{array}\right\}, \tag{5}$$

we obtain the quiescent state solution in the form

$$\left.\begin{aligned} T_b(z) &= T_0 + \Delta T - \tfrac{\Delta T}{h} z, \\ \rho_b(z) &= \rho_0[1 - \alpha(T_b - T_0)], \\ p_b(z) &= -g \int \rho_b(z) dz + c_1, \end{aligned}\right\}, \tag{6}$$

where c_1 is the constant of integration. On the quiescent basic state, we superimpose perturbation in the form:

$$\left.\begin{aligned} \vec{q} &= \vec{q}'(x,z,t), \\ T &= T_b(z) + T'(x,z,t), \\ \rho &= \rho_b(z) + \rho'(x,z,t), \\ p &= p_b(z) + p'(x,z,t), \end{aligned}\right\}, \tag{7}$$

where the primes indicate a perturbed quantity.

Using Eq. (7) in Eqs. (1)-(4), nondimensionalizing the resulting equation using the following definition:

$$\tau = \tfrac{\chi\, t}{h^2}, (X,Z) = \left(\tfrac{x}{h}, \tfrac{z}{h}\right), \vec{q}^{\,*} = \tfrac{h\,\overrightarrow{q'}}{\chi}, p^* = \tfrac{h^2\, p'}{\chi\, \mu}\,, W = \tfrac{w\, h}{\chi}\,, \Theta^* = \tfrac{T'}{\triangle T}\,, \tag{8}$$

the dimensionless form of the governing equations are given by (after omitting asterisks):

$$\nabla . \vec{q} = 0, \tag{9}$$

$$\tfrac{1}{Pr} \tfrac{\partial \vec{q}}{\partial \tau} = -\nabla p + \nabla^2 \vec{q} + Ra\, \Theta\, \hat{e}_Z - \sqrt{Ta}\, (\hat{e}_Z \times \vec{q}), \tag{10}$$

$$\tfrac{\partial \Theta}{\partial \tau} = W + \nabla^2 \Theta - (\vec{q} . \nabla)\Theta, \tag{11}$$

where,

$Pr = \tfrac{\mu}{\rho_0\, \chi}$ is the Prandtl Number,

$Ra = \tfrac{\alpha\, \rho_0\, g\, \Delta T\, h^3}{\mu\, \chi}$ is the Rayleigh Number and

$Ta = \tfrac{4\, \Omega^2\, h^4}{\nu^2}$ is the Taylor number.

Operating curl twice on Eq. (10), we get

$$\tfrac{1}{Pr} \tfrac{\partial}{\partial \tau} (\nabla^2 W) = \nabla^4 W + Ra \nabla_2^2 \Theta + \sqrt{Ta} D \omega_Z. \tag{12}$$

Now operating curl once on Eq. (10) and taking the Z-component of the resulting equation, we get

$$\frac{1}{Pr}\frac{\partial \omega_Z}{\partial \tau} = \nabla^2 \omega_Z + \sqrt{Ta} DW. \tag{13}$$

The boundary conditions for solving Eqs. (11)-(13) are:

$$\left.\begin{array}{lllllllll} W & = & DW & = & \Theta & = & \omega_Z & = & 0 \; at \; Z = -\frac{1}{2} \\ W & = & DW & = & \Theta & = & \omega_Z & = & 0 \; at \; Z = \frac{1}{2} \end{array}\right\}. \tag{14}$$

The linear stability analysis of the system (11)-(13), subjected to the condition (14), gives the Rayleigh number of stationary convection in the form:

$$R_0 = \frac{\pi\delta^2\left(\left(k^2 Q_4 + Q_5\right)\left(Q_2\left(k^4 + \mu 1^4\right) + 2k^2 Q_3\right) - Q_3 Q_6 \mathrm{Ta}\right)}{2k^2 Q_1^2 \left(k^2 Q_4 + Q_5\right)}. \tag{15}$$

Minimising R_0 with respect to k, we get $R_{0_c} = 1728.38$ and $k_c = 3.097$ for $Ta = 0$. The various quantities appearing in the expression of the above Rayleigh number are recorded in the appendix.

Now we study the marginal stationary convection in the next section.

3 Lorenz model for primary instability-marginal stationary convection

Expansions for the different fields are given by

$$\left.\begin{array}{ll} U(X,Z,\tau) & = -\frac{\sqrt{2}\delta^2}{k\pi} A(\tau) \sin(k_c X)\, C_{f'}(Z), \\ W(X,Z,\tau) & = \frac{\sqrt{2}\delta^2}{\pi} A(\tau) \cos(k_c X)\, C_f(Z), \\ \omega_Z(X,Z,\tau) & = \frac{\sqrt{2}\delta^3}{\pi} G(\tau) \cos(k_c X)\, C_{f'}(Z), \\ \Theta(X,Z,\tau) & = \frac{\sqrt{2}\delta^6}{k^2\pi \mathrm{Ra}} B(\tau) \cos(k_c X) \sin\left[\pi\left(Z + \frac{1}{2}\right)\right] - \frac{\delta^6}{\pi k^2 \mathrm{Ra}} C(\tau)\, F(Z), \end{array}\right\}, \tag{16}$$

where,

$$C_f(Z) = \frac{\cosh(\mu_1 Z)}{\cosh\left(\frac{\mu_1}{2}\right)} - \frac{\cos(\mu_1 Z)}{\cos\left(\frac{\mu_1}{2}\right)}, \tag{17}$$

$$\left.\begin{aligned} F(Z) \quad &= \frac{4\pi\mu_1 \operatorname{sech}\left(\frac{\mu_1}{2}\right)}{\left(\mu_1^2+\pi^2\right)^2}\cos(\pi Z)\sinh(\mu_1 Z) \\ &+ \frac{2\left(\pi^2-\mu_1^2\right)\operatorname{sech}\left(\frac{\mu_1}{2}\right)}{\left(\mu_1^2+\pi^2\right)^2}\sin(\pi Z)\cosh(\mu_1 Z) \\ &-\sec\left(\frac{\mu_1}{2}\right)\left(\frac{\sin((\pi-\mu_1)Z)}{(\pi-\mu_1)^2}+\frac{\sin((\mu_1+\pi)Z)}{(\mu_1+\pi)^2}\right)+1.37137\,Z \end{aligned}\right\} \tag{18}$$

and $\mu_1 = 4.73004074\ (4)$.

Substituting Eq. (16) into Eqs. (11)-(13) and using the orthogonalization procedure of the Galerkin technique, the following Lorenz model is obtained:

$$\frac{dA}{d\tau} = \Pr(-q_{11}(k_c,\mu_1)\,A + q_{13}(k_c,\mu_1)\,B + q_{12}(k_c,\mu_1)\,t_1\,G), \tag{19}$$

$$\frac{dG}{d\tau} = -\Pr(q_{21}(k_c,\mu_1)\,G + q_{22}(k_c,\mu_1)\,t_1\,A), \tag{20}$$

$$\frac{dB}{d\tau} = -q_{314}(k_c,\mu_1)\,AC + q_{31}(k_c,\mu_1)\,rA - B, \tag{21}$$

$$\frac{dC}{d\tau} = q_{413}(k_c,\mu_1)\,AB - b\,C, \tag{22}$$

where, $b = \frac{4\pi^2}{\delta^2}, \delta = \sqrt{\pi^2+k_c^2}, t_1 = \frac{\pi\sqrt{Ta}}{\delta^3}$ and the other quantities are recorded in the appendix.

The above Lorenz model does not take care of interaction of rolls. In the next section we consider such an interaction.

4 Lorenz model for secondary instability – Küppers-Lortz

In this section we extend the above Lorenz model to account for the KL-instability which is three-dimensional. We now introduce Y-dependence in the fields and so we take

$$\left.\begin{aligned} U[X,Y,Z,\tau] = -\frac{\sqrt{2}\delta^2}{k\pi}A(\tau)\sin(k_c X)\ C_{f'}(Z) \\ -\frac{\sqrt{2}\delta^2}{k^2\pi}\left[k_1 A_1(\tau)+k_2\,\delta\,G_1(\tau)\right]\sin(k_1 X+k_2 Y)\,C_{f'}(Z) \end{aligned}\right\}, \tag{23}$$

$$\left.\begin{aligned} V(X,Y,Z,\tau) = \frac{\sqrt{2}\delta^3}{k\pi}G(\tau)\sin(k_c X)\,C_{f'}(Z) \\ -\frac{\sqrt{2}\delta^2}{k^2\pi}\left[k_2 A_1(\tau)+k_1\,\delta\,G_1(\tau)\right]\sin(k_1 X+k_2 Y)\,C_{f'}(Z) \end{aligned}\right\}, \tag{24}$$

$$W[X,Y,Z,\tau] = \frac{\sqrt{2}\delta^2}{\pi}\left[A(\tau)\, C_f(Z)\cos(k_c X) + A_1(\tau)\, C_f(Z)\cos(k_1 X + k_2 Y)\right], \quad (25)$$

$$\omega_Z(X,Y,Z,\tau) = \frac{\sqrt{2}\delta^3}{\pi}\left[G(\tau)\, C_{f'}(Z)\cos(k_c X) + G_1(\tau)\, C_{f'}(Z)\cos(k_1 X + k_2 Y)\right], \quad (26)$$

$$\left.\begin{aligned}\Theta(X,Y,Z,\tau) = \frac{\sqrt{2}\delta^6}{\pi k^2 \mathrm{Ra}}\, B(\tau)\cos(k_c X)\sin\left[\pi\left(Z+\tfrac{1}{2}\right)\right] \\ + \frac{\delta^6}{\pi k^2 \mathrm{Ra}}\, C(\tau)\, F[Z] \\ + \frac{\sqrt{2}\delta^6}{\pi k^2 \mathrm{Ra}}\, B_1(\tau)\cos(k_1 X + k_2 Y)\sin\left[\pi\left(Z+\tfrac{1}{2}\right)\right] \\ + \frac{\delta^6}{\pi k^2 \mathrm{Ra}}\, C_1(\tau)\cos(X(k_c + k_1) + k_2 Y)\, F(Z) \\ + \frac{\delta^6}{\pi k^2 \mathrm{Ra}}\, C_2(\tau)\cos(X(-k_c + k_1) + k_2 Y)\, F(Z)\end{aligned}\right\}. \quad (27)$$

The ninth-order Lorenz model is now obtained using Eqs. (11), (12), (13), (23)-(27) as follows:

$$\frac{dA}{d\tau} = \mathrm{Pr}(-q_{11}(k_c,\mu_1)\, A + q_{13}(k_c,\mu_1)\, B + q_{12}(k_c,\mu_1)\, t_1\, G), \quad (28)$$

$$\frac{dG}{d\tau} = -\mathrm{Pr}(q_{21}(k_c,\mu_1)\, G + q_{22}(k_c,\mu_1)\, t_1\, A), \quad (29)$$

$$\left.\begin{aligned}\frac{dB}{d\tau} = -q_{314}(k_c,\mu_1)\, AC + q_{31}(k_c,\mu_1)\, rA - B \\ -q_{358}(k_c,\mu_1,\psi)\, A_1 C_1 \frac{1-\cos(\psi)}{4} - q_{359}(k_c,\mu_1,\psi)\, A_1 C_2 \frac{1+\cos(\psi)}{4} \\ -q_{368}(k_c,\mu_1)\, G_1 C_1 c \frac{\sin(\psi)}{4} + q_{368}(k_c,\mu_1)\, G_1 C_2 c \frac{\sin(\psi)}{4}\end{aligned}\right\}, \quad (30)$$

$$\frac{dC}{d\tau} = q_{413}(k_c,\mu_1)\, AB + q_{413}(k_c,\mu_1)\, A_1 B_1 - bC, \quad (31)$$

$$\frac{dA_1}{d\tau} = \mathrm{Pr}(-q_{55}(k_c,\mu_1,\psi)\, A_1 + q_{12}(k_c,\mu_1)\, B_1 + q_{13}(k_c,\mu_1)\, t_1\, G_1), \quad (32)$$

$$\frac{dG_1}{d\tau} = -\mathrm{Pr}(q_{66}(k_c,\mu_1,\psi)\, G_1 + q_{65}(k_c,\mu_1)\, t_1\, A_1), \quad (33)$$

$$\left.\begin{aligned}\frac{dB_1}{d\tau} = -q_{754}(k_c,\mu_1)\, A_1 C + q_{75}(k_c,\mu_1)\, rA_1 - B_1 \\ -q_{718}(k_c,\mu_1,\psi)\, AC_1 \frac{1-\cos(\psi)}{4} - q_{719}(k_c,\mu_1,\psi)\, AC_2 \frac{1+\cos(\psi)}{4} \\ +q_{728}(k_c,\mu_1)\, c\frac{\sin(\psi)}{4}\, GC_1 - q_{728}(k_c,\mu_1)\, c\frac{\sin(\psi)}{4}\, GC_2\end{aligned}\right\}, \quad (34)$$

$$\frac{dC_1}{d\tau} = q_{835}(k_c,\mu_1,\psi)\frac{(1-\cos\psi)}{2}(BA_1 + AB_1) - b_+ C_1 + q_{863}(\mu_1)\, c\frac{\sin\psi}{2}(G_1 B - GB_1), \quad (35)$$

$$\frac{dC_2}{d\tau} = q_{935}(k_c,\mu_1,\psi)\frac{(1+\cos\psi)}{2}(BA_1 + AB_1) - b_- C_2 + q_{863}(\mu_1)\, c\frac{\sin\psi}{2}(GB_1 - G_1 B), \quad (36)$$

where $k_1 = k_c\, cos(\psi), k_2 = k_c\, sin(\psi), k_c^2 = k_1^2 + k_2^2, c = \frac{\delta}{\pi}$ and

$$b_{\pm} = \frac{4\pi^2 + 2k_c^2(1 \pm \cos(\psi))}{\pi^2 + k_c^2}.$$

The other quantities appearing in the Lorenz model are recorded in the appendix. Assuming the solution of the form e^{pt} for the linearized nine-mode Lorenz model Eqs. (28)-(36), we get an equation of 5th degree in p. In obtaining this we have linearized the Lorenz model around the trivial solution (0,0,0,0,0,0,0,0,0) and disregarded those equations that are independent of other variables. The fifth-degree polynomial so obtained is

$$p^5 + l_4\, p^4 + l_3\, p^3 + l_2\, p^2 + l_1\, p + l_0 = 0, \tag{37}$$

where the $l_i{}'s$ are complicated functions of the parameters of the problem and are not recorded here due to paucity of space. From Eq. (37) we have the condition $l_0 = 0$, which gives us the least value of p to be zero. This condition yields an expression for the angle of inclination in terms of the scaled Taylor number, Ta, the wave number, k, and the Prandtl number, Pr.

The critical angle and the critical Taylor number at which the KL-instability occurs are $\psi_c = 58.74$ and $Ta_c = 2583.99$ respectively.

5 Conclusion

Comparing the results of our study using rigid isothermal boundaries with the corrected values (Kanchana et al. (9)) of those of stress-free isothermal boundaries by Bhattacharjee and McKane (1), we find that

$$Ta_c^{RR} > Ta_c^{FF} \text{ and } \psi_c^{RR} > \psi_c^{FF}.$$

We also mention here that the values given above are estimates but nevertheless serve the purpose of qualitative comparison between the results of the two boundaries.

Acknowledgement

One of the authors (B. N. Shivakumar) would like to thank the Department of Backward Classes Welfare, Government of Karnataka for providing fellowship to carry out his research work. The authors would like to thank the Bangalore University for support.

References

J. K. Bhattacharjee and A. J. McKane. Lorenz model for the rotating Rayleigh-Bénardproblem. Journal of Physics A: Mathematical and General, 21: L555–L558, 1988.

J. K. Bhattacharjee. Convection in rotating binary mixtures. I. Thresholds. Physics of Fluids, 31:2456–2461, 1988.

E. Bodenschatz, D. S. Cannell, J. R. de Bruyn, R. Ecke, Y. Hu, K. Lerman, and G. Ahlers. Experiments on three systems with non-variational aspects. Physica D: Nonlinear Phenomena, 61:77–93, 1992.

S. Chandrasekhar and W. H. Reid. On the expansion of functions which satisfy four boundary conditions. Proceedings of the National Academy of Sciences, 43:521–527, 1957.

S. Chandrasekhar. The instability of a layer of fluid heated below and subject to Coriolis forces. Proceedings of the Royal Society of London. Series A. Mathematical and Physical Sciences, 217:306–327, 1953.

S. Chandrasekhar. Hydrodynamic and Hydrodynamic stability. Oxford University Press, New York, 1961.

T. Clune and E. Knobloch. Pattern selection in rotating convection with experimental boundary conditions. Physical Review E, 47:2536–2550, 1993.

T. Desaive, M. Hennenberg, and G. Lebon. Thermal instability of a rotating saturated porous medium heated from below and submitted to rotation. The European Physical Journal B-Condensed Matter and Complex Systems, 29:641–647, 2002.

C. Kanchana, Yi Zhao and P. G. Siddheshwar. Küppers–Lortz instability in rotating Rayleigh–Bénard convection bounded by rigid/free isothermal boundaries. Applied Mathematics and Computation, 385: 125406-1--125406-25, 2020.

G. Küppers and D. Lortz. Transition from laminar convection to thermal turbulence in a rotating fluid layer. Journal of Fluid Mechanics, 35:609–620, 1969.

L. Ning and R. E. Ecke. Küppers-Lortz transition at high dimensionless rotation rates in rotating Rayleigh-Bénard convection. Physical Review E, 47: R2991, 1993.

Y. Rameshwar, S. Sultana, and S. G. Tagare. Küppers-Lortz instability in rotating Rayleigh-Bénard convection in a porous medium. Meccanica, 48:2401–2414, 2013.

A. Rubio, J. M. Lopez, and F. Marques. Onset of Küppers–Lortz-like dynamics in finite rotating thermal convection. Journal of Fluid Mechanics, 644:337–357, 2010.

P. G. Siddheshwar and T. N. Sakshath. Rayleigh–Bénard–Taylor convection of Newtonian nanoliquid. World Acad. Sci. Eng. Technol. Int. J. Mech. Aerosp. Ind. Mech. Manuf. Eng, 11:1131–1135, 2017.

P. G. Siddheshwar, C. Siddabasappa, and D. Laroze. Küppers–Lortz instability in the rotaing Brinkman–Bénard problem. Journal of Fluid Mechanics, 2019, Submitted to the Journal.

R. Toral, M. San Miguel, and R. Gallego. Period stabilization in the Busse–Heikes model of the Küppers–Lortz instability. Physica A: Statistical Mechanics and its Applications, 280:315–336, 2000.

F. Zhong, R. E. Ecke, and V. Steinberg. Rotating Rayleigh-Bénard convection: the Küppers-Lortz transition. Technical report, Los Alamos National Lab., NM (USA), 1990.

Appendix

Q_1 to Q_6 are functions of μ_1 and are given by

$$Q_1 = \frac{4\pi^2\mu_1^2}{\pi^4-\mu_1^4},\ Q_2 = \frac{\pi\left((\mu_1-\sin(\mu_1))\sec^2\left(\frac{\mu_1}{2}\right)+(\mu_1-\sinh(\mu_1))\operatorname{sech}^2\left(\frac{\mu_1}{2}\right)\right)}{2\mu_1},$$

$$Q_3 = \frac{1}{2}\pi\mu_1\left((\mu_1+\sin(\mu_1))\sec^2\left(\frac{\mu_1}{2}\right)-\frac{2(\mu_1+\sinh(\mu_1))}{\cosh(\mu_1)+1}\right),$$

$$Q_4 = \frac{1}{2}\pi\mu_1\left((\mu_1+\sinh(\mu_1))\operatorname{sech}^2\left(\frac{\mu_1}{2}\right)-\frac{2(\mu_1+\sin(\mu_1))}{\cos(\mu_1)+1}\right),$$

$$Q_5 = \frac{1}{2}\pi\mu_1^3\left((\sin(\mu_1)-\mu_1)\sec^2\left(\frac{\mu_1}{2}\right)+(\sinh(\mu_1)-\mu_1)\operatorname{sech}^2\left(\frac{\mu_1}{2}\right)\right),$$

$$Q_6 = \frac{1}{2}\pi\mu_1\left(-2\tanh\left(\frac{\mu_1}{2}\right)+(-\mu_1)\operatorname{sech}^2\left(\frac{\mu_1}{2}\right)+(\mu_1+\sin(\mu_1))\sec^2\left(\frac{\mu_1}{2}\right)\right).$$

The coefficients of the Lorenz model are given by

$$q_{11}(k_c,\mu_1) = \frac{p_4k_c^2+p_5k_c^4+p_3}{(k_c^2+\pi^2)(p_5k_c^2+p_6)}, q_{12}(k_c,\mu_1) = \frac{p_2(k_c^2+\pi^2)}{\pi(p_5k_c^2+p_6)},$$

$$q_{13}(k_c,\mu_1) = -\frac{p_1(k_c^2+\pi^2)}{p_5k_c^2+p_6}, q_{21}(k_c,\mu_1) = \frac{3\pi^2}{k_c^2+\pi^2}+1,$$

$$q_{22}(k_c,\mu_1) = \frac{2\,p_2}{\pi}, q_{31}(k_c,\mu_1) = \frac{13827.04\pi\mu_1^2(\mu_1^4-81\pi^4)}{p_8},$$

$$q_{314}(k_c,\mu_1) = \frac{16\pi\mu_1^2(\mu_1^4+39\pi^4)}{p_8}, q_{413}(k_c,\mu_1) = \frac{8\pi p_9}{p_8},$$

$$q_{358}(k_c,\mu_1,\psi) = -\frac{32\pi^3\mu_1^2\csc(\psi)\sec(\psi)\left((\mu_1^4+9\pi^4)\cos(2\psi)+30\pi^4\right)}{p_8k_c^2(\cos(\psi)-1)},$$

$$q_{359}(k_c,\mu_1,\psi) = \frac{32\pi\mu_1^2(2(\mu_1^4+9\pi^4)\cos(\psi)-\mu_1^4+21\pi^4)}{p_8(\cos(\psi)+1)},$$

$$q_{368}(k_c,\mu_1) = \frac{64\pi^2\mu_1^2(\mu_1^4+9\pi^4)}{p_8},$$

$$q_{55}(k_c,\mu_1,\psi)=\frac{a_c^4\left((2p_5-p_7)\cos(4\psi)+6p_5+p_7\right)+8p_4k_c^2\cos^2(\psi)+8p_3}{8(k_c^2+\pi^2)(p_5k_c^2+p_6)},$$

$$q_{65}(k_c,\mu_1)=-\frac{2p_1}{\pi},q_{66}(k_c,\mu_1,\psi)=-\frac{k_c^2\cos^2(\psi)+4\pi^2}{k_c^2+\pi^2},$$

$$q_{754}(k_c,\mu_1)=\frac{16\pi\mu_1^2(\mu_1^4+39\pi^4)}{p_8},q_{75}(k_c,\mu_1)=\frac{8\pi\mu_1^2(\mu_1^4-81\pi^4)}{p_8},$$

$$q_{718}(k_c,\mu_1)=\frac{32\pi\mu_1^2(2(\mu_1^4+9\pi^4)\cos(\psi)+\mu_1^4-21\pi^4)}{p_8(\cos(\psi)-1)},$$

$$q_{719}(k_c,\mu_1)=\frac{32\pi\mu_1^2(2(\mu_1^4+9\pi^4)\cos(\psi)-\mu_1^4+21\pi^4)}{p_8(\cos(\psi)+1)},$$

$$q_{728}(k_c,\mu_1)=\frac{64\pi^2\mu_1^2(\mu_1^4+9\pi^4)}{p_8},$$

$$q_{835}(k_c,\mu_1,\psi)=\frac{32\pi\mu_1^2(2(\mu_1^4+9\pi^4)\cos(\psi)+\mu_1^4-21\pi^4)}{p_8(\cos(\psi)-1)},$$

$$q_{863}(\mu_1)=\frac{64\pi^2\mu_1^2(\mu_1^4+9\pi^4)}{p_8},$$

$$q_{935}(k_c,\mu_1,\psi)=\frac{32\pi\mu_1^2(2(\mu_1^4+9\pi^4)\cos(\psi)-\mu_1^4+21\pi^4)}{p_8(\cos(\psi)+1)},$$

p_1 to p_9 are functions of μ_1 and are given by

$$p_1=\frac{2\pi}{\pi^2-\mu_1^2}-\frac{2\pi}{\mu_1^2+\pi^2},p_2=\frac{4\pi\mu_1\tan\left(\frac{\mu_1}{2}\right)}{\mu_1^2-4\pi^2}-\frac{4\pi\mu_1\tanh\left(\frac{\mu_1}{2}\right)}{\mu_1^2+4\pi^2},$$

$$p_3=\frac{\mu_1^3(\mu_1+\sin(\mu_1))}{\cos(\mu_1)+1}-2\mu_1^3\left(\tan\left(\frac{\mu_1}{2}\right)+\tanh\left(\frac{\mu_1}{2}\right)\right)+\frac{\mu_1^3(\mu_1+\sinh(\mu_1))}{\cosh(\mu_1)+1},$$

$$p_4=\mu_1(\mu_1+\sin(\mu_1))\sec^2\left(\frac{\mu_1}{2}\right)-\mu_1(\mu_1+\sinh(\mu_1))\operatorname{sech}^2\left(\frac{\mu_1}{2}\right),$$

$$p_5=\frac{\mu_1+\sin(\mu_1)}{\mu_1(\cos(\mu_1)+1)}-\frac{2\left(\tan\left(\frac{\mu_1}{2}\right)+\tanh\left(\frac{\mu_1}{2}\right)\right)}{\mu_1}+\frac{\mu_1+\sinh(\mu_1)}{\mu_1(\cosh(\mu_1)+1)},$$

$$p_6=\frac{\mu_1(\mu_1+\sin(\mu_1))}{\mathrm{Pr}(\cos(\mu_1)+1)}-\frac{\mu_1(\mu_1+\sinh(\mu_1))}{\mathrm{Pr}(\cosh(\mu_1)+1)},$$

$$p_7 = -\frac{4\left(\tan\left(\frac{\mu_1}{2}\right)+\tanh\left(\frac{\mu_1}{2}\right)\right)}{\mu_1}+\frac{(\mu_1+\sin(\mu_1))\sec^2\left(\frac{\mu_1}{2}\right)}{\mu_1} + \frac{(\mu_1+\sinh(\mu_1))\operatorname{sech}^2\left(\frac{\mu_1}{2}\right)}{\mu_1},$$

$$p_8 = \mu_1^8 - 82\pi^4\mu_1^4 + 81\pi^8, \qquad p_9 = 2\mu_1^6 + 78\pi^4\mu_1^2.$$

Tab. 1: Comparison of ψ_c and Ta_c of rigid isothermal boundaries with those of free isothermal boundaries.

Authors	Pr	ψ_c	Ta_c	Boundaries
Bhattacharjee & McKane (1988)	∞	58.52 (corrected value)	2337.82 (corrected value)	Free-isothermal
Present paper	∞	58.74	2583.99	Rigid-isothermal

Nomenclature

Latin Symbols	Definition
$A, G, B, C,$ A_1, G_1, B_1, C_1, C_2	amplitudes
$\vec{g}$	acceleration due to gravity, $(0,0,-g)$, (m/s^2)
h	dimensional liquid layer depth (m)
p	pressure (Pa)
$\vec{q}$	velocity vector (m/s)
t	dimensional time (s)
T	dimensional temperature (K)
x	dimensional horizontal coordinate (m)
X	non-dimensional horizontal coordinate
z	dimensional vertical coordinate (m)
Z	non-dimensional vertical coordinate
Greek Symbols	
α	coefficient of thermal expansion
χ	thermal diffusivity
μ	dynamic coefficient of viscosity
ρ	fluid density
τ	non-dimensional time
Θ	non-dimensional temperature
Subscripts	
b	basic state
c and o	critical and reference value at $T = T_o$ respectively

B. Mahanthesh

Quadratic radiation and quadratic Boussinesq approximation on hybrid nanoliquid flow

On quadratic Rosseland approximation

Abstract: A novel quadratic Rosseland radiative heat phenomenon along with quadratic density temperature variation (QDT) is proposed in this study to scrutinize the heat transfer characteristics of hybrid nanoliquid past a vertical plate, numerically. The effect of quadratic thermal radiation on the dynamics of fluid is studied for the first time. The analysis is carried out for single-phase water (H_2O) based $Cu - Al_2O_3$ hybrid nanoliquid. The Response Surface Methodology (RSM) is utilized to perform the optimization procedure. Three physical parameters of quadratic radiative heat ($1 \leq R \leq 3$), quadratic convection ($0.1 \leq \alpha \leq 0.9$), and nanoparticle volume fraction ($0.01 \leq \phi 1 \leq 0.03$) of in three levels were chosen to achieve maximum heat transfer. Further, a parametric analysis is carried for the wall heat transfer flux, and the wall shear stress. The nonlinear equations are treated by using the Runge-Kutta-Felhberg based shooting method. The results showed that the thermal field in the case of quadratic thermal radiation higher than the linear thermal radiation case. Also, the sensitivity of wall heat flux to quadratic thermal radiation is positive whereas its sensitivity is negative to quadratic convection.

Keywords: Hybrid nanofluid; Quadratic Rosseland thermal radiation; Quadratic density temperature variation; Response Surface Methodology; Sensitivity analysis.

1 Introduction

1.1 Quadratic density temperature variation

The density of liquids commonly depends on the pressure, temperature, and concentration, and can be estimated by some subsequent equation of state. According to the Boussinesq approximation, i) the density fluctuation can be ignored in all but not in the body force term, i.e., the density can be treated as unvarying in the expressions of conservation laws of mass and momentum, except when it is associated with acceleration due to gravity in the buoyancy force. ii) the density variation in

B. Mahanthesh, Department of Mathematics, CHRIST (Deemed to be University), Bengaluru-560029, India, mahanthesh.b@christuniversity.in

https://doi.org/10.1515/9783110696080-002

the advent of motion due to mainly thermal characteristics. The processes wherein the buoyancy force takes place solely due to thermal difference have gained significant consideration for both non-transient and transient, internal and external flows, both turbulent and laminar, and with various additional imposed conditions and effects. For a treatise on the validity of this approximation see Gray and Giorgini (1). Boussinesq in the year 1903 proposed the mathematical model to govern the buoyant driven flow of liquids over vertical geometries by considering body force term. According to Joseph Valentine Boussinesq, if ρ_∞ signify the ambient density of the fluid at the free stream where the temperature/concentration is sufficiently low T_∞/C_∞. The density model by using Taylor series expansion for $\beta\Delta T \ll 1$ and $\beta\Delta C \ll 1$ is presented as (see Gebhart (2)).

$$g(\rho_\infty - \rho) = g\rho[\beta(T - T_\infty) + \beta^*(C - C_\infty)],$$

where $\beta = -\frac{1}{\rho}\left(\frac{\partial\rho}{\partial T}\right)_{C,p}$ and $\beta^* = -\frac{1}{\rho}\left(\frac{\partial\rho}{\partial C}\right)_{T,p}$ are the thermal expansion coefficient and solute expansion coefficient respectively.

Gebhart and Pera (3) studied the laminar boundary layer flow driven by the product of gravitational force and density difference. The set of relevant equations is reduced by using the Boussinesq and boundary layer approximations and subsequent equations are treated by using the similarity approach. They established that "the effect of multiple buoyancy mechanisms upon laminar stability is seen to be very simple for all flows for which the Prandtl and Schmidt numbers are equal. However, multiple buoyancy mechanisms arise in the flows which are likely to have quite complicated and variable stability characteristics. Analysis of such problems must include the coupling of disturbances through buoyancy". Demuren and Grotjans (4) investigated the Buoyancy-driven flows to establish the limits of applicability of the Boussinesq approximation. Aman and Ishak (5) scrutinized the non-transient transport over an impermeable vertical plate by using linear Boussinesq approximation. This research proved that the friction factor and the rate of heat transfer at the plate amplify as Prandtl number increases for the supplementary flow, while two solutions were found to exist for the contrasting flow. Makinde and Olanrewaju (6) used linear Boussinesq approximation to study the influence of thermal buoyancy in the boundary layer transport of fluid having $Pr = 0.72$ about a convectively heated vertical plate. They achieved the similarity solution by using Runge-Kutta numerical method when the thermal expansion coefficient is proportional to x^{-1}. Makinde and Sibanda (7) utilized the linear Boussinesq approximation to investigate the influence of the Buoyancy force on a steady laminar transport over a vertical plate in the presence of a magnetic field. Mahanthesh et al (8) studied the flow of a viscous fluid suspended with dust particles in a vertical squeezing channel in the presence of buoyancy force. Considerable attempts have been reported on fluid dynamics subjected to the linear Boussinesq approximation.

It is well known that, in processes like solar collectors, nuclear reactors, thermal exchangers, radiators, electronic equipment cooling devices, and combustion chambers the thermal difference is not necessarily sufficiently small. Hence, the density fluctuation is nonlinear and the linear Boussinesq approximation is no more appropriate in such applications. Because of this Goren (9) in the year 1966, considered density variation to vary as follows

$$\rho_\infty - \rho = \rho\gamma(T - T_\infty)^2 \text{ with} = -\frac{1}{\rho}\left(\frac{\partial\rho}{\partial T}\right)^2_{C,p},$$

γ is the thermal expansion coefficient having the dimension T^{-2}. This assumption is valid for temperature variations of magnitude $\pm 4^0$C away from 4^0C. The work of Goren (9) considered the boundary layer transport with free convection due to a semi-infinite plate maintained with uniform temperature. He obtained the similarity solution. Afterward, Sinha (10) followed the work of Goren (9) to investigate a steady-state free convection transport of H_2O between long parallel flat plates oriented in the direction of the generating body force with the effects of frictional heating and constant plate temperature. He also included the impact of quadratic density temperature variation in the analysis. On the other hand, Vajravelu and Sastri (11) seen the density fluctuation with respect to temperature from a different dimension, that is, they expressed density ($\rho(T)$) by using Taylor series about surface temperature (T_s) as follows

$$\rho(T) = \rho(T_s) + \left(\frac{\partial\rho}{\partial T}\right)_s (T - T_s) + \left(\frac{\partial^2\rho}{\partial T^2}\right)_s (T - T_s)^2 + \cdots$$

and then they truncated the series up to second-order. Hence, the density difference yields

$$\rho_\infty - \rho = \rho\beta(T - T_s) + \rho\gamma(T - T_s)^2$$

with $\beta = -\frac{1}{\rho}\left(\frac{\partial\rho}{\partial T}\right)_s$ and $\gamma = -\frac{1}{\rho}\left(\frac{\partial^2\rho}{\partial T^2}\right)_s$. Where, β and γ is thermal expansion coefficients having the dimension T^{-1} and T^{-2} correspondingly. Here in the above series expansion authors may have missed $1/2$! in the third term from the right-hand side. In this chapter, this error has been corrected in the following mathematics formulation section. Using the above relation for density difference, Vajravelu and Sastri (11) studied the heat transfer between two parallel vertical plates with free convection. In their problem, a new physical dimensionless parameter named as NDT parameter found to exist, which measures the impact of quadratic density temperature variation. They established that the temperature as well as the velocity field notably increased with positive values of the NDT parameter and declined for negative values.

Recently by following the work of Vajravelu and Sastri (11), Partha (12) investigated the effects of nonlinear temperature-concentration-dependent density relation in the flow of fluid in a non-Darcy porous medium. They also proved that the velocity profile increases with the increase of nonlinear convection parameters. Kameswaran et al (13) scrutinized the effects of nonlinear thermal and solute convection in a non-transient boundary layer transport over a vertical impermeable wall. The nonlinear/quadratic Boussinesq approximation has been employed by RamReddy (14) to study the natural convective flow of a power-law liquid over an inclined plate. Recent researches about nonlinear Boussinesq approximation are elaborated in the references (see (15)-(20) and therein).

1.2 Nanofluid

The thermally effective working liquids are essential to reduce the manufacturing and functioning price of microelectronics, nano-electronics, pharmaceutical products, hybrid power engines, and fuel cells. The performance of heat transportation can be augmented by using passive and active techniques. An increase in the heat flow via passive methods can be obtained by regulating surface geometry/roughness, functioning liquid properties, fluid movement (laminar against turbulent), liquid additives (ultra-fine nano or microparticles) and liquid suction/injection. Whereas for inactive methods external energy sources are required, i.e., via thermal radiation aspect, vibration, internal heat source/sink, mechanical mixing, magnetic field, and rotation. These modulations have been efficiently employed to augment heat transportation, leading towards useful in heat pumps, faster processing, reactors, solar collectors, and separators. Nevertheless, external energy involvement is high-priced and inappropriate under compact circumstances. Hence, the impact of the solid-liquid suspension on strengthening the performance of heat transport is elaborated experimentally and theoretically by numerous researchers following Maxwell (21). However, this idea of combining working liquids and micro-sized particles encountered significant problems such as agglomeration, clogging, fouling, abrasion, and additional pressure shortfall of the system, which turn out to be additional challenges to address. To overcome these challenges, for the first time Choi (22) introduced nanoliquids by suspending ultra-fine nanoparticles (< 50nm in diameter) disseminated in base liquid. Experimentally and theoretically, it is proved that nanoparticles (NPs) suspension in a liquid enhances the thermophysical aspects of the base liquid. NPs possess exceptional thermal, optical, magnetic, electrical, and mechanical characteristics. Some commonly used NPs are Cu, Ag, Al, Fe (made up of metals), carbon nanotubes, graphite's (made up of non-metals), TiO_2, CuO, Al_2O_3 (made up of oxides), SiC, TiC (made up of carbide pottery), alloys, etc. The NPs effectively enlarge the radiative features of liquids

which consequently improve the performance of solar collectors and many other devices where the heating and cooling process can be found.

1.3 Hybrid nanofluid

Nanoliquids are assured functioning liquids in numerous applications involving the heating/cooling process as they proficient well and exposed significant outcomes. This fact inspired the researchers to think about the suspending mixture of NPs in the functioning base liquids. Such liquids are called "hybrid nanoliquids". Hybrid nanoliquids possess higher thermophysical, chemical, and hydrodynamic properties in comparison with mono nanoliquid. Suresh et al (23) proved that the thermal performance of Al_2O_3-Cu-H_2O hybrid nanoliquid is superior to that of mono nanoliquid. They also established that inserting metallic and non-metallic NPs advance the thermophysical and chemical features of working fluids. The spinning flow of Ag-CuO-H_2O nanofluid over a flat plate was studied by Hayat and Nadeem (24) and they found that the thermal field is higher in the case of hybrid nanoliquid than that of ordinary nanoliquid. Heat transport in hybrid base fluid ($C_2H_6O_2$-H_2O/ethylene glycol-water (50-50%)) submerged with hybrid nanoparticles (MoS_2-Ag)) with natural convection and radiative heat is investigated by Ghadikolaei (25). The effects of Hall current in the transport of hybrid nanoliquid past a rotating plate under nonlinear Boussinesq approximation were analyzed by Amala and Mahanthesh (26). Ashlin and Mahanthesh (27) studied the heat transport characteristics of Cu-Al_2O_3-H_2O hybrid nanoliquid with the non-coaxial rotation of the plate. Arani et al (28) have used experimental data to investigate numerically the problem of hybrid nanoliquid transport with radiative heat transfer. Shruthy and Mahanthesh (29) studied the Rayleigh-B*é*nard convection in hybrid nanoliquid. They found that hybrid nanoliquid delays the onset of convection in comparison with mono nanoliquid. Later, Kanchana et al (30) analytically examined the impact of hybrid nanoparticles in Rayleigh-B*é*nard convection by using rigid isothermal boundary conditions. Their study shows that heat transfer augmentation in H_2O due to the insertion of Al_2O_3-Cu hybrid nanoparticles is roughly double than that of Al_2O_3 nanoparticles.

1.4 Quadratic Rosseland thermal radiation

The pioneering study on the radiative heat phenomena in the boundary layer heat flow is carried out by Smith (31). The Rosseland approximation (Rosseland (32)) had employed by Viskanta and Grosh (33) to investigate the radiative heat aspect in the flow and heat transport of a radiating fluid past a wedge. The radiative heat aspect relevance can be found in various applications such as power plants, missile re-entry, nuclear reactors, rocket combustion chambers, and solar collectors. Perdikis

and Raptis (34) studied the linearized radiative heat aspect in the dynamics of the fluid. Later, many researchers followed the work of Perdikis and Raptis (34) to investigate the linearized Rosseland radiative heat. The work of Cortell (35) extended by Pantokratoras and Fang (36) by considering the nonlinear Rosseland radiative heat aspect in the Sakiadis flow of viscous fluid, whereas Cortell (35) studied the linearized radiative heat aspect. The non-transient free convection over a vertical isothermal plate in the presence of linear or nonlinear Rosseland radiative heat was investigated by Pantokratoras (37). He considered the linear Boussinesq approximation in the buoyancy force. The nonlinear radiative heat analysis is carried out by Mahanthesh et al (38) in the study of 3D flow water-based nanoliquid over a convectively heated plate. A huge amount of research can be found in the literature concerned with both linearized thermal radiation and nonlinear thermal radiation aspect in the dynamics of fluid with various physical conditions. As stated, before this study deals with quadratic density temperature fluctuation in which temperature difference (ΔT) is assumed to be quite large. Hence, both linear and nonlinear Rosseland radiative heat aspect is inappropriate when quadratic density temperature fluctuation took into account. Hence, the prime focus of the study is to investigate the aspects of quadratic radiative heat along with quadratic density temperature variation in the Sakiadis flow of a hybrid nanofluid past a vertical plate.

1.5 Response Surface Methodology (RSM)

The Response Surface Methodology (RSM) is a statistical method used for improving and optimizing processes. It has various applications in improving the present design of products. In the industrial world, there are situations where several potential input variables impact the performance of the product or process. The origin of RSM is attributed to Box and Wilson (39) where they also explained the application of RSM in manufacturing and industrial processes. The sensitivity of the input variables is crucial in the modification of products. Hence, the researchers have started to study the sensitivity of various input variables involved in the system. Shirvan et al. (40) studied the sensitivity of the heat transfer rate with respect to the parameters for the porous solar cavity receiver by utilizing RSM. The heat transfer process of a nanofluid in a solar heat exchanger was analyzed by using the Response surface methodology and sensitivity analysis by Mamourian et al (41). The sensitivity of mean total Nusselt number and pressure drop ratio was analyzed for the variation of the effective parameters chosen. They reported that the Nusselt number has a negative sensitivity towards the Richardson number which is more than the sensitivity towards the pressure drop ratio. Recently, the response surface of the average Nusselt number was scrutinized by Pordanjani et al. (42) to study the sensitivity of the heat transfer rate towards magnetic field strength, fin relative thermal conductivity, and fin angle. The sensitivity analysis of heat transport of hybrid nanoliquid

along a vertical plate is still an open question. Hence in this chapter, the sensitivity analysis of surface heat flux and surface shear stress is proposed.

Finally, a detailed literature survey indicates that there is no such examination that addresses the aspects of quadratic Rosseland thermal radiative heat and quadratic convection (quadratic density temperature variation) on Sakiadis flow past a vertical plate. Thus, the current analysis aims to examine the mutual impact of quadratic convection and quadratic radiation aspects in the flow of a hybrid nanofluid past a vertical plate. The thermal conductivity, density, specific heat, thermal expansion coefficient, and viscosity of the composite nanoliquid depend upon nanoparticles volume fraction and computed by using phenomenological laws and conventional mixture theory. The relevant systems are computed by the Runge-Kutta-Fehlberg based shooting technique. Graphical representations reflect the behavior of various physical variables. Also, the shear effect and Nusselt number are estimated and narrated briefly for the relevant variables. The optimization procedure is carried out by using Response Surface Methodology (RSM) for the effective parameters namely, quadratic radiation parameter ($1 \leq R \leq 3$), quadratic convection parameter ($0.1 \leq \alpha \leq 0.9$) and nanoparticle volume fraction of Cu ($0.01 \leq \phi 1 \leq 0.03$) on the wall heat transfer flux (Hw) and the wall shear stress (Sw).

2 Mathematical Statement

2.1 Formulation of the Problem

The governing equations for the time-dependent flow of an incompressible hybrid nanoliquid with radiative heat flux are given below (see (11), (26), (36) and (37)):

Conservation of Mass

$$\nabla \cdot \boldsymbol{V} = 0, \tag{1}$$

Conservation of Momentum

$$\rho_{hnl}\left[\frac{\partial \boldsymbol{V}}{\partial t} + (\boldsymbol{V} \cdot \nabla)\boldsymbol{V}\right] = -\nabla p + \mu_{hnl}\nabla^2 \boldsymbol{V} + \rho_{hnl}\boldsymbol{g}, \tag{2}$$

Conservation of Energy

$$(\rho C_p)_{hnl}\left[\frac{\partial T}{\partial t} + (\boldsymbol{V} \cdot \nabla)T\right] = -\nabla(\boldsymbol{q} + q_r) + \mu_{\mathrm{hnl}}\,\Phi, \tag{3}$$

The q is heat flux and it is given by

$$\boldsymbol{q} = -k_{hnl}\nabla T. \tag{4}$$

The q_r is the net radiative heat flux subjected to the Rosseland approximation (32) for optically thick media and it is given below;

$$q_r = -\frac{4}{3k^*}\nabla(\mathrm{e_b}) \text{ where } e_b = \sigma^* T^4. \tag{5}$$

In the Eqns. (1)-(5), $\boldsymbol{V} = (u, v, w)$ is the velocity vector, T is the fluid temperature, $\boldsymbol{g}$ is the acceleration due to gravity, C_p is the specific heat, ρ is the density, k is the thermal conductivity, Φ is the conventional function related with the thermal effect of the viscous heating of energy, μ is the dynamic viscosity, $\nu = \mu/\rho$ is kinematic viscosity, p is the pressure, e_b is the blackbody emissive power, which is given in terms of the absolute temperature T by the Stefan-Boltzmann radiation law, $\sigma^* = 5.6697 \times 10^{-8}\ \mathrm{Wm^{-2}K^{-4}}$ is the Stefan–Boltzmann constant and k^* is the Rosseland mean spectral absorption coefficient. Here the subscript hnl is for hybrid nanoliquid.

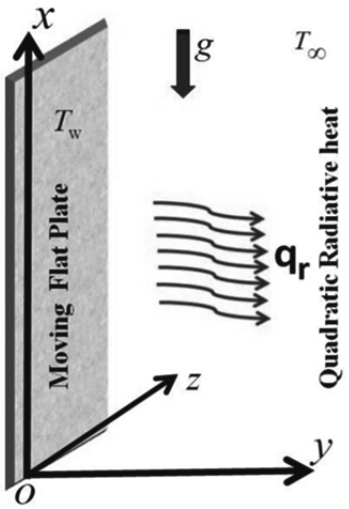

Fig. 1: The geometry of the Problem.

Here two-dimensional transport of a hybrid nanofluid past a vertical plate is considered. The plate is along the x -axis and the y-axis is perpendicular to it (see Fig. 1). The steady-state component form of governing equations under boundary layer approximations are given below;

$$\frac{\partial u}{\partial x}+\frac{\partial v}{\partial y}=0, \tag{6}$$

$$\rho_{hnl}\left(u\frac{\partial u}{\partial x}+v\frac{\partial u}{\partial y}\right)=-\frac{\partial p}{\partial x}+\mu_{hnl}\frac{\partial^2 u}{\partial y^2}+\rho_{hnl}b_x, \tag{7}$$

$$0=-\frac{\partial p}{\partial y}+\rho_{hnl}b_y, \tag{8}$$

$$(\rho C_p)_{hnl}\left(u\frac{\partial T}{\partial x}+v\frac{\partial T}{\partial y}\right)=k_{hnl}\frac{\partial^2 T}{\partial y^2}+\frac{\partial}{\partial y}\left[\frac{4\sigma^*}{3k^*}\frac{\partial T^4}{\partial y}\right]. \tag{9}$$

Since, the flow is driven along the x-direction, $b_x=-g_x$ and $b_y=0$. Then the Eqs. (7) and (8) reduced to

$$\rho_{hnl}\left(u\frac{\partial u}{\partial x}+v\frac{\partial u}{\partial y}\right)=-\frac{\partial p}{\partial x}+\mu_{hnl}\frac{\partial^2 u}{\partial y^2}-\rho_{hnl}g_x, \tag{10}$$

$$0=\frac{\partial p}{\partial y}, \tag{11}$$

now the Eqn. (11) indicate that p is not a function of y. Thus, the pressure near to the plate along y-direction is the same as that far away from the plate. For this reason, Eqn. (10) yields

$$0=-\frac{\partial p}{\partial x}-g_x\rho_{\infty_{hnl}}\,. \tag{12}$$

Here $\rho_{\infty_{hnl}}$ the density of the fluid far away from the plate. Now by eliminating $\partial p/\partial x$ from the equation (10) yields

$$\rho_{hnl}\left(u\frac{\partial u}{\partial x}+v\frac{\partial u}{\partial y}\right)=\mu_{hnl}\frac{\partial^2 u}{\partial y^2}+g_x\left(\rho_{\infty_{hnl}}-\rho_{hnl}\right). \tag{13}$$

The last term of the above equation, $g_x\left(\rho_{\infty_{hnl}}-\rho_{hnl}\right)$, where g_x is the scale of the gravity field, downward in a coordinate system taken positive upward, with condensed density assumed produced over most of the flow region as the net influence of thermal/mass diffusion. A series development of $\left(\rho_{\infty_{hnl}}-\rho_{hnl}\right)$ in terms of T, p and C, at a given increase designates that the pressure (p) effect may be ignored and also as this study only concerned about heat transfer of hybrid nanofluid flow, the temperature influence needs to be retained. A number of the thermal applications such as solar collectors, nuclear reactors, combustion, and car radiators function at reasonable to exceptionally elevated temperatures and in such circumstances, the density fluctuates nonlinearly with temperature/concentration. It can't be ignored as it affects fluid dynamic characteristics significantly. Unlike conventional studies, in this study nonlinear Boussinesq approximation (specifically quadratic Boussinesq approximation) has been employed for modeling buoyancy force (by follow-

ing (11)). Now consider density relation in terms of temperature by using Taylor series as follows;

$$\rho_{hnl}(T) = \rho_{hnl}(T_\infty) + \left(\frac{\partial \rho_{hnl}}{\partial T}\right)(T - T_\infty) + \frac{1}{2}\left(\frac{\partial^2 \rho_{hnl}}{\partial T^2}\right)(T - T_\infty)^2 + \cdots$$

Retaining only second-order terms, one can get

$$\Rightarrow \rho_{hnl} \approx \rho_{\infty_{hnl}} + \left(\frac{\partial \rho_{hnl}}{\partial T}\right)(T - T_\infty) + \frac{1}{2}\left(\frac{\partial^2 \rho_{hnl}}{\partial T^2}\right)(T - T_\infty)^2 ,$$

$$\Rightarrow \rho_{\infty_{hnl}} - \rho_{hnl} \approx -\left(\frac{\partial \rho_{hnl}}{\partial T}\right)(T - T_\infty) - \frac{1}{2}\left(\frac{\partial^2 \rho_{hnl}}{\partial T^2}\right)(T - T_\infty)^2,$$

$$\Rightarrow \frac{\rho_{\infty_{hnl}} - \rho_{hnl}}{\rho_{hnl}} \approx \beta_{0_{hnl}}(T - T_w) + \beta_{1_{hnl}}(T - T_w)^2 ,$$

$$\Rightarrow \left(\rho_{\infty_{hnl}} - \rho_{hnl}\right) \approx (\rho\beta_0)_{hnl}(T - T_w) + (\rho\beta_1)_{hnl}(T - T_w)^2. \tag{14}$$

The quadratic term of the warmth effect need be retained for $\beta_{1_{hnl}}(\Delta T)^2 \ll 1$, where $\beta_{0_{hnl}} = -\frac{1}{\rho_{hnl}}\left(\frac{\partial \rho_{hnl}}{\partial T}\right)$ and $\beta_{1_{hnl}} = -\frac{1}{2\rho_{hnl}}\left(\frac{\partial^2 \rho_{hnl}}{\partial T^2}\right)$, are the linear and quadratic volumetric coefficient of thermal expansion correspondingly.

Now in terms of Eqn. (14), the Eqn. (13) become

$$\rho_{hnl}\left(u\frac{\partial u}{\partial x} + v\frac{\partial u}{\partial y}\right) = \mu_{hnl}\frac{\partial^2 u}{\partial y^2} + g_x[(\rho\beta_0)_{hnl}(T - T_\infty) + (\rho\beta_1)_{hnl}(T - T_\infty)^2].$$

So far the aspect of thermal radiation by using Rosseland (1931) approximation is studied in two ways. First, the aspect of thermal radiation is studied in the original form as given in equation (9) and it is known as nonlinear thermal radiation. This approach results in an additional physical parameter (i.e., the temperature ratio parameter ($\theta_w = T_w/T_\infty$)). In this method, the energy equation readily takes the following form;

$$(\rho C_p)_{hnl}\left(u\frac{\partial T}{\partial x} + v\frac{\partial T}{\partial y}\right) = k_{hnl}\frac{\partial^2 T}{\partial y^2} + \frac{\partial}{\partial y}\left[\frac{16\sigma^*}{3k^*}T^3\frac{\partial T}{\partial y}\right]. \tag{15}$$

Whereas in the second method, the temperature difference is taken to very small and temperature T is expressed about T_∞ by using Taylor series as given below

$$T^4 = T_\infty^4 + 4T_\infty^3(T - T_\infty) + 6T_\infty^2(T - T_\infty)^2 + \cdots \tag{16}$$

As temperature difference supposed to be is very small, the higher-order terms are ignored. Thus, the above equation (linearized thermal radiation) yields

$$T^4 \approx 4T_\infty^3 T - 3T_\infty^4. \tag{17}$$

Upon using Eqn. (17), the temperature Eqn. (9) takes the following form

$$u\frac{\partial T}{\partial x} + v\frac{\partial T}{\partial y} = \frac{1}{(\rho C_p)_{hnl}}\left(k_{hnl} + \frac{16\sigma^* T_\infty^3}{3k^*}\right)\frac{\partial^2 T}{\partial y^2}. \tag{18}$$

This is known as linearized Rosseland thermal radiation effect. As one can observe from the above equation, the thermal radiation aspect is just an add on to the thermal conduction term.

Importantly unlike the above two methods, the novel quadratic thermal radiation aspect is considered in this chapter for the first time. The temperature T is expressed about the ambient temperature T_∞ using Taylor series and then series is truncated after the second-order term (higher-order terms are ignored after quadratic term). As density temperature variation is assumed to be quadratic to model buoyancy force (nonlinear/quadratic Boussinesq approximation). In this case T^4 can be expressed as

$$T^4 \approx T_\infty^4 + 4T_\infty^3(T - T_\infty) + 6T_\infty^2(T - T_\infty)^2,$$

$$T^4 \approx 3T_\infty^4 + 6T_\infty^2 T^2 - 8T_\infty^3,$$

By the virtue of the above equation, the energy Eqn. (9) become

$$(\rho C_p)_{hnl}\left(u\frac{\partial T}{\partial x} + v\frac{\partial T}{\partial y}\right) = \left(k_{hnl} - \frac{32\sigma^* T_\infty^3}{3k^*}\right)\frac{\partial^2 T}{\partial y^2} + \frac{24\sigma^* T_\infty^3}{3k^*}\frac{\partial^2}{\partial y^2}(T^2), \tag{19}$$

This aspect is termed as quadratic Rosseland radiation effect.

Boundary Conditions

The governing equations are solved by using the following boundary equations:

$$\text{At } y = 0\text{: } u = U_w \text{ (Plate velocity)}$$

$$v = 0 \text{ (No suction or injection velocity)}$$

$$T = T_w \text{ (Temperature of the plate)}$$

$$\text{As } y \to 0\text{: } u = 0 \text{ (velocity is zero far away from the plate)}$$

$$T = T_\infty \text{ (Constant Temperature).} \tag{20}$$

The hybrid nanoliquid thermal properties such as dynamic viscosity, thermal conductivity, specific heat, density, and thermal expansion coefficient are calculated by using phenomenological laws and conventional mixture theory.

Phenomenological laws (see (25), (27), (30))

$$\mu_{hnf} = \frac{\mu_f}{(1-\phi)^{2.5}}, \quad \phi = \phi_{Cu} + \phi_{Al_2O_3},$$

$$k_{hnf} = k_{bf}\left(\frac{k_{Al_2O_3}+(n-1)k_{bf}-(n-1)\phi_{Al_2O_3}(k_{bf}-k_{Al_2O_3})}{k_{Al_2O_3}+(n-1)k_{bf}+\phi_{Al_2O_3}(k_{bf}-k_{Al_2O_3})}\right),$$

$$k_{bf} = k_f\left(\frac{k_{Cu}+(n-1)k_f-(n-1)\phi_{Cu}(k_f-k_{Cu})}{k_{Cu}+(n-1)k_f+\phi_{Cu}(k_{bf}-k_{Cu})}\right).$$

Mixture theory

$$\rho_{hnf} = (1-\phi)\rho_f + (\phi\rho)_{Cu} + (\phi\rho)_{Al_2O_3},$$

$$\left(\rho C_p\right)_{hnf} = (1-\phi)\left(\rho C_p\right)_f + \phi_{Cu}\left(\rho C_p\right)_{Cu} + \phi_{Al_2O_3}\left(\rho C_p\right)_{Al_2O_3},$$

$$(\rho\beta_0)_{hnf} = (1-\phi)(\rho\beta_0)_f + \phi_{Cu}(\rho\beta_0)_{Cu} + \phi_{Al_2O_3}(\rho\beta_0)_{Al_2O_3},$$

$$(\rho\beta_1)_{hnf} = (1-\phi)(\rho\beta_1)_f + \phi_{Cu}(\rho\beta_1)_{Cu} + \phi_{Al_2O_3}(\rho\beta_1)_{Al_2O_3},$$

Also, the specific heat and thermal expansion coefficients of hybrid nanoliquid are estimated by using the following expressions:

$$C_{p_{hnf}} = \frac{(\rho C_p)_{hnf}}{\rho_{hnf}}, \quad \beta_{0_{hnf}} = \frac{(\rho\beta_0)_{hnf}}{\rho_{hnf}}, \quad \beta_{1_{hnf}} = \frac{(\rho\beta_1)_{hnf}}{\rho_{hnf}}.$$

3 Similarity Solution of the Problem

The similarity approach drops out the continuity equation from the set of governing equations by the introduction of the non-dimensional stream function $\Psi(x, y)$ as given below:

$$u = \frac{\partial\Psi}{\partial y} \text{ and } v = -\frac{\partial\Psi}{\partial x}. \tag{21}$$

Upon substituting the above equation, the continuity equation is identically satisfied, the other governing equations along with the boundary conditions become

Momentum equation

$$\rho_{hnl}\left(\frac{\partial\Psi}{\partial y}\frac{\partial^2\Psi}{\partial x\partial y}-\frac{\partial\Psi}{\partial x}\frac{\partial^2\Psi}{\partial y^2}\right)=\mu_{hnl}\frac{\partial^3\Psi}{\partial y^3}+g_x[(\rho\beta_0)_{hnl}(T-T_\infty)+(\rho\beta_1)_{hnl}(T-T_\infty)^2]. \quad (22)$$

Energy equation with linear thermal radiation

$$\left(\rho C_p\right)_{hnl}\left(\frac{\partial\Psi}{\partial y}\frac{\partial T}{\partial x}-\frac{\partial\Psi}{\partial x}\frac{\partial T}{\partial y}\right)=\left(k_{hnl}+\frac{16\sigma^*T_\infty^3}{3k^*}\right)\frac{\partial^2T}{\partial y^2}. \quad (23)$$

Energy equation with nonlinear thermal radiation

$$(\rho C_p)_{hnl}\left(\frac{\partial\Psi}{\partial y}\frac{\partial T}{\partial x}-\frac{\partial\Psi}{\partial x}\frac{\partial T}{\partial y}\right)=k_{hnl}\frac{\partial^2T}{\partial y^2}+\frac{\partial}{\partial y}\left[\frac{16\sigma^*}{3k^*}T^3\frac{\partial T}{\partial y}\right]. \quad (24)$$

Energy equation with quadratic thermal radiation

$$(\rho C_p)_{hnl}\left(\frac{\partial\Psi}{\partial y}\frac{\partial T}{\partial x}-\frac{\partial\Psi}{\partial x}\frac{\partial T}{\partial y}\right)=\left(k_{hnl}-\frac{32\sigma^*T_\infty^3}{3k^*}\right)\frac{\partial^2T}{\partial y^2}+\frac{24\sigma^*T_\infty^3}{3k^*}\frac{\partial^2}{\partial y^2}(T^2). \quad (25)$$

With the boundary equations:

$$\text{At } y=0:\frac{\partial\Psi}{\partial y}=U_w\,;\frac{\partial\Psi}{\partial x}=0\,;T=T_w$$

$$\text{As } y\to 0:\frac{\partial\Psi}{\partial y}=0;\ T=T_\infty\,. \quad (26)$$

Now, introduce dimensionless variables for stream function and temperature as follows;

$$\Psi(x,y)=\sqrt{\nu_l x U_w}f(\eta),$$

$$u=U_w f'(\eta),$$

$$v=-\frac{1}{2}\sqrt{\frac{\nu_l U_w}{x}}\left(\eta f'(\eta)-f(\eta)\right),$$

$$T(x,y)=\theta(\eta)(T_w-T_\infty)+T_\infty \text{ or } T(x,y)=T_\infty(\theta(\eta)(\theta_w-1)+1), \quad (27)$$

here $\eta(x,y)=\frac{y}{x}\sqrt{Re_x}=\frac{y}{\sqrt{x}}\sqrt{\frac{U_w}{\nu_l}}$ is the similarity variable and it combines two variables (x and y) into a single variable η. It is easy to verify that $\eta(x,y)$ will be non-dimensional by substituting the units of ν_l, U_w, x and y. The local Reynolds number is signified as $Re_x=\frac{\mathrm{U_w}x}{\nu_l}$.

In terms of above dimensionless variables, the following nonlinear differential equations are obtained from equations (22)-(26):

$$f'''+\frac{A_1}{2A_2}ff''+\frac{A_3}{A_2}Gr(\theta+A_4\alpha\theta^2)=0, \tag{28}$$

$$\theta''+\frac{R}{3A_5(\theta_w-1)}\frac{\partial^2}{\partial\eta^2}((\theta(\theta_w-1)+1)^4)+\frac{A_6}{2A_5}Pr\,f\theta'=0, \tag{29}$$

$$\left(A_5+\frac{4}{3}R\right)\theta''+\frac{A_6Pr}{2}f\theta'=0, \tag{30}$$

$$\left(A_5-\frac{8}{3}R\right)\theta''+\frac{A_6}{2}Pr\,f\theta'+\frac{2R}{(\theta_w-1)}\frac{\partial^2}{\partial\eta^2}(\theta(\theta_w-1)+1)^2=0, \tag{31}$$

The corresponding boundary conditions are as follows:

$$f=0, f'=1, \theta=1 \text{ at } \eta=0,$$

$$f'=0, \theta=0 \text{ as } \eta\to\infty. \tag{32}$$

The non-dimensional parameters and the constants which are involved in the above equations are given below:

$$Pr=\frac{\mu_l C_{p_l}}{k_l}, \text{ (Prandtl number)}$$

$$R=\frac{4\sigma^* T_\infty^3}{k^* k}, \text{ (Radiation parameter)}$$

$$Gr=\frac{g\beta_{0_l}(T_w-T_\infty)x}{U_w^2}, \text{ (local Grashof number)}$$

$$\alpha=\frac{\beta_{1_l}(T_0-T_H)}{\beta_{0_l}}, \text{ (nonlinear convection parameter)}$$

$$\theta_w=\frac{T_w}{T_\infty}, \text{ (temperature parameter)}$$

$$A_1=(1-\phi)+\frac{\phi_{Al_2O_3}\rho_{Al_2O_3}}{\rho_l}+\frac{\phi_{Cu}\rho_{Cu}}{\rho_l},$$

$$A_2=\frac{1}{(1-\phi)^{2.5}},$$

$$A_3 = (1-\phi) + \frac{\phi_{Cu}(\rho\beta_0)_{Cu}}{(\rho\beta_0)_l} + \frac{\phi_{Al_2O_3}(\rho\beta_0)_{Al_2O_3}}{(\rho\beta_0)_l},$$

$$A_4 = (1-\phi) + \frac{\phi_{Cu}(\rho\beta_1)_{Cu}}{(\rho\beta_1)_l} + \frac{\phi_{Al_2O_3}(\rho\beta_1)_{Al_2O_3}}{(\rho\beta_1)_l},$$

$$A_4 = \left(\frac{k_{Al_2O_3}+(n-1)k_l-(n-1)\phi_{Al_2O_3}(k_l-k_{Al_2O_3})}{k_{Al_2O_3}+(n-1)k_l+\phi_{Al_2O_3}(k_l-k_{Al_2O_3})}\right)\left(\frac{k_{Cu}+(n-1)k_{bl}-(n-1)\phi_{Cu}(k_{bl}-k_{Cu})}{k_{Cu}+(n-1)k_{bl}+\phi_{Cu}(k_{bl}-k_{Cu})}\right),$$

$$A_5 = (1-\phi) + \frac{\phi_{Cu}(\rho c_p)_{Cu}}{(\rho c_p)_l} + \frac{\phi_{Al_2O_3}(\rho c_p)_{Al_2O_3}}{(\rho c_p)_l}.$$

The wall shear stress and the wall heat transfer flux are (see (36))

$$f''(0) = \frac{\nu_l}{U_w^2} Re^{0.5} \left(\frac{du}{dy}\right)_{y=0},$$

$$\theta'(0) = -\frac{x}{T_w - T_\infty} Re^{-0.5} \left(\frac{dT}{dy}\right)_{y=0}. \tag{33}$$

4 Numerical Solution of the Problem

The subsequent set of prevailing equations (28) and (31) along with the boundary conditions (32) are strongly nonlinear and coupled in nature. It is arduous to obtain any analytical solution to this problem. This set of equations can be mutated into first-order coupled ordinary differential equations maneuvering reduction of order. The solution of the subsequent initial value problem is obtained by using the Runge-Kutta-Fehlberg method with an aid of shooting technique. The most crucial step in this routine is the selection of η_{max}. For computation, the suitable value of η_{max} is taken as 10 such that

$$f'(10) = 0 \text{ and } \theta(10) = 0.$$

Also, to achieve the convergence of the numerical solution the tolerance is set to 10^{-6}.

5 Validation of the Solution

To validate the accuracy of the present solutions, the numeric values of f, f' and Sw are obtained and compared with those of Cortell (34) when $Pr = 0.7, R = \alpha = \phi 1 = \phi 2 = 0$. From Table 1, it is inferred that comparison results are found to be an excellent agreement.

Tab. 1: Comparison of computed numerical values of f, f' and $-Sw$ with those of Cortell (34) when $Pr = 0.7, R = \alpha = \phi 1 = \phi 2 = 0$.

η	Cortell (34)			Present Results		
	f	f'	$-Sw$	f	f'	$-Sw$
0	0	1	0.4437	0	1	0.4439
0.1	0.0977	0.9557	0.4427	0.0978	0.9556	0.4428
0.2	0.1911	0.9115	0.4395	0.1911	0.9115	0.4396
0.3	0.2801	0.8678	0.4343	0.2801	0.8678	0.4345
0.4	0.3647	0.8247	0.4274	0.3647	0.8247	0.4275
0.5	0.4451	0.7824	0.4188	0.4451	0.7823	0.4189
0.6	0.5212	0.7410	0.4088	0.5212	0.7409	0.4089
0.7	0.5933	0.7007	0.3975	0.5933	0.7006	0.3977
0.8	0.6614	0.6616	0.3853	0.6614	0.6614	0.3854
0.9	0.7257	0.6237	0.3721	0.7256	0.6235	0.3723
1	0.7862	0.5872	0.3583	0.7861	0.5870	0.3584

6 Results and Discussion

6.1 Parametric study

This subsection analyses the impact of Grashof number (Gr), quadratic convection parameter (α), quadratic thermal radiation parameter (R), temperature ratio parameter (θ_w) and nanoparticle volume fractions $(\phi 1 \,\&\, \phi 2)$ on velocity $(f(\eta) \,\&\, f'(\eta))$, temperature $(\theta(\eta))$, wall shear stress (Sw), and wall heat transfer flux (Hw) profiles. Throughout the analysis, the value of shape factor (n) and Prandtl number (Pr) is respectively taken as 3 and 6.0674 for water and spherical shaped nanoparticles. The value of Pr is calculated using $\mu_f = 0.00089\ kg\,m/s$, $k_f = 0.613\ W/m\,K$, $C_{p_f} = 4179\ J/kg\,K$ and it is equal to 6.0674. Also, the thermophysical properties of based liquid H_2O and nanoparticles (Cu,Al_2O_3) are taken from Table 2.

Tab. 2: Thermophysical properties of base liquid and nanoparticles ((27)).

Physical Properties	Density (ρ)	Specific heat (C_p)	Thermal conductivity (k)	Electrical conductivity (σ)	Thermal expansion coefficient (β)
Cu	8933	385	401	$5.96X10^{7}$	$1.67X10^{-5}$
Al_2O_3	3970	765	40	$3.5X10^{7}$	$0.85X10^{-5}$
H_2O	997.1	4179	0.613	$5.5X10^{-6}$	$21X10^{-5}$

The comparison between hybrid nanoliquid (Cu-Al_2O_3-H_2O), mono nanoliquid (Al_2O_3-H_2O) and base liquid (H_2O) along with linear, quadratic and nonlinear thermal radiation effects on velocities ($f(\eta)$ & $f'(\eta)$) and temperature $\left(\theta(\eta)\right)$ distributions are presented in Figs. 2-4. In these figures, the solid lines, dash lines, and dotted lines respectively correspond to linear, quadratic, and nonlinear thermal radiation effects. Equations (29) and (30) are used to compute the results of nonlinear thermal radiation and linear thermal radiation correspondingly. It is noticed that the velocity ($f(\eta)$ & $f'(\eta)$) of the base liquid (H_2O) is greater than the mono nanoliquid (Al_2O_3-H_2O) and hybrid nanoliquid (Cu-Al_2O_3-H_2O) but, just opposite results are observed in the case of temperature $\left(\theta(\eta)\right)$ distribution. This is because of due to the addition of nanoparticles which exert more energy causing an enhancement in the temperature. The velocities ($f(\eta)$ & $f'(\eta)$) and temperature $\left(\theta(\eta)\right)$ profiles are found to be higher for nonlinear thermal radiation than that of quadratic thermal radiation followed by linear thermal radiation. Hence, utilizing nonlinear thermal radiation is more convenient for heating processes like thermal energy storage and nuclear power plants.

Figs. 5-7 depict the effect of quadratic convection parameter (α) on velocities ($f(\eta)$ & $f'(\eta)$) and temperature $\left(\theta(\eta)\right)$ profiles. It is seen that an increase α causes an enhancement in the velocity ($f(\eta)$ & $f'(\eta)$) profile because of the stronger buoyancy force. Whereas the effect of α on temperature $\left(\theta(\alpha)\right)$ profile shows the declining nature related to higher values of α. Here, $\alpha = 0$ represents a linear convective flow situation. On the other hand, the Grashof number is involved in the term $+Gr_x(\theta + A_4\alpha\theta^2)$ of Eqn. (29). Clearly, Gr is the factor of α, this indicates the impact of Grashof number will be the same as that of the quadratic convection parameter. That is an increase in local Grashof number (Gr) leads to an increase in velocity ($f(\eta)$ & $f'(\eta)$) profile due to the stronger buoyancy force caused by an increase in the positive values Grashof number. Whereas the reverse nature can be found for temperature profile $\left(\theta(\eta)\right)$.

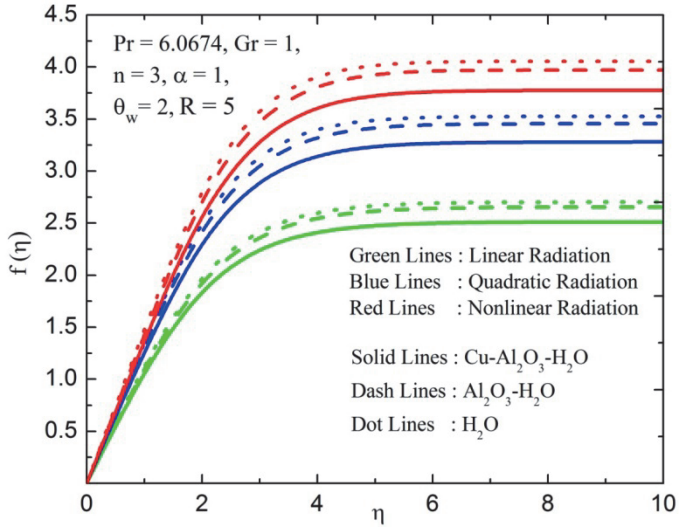

Fig. 2: Transverse Velocity profile $(f(\eta))$ versus η.

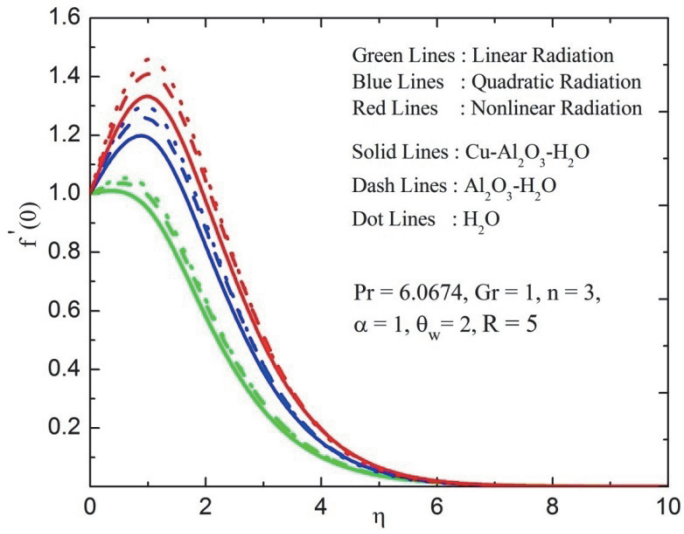

Fig. 3: Axial velocity profile $(f'(\eta))$ versus η.

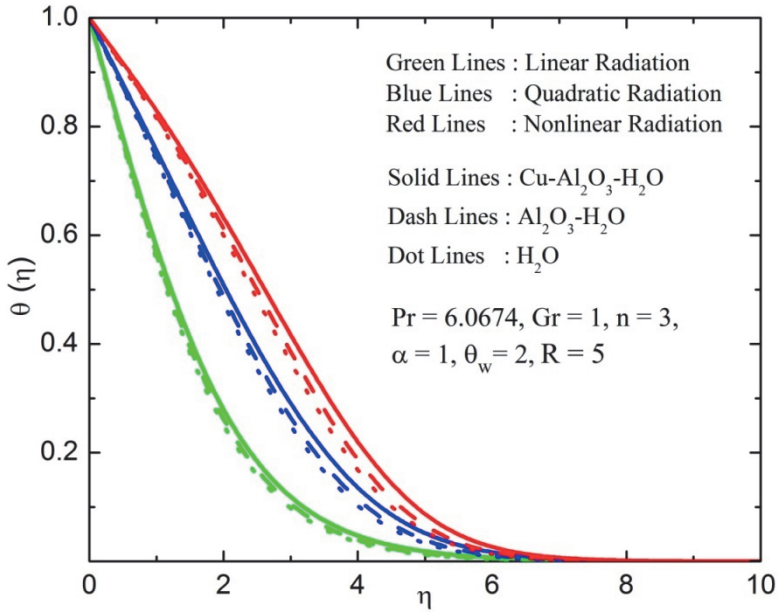

Fig. 4: Temperature profile $(\theta(\eta))$ versus η.

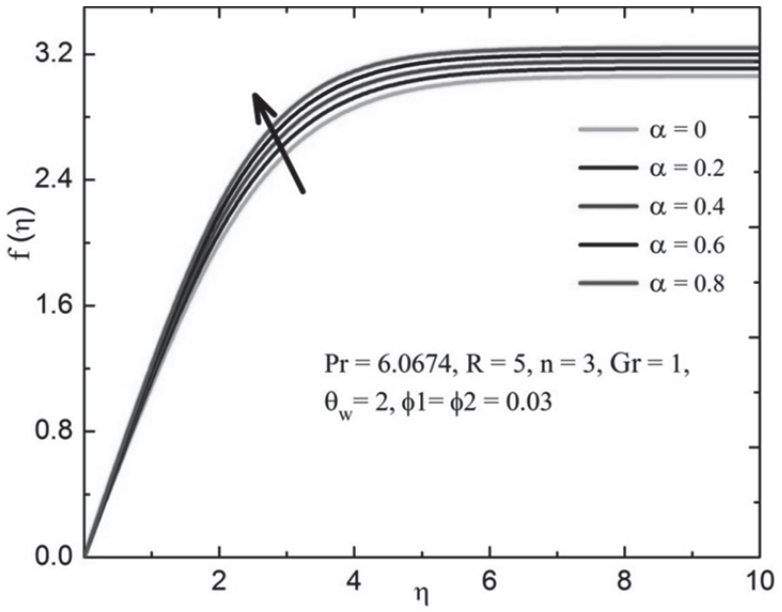

Fig. 5: Transverse Velocity profile $(f(\eta))$ for different values of quadratic convection parameter (α).

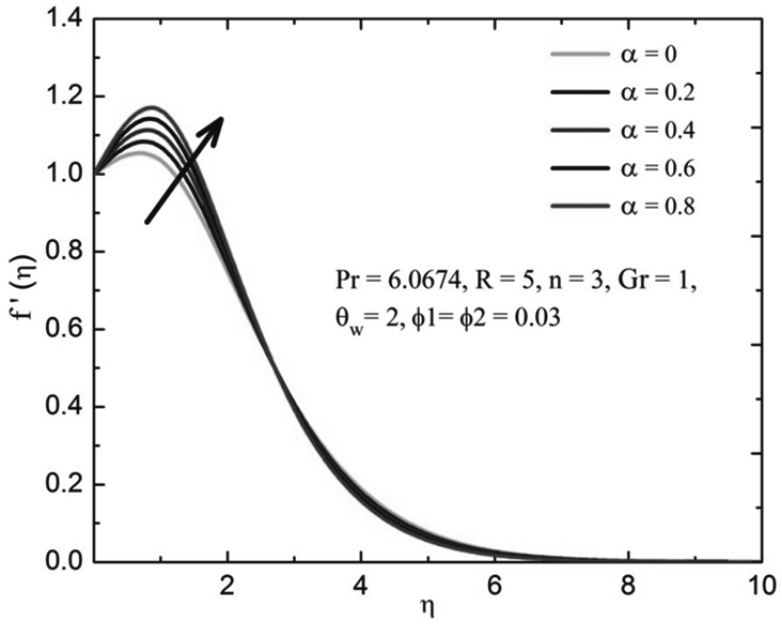

Fig. 6: Axial velocity profile $\left(f'(\eta)\right)$ for different values of quadratic convection parameter (α).

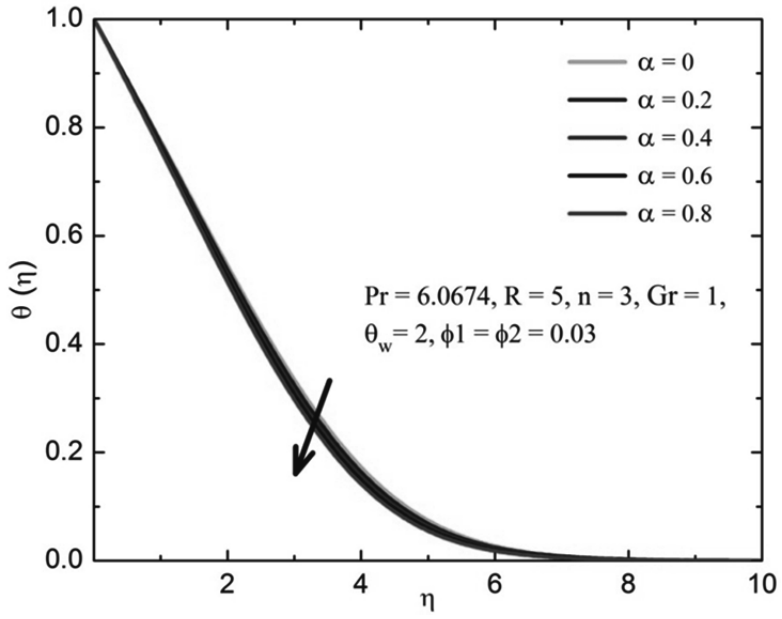

Fig. 7: Temperature profile $\left(\theta(\eta)\right)$ for different values of quadratic convection parameter (α).

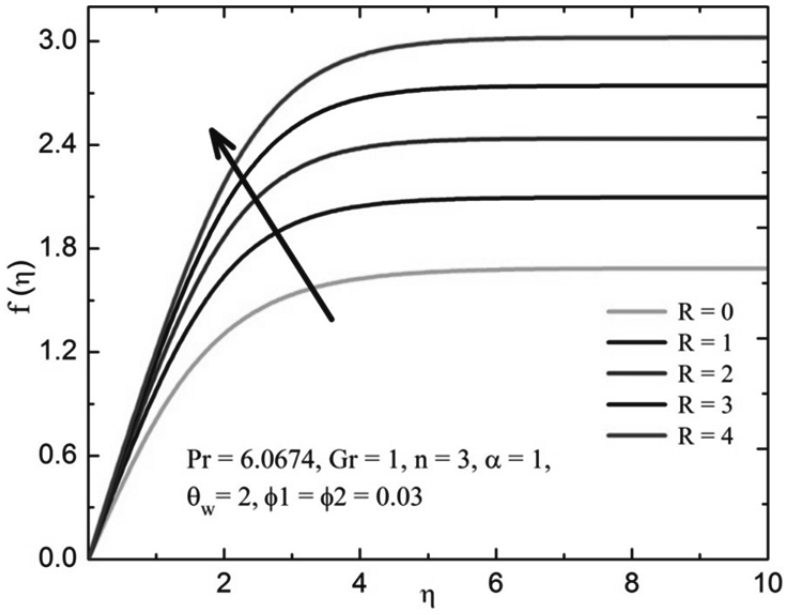

Fig. 8: Transverse Velocity profile $\left(f(\eta)\right)$ for different values of quadratic radiation parameter (R).

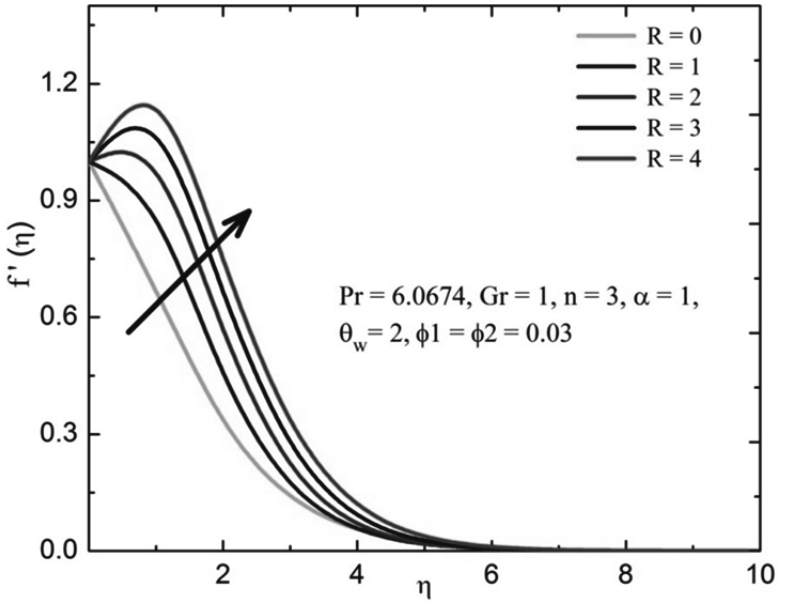

Fig. 9: Axial velocity profile $\left(f'(\eta)\right)$ for different values of quadratic radiation parameter (R).

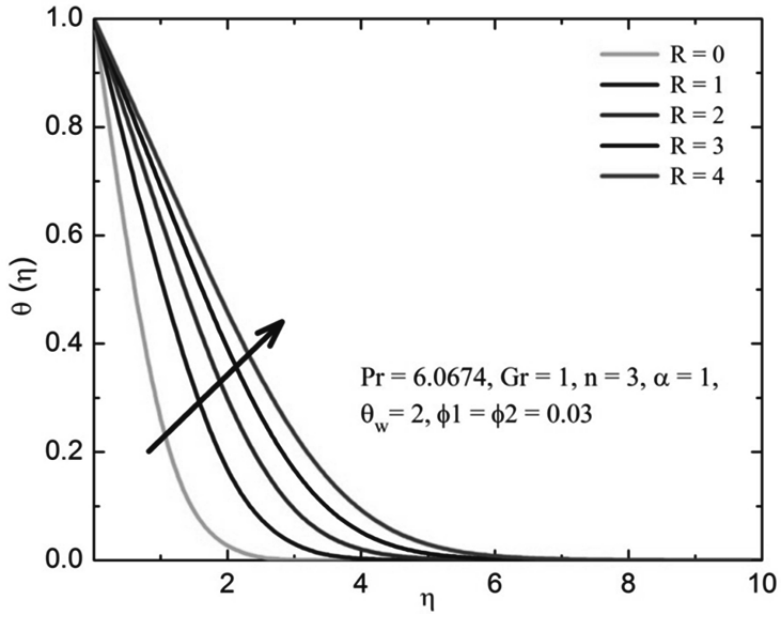

Fig. 10: Temperature profile $(\theta(\eta))$ for different values of quadratic radiation parameter (R).

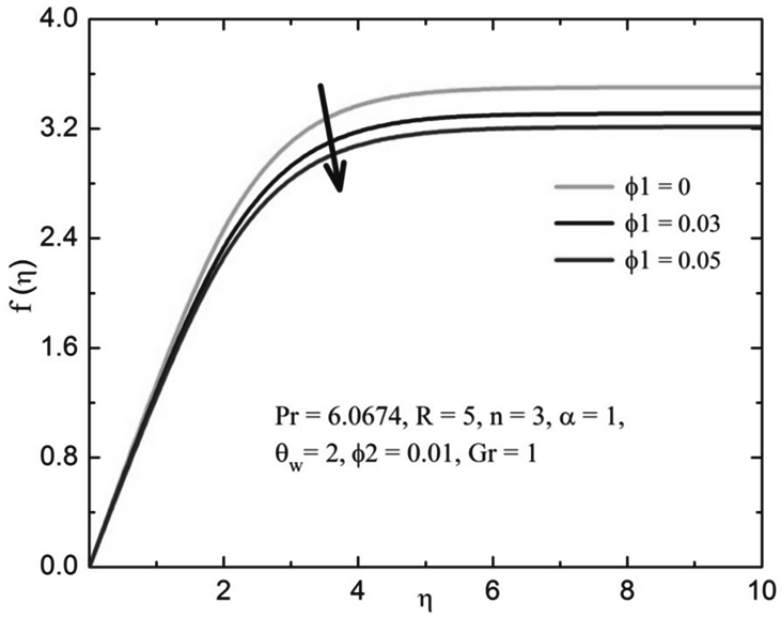

Fig. 11: Transverse Velocity profile $(f(\eta))$ for different values of nanoparticle volume fraction $(\phi 1)$.

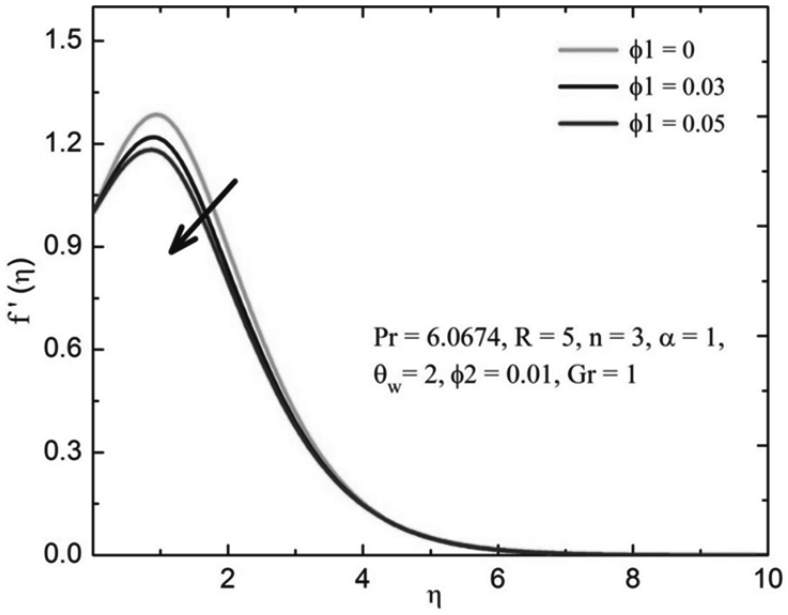

Fig. 12: Axial velocity profile $\left(f'(\eta)\right)$ for different values of nanoparticle volume fraction $(\phi 1)$.

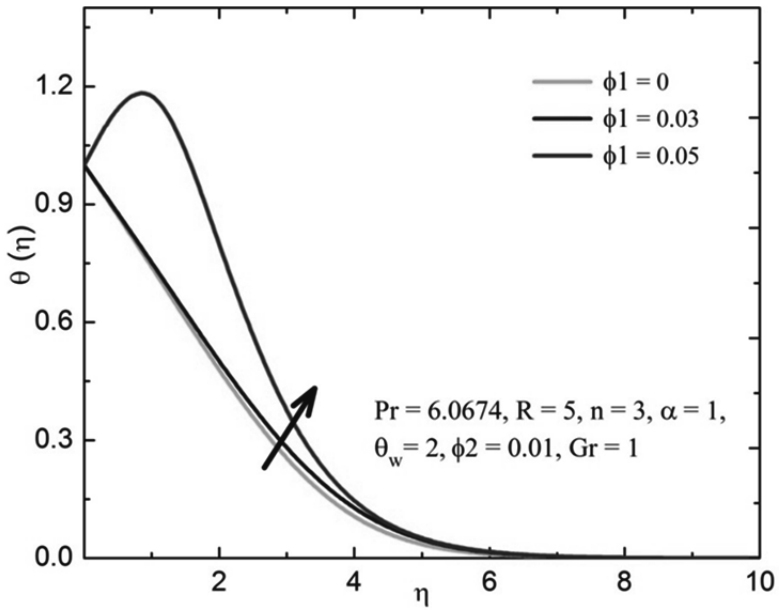

Fig. 13: Temperature profile $\left(\theta(\eta)\right)$ for different values of nanoparticle volume fraction $(\phi 1)$.

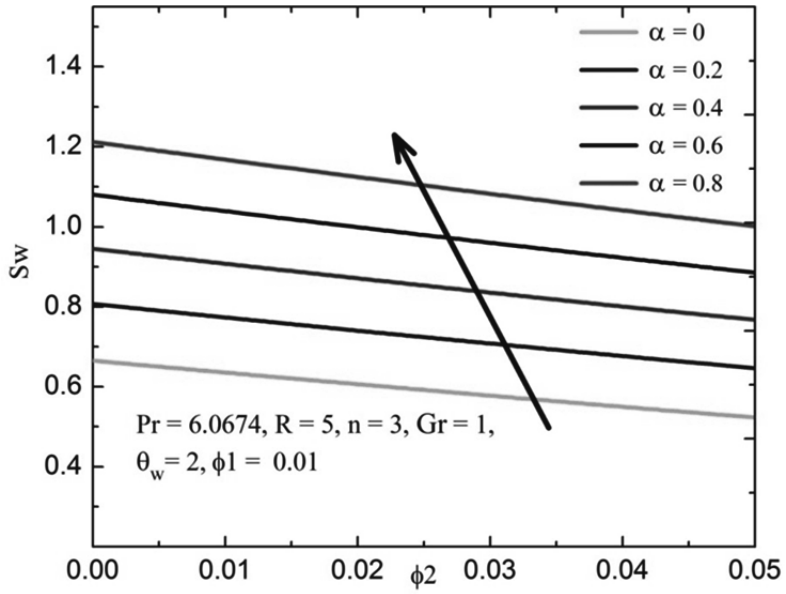

Fig. 14: Wall shear stress (Sw) for different values of quadratic convection parameter (α).

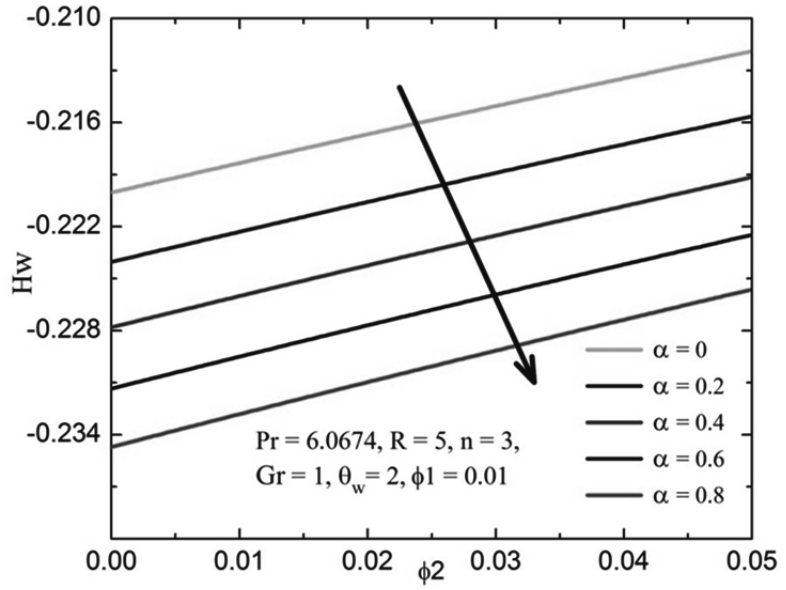

Fig. 15: Wall heat transfer flux (Hw) for different values of quadratic convection parameter (α).

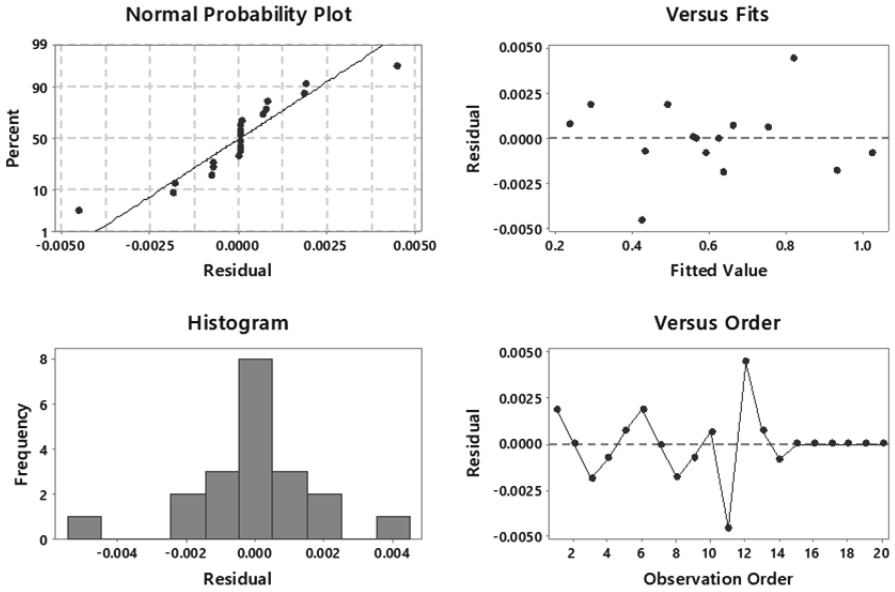

Fig. 16: Residual Plots for Sw

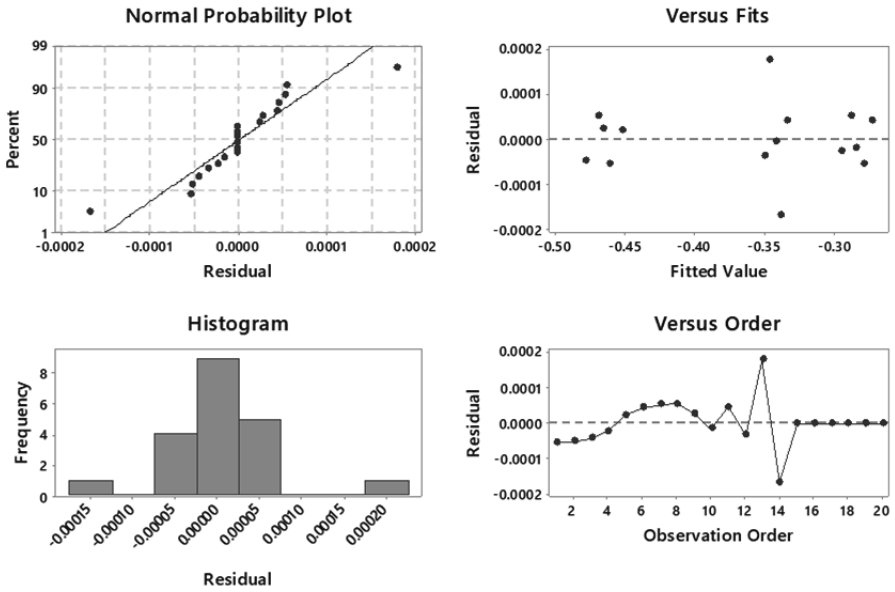

Fig. 17: Residual Plots for Hw.

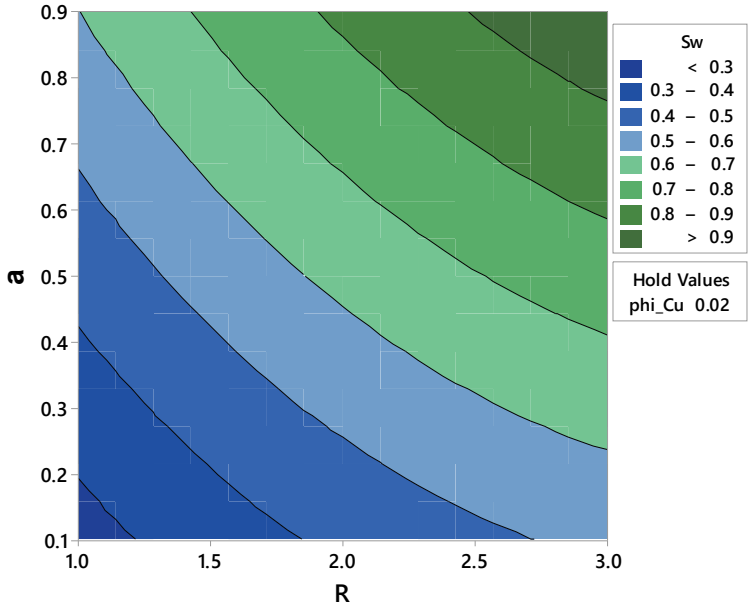

(a)

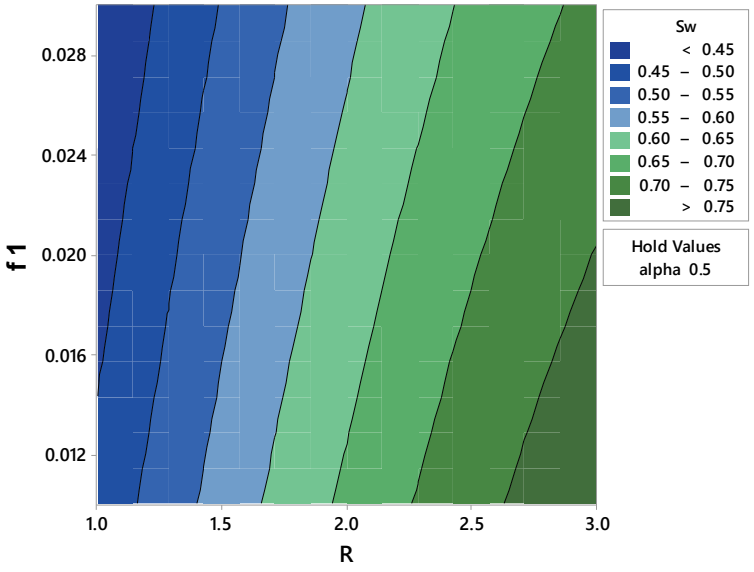

(b)

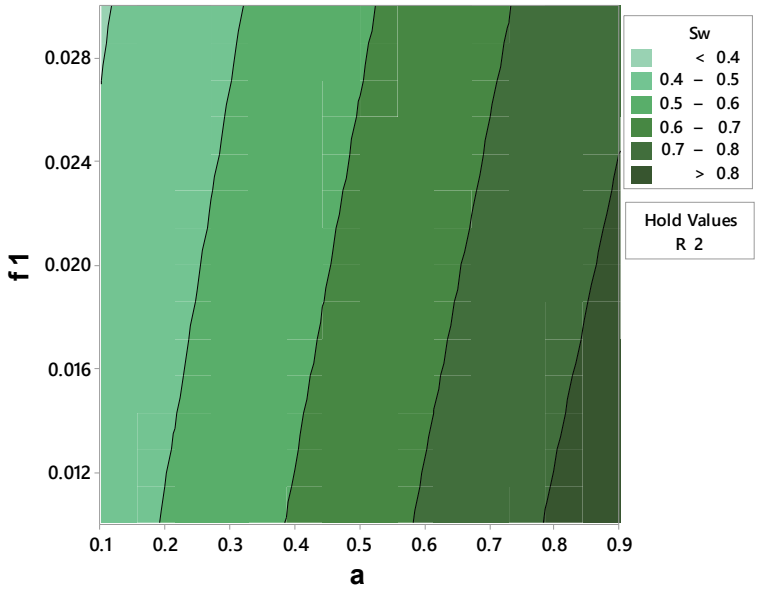

(c)

Fig. 18: Contour plots of Sw with respect to all combinations of the factor variables.

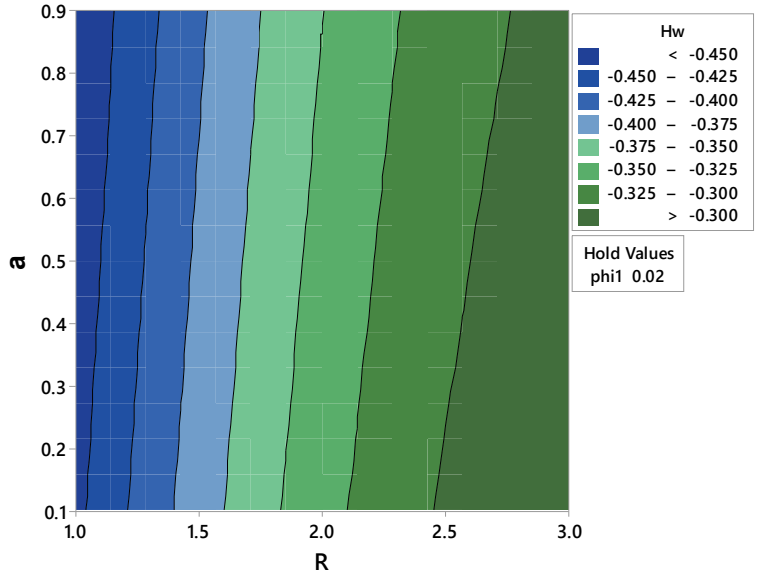

(a)

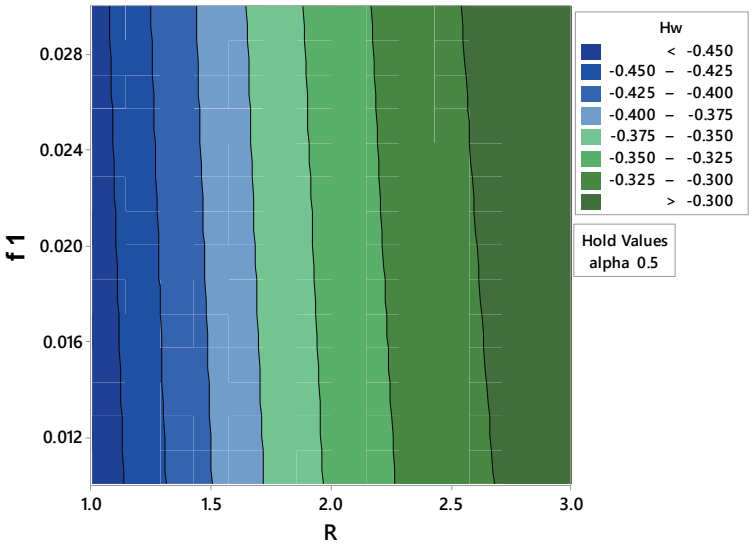

(b)

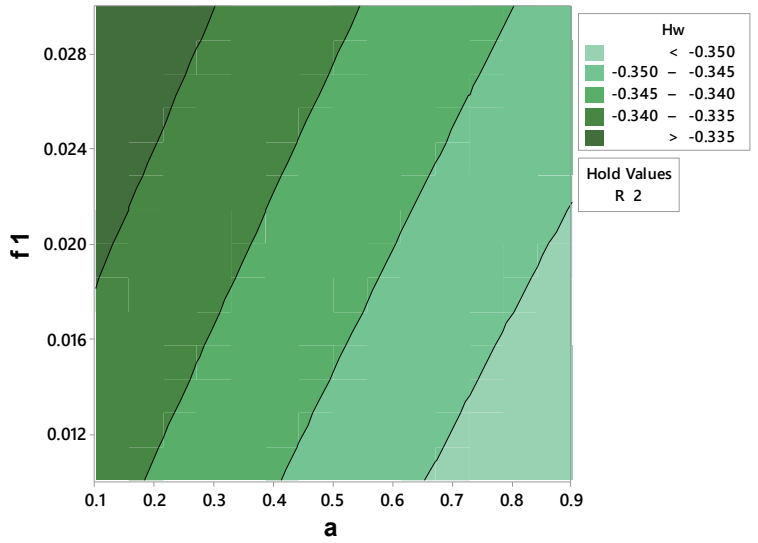

(c)

Fig. 19: Contour plots of Hw with respect to all combinations of the factor variables.

Tab. 3: Wall shear stress (Sw) and heat transfer (Hw) for different values of Gr when $\alpha = 1, R = 5, n = 3, \phi 1 = 0.03$ and $\phi_2 = 0.03$.

Gr	Linear Thermal Radiation		Quadratic Thermal Radiation		Nonlinear Thermal Radiation	
	Sw	Hw	Sw	Hw	Sw	Hw
0	-0.4730	-0.3627	-0.4730	-0.1379	-0.4730	-0.0813
1	0.6836	-0.4778	1.1050	-0.2265	1.3252	-0.1481
1.5	1.1576	-0.5070	1.7208	-0.2444	2.0149	-0.1608
2	1.6009	-0.5306	2.2933	-0.2586	2.6548	-0.1708
2.5	2.0222	-0.5507	2.8350	-0.2705	3.2595	-0.1791
Slope	0.9973	-0.0746	1.3209	-0.0523	1.4899	-0.0385

Tab. 4: Wall shear stress (Sw) and heat transfer(Hw) for different values of R when $\alpha = 1, Gr = 1, n = 3, \phi 1 = 0.03$ and $\phi 2 = 0.03$.

R	Linear Thermal Radiation		Quadratic Thermal Radiation		Nonlinear Thermal Radiation	
	Sw	Hw	Sw	Hw	Sw	Hw
0	0.0943	-1.2160	0.0943	-1.2160	0.0943	-1.2160
1	0.2968	-0.8339	0.5466	-0.4651	0.7057	-0.3147
2	0.4307	-0.6759	0.7610	-0.3441	0.9515	-0.2282
3	0.5323	-0.5843	0.9061	-0.2865	1.1116	-0.1886
4	0.6145	-0.5228	1.0162	-0.2511	1.2306	-0.1646
Slope	0.1276	0.1636	0.2203	0.2108	0.2679	0.2229

Tab. 5: Wall shear stress (Sw) and heat transfer(Hw) for different values of $\phi 1$ when $\alpha = 1, R = 5, n = 3, Gr = 1$ and $\phi 2 = 0.03$.

$\phi 1$	Linear Thermal Radiation		Quadratic Thermal Radiation		Nonlinear Thermal Radiation	
	Sw	Hw	Sw	Hw	Sw	Hw
0	0.8677	-0.5029	1.3490	-0.2393	1.6003	-0.1570
0.02	0.7859	-0.4909	1.2421	-0.2329	1.4800	-0.1524
0.03	0.7473	-0.4853	1.1916	-0.2299	1.4233	-0.1504
0.04	0.7102	-0.4799	1.1430	-0.2272	1.3686	-0.1485

$\phi 1$	Linear Thermal Radiation		Quadratic Thermal Radiation		Nonlinear Thermal Radiation	
	Sw	Hw	Sw	Hw	Sw	Hw
0.05	0.6745	-0.4747	1.0961	-0.2245	1.3158	-0.1466
Slope	-3.8680	0.5653	-5.0640	0.2949	-5.6970	0.2074

Tab. 6: Wall shear stress (Sw) and heat transfer (Hw) for different values of $\phi 2$ when $\alpha = 1, R = 5, n = 3, \phi 1 = 0.03$ and $\mathrm{Gr} = 1$.

$\phi 2$	Linear Thermal Radiation		Quadratic Thermal Radiation		Nonlinear Thermal Radiation	
	Sw	Hw	Sw	Hw	Sw	Hw
0	0.8611	-0.5008	1.3420	-0.2379	1.5927	-0.1560
0.02	0.7916	-0.4928	1.2480	-0.2341	1.4864	-0.1533
0.03	0.7581	-0.4888	1.2025	-0.2322	1.4350	-0.1521
0.04	0.7254	-0.4850	1.1581	-0.2304	1.3847	-0.1508
0.05	0.6934	-0.4811	1.1147	-0.2286	1.3355	-0.1496
Slope	-3.3560	0.3939	-4.5510	0.1857	-5.1480	0.1264

Figs. 8–10 are plotted to analyze the effect of quadratic thermal radiation parameter (R) on velocities $(f(\eta)$ & $f'(\eta))$ and temperature $\big(\theta(\eta)\big)$ profiles. Here $f(\eta)$, $f'(\eta)$ and $\theta(\eta)$ are increased with increasing values of R. Physically, an increase in R contributes more heat into the system as a result the fluid particles tend to move faster. Figs. 11-13 depict the behavior of nanoparticles volume fraction $(\phi 1)$ on $f(\eta)$, $f'(\eta)$ and $\theta(\eta)$. The inclusion of more nanoparticles makes the liquid to become denser, as a result, the velocity becomes a declining function of $\phi 1$. Whereas, $\theta(\eta)$ increases with increases in nanoparticles volume fraction due to the advance in the diffusivity of base liquid. The outcomes of variation of $\phi 2$ are qualitatively the same as the outcomes of $\phi 1$. Figs. 14-15 explore the effect of α versus $\phi 2$ on wall shear stress (Sw) and wall heat transfer flux (Hw). These figures show that Sw is an increasing function of α whereas Hw is a decreasing function of α.

The numerical values of Sw and Hw for different values of Gr when $\mathrm{R} = 5, \phi 1 = \phi 2 = 0.03, \mathrm{n} = 3,\ \theta_w = 2$ and $\mathrm{Pr} = 6.0674$ are noted for the cases of i) linear, thermal radiation, ii) quadratic thermal radiation and iii) nonlinear thermal radiation in Table 3. Further, the amount of heightening/decline in the Sw and Hw are estimated by using the slope of linear regression with the help of data points. From Table 3 it is inferred that in all three cases Sw and Hw respectively heighten and decline as the value of Gr increases. Also, it is observed that the influence of Gr on Sw is more

significant for nonlinear thermal radiation compares to that of linear and quadratic thermal radiation.

Tables 4 present the numerical values of Sw and Hw for different values of R when $Gr = 1, \phi1 = \phi2 = 0.03, \alpha = 1,\ \theta_w = 2$ and $Pr = 6.0674$. It is found that Sw and Hw heightens as the value of R increases. The effect of R on Sw and Hw is found to be more significant for nonlinear thermal radiation compares to that of linear and quadratic thermal radiation. The effect of nanoparticle volume fraction $\phi1$ and $\phi2$ on Sw and Hw are recorded in the Tables 5-6 and it is found that Sw and Hw are respectively decreasing and increasing functions of nanoparticles volume fraction. It is also depicted that; the nonlinear thermal radiation is more significant compared to quadratic and linear thermal radiation.

7 Optimization Procedure

7.1 Response Surface Methodology

The simultaneous description of parameters of interest can be obtained with the smallest possible quantitative data and resources utilizing an appropriate test design. This experimental design aims at optimizing the response variable which is affected by the independent factor variables. It is also a powerful statistical method to analyze the interaction of independent factors. The RSM method gives rise to a mathematical expression that relates the dependent variable to the factor variables. The most appropriate model was found to be a quadratic model as it depicts the interaction and square effects of the factor variables in addition to the linear effects. Hence, the quadratic model for three-factor variables is given as follows:

$$Res = \beta_0 + \sum_{i=1}^{3} \beta_i x_i + \sum_{i=1}^{3} \beta_{ii} x_i x_i + \sum_{i=1}^{3} \beta_{ij} x_i x_j, \tag{34}$$

where, β_0 is the intercept, β_i are the regression coefficients of the i^{th} linear factors, β_{ii} are the regression coefficients of the quadratic effect of the i^{th} factors, β_{ij} are the regression coefficients due to the interaction of the i^{th} and j^{th} factors and Res is the response variable (dependent variable).

7.2 Test Method

The effective parameters, quadratic thermal radiation (R), quadratic convection parameter (α) and nanoparticle volume fraction of Cu ($\phi1$) are chosen to study their impacts on the wall heat transfer flux (Hw) and the wall shear stress (Sw) by using the RSM model. The range of the model parameters are as follows:

– Quadratic thermal radiation parameter ($1 \leq R \leq 3$)

– Quadratic convection parameters ($0.1 \leq \alpha \leq 0.9$)
– Nanoparticles volume fraction of Cu ($0.01 \leq \phi 1 \leq 0.03$).

These parameters and their levels are tabulated in Table 7. -1, 0 and 1 correspond to the low, medium, and high levels respectively.

Tab. 7: Levels of the chosen effectual parameters.

Parameter	Symbol	Low (-1) Level	Medium (-1) Level	High (-1) Level
R	A	1	2	3
α	B	0.1	0.5	0.9
$\phi 1$	C	0.01	0.02	0.03

A face-centered central composite design (CCF) is used to fit the polynomial in the equation. The number of experimental runs required is given below:

$$r = 2^k + 2k + d, \tag{35}$$

where k is the number of effective parameters (Here, $n = 3$) and d is the number of central points ($d = 6$). Also, in the equation (35), 2^k denotes the number of cube points, $2k$ denotes the number of axial points. Hence, in this model, there are 20 runs with 8 cube points, 6 center points, and 6 axial points for the three independent parameters with three levels each. The experimental design and the responses for twenty runs are tabulated in Table 8.

Tab. 8: Experimental Design and Responses.

Runs	Coded values			Actual Values			Responses	
	A	B	C	R	α	$\phi 1$	Sw	Hw
1	-1	-1	-1	1	0.1	0.01	0.2882	-0.4613
2	1	-1	-1	3	0.1	0.01	0.5568	-0.2801
3	-1	1	-1	1	0.9	0.01	0.6331	-0.4788
4	1	1	-1	3	0.9	0.01	1.0189	-0.2958
5	-1	-1	1	1	0.1	0.03	0.2338	-0.4525
6	1	-1	1	3	0.1	0.03	0.4891	-0.2737
7	-1	1	1	1	0.9	0.03	0.5629	-0.4695

Runs	Coded values				Actual Values		Responses	
	A	B	C	R	α	$\phi 1$	Sw	Hw
8	1	1	1	3	0.9	0.03	0.9296	-0.2889
9	-1	0	0	1	0.5	0.02	0.4312	-0.4658
10	1	0	0	3	0.5	0.02	0.7520	-0.2849
11	0	-1	0	2	0.1	0.02	0.4166	-0.3343
12	0	1	0	2	0.9	0.02	0.8220	-0.3507
13	0	0	-1	2	0.5	0.01	0.6597	-0.3467
14	0	0	1	2	0.5	0.03	0.5874	-0.3393
15	0	0	0	2	0.5	0.02	0.6228	-0.3429
16	0	0	0	2	0.5	0.02	0.6228	-0.3429
17	0	0	0	2	0.5	0.02	0.6228	-0.3429
18	0	0	0	2	0.5	0.02	0.6228	-0.3429
19	0	0	0	2	0.5	0.02	0.6228	-0.3429
20	0	0	0	2	0.5	0.02	0.6228	-0.3429

7.2.1 Accuracy of the Model

The ANOVA table for *Sw* and *Hw* are given in Tables 9 and 10 correspondingly. The percentage of the variation in the response variable that can be explained by the predictor variables in the linear model is called the coefficient of determination (R^2). The value of R^2 lies in the range from 0% to 100%. Adjusted - R^2 is the coefficient of determination that is adjusted for the number of predictor variables in the model. It can be observed that both models have a very high coefficient of determination ($R^2 =$ 99.99% and 100 % respectively). Although the Adjusted R^2 is lesser than the R^2 values, the model fits the data satisfactorily. Also, the F-values for the models are 12961.62 and 1204729.73 respectively which are significantly large (when compared with 1). This proves the meaningfulness of the models. The F-value is the ratio of residual variances in a model without and with the independent predictor variables. If the predictor variables are not related to the response variable, then the expected F-value is 1. Hence, for a parameter to be significant, the F-value should be sufficiently large. Also, the p-value should be less than 0.05.

Tab. 9: ANOVA table for Sw.

Source	Degrees Of Freedom	Adjusted sum of squares	Adjusted mean Square	F-value	P-value	Remarks
Model	9	0.6725	0.0747	12961.62	0	Significant
Linear	3	0.6603	0.2201	38178.82	0	Significant
R	1	0.2551	0.2550	44238.21	0	Significant
α	1	0.3927	0.3928	68124.54	0	Significant
$\phi 1$	1	0.0125	0.0125	2173.71	0	Significant
Square	3	0.0054	0.0018	310.63	0	Significant
R*R	1	0.0026	0.0026	461.72	0	Significant
$\alpha * \alpha$	1	0.0003	0.0001	5.67	0.039	Significant
$\phi 1$*$\phi 1$	1	0.0001	0.0001	0.34	0.575	Insignificant
Interaction	3	0.0069	0.0022	395.40	0	Significant
R*α	1	0.0065	0.0065	1133.03	0	Significant
R*$\phi 1$	1	0.0001	0.0002	22.98	0.001	Significant
α*$\phi 1$	1	0.0002	0.0002	30.19	0	Significant
Error	10	0.0001	0.0001			
Lack-of-Fit	5	0.0001	0.0001	*	*	
Pure Error	5	0	0			
Total	19	0.6726				
			R^2 = 99.99%		Adjusted R^2=99.98%	

Tab. 10: ANOVA table for Hw.

Source	Degrees Of Freedom	Adjusted sum of squares	Adjusted mean Square	F-value	P-value	Remarks
Model	9	0.0878	0.0098	1204729.73	0	Significant
Linear	3	0.0826	0.0275	3399446.01	0	Significant
R	1	0.0818	0.0818	10096896.40	0	Significant
α	1	0.0007	0.0007	82934.71	0	Significant
$\phi 1$	1	0.0002	0.0002	18506.94	0	Significant
Square	3	0.0052	0.0017	214560.1	0	Significant
R*R	1	0.0029	0.0029	357909.4	0	Significant
$\alpha * \alpha$	1	0	0	51.57	0	Significant
$\phi 1$*$\phi 1$	1	0	0	2.94	0.117	Insignificant

Source	Degrees Of Freedom	Adjusted sum of squares	Adjusted mean Square	F-value	P-value	Remarks
Interac-tion	3	0	0	183.09	0	Significant
R*α	1	0	0	186.66	0	Significant
R*$\phi 1$	1	0	0	347.71	0	Significant
α*$\phi 1$	1	0	0	14.89	0.003	Significant
Error	10	0	0			
Lack-of-Fit	5	0	0	*	*	
Pure Error	5	0	0			
Total	19	0.0878				
			R^2 = 100%			Adjusted R^2=100%

It can be observed that the square term of $\phi 1$ is not significant for both the models as the p-values are more than 0.05 (p-values are 0.575 and 0.117). Therefore, the square term of $\phi 1$ will be removed from the model. Using the significant regression coefficients from Tables 11 and 12, the models for Sw and Hw can be given as follows:

$$Sw = 0.622764 + 0.159707\,\mathrm{R} + 0.198188\,\alpha - 0.035402\,\phi 1 - 0.03111\,\mathrm{R} * \mathrm{R} - 0.00345\,\alpha * \alpha + 0.028576\,\mathrm{R} * \alpha - 0.00407\,\mathrm{R} * \phi 1 - 0.004664\alpha * \phi 1,$$

$$Hw = -0.342884 + 0.090444\,\mathrm{R} - 0.008197\alpha + 0.003872\,\phi 1 - 0.032472\,\mathrm{R} * \mathrm{R} + 0.00039\,\alpha * \alpha + 0.000435\,\mathrm{R} * \alpha - 0.000593\,\mathrm{R} * \phi 1 + 0.000123\alpha * \phi 1.$$

Tab. 11: Regression coefficients of the RSM model for Sw

Term	Coefficient	p-value	Remarks
Constant	0.6227	0	Significant
R	0.1597	0	Significant
α	0.1982	0	Significant
$\phi 1$	-0.0354	0	Significant
R*R	-0.0311	0	Significant
$\alpha * \alpha$	-0.0034	0.0390	Significant
$\phi 1 * \phi 1$	0.0008	0.5750	Insignificant
R*α	0.0285	0	Significant
R*$\phi 1$	-0.0040	0.0010	Significant

Term	Coefficient	p-value	Remarks
α*ϕ1	-0.0046	0	Significant

Tab. 12: Regression coefficients of the RSM model for Hw.

Term	Coefficient	p-value	Remarks
Constant	-0.3429	0	Significant
R	0.0904	0	Significant
α	-0.0082	0	Significant
ϕ1	0.0039	0	Significant
R*R	-0.0324	0	Significant
$\alpha * \alpha$	0.0004	0	Significant
ϕ1*ϕ1	-0.0001	0.1170	Insignificant
R*α	0.0004	0	Significant
R*ϕ1	-0.0006	0	Significant
α*ϕ1	0.0001	0.0030	Significant

The residual plots in Figs. 16 and 17 are used to further evaluate the accuracy of the models. The points in the normal probability plot are aligned along the straight line which suggests the normality of the data. The histograms indicate that the data is roughly symmetric (bell-shaped) without much skewness. In the residual versus fitted values plot, it can be observed that the maximum deviation is 0.005 and 0.0002 respectively which indicates high accuracy. Considering the above discussion, it can be concluded that the model is a good fit and is meaningful.

In Figs. 18 and 19, the contour plots of Sw and Hw are displayed to study the interaction of (a) α-R, (b) ϕ_1- R and (c) α - ϕ_1 when the third parameter is maintained at the medium level. From Fig. 18, it can be concluded that:

- Increase in α and R enhances Sw. The highest value for Sw is observed for the high level of both α and R.
- The Sw gets enhanced by increasing R and decreasing ϕ_1. It reaches the highest value when R is at a high level and ϕ1 is at a low level.
- The increase in α and decrease in ϕ1 leads to an enhancement in Sw. The highest value for Sw is obtained for the high level of α and a low level of ϕ1.

Similarly, from Fig. 19, it can be concluded that:

- An increase in R enhances Hw. It can also be noted that the increase in α has a negligible effect on Hw (Though negligible, the increase in α decreases Hw).

- The highest value for Hw is observed for the high level of R for all levels of α. The Hw gets enhanced by increasing R. The nanoparticle volume fraction of Cu has a negligible decreasing effect on Hw. It reaches the highest value when R is at a high level for all levels of $\phi 1$.
- The decrease in α and increase in $\phi 1$ leads to an enhancement in Hw. Therefore, the highest value for Hw is obtained for the high level of $\phi 1$ and low level of α.

7.3 Sensitivity Analysis

Understanding the sensitivity of the model output towards the changes in the model inputs is of utmost importance. The models for various practical applications can be made more efficient if the sensitivity of the response variable is understood. Hence, sensitivity analysis is an important part of the computational procedure of this chapter. The partial derivatives of the response variables with respect to the factor variables are called the sensitivity functions. These are further investigated to study the sensitivity of the response variables.

The sensitivity functions for Sw are:

$$\frac{\partial Sw}{\partial A} = 0.159707 - 0.06222\,A + 0.028576\,B - 0.00407C,$$

$$\frac{\partial Sw}{\partial B} = 0.198188 + 0.028576\,A + 0.0069\,\mathrm{B} - 0.004664\,C,$$

$$\frac{\partial Sw}{\partial C} = -0.035402 - 0.00407A - 0.004664\,B.$$

The sensitivity functions for Hw are:

$$\frac{\partial Hw}{\partial A} = 0.090444 - 0.064944\,\mathrm{A} + 0.000435\,B - 0.000593\,C,$$

$$\frac{\partial Hw}{\partial B} = -0.008197 + 0.000435\,A + 0.00078\,B + 0.000123\,C,$$

$$\frac{\partial Hw}{\partial C} = 0.003872 - 0.000593\,A + 0.000123\,B.$$

As mentioned earlier here the symbols A, B and C are signify R, α and $\phi 1$ respectively. A positive value for the sensitivity implies an enhancement in the response variable due to the increase in the factor variable. Similarly, a negative value for the sensitivity implies that an increase in the factor variable causes a decrease in the response variable. The sensitivity is calculated for $A = 0$.

From Table 13, it can be concluded that the sensitivity of Sw to R and α is positive but is negative to $\phi 1$. When B is at the low level and the level of C is increased, a

small decrease in the sensitivity of Sw towards A and B is observed whereas the sensitivity of C remains unchanged. A similar trend is observed when B is in the medium and high levels. Also, an increase in the sensitivity towards A and $B$is observed when the level of B is incremented whereas the sensitivity towards C becomes more negative.

Tab. 13: Sensitivity of Sw and Hw when A = 0.

B	C	$\frac{\partial Sw}{\partial A}$	$\frac{\partial Sw}{\partial B}$	$\frac{\partial Sw}{\partial C}$	$\frac{\partial Hw}{\partial A}$	$\frac{\partial Hw}{\partial B}$	$\frac{\partial Hw}{\partial C}$
	-1	0.1352	0.1960	-0.0307	0.0906	-0.0091	0.0037
-1	0	0.1311	0.1913	-0.0307	0.0900	-0.0090	0.0037
	1	0.1271	0.1866	-0.0307	0.0894	-0.0089	0.0037
	-1	0.1638	0.2029	-0.0354	0.0910	-0.0083	0.0039
0	0	0.1597	0.1982	-0.0354	0.0904	-0.0082	0.0039
	1	0.1556	0.1935	-0.0354	0.0899	-0.0081	0.0039
	-1	0.1924	0.2098	-0.0401	0.0915	-0.0075	0.0040
1	0	0.1883	0.2051	-0.0401	0.0909	-0.0074	0.0040
	1	0.1842	0.2004	-0.0401	0.0903	-0.0073	0.0040

From Table 13, it can be concluded that the sensitivity of Hw to R and $\phi 1$ is positive but is negative to α. When B is in the low level ($B = -1$ and the level of C is increased, a small decrease in the sensitivity of Hw towards Awhereas the sensitivity of Hw towards B becomes less negative. The sensitivity of C remains unchanged. A similar trend is observed when B is in the medium and high levels. Also, an increase in the sensitivity towards A and C is observed when the level of B is incremented whereas the sensitivity towards B becomes less negative.

8 Concluding Remarks

A novel quadratic thermal radiation effect is proposed to study the Sakiadis flow of hybrid nanoliquid past a vertical plate with quadratic Boussinesq approximation. The following findings can be summarized from the results obtained:

– The quadratic Rosseland thermal radiation effect is studied for the first time and this aspect more suitable when quadratic density thermal fluctuation had taken into account.
– The temperature field is higher in the case of quadratic thermal radiation in comparison with the linearized thermal radiation effect.
– The velocity field increases with increasing quadratic convection parameter.

- By increasing the quadratic radiation parameter, the velocity and temperature fields increase.
- The temperature ratio parameter is directly proportional to the thermal field.
- The wall heat flux is higher in the case of linear thermal convection than quadratic convection.
- An increase in both quadratic convection and quadratic radiation enhances shear stress at the wall.
- The sensitivity of wall shear stress to quadratic radiation and quadratic convection is positive.
- The sensitivity of wall heat flux to quadratic thermal radiation is positive whereas its sensitivity is negative to quadratic convection.
- The nanoparticle volume fractions have a positive effect on wall heat flux.

As this is the first investigation dealt with quadratic thermal radiation effect. This effect can be included along with quadratic convection on various surfaces with distinct physical conditions.

Acknowledgment

The author is grateful to the Management of CHRIST (Deemed to be University), Bangalore, India for the support through the Major Research Project (MRPDSC-1724).

Bibliography

Gray DD, Giorgini A. The validity of the Boussinesq approximation for liquids and gases. International Journal of Heat and Mass Transfer. 1976 May 1;19(5):545-51.

Gebhart B. Heat Transfer. 2nd Ed. McGraw-Hill, New York, 1971.

Gebhart B, Pera L. The nature of vertical natural convection flows resulting from the combined buoyancy effects of thermal and mass diffusion. International journal of heat and mass transfer. 1971 Dec 1;14(12):2025-50.

Demuren A, Grotjans H. Buoyancy-driven flows—Beyond the boussinesq approximation. Numerical Heat Transfer, Part B: Fundamentals. 2009 Jun 9;56(1):1-22.

Aman F, Ishak A. Mixed convection boundary layer flow towards a vertical plate with a convective surface boundary condition. Mathematical Problems in Engineering. 2012 Jan 1;2012.

Makinde OD, Olanrewaju PO. Buoyancy effects on thermal boundary layer over a vertical plate with a convective surface boundary condition. Journal of Fluids Engineering. 2010 Apr 1;132(4).

Makinde OD, Sibanda P. Magnetohydrodynamic mixed-convective flow and heat and mass transfer past a vertical plate in a porous medium with constant wall suction. Journal of Heat transfer. 2008 Nov 1;130(11).

Mahanthesh B, Gireesha BJ, Thammanna GT, Hayat T, Alsaedi A. Magnetohydrodynamic squeezing two-phase flow of particulate suspension in a rotating channel with transpiration cooling. Pro-

ceedings of the Institution of Mechanical Engineers, Part C: Journal of Mechanical Engineering Science. 2019 Feb;233(4):1224-35.
Goren SL. On free convection in water at 4 C. Chemical Engineering Science. 1966 Jun 1;21(6-7):515-8.
Sinha PC. Fully developed laminar free convection flow between vertical parallel plates. Chemical Engineering Science. 1969 Jan 1;24(1):33-8.
Vajravelu K, Sastri KS. Fully developed laminar free convection flow between two parallel vertical walls—I. International Journal of Heat and Mass Transfer. 1977 Jun 1;20(6):655-60.
Partha MK. Nonlinear convection in a non-Darcy porous medium. Applied Mathematics and Mechanics. 2010 May 1;31(5):565-74.
Kameswaran PK, Sibanda P, Partha MK, Murthy PV. Thermophoretic and nonlinear convection in non-Darcy porous medium. Journal of Heat Transfer. 2014 Apr 1;136(4).
RamReddy C, Naveen P, Srinivasacharya D. Influence of non-linear Boussinesq approximation on natural convective flow of a power-law fluid along an inclined plate under convective thermal boundary condition. Nonlinear Engineering. 2019 Jan 28;8(1):94-106.
Mahanthesh B, Animasaun IL, Rahimi-Gorji M, Alarifi IM. Quadratic convective transport of dusty Casson and dusty Carreau fluids past a stretched surface with nonlinear thermal radiation, convective condition and non-uniform heat source/sink. Physica A: Statistical Mechanics and its Applications. 2019 Dec 1;535:122471.
Kumar PS, Mahanthesh B, Gireesha BJ, Shehzad SA. Quadratic convective flow of radiated nano-Jeffrey liquid subject to multiple convective conditions and Cattaneo-Christov double diffusion. Applied Mathematics and Mechanics. 2018 Sep;39(9):1311-26.
Mahanthesh B, Gireesha BJ, Thammanna GT, Shehzad SA, Abbasi FM, Gorla RS. Nonlinear convection in nano Maxwell fluid with nonlinear thermal radiation: A three-dimensional study. Alexandria Engineering Journal. 2018 Sep 1;57(3):1927-35.
Gireesha BJ, Kumar PS, Mahanthesh B, Shehzad SA, Abbasi FM. Nonlinear gravitational and radiation aspects in nanoliquid with exponential space dependent heat source and variable viscosity. Microgravity Science and Technology. 2018 May;30(3):257-64.
Athira PR, Mahanthesh B, Gireesha BJ, Makinde OD. Non-linear convection in chemically reacting fluid with an induced magnetic field across a vertical porous plate in the presence of heat source/sink. Indefect and diffusion forum 2018 (Vol. 387, pp. 428-441). Trans Tech Publications Ltd.
Jha BK, Gwandu BJ. MHD free convection in a vertical slit micro-channel with super-hydrophobic slip and temperature jump: non-linear Boussinesq approximation approach. SN Applied Sciences. 2019 Jun;1(6):1-0.
Maxwell JC. A treatise on electricity and magnetism. Oxford: Clarendon Press; 1873.
Choi SUS, Eastman JA. Enhancing thermal conductivity of áuids with nanoparticles: The Proceedings of the 1995 ASME International Mechanical Engineering Congress and Exposition, San Francisco, USA, ASME, FED 231/MD, 1995; 66: 99-105.
Suresh S, Venkitaraj KP, Selvakumar P, Chandrasekar M. Synthesis of Al2O3–Cu/water hybrid nanofluids using two step method and its thermo physical properties. Colloids and Surfaces A: Physicochemical and Engineering Aspects. 2011 Sep 5;388(1-3):41-8.
Hayat T, Nadeem S. Heat transfer enhancement with Ag–CuO/water hybrid nanofluid. Results in physics. 2017 Jan 1;7:2317-24.
Ghadikolaei SS, Gholinia M, Hoseini ME, Ganji DD. Natural convection MHD flow due to MoS2–Ag nanoparticles suspended in C2H6O2H2O hybrid base fluid with thermal radiation. Journal of the Taiwan Institute of Chemical Engineers. 2019 Apr 1;97:12-23.

Amala S, Mahanthesh B. Hybrid nanofluid flow over a vertical rotating plate in the presence of hall current, nonlinear convection and heat absorption. Journal of Nanofluids. 2018 Dec 1;7(6):1138-48.

Ashlin TS, Mahanthesh B. Exact solution of non-coaxial rotating and non-linear convective flow of Cu–Al2O3–H2O hybrid nanofluids over an infinite vertical plate subjected to heat source and radiative heat. Journal of Nanofluids. 2019 Apr 1;8(4):781-94.

Arani AA, Monfaredi F, Aghaei A, Afrand M, Chamkha AJ, Emami H. Thermal radiation effect on the flow field and heat transfer of Co3O4-diamond/EG hybrid nanofluid using experimental data: a numerical study. The European Physical Journal Plus. 2019 Jan 1;134(1):13.

Shruthy M, Mahanthesh B. Rayleigh-Bénard convection in Casson and hybrid nanofluids: an analytical investigation. Journal of Nanofluids. 2019 Jan 1;8(1):222-9.

Kanchana C, Siddheshwar PG, Zhao Y. A study of Rayleigh–Bénard convection in hybrid nanoliquids with physically realistic boundaries. The European Physical Journal Special Topics. 2019 Dec;228(12):2511-30.

Smith JW. Effect of gas radiation in the boundary layer on aerodynamic heat transfer. Journal of the Aeronautical Sciences. 1953 Aug;20(8):579-80.

Rosseland S. Astrophysik aud Atom-Theoretische Grundlagen (Berlin: Springer), 1931; 41–4.

Viskanta R, Grosh RJ. Boundary layer in thermal radiation absorbing and emitting media. International Journal of Heat and Mass Transfer. 1962 Sep 1;5(9):795-806.

Cortell R. A numerical tackling on Sakiadis flow with thermal radiation. Chinese Physics Letters. 2008 Apr;25(4):1340.

Perdikis C, Raptis A. Heat transfer of a micropolar fluid by the presence of radiation. Heat and Mass transfer. 1996 Aug;31(6):381-2.

Perdikis C, Raptis A. Heat transfer of a micropolar fluid by the presence of radiation. Heat and Mass transfer. 1996 Aug;31(6):381-2.

Pantokratoras A. Natural convection along a vertical isothermal plate with linear and non-linear Rosseland thermal radiation. International journal of thermal sciences. 2014 Oct 1;84:151-7.

Mahanthesh B, Gireesha BJ, Gorla RS. Nonlinear radiative heat transfer in MHD three-dimensional flow of water based nanofluid over a non-linearly stretching sheet with convective boundary condition. Journal of the Nigerian Mathematical Society. 2016 Apr 1;35(1):178-98.

Box GE, Wilson KB. On the experimental attainment of optimum conditions. Journal of the royal statistical society: Series b (Methodological). 1951 Jan;13(1):1-38.

Shirvan KM, Mamourian M, Mirzakhanlari S, Ellahi R, Vafai K. Numerical investigation and sensitivity analysis of effective parameters on combined heat transfer performance in a porous solar cavity receiver by response surface methodology. International Journal of Heat and Mass Transfer. 2017 Feb 1;105:811-25.

Shirvan KM, Mamourian M, Mirzakhanlari S, Ellahi R. Two phase simulation and sensitivity analysis of effective parameters on combined heat transfer and pressure drop in a solar heat exchanger filled with nanofluid by RSM. Journal of Molecular Liquids. 2016 Aug 1;220:888-901.

Pordanjani AH, Vahedi SM, Rikhtegar F, Wongwises S. Optimization and sensitivity analysis of magneto-hydrodynamic natural convection nanofluid flow inside a square enclosure using response surface methodology. Journal of Thermal Analysis and Calorimetry. 2019 Jan;135(2):1031-45.

F. Mebarek-Oudina, A. Aissa

Convective heat transfer of magneto flow of Fe3O4-MWCNT/H2O hybrid nanofluid in a porous space between two concentric cylinders

Magneto-hybrid nanofluid flow in a porous space

Abstract: In this chapter, MHD free convection of hybrid-nanofluid in the porous cavity is investigated numerically using Control Volume Finite Element Method. The porous cavity has two circular sides, the inside heated and the outside cooled, while the rest of the walls are adiabatic. The hybrid NPs volume fraction, Hartmann number, Rayleigh number, Darcy number, and the porosity are the parameters used to control and visualize the fluid flow through the isotherms, streamlines, and the average Nusselt number. The above parameters directly influence the convective flow, where the heat transport decreases with the increase in the magnetic field intensity and gradually increases with the increase in the other parameters.

Keywords: Convection; Fe_3O_4-MWCNT/H_2O hybrid nanofluid; Magnetic field; Nusselt number; Porous cavity.

1 Introduction

Renewable energies and especially solar energy are the solutions to the enormous consumption of energy as well as all the environmental concerns of this new century. The solar radiation is absorbed and its thermal energy is collected by the solar collectors. So, solar thermal systems collect and store thermal energy via thermally insulated collectors and supply thermal energy to the system for use. The DASC, direct absorption solar collector, is the best choice due to its efficiency to exploit solar energy, it is characterized by a good capacity to absorb energy directly from the sun with a minimum of heat loss. Therefore, the development of this technology requires a new working fluid which efficiently absorbs solar energy with minimal heat loss.

The choice of this working fluid, starting with the nanofluids and now the hybrid nanofluids, with their exceptional thermal and optical properties are the subject of

F. Mebarek-Oudina, Department of Physics, Faculty of Sciences, University of 20 août 1955 - Skikda, B.P 26 Road El-Hadaiek, Skikda 21000, Algeria, oudina2003@yahoo.fr
A. Aissa, Laboratoire de Physique Quantique de la Matière et Modélisation Mathématique (LPQ3M), Mascara University, Algeria

https://doi.org/10.1515/9783110696080-003

interest of several researchers around the world. (2, 3).

The nanofluid heat transport rate is influenced by the thermal conductivity of nanoparticles (NPs). Especially this type of fluids is very used to improve the thermal conductivity of the traditional fluids; ethylene glycol, water, etc. For this, there are many biomedical and industrial applications such as cancer therapy, food processing, cooling, etc. MWCNT (Multi-Wall Carbon Nanotube) nano additives used in this study have very unique physical properties, which makes them important in the advancement of systems. Mohebbi et al. (1) has shown numerically that for all the cases of their study, the heat transfer rate increases with the insertion of MWCNT-Fe_3O_4/water hybrid nanofluid. Shi et al. (4) used the Fe_3O_4-CNT nanofluid to control the heat exchange, they determined that the heat transport rate is directly related to the direction of the magnetic field and its intensity. In the presence of a magnetic field, the Fe_3O_4 nanofluid has immense potential to improve thermal properties depending on its intensity and direction. Sheikholeslami et al. (5) conducted a numerical study of magneto-convection heat transfer in a lid-driven semi-annulus enclosure filled with Fe_3O_4–H_2O nanofluid. Their results indicate that Nusselt number increases with Reynolds number, NPs volume fraction and reduces with Hartmann number. Medebber et al. (6) demonstrated that the Rayleigh number and Nusselt number are proportional through their analysis of nanofluid heat transfer in the cylindrical annulus. The NPs concentration is completely correlated with the Nusselt number. Zeeshan et al. (7) studied numerically the convective Poiseuille boundary layer flow of $Al_2O_3/C_2H_6O_2$ nanofluid through a porous wavy channel. Mei et al. (8) carried out experimental research on the influence of the parallel magnetic field on thermo-hydraulic performances of Fe_3O_4-H_2O nanofluids flowing in a circular tube. They found that for a low magnetic induction intensity and a high fraction of NPs, the exergy efficiency is perceptive to turbulent flow. Zhou et al. (9) studied forced convection in a circular tube filled with nanofluids based on the liquid metal. Heat transfer is better for nanofluids with liquid metal as base fluid than with water as a base fluid. The effect of a heat source on the flow of the Cu-H_2O MHD nanofluid through a plate taking into account the heterogeneous-homogeneous reactions and thermal radiation, using a Corcione correlation for the dynamic viscosity and thermal conductivity of the nanofluid is investigated by Dogonchi et al. (10). The concentration profile decreases with the increase in the heterogeneous parameter and the homogeneous reaction parameter. As well as the heat transport decreases with the increase of the internal parameters of the heat source.

The MHD flow and heat transfer have various manufacturing and industrial applications such as cooling of underground electric cables, nuclear reactors, geothermal energy extractions, plastic sheets, and artificial fibers. In the last years, many studies are conducted on MHD and nanofluids (11-52). The study of natural convection in a porous medium is of great attention due to its importance in engineering and technological applications such as mechanical and civil engineering, heat exchangers, geothermal reservoirs and the prevention of pollution. Darcy-

Forchheimer flow of carbon nanotubes (SWCNT and MWCNTs) with various base fluids over a rotating disk with partial slip and temperature jump conditions are analyzed by Hayat et al. (53). The heat transport rate improves by varying the estimation of Forchheimer number and NPs volume fraction.

The main objective of this work is to use the CVFEM method to resolve the flow of Hybrid-nanofluids in porous media. Where the effect of MWCNT- Fe_3O_4 hybrid NPs on natural convection will be determined. We will simulate the flow and temperature fields taking into account the following parameters; Hartmann number, Darcy number, Rayleigh number, porosity, and the volume fraction of NPs.

2 Mathematical Statement

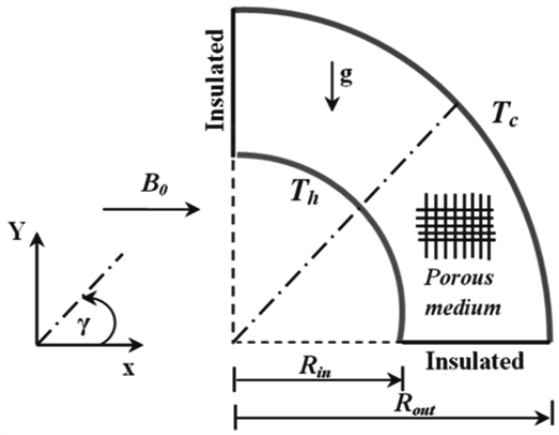

Fig. 1: Geometry of the problem.

The outer and inner circular walls are maintained at constant temperatures T_c and T_h, respectively ($T_h > T_c$) while the other walls are adiabatic. Darcy-Brinkman model is used for modeling the porous media with hybrid nanofluid. The problem is shown schematically in Fig. 1.

Conservation of Mass

$$\frac{\partial u_{hnf}}{\partial x} + \frac{\partial v_{hnf}}{\partial y} = 0, \tag{1}$$

Conservation of Momentum along x-direction

$$\left.\begin{aligned}\rho_{hnf}\left(u_{hnf}\frac{\partial u_{hnf}}{\partial x}+v_{hnf}\frac{\partial u_{hnf}}{\partial y}\right)=-\varepsilon^2\frac{\partial p}{\partial x}+\varepsilon\mu_{hnf}\left(\frac{\partial^2 u_{hnf}}{\partial x^2}+\frac{\partial^2 u_{hnf}}{\partial y^2}\right)\\ -\varepsilon^2\frac{\mu_{hnf}}{\kappa}u_{hnf}\end{aligned}\right\}, \tag{2}$$

Conservation of Momentum along y-direction

$$\left.\begin{aligned}\rho_{hnf}\left(u_{hnf}\frac{\partial v_{hnf}}{\partial x}+v_{hnf}\frac{\partial v_{hnf}}{\partial y}\right)=-\varepsilon^2\frac{\partial p}{\partial x}+\varepsilon\mu_{hnf}\left(\frac{\partial^2 v_{hnf}}{\partial x^2}+\frac{\partial^2 v_{hnf}}{\partial y^2}\right)\\ -\varepsilon^2\frac{\mu_{hnf}}{\kappa}v_{hnf}-\sigma B_0^2 v_{hnf}\\ +\beta_{hnf}\rho_{hnf}g(T-T_c)\,,\end{aligned}\right\}, \tag{3}$$

Conservation of Energy

$$u_{hnf}\frac{\partial T_{hnf}}{\partial x}+v_{hnf}\frac{\partial T_{hnf}}{\partial y}=\alpha_{hnf}\left(\frac{\partial^2 T_{hnf}}{\partial x^2}+\frac{\partial^2 T_{hnf}}{\partial y^2}\right), \tag{4}$$

The Eqs. (1–4) are transferred to a dimensionless form after considering the following specifications:

Dimensionless scales

$$X,Y=\frac{x,y}{L},U,V=\frac{(u,v)L}{\alpha_{fl}},\theta=\frac{T-T_c}{T_h-T_c},$$

Dimensionless numbers

$$Da=\frac{\lambda}{L^2},\text{ (Darcy number)}$$

$$Pr=\frac{\upsilon_{fl}}{\alpha_{fl}},\text{ (Prandtl number)}$$

$$Ra=\frac{g\beta_{fl}(T_h-T_c)L^3}{\alpha_{fl}\upsilon_{fl}},\text{ (Rayleigh number)}$$

$$P=\frac{(p+\rho_{hnf}g_y)L^2}{\rho_{fl}\alpha_{fl}^2}.$$

The heat capacity and the density of Fe_3O_4- MWCNT/H_2O nanofluid are determined as follows:

$$\left.\begin{aligned}\rho_{hna} &= (1-\phi)\rho_{fl} + \phi_s \\ (\rho C_p)_{hna} &= (1-\phi)(\rho C_p)_{fl} + \phi(\rho C_p)_s\end{aligned}\right\}, \tag{5}$$

The coefficient of thermal expansion of Fe_3O_4- MWCNT/H_2O nanofluid is defined as:

$$(\rho\beta)_{hna} = (1-\phi)\rho_{fl} + \phi(\rho\beta)_s, \tag{6}$$

The thermal conductivity and the viscosity of Fe_3O_4- MWCNT / H_2O nanofluid are expressed as:

$$\mu_{hna} = \frac{\mu_{fl}}{(1-\phi)^{0.25}}, \tag{7}$$

$$\frac{k_{hna}}{k_{fl}} = \frac{k_s + 2k_{fl} - 2\phi(k_{fl} - k_s)}{k_s + 2k_{fl} + 2\phi(k_{fl} - k_s)}, \tag{8}$$

For the NPs of Fe_3O_4 and MWCNT, the properties are:

$$\phi = \phi_{Fe_3O_4} + \phi_{MWCNT}, \tag{9}$$

$$\rho_{hnp} = \frac{\phi_{Fe_3O_4}\,\rho_{Fe_3O_4} + \phi_{MWCNT}\,\rho_{MWCNT}}{\phi}, \tag{10}$$

$$(C_p)_{hnp} = \frac{\phi_{Fe_3O_4}\,(C_p)_{Fe_3O_4} + \phi_{MWCNT}\,(C_p)_{MWCNT}}{\phi}, \tag{11}$$

$$\beta_{hnp} = \frac{\phi_{Fe_3O_4}\,\beta_{Fe_3O_4} + \phi_{MWCNT}\,\beta_{MWCNT}}{\phi}, \tag{12}$$

$$k_{hnp} = \frac{\phi_{Fe_3O_4}\,k_{Fe_3O_4} + \phi_{MWCNT}\,k_{MWCNT}}{\phi}, \tag{13}$$

$$\sigma_{hnp} = \frac{\phi_{Fe_3O_4}\,\sigma_{Fe_3O_4} + \phi_{MWCNT}\,\sigma_{MWCNT}}{\phi}, \tag{14}$$

The local and average Nusselt numbers along the circular heated wall are calculated from the following two equations:

$$\left.\begin{aligned}Nu_{loc} &= -\frac{k_{eff}}{k_{fl}}\left(\frac{\partial\theta_{po}}{\partial Y}\right)_{Y=0} \\ Nu_{ave} &= \int_0^1 Nu_{loc}\,dX\end{aligned}\right\}. \tag{15}$$

2.1 Boundary conditions

$$T = 1 \quad \psi = 0 \text{ on the inner wall} \tag{16}$$

$$T = 0 \ \ \psi = 0 \text{ on the outer wall} \tag{17}$$

$$\frac{\partial T}{\partial n} \ \ \psi = 0 \text{ on the other walls} \tag{18}$$

The base fluid and NPs properties are presented in Table 1.

Tab. 1: Thermo-physical properties of the Fe_3O_4, MWCNT, and H_2O ((1) and (52)).

Physical Properties	Density (ρ)	Specific heat (C_p)	Thermal conductivity (k)	Electrical conductivity (σ)	Thermal expansion coefficient (β)
$MWCNT$	2100	711	3000	1.9X10^{-4}	4.2X10
Fe_3O_4	5810	670	6	2.5X10^{-4}	1.3X10^{-5}
H_2O	997.1	4179.0	0.613	550X10^{-4}	21X10^{-5}

2.2 Grid Analysis and Validation

2.2.1 Grid analysis

The mixture between the two methods FEM and FVM constitutes the CVFEM method. The latter is used to solve the nonlinear algebraic system. Large documentation on these methods and their uses are available in the literature (10, 37-46, 52).

Various non-uniform meshes are used to obtain precise results and to optimize the calculation time. A semi-implicit running time is used to advance the solution. Table 2 presents a comparison of the average Nusselt number for diverse meshes, we found that the mesh of 19101 is the best for this study.

Tab. 2: Average Nusselt number, Nu_{avg} for diverse grids.

Mesh	Nu_{avg}
770	5.1795
1184	5.2285
5266	5.3280

Mesh	Nu_{avg}
19101	5.3671
20841	5.3688

2.3 Validation

The governing equations have been discretized by the CVFEM method using a triangular Lagrange finite elements different orders for the variables flow of and quadratic elements in the computational domain. For airflow in a cavity, a comparison of our numerical results with those of (24) is carried out in order to verify the used code. A good agreement between the two results is obtained from the dimensionless temperature profile with a deviation that does not exceed 2%. (see Fig. 2)

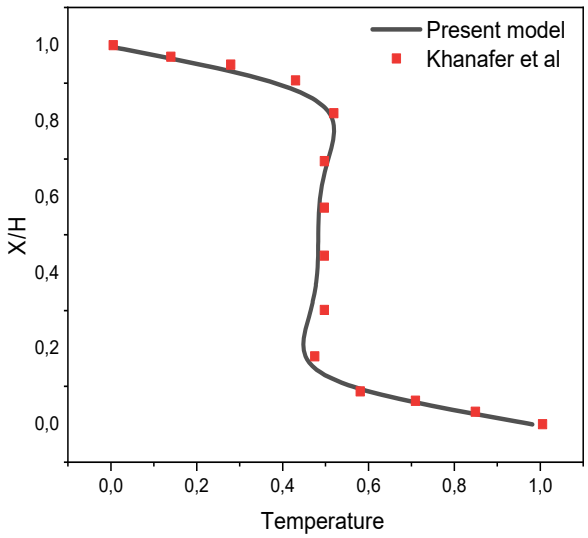

Fig. 2: Validation of our work with that of Khanfer et al. (24).

3 Results and discussion

In this study, numerical analysis is accomplished to study the influences of the controlling parameters such as Hartmann number ($Ha = 0–100$), Rayleigh number ($Ra = 10^3, 10^4, 10^5$ and 10^6), Porosity ($\varepsilon = 0.1, 0.4, 0.6, 0.9$), Darcy number

($Da = 10^{-2}, 10^{-3}, 10^{-4}$ and 10^{-5}) and volume fraction of Fe_3O_4-MWCNT (50/50%) hybrid NPs ($\phi = 0, 0.2, 0.4, 0.8$) on the free convection of magnetic hybrid-nanofluid in the porous cavity.

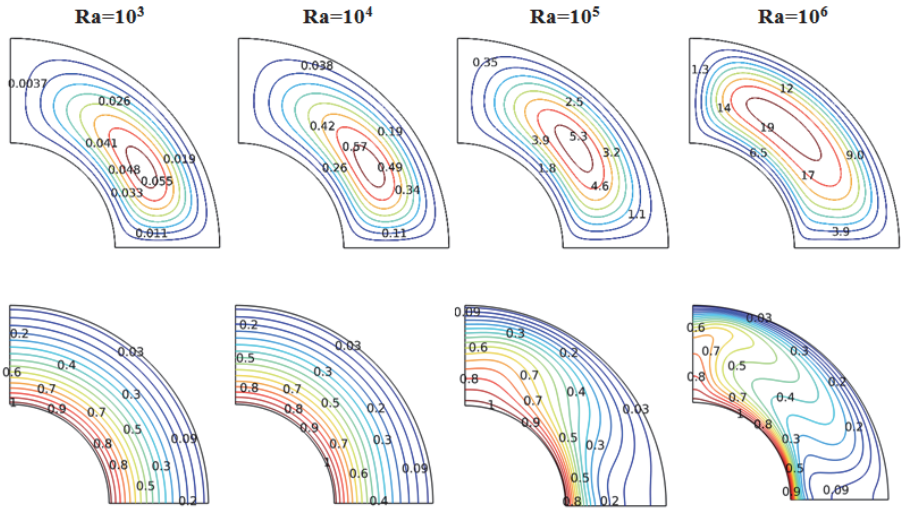

Fig. 3: Isotherms and Streamlines for various Ra.

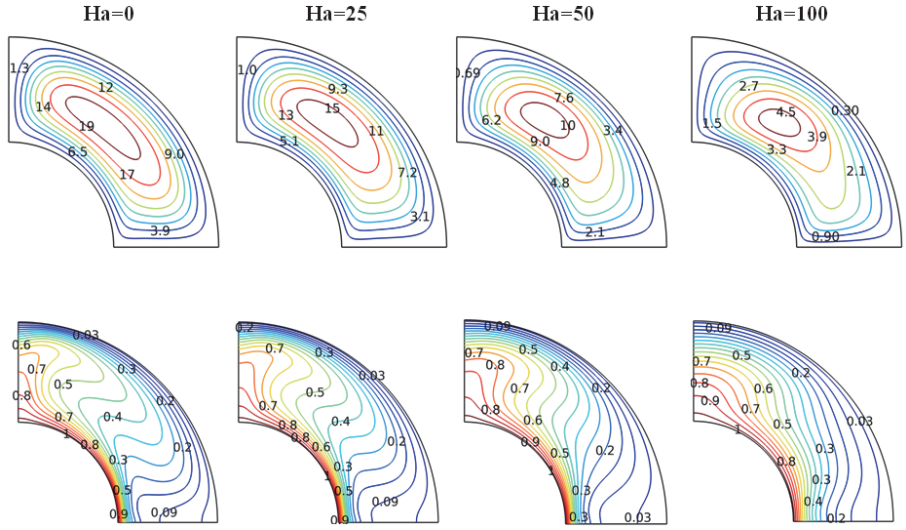

Fig. 4: Streamlines and isotherms for various Ha.

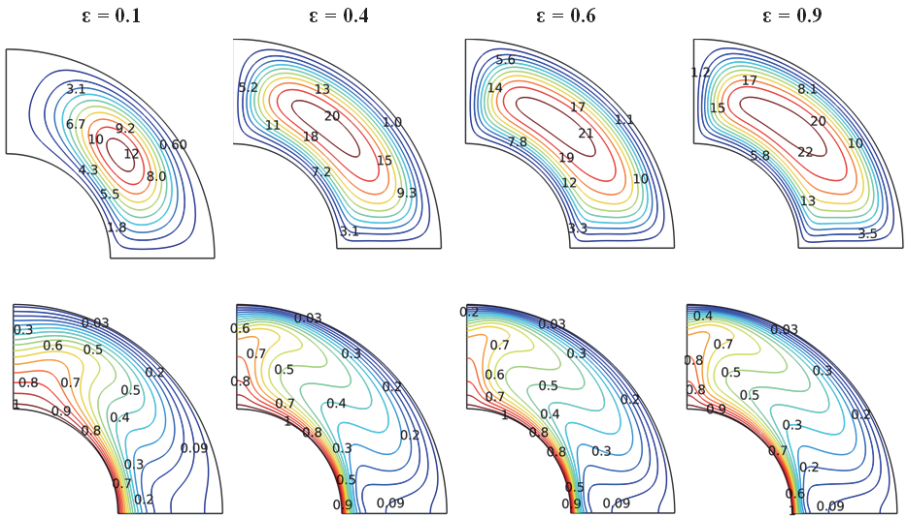

Fig. 5: Isotherms and streamlines for various ε.

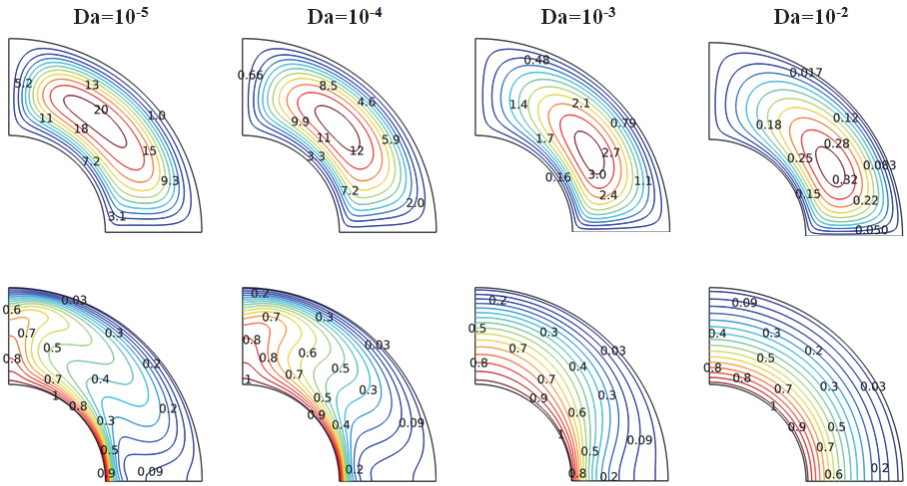

Fig. 6: Isotherms and streamlines for various Da.

Figures. 3 and 4 depict the effects of the Hartmann and Rayleigh numbers on the isotherms and streamlines respectively. The maximum value of the current lines is directly related to the Rayleigh number and an inverse relationship with Hartmann's number; thus, the convection intensity increases with Ra number and decreases with Ha number. The magnetic field plays a great role in controlling heat transfer, so Lorentz forces eliminate buoyancy forces. With the growth of the Ha, the fluid

rises along the outer circular wall with a stretching of the central line. The dominant heat mode for the low Rayleigh number is the conduction, from where the viscous forces defeat buoyancy forces, and on the contrary, when Ra increases, the convective mode dominates the heat transfer. For upper Ra and lower Ha, a temperature stratification is formed by the distortion of the isotherms.

In another way, along the interior and outer circular walls, a thermal boundary layer is formed. The isotherms are paralyzed by the high Ha numbers, and conduction is the dominant mode of transport. In this case, the thermal boundary layer will be faded along the inner and outer circular walls. The influence of ε and Darcy number on the isotherms and streamlines are showed in Figures 5 and 6, respectively. The intensity of the flow inside the cavity is the permeability of a porous medium where it presents here by the Darcy number. The low Darcy numbers lead to a weak circulation of the flow, and this circulation will be intensified with the increase in the Da number therefore a very good permeability. From these figures, we notice that the conductive transfer mode is dominant for low Darcy values with parallel isotherms close to each other. With the growth of Da, the isotherms deform and the convective mode dominates the heat transfer. The same result for the parameter ε is found during the processing of isotherms.

Figures 7-10 depicts the variation of the mean Nu number (Nuavg) for various values of Rayleigh number, Darcy number, Hartmann number, and porosity. It is obvious that in all cases, the maximum value of the average Nu number occurs near the lower adiabatic wall. The average Nu number value increases with the increase in Ra number, Da number, and porosity while it reduces with increasing Hartmann number. The convection heat transport mode dominates due to the increase in Ra, Da, and ε while the increase in Ha favors the conduction mode. The Hartmann number has a very small effect on the average Nusselt number for low values of the Ra number. The evolution of the local Nu number along the hot circular wall is presented for different values of the Rayleigh number in figure 11 and for different values of the Hartmann number in figure 12. According to these two figures, the best heat transfer is found for the small Rayleigh number value, without magnetic field and at the beginning of the hot circular wall.

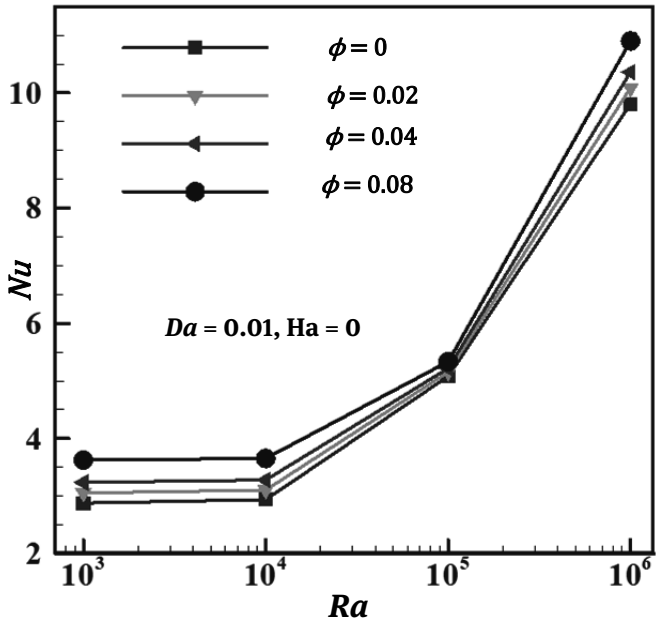

Fig. 7: Nu_{avg} vs Ra for various ϕ.

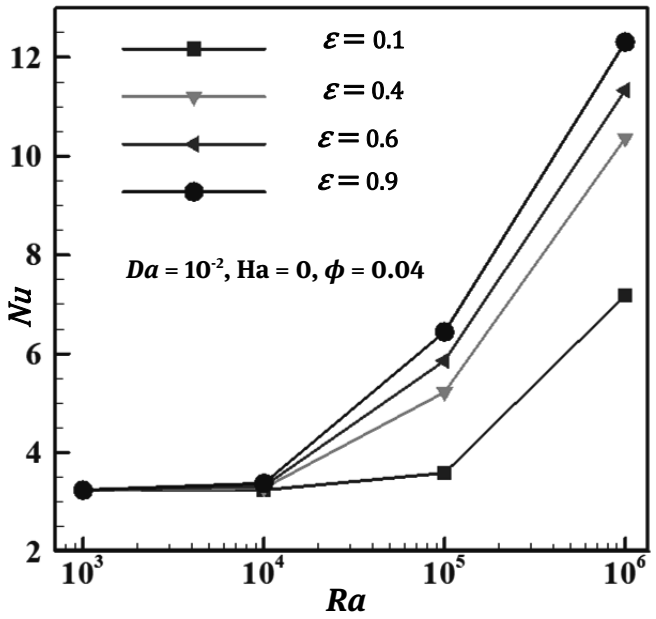

Fig. 8: Nu_{avg} vs Ra for various ϵ.

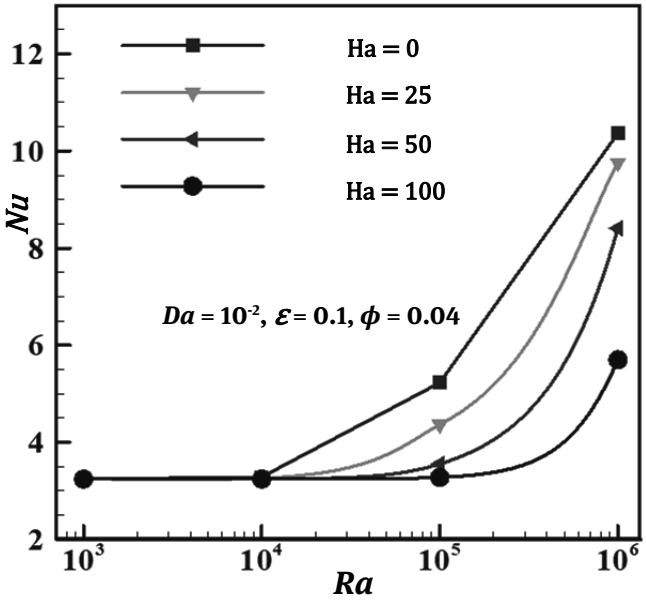

Fig. 9: Nu_{avg} vs Ra for various Ha.

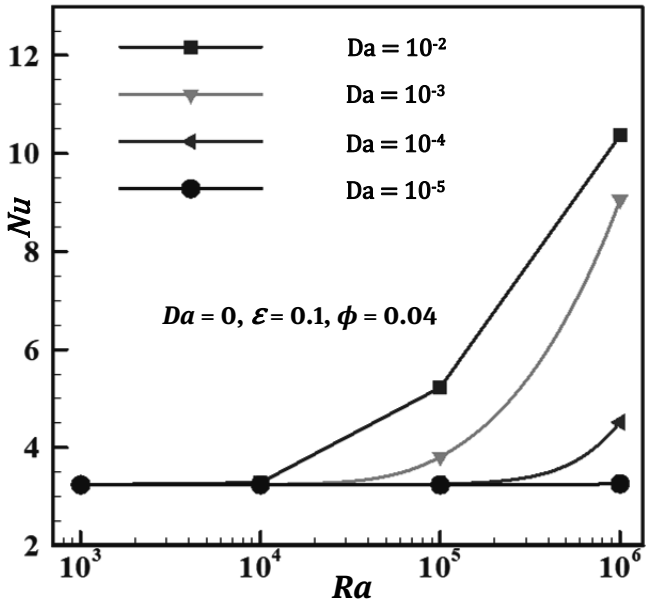

Fig. 10: Nu_{avg} vs Ra for various Da.

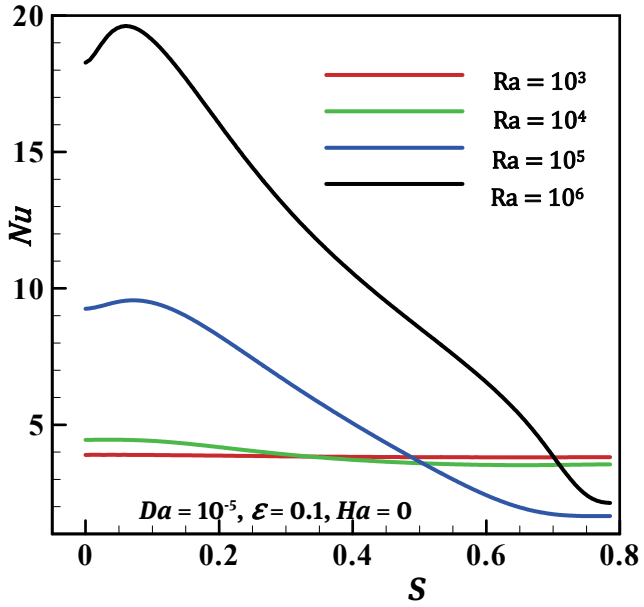

Fig. 11: Nu_{Loc} vs S for various Ra.

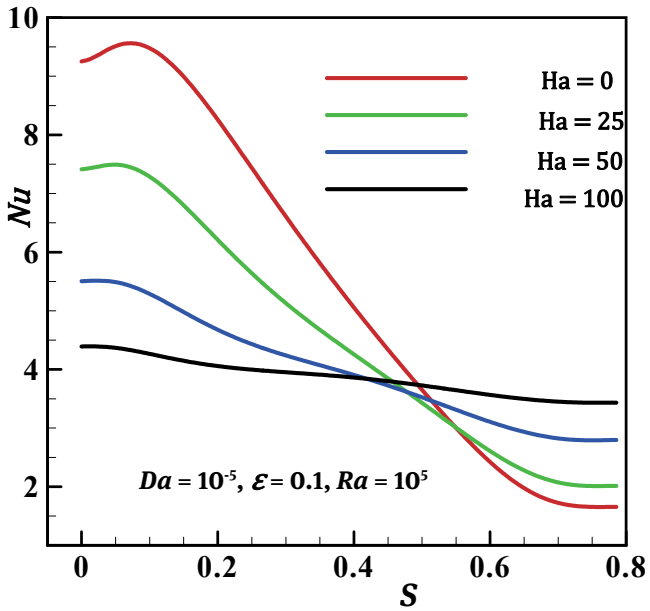

Fig. 12: Nu_{Loc} vs S for various Ha.

4 Concluding Remarks

The magneto-hydrodynamic natural convective flow between two coaxial cylinders filled with Fe3O4-MWCNT/H2O (50/50%) hybrid-nano-fluids is investigated numerically. The Control Volume Finite Element Method is utilized to achieve the necessary simulations. From the obtained results, the main conclusions are:

- The increase in the average Nu number with the increase in the Ra number, the Darcy number, and the volume fraction of the hybrid NPs while it reduces with the increase in the Ha number.
- The porosity of the porous medium increases with the Ra number but this increase is slightly for low temperatures.
- The Hartmann number, Da number, ε parameter have a negligible effect on the average Nusselt number for lower values of the Rayleigh number.
- The use of the Fe3O4-MWCNT/H2O hybrid nanofluid has a harmful effect on the hydrothermal aspects of the porous cavity studied.

Acknowledgment

This research is supported by the project n° B00L02UN210120180002 and DGRSDT, Algeria.

Bibliography

Mohebbi R, Izadi M, Amiri Delouei A, Sajjadi H. Effect of MWCNT–Fe_3O_4/water hybrid nanofluid on the thermal performance of ribbed channel with apart sections of heating and cooling. Journal of Thermal Analysis and Calorimetry, (2019). 135, 3029-3042.

Mebarek-Oudina F. Convective heat transfer of Titania nanofluids of different base fluids in cylindrical annulus with discrete heat source. Heat Transfer—Asian Research. 2019 Jan;48(1):135-47.

Qu J, Zhang R, Wang Z, Wang Q. Photo-thermal conversion properties of hybrid CuO-MWCNT/H2O nanofluids for direct solar thermal energy harvest. Applied Thermal Engineering. 2019 Jan 25;147:390-8.

Shi L, He Y, Hu Y, Wang X. Thermophysical properties of Fe3O4@ CNT nanofluid and controllable heat transfer performance under magnetic field. Energy Conversion and Management. 2018 Dec 1;177:249-57.

Sheikholeslami M, Rashidi MM, Ganji DD. Effect of non-uniform magnetic field on forced convection heat transfer of Fe3O4–water nanofluid. Computer Methods in Applied Mechanics and Engineering. 2015 Sep 1;294:299-312.

Medebber MA, Aissa A, Slimani ME, Retiel N. Numerical study of natural convection in vertical cylindrical annular enclosure filled with Cu-water nanofluid under magnetic fields. InDefect and Diffusion Forum 2019 (Vol. 392, pp. 123-137). Trans Tech Publications Ltd.

Zeeshan A, Shehzad N, Ellahi R, Alamri SZ. Convective Poiseuille flow of Al 2 O 3-EG nanofluid in a porous wavy channel with thermal radiation. Neural Computing and Applications. 2018 Dec;30(11):3371-82.

Mei S, Qi C, Liu M, Fan F, Liang L. Effects of paralleled magnetic field on thermo-hydraulic performances of Fe3O4-water nanofluids in a circular tube. International Journal of Heat and Mass Transfer. 2019 May 1;134:707-21.

Zhou X, Li X, Cheng K, Huai X. Numerical study of heat transfer enhancement of nano liquid-metal fluid forced convection in circular tube. Journal of Heat Transfer. 2018 Aug 1;140(8).

Dogonchi AS, Chamkha AJ, Hashemi-Tilehnoee M, Seyyedi SM, Ganji DD. Effects of homogeneous-heterogeneous reactions and thermal radiation on magneto-hydrodynamic Cu-water nanofluid flow over an expanding flat plate with non-uniform heat source. Journal of Central South University. 2019 May;26(5):1161-71.

Raza J, Mebarek-Oudina F, Chamkha AJ. Magnetohydrodynamic flow of molybdenum disulfide nanofluid in a channel with shape effects. Multidiscipline Modeling in Materials and Structures. 2019 Jul 1;15(4):737-57.

Mebarek-Oudina F, Bessaïh R. Stabilité Magnétohydrodynamique des ecoulements de convection naturelle dans une configuration cylindrique de type Czochralski. Société Française de Thermique. 2007;1:451-7.

Mebarek-oudina, F., & Bessaïh, R. (2014). Numerical modeling of MHD stability in a cylindrical configuration. Journal of the Franklin Institute, 351(2), 667-681.

Mebarek-Oudina F, Bessaih R. Oscillatory magnetohydrodynamic natural convection of liquid metal between vertical coaxial cylinders. J. Appl. Fluid Mech. 2016 Jan 1;9(4):1655-65.

Mebarek-Oudina F. Numerical modeling of the hydrodynamic stability in vertical annulus with heat source of different lengths. Engineering science and technology, an international journal. 2017 Aug 1;20(4):1324-33.

Mebarek-Oudina F, Bessaïh R. Oscillatory mixed convection flow in a cylindrical container with rotating disk under axial magnetic field and various wall electrical conductivity. International review of physics. 2010 Aug;4(1):45-51.

Mebarek-Oudina F, Bessaïh R. Magnetohydrodynamic stability of natural convection flows in Czochralski crystal growth. World Journal of Engineering. 2007;4(4):15-22.

Mebarek-Oudina F, Aissa A, Mahanthesh B, Öztop HF. Heat transport of magnetized Newtonian nanoliquids in an annular space between porous vertical cylinders with discrete heat source. International Communications in Heat and Mass Transfer. 2020 Oct 1;117:104737.

Raza J, Farooq M, Mebarek-Oudina F, Mahanthesh B. Multiple slip effects on MHD non-Newtonian nanofluid flow over a nonlinear permeable elongated sheet. Multidiscipline Modeling in Materials and Structures. 2019 Sep 2; 15(5):913-31.

Raza J, Mebarek-Oudina F, Mahanthesh B. Magnetohydrodynamic flow of nano Williamson fluid generated by stretching plate with multiple slips. Multidiscipline Modeling in Materials and Structures. 2019 Sep 2; 15(5):871-94.

Reza J, Mebarek-Oudina F, Makinde OD. MHD slip flow of Cu-Kerosene nanofluid in a channel with stretching walls using 3-stage Lobatto IIIA formula. InDefect and Diffusion Forum 2018 (Vol. 387, pp. 51-62). Trans Tech Publications Ltd.

Mebarek-Oudina F, Bessaïh R. Numerical simulation of natural convection heat transfer of copper-water nanofluid in a vertical cylindrical annulus with heat sources. Thermophysics and Aeromechanics. 2019 May;26(3):325-34.

Mahanthesh B, Lorenzini G, Oudina FM, Animasaun IL. Significance of exponential space-and thermal-dependent heat source effects on nanofluid flow due to radially elongated disk with Coriolis and Lorentz forces. Journal of Thermal Analysis and Calorimetry. 2019 Nov 21:1-8.

Khanafer K, Vafai K, Lightstone M. Buoyancy-driven heat transfer enhancement in a two-dimensional enclosure utilizing nanofluids. International journal of heat and mass transfer. 2003 Sep 1;46(19):3639-53.

Laouira H, Mebarek-Oudina F, Hussein AK, Kolsi L, Merah A, Younis O. Heat transfer inside a horizontal channel with an open trapezoidal enclosure subjected to a heat source of different lengths. Heat Transfer—Asian Research. 2020 Jan;49(1):406-23.

Mebarek-Oudina F, Hamrelaine S, Sari MR. Analysis of MHD Jeffery Hamel flow with suction/injection by homotopy analysis method. Journal of Advanced Research in Fluid Mechanics and Thermal Sciences. 2019;58(2):173-86.

Alkasassbeh M, Omar Z, Mebarek-Oudina F, Raza J, Chamkha A. Heat transfer study of convective fin with temperature-dependent internal heat generation by hybrid block method. Heat Transfer—Asian Research. 2019 Jun;48(4):1225-44.

Mebarek-Oudina F, Makinde OD. Numerical simulation of oscillatory MHD natural convection in cylindrical annulus: Prandtl number effect. InDefect and Diffusion Forum 2018 (Vol. 387, pp. 417-427). Trans Tech Publications Ltd.

Gourari S, Mebarek-Oudina F, Hussein AK, Kolsi L, Hassen W, Younis O. Numerical study of natural convection between two coaxial inclined cylinders. Int J Heat Technol. 2019 Sep;37(3):779-86.

Mebarek-Oudina F, Bessaih R, Mahanthesh B, Chamkha AJ, Raza J. Magneto-thermal-convection stability in an inclined cylindrical annulus filled with a molten metal. International Journal of Numerical Methods for Heat & Fluid Flow. 2020 Aug 7.

Chauhan PR, Kumar K, Kumar R, Rahimi-Gorji M, Bharj RS. Effect of thermophysical property variation on entropy generation towards micro-scale. Journal of Non-Equilibrium Thermodynamics. 2020 Jan 28;45(1):1-7.

Slimani R, Aissa A, Mebarek-Oudina F, Khan U, Sahnoun M, Chamkha AJ, Medebber MA. Natural convection analysis flow of Al2O3-Cu/water hybrid nanofluid in a porous conical enclosure subjected to the magnetic field. The European Physical Journal Applied Physics. 2020 Oct 1;92(1):10904.

Swain K, Mahanthesh B, Mebarek-Oudina F. Heat transport and stagnation-point flow of magnetized nanoliquid with variable thermal conductivity, Brownian moment, and thermophoresis aspects. Heat Transfer. 2021 Jan;50(1):754-67.

Abo-Dahab SM, Abdelhafez MA, Mebarek-Oudina F, Bilal SM. MHD Casson Nanofluid Flow over Nonlinearly Heated Porous Medium in presence of extending Surface effect with Suction/Injection, Indian Journal of Physics. 2021 Jan 2.

Ismael MA, Hussein AK, Mebarek-Oudina F, Kolsi L. Effect of driven sidewalls on mixed convection in an open trapezoidal cavity with a channel. Journal of Heat Transfer. 2020 Aug 1;142(8).

Dutta A, Chattopadhyay H, Yasmin H, Rahimi-Gorji M. Entropy generation in the human lung due to effect of psychrometric condition and friction in the respiratory tract. Computer methods and programs in biomedicine. 2019 Oct 1;180:105010.

Mebarek-Oudina F, Reddy NK, Sankar M. Heat source location effects on buoyant convection of nanofluids in an annulus. InAdvances in Fluid Dynamics 2021 (pp. 923-937). Springer, Singapore.

Seikh AH, Akinshilo AT, Taheri MH, Rahimi-Gorji M, Alharthi N, Khan I, Khan AR. Influence of the nanoparticles and uniform magnetic field on the slip blood flows in arterial vessels. Physica Scripta. 2019 Sep 26;94(12):125218.

Souayeh B, Kumar KG, Reddy MG, Rani S, Hdhiri N, Alfannakh H, Rahimi-Gorji M. Slip flow and radiative heat transfer behavior of Titanium alloy and ferromagnetic nanoparticles along with suspension of dusty fluid. Journal of Molecular Liquids. 2019 Sep 15;290: 111223.

Kahshan M, Lu D, Rahimi-Gorji M. Hydrodynamical study of flow in a permeable channel: Application to flat plate dialyzer. International journal of hydrogen energy. 2019 Jun 21;44(31):17041-7.

Uddin S, Mohamad M, Rahimi-Gorji M, Roslan R, Alarifi IM. Fractional electro-magneto transport of blood modeled with magnetic particles in cylindrical tube without singular kernel. Microsystem Technologies. 2020 Feb;26(2):405-14.

Khan U, Zaib A, Mebarek-Oudina F. Mixed Convective Magneto Flow of SiO 2–MoS 2/C 2 H 6 O 2 Hybrid Nanoliquids Through a Vertical Stretching/Shrinking Wedge: Stability Analysis. Arabian Journal for Science and Engineering. 2020 Nov;45:9061-73.

Hashemi-Tilehnoee M, Dogonchi AS, Seyyedi SM, Chamkha AJ, Ganji DD. Magnetohydrodynamic natural convection and entropy generation analyses inside a nanofluid-filled incinerator-shaped porous cavity with wavy heater block. Journal of Thermal Analysis and Calorimetry. 2020 Jan 11:1-3.

Molana M, Dogonchi AS, Armaghani T, Chamkha AJ, Ganji DD, Tlili I. Investigation of hydrothermal behavior of Fe3O4-H2O nanofluid natural convection in a novel shape of porous cavity subjected to magnetic field dependent (MFD) viscosity. Journal of Energy Storage. 2020 Aug 1;30:101395.

Dogonchi AS, Nayak MK, Karimi N, Chamkha AJ, Ganji DD. Numerical simulation of hydrothermal features of Cu–H_2O nanofluid natural convection within a porous annulus considering diverse configurations of heater. Journal of Thermal Analysis and Calorimetry, 2020; 1-17.

Dogonchi AS, Chamkha AJ, Seyyedi SM, Hashemi-Tilehnoee M, Ganji DD. Viscous dissipation impact on free convection flow of Cu-water nanofluid in a circular enclosure with porosity considering internal heat source. Journal of Applied and Computational Mechanics. 2019 Jun 1;5(4):717-26.

Farhan M, Omar Z, Mebarek-Oudina F, Raza J, Shah Z, Choudhari RV, Makinde OD. Implementation of the one-step one-hybrid block method on the nonlinear equation of a circular sector oscillator. Computational Mathematics and Modeling. 2020 Jan;31(1):116-32.

Marzougui S, Mebarek-Oudina F, Assia A, Magherbi M, Shah Z, Ramesh K. Entropy generation on magneto-convective flow of copper–water nanofluid in a cavity with chamfers. Journal of Thermal Analysis and Calorimetry. 2021; 143:2203-14.

Raza J, Mebarek-Oudina F, Ram P, Sharma S. MHD flow of non-Newtonian molybdenum disulfide nanofluid in a converging/diverging channel with Rosseland radiation. InDefect and Diffusion Forum 2020 (Vol. 401, pp. 92-106). Trans Tech Publications Ltd.

Aissa A, Slimani MEA, Mebarek-Oudina F, Fares R, Zaim A, Kolsi L, Ganaoui ME. Pressure-Driven Gas Flows in Micro Channels with a slip boundary: A numerical investigation, Fluid Dynamics & Materials Processing, 2020; 16(2): 147-159.

Abdel-Nour Z, Aissa A, Mebarek-Oudina F, Rashad AM, Ali HM, Sahnoun M, El Ganaoui M. Magneto-hydrodynamic natural convection of hybrid nanofluid in a porous enclosure: numerical analysis of the entropy generation. Journal of Thermal Analysis and Calorimetry. 2020 Sep;141(5):1981-92.

Dogonchi AS, Asghar Z, Waqas M. CVFEM simulation for Fe3O4-H2O nanofluid in an annulus between two triangular enclosures subjected to magnetic field and thermal radiation. International Communications in Heat and Mass Transfer. 2020 Mar 1;112: 104449.

Hayat T, Nasir T, Khan MI, Alsaedi A. Non-Darcy flow of water-based single (SWCNTs) and multiple (MWCNTs) walls carbon nanotubes with multiple slip conditions due to rotating disk. Results in Physics. 2018 Jun 1;9:390-9.

Nomenclature

Symbols	Definition
Da	Darcy number
Nu	Nusselt number
K	Permeability of porous medium (m^2)
P	Dimensionless pressure
p	Pressure (N/m^2)
Pr	Prandtl number
Ra	Rayleigh number
R_{in}	Inner radii (m)
R_{out}	Outer radii (m)
S	Circular heated wall length
T	Temperature (^oC)
U	Dimensionless velocity component in X-direction
u	Velocity component in x-direction (m/sec)
V	Dimensionless velocity component in Y-direction
v	Velocity component in y-direction (m/sec)
X	Dimensionless coordinate in the horizontal direction (m)
x	Cartesion coordinate in the horizontal direction (m)
Y	Dimensionless coordinate in the vertical direction
y	Cartesian coordinate in the vertical direction (m)
Greek symbols	
α	Thermal diffusivity (m^2/s)
β	Thermal expansion coefficient ($1/K$)
γ	Angle (^{o})
σ	Electrical conductivity ($1/\Omega$ m)
ρ	Density (kg/m^3)
θ	Dimensionless temperature
μ	Dynamic viscosity (kg/m s)
ν	Kinematic viscosity (m^2/s)
ϕ	Volume fraction (%)
ϵ	Porosity
ψ	Stream function
Subscripts	
Avg	Average\nu
Loc	Local
c	Cold
h	Hot
hnf	Hybrid nanofluid
fl	Fluid de base
Abbreviation	
NPs	Nanoparticles
MHD	Magnetohydrodynamic
$CVFEM$	Control volume finite element method
FEM	Finite element method
FVM	Finite volume method
Fe_3O_4	Magnetite

Symbols	Definition
$MWCNT$	Multi-wall carbon nanotubes
H_2O	Water

Taseer Muhammad, Hassan Waqas, B. Mahanthesh

Computational analysis of bioconvection in magnetized flow of thixotropic nanofluid with gyrotactic microorganisms

Bioconvection in magnetized nanofluid flow

Abstract: During the past few years, multiple efforts have been made to apply different techniques to boost the heat transfer in different thermal systems. Achieving higher heat transfer can contribute to the development of more versatile heat transfer systems with higher thermal efficiencies. Therefore, the development of an improved heat flow process has generated tremendous demand for new heat transfer technologies. The current work consists of a model that is developed for this purpose. The simulation of magnetohydrodynamics flow of thixotropic nanoliquid having motile microorganisms is addressed in the current analysis. Thixotropic nanofluid model depicts important rheological aspects of fluid dynamics. Moreover, the nanofluid mass and heat efficiencies are achieved by testing the famous Buongiorno model which leads to Brownian motion and thermophoretic diffusion. Furthermore, the existence of thermal radiation, heat generation, and Joule dissipation is examined in the heat transport system. By introducing acceptable similarity transformations, the non-linear governing flow equations (PDEs) are changed into the nonlinear ordinary differential expressions (ODEs). The obtained nonlinear ODEs are solved numerically by using bvp4c solver in computational software MATLAB. Numerical and graphical results are obtained by employing various estimations of physical numbers. Both temperature and volumetric concentration of nanoparticles depict decreasing trend for enhancing estimation of mixed convection parameter.

Keywords: Activation energy; Bioconvection; Motile microorganisms; Numerical solution; Thermal radiation; Thixotropic nanofluid.

Taseer Muhammad, Department of Mathematics, College of Sciences, King Khalid University, Abha 61413, Saudi Arabia, taseer_qau@yahoo.com
Hassan Waqas, Department of Mathematics, Government College University Faisalabad, Layyah Campus 31200, Pakistan
B. Mahanthesh, Department of Mathematics, CHRIST (Deemed to be University), Bengaluru-560029, India, mahanthesh.b@christuniversity.in

https://doi.org/10.1515/9783110696080-004

1 Introduction

In current years, non-Newtonian liquids have fascinated many researchers and scientists due to their interdisciplinary features, rheology, and wide range of applications in the industrial and engineering sector. These fluids are utilized in the processing process, technology of fiber, china clay, nuclear and chemical industries, oil industries, material handling, cooling of microelectronics, and many others. Several fluids like animal blood, mud, condensed milk, shampoos, detergents, polymer solution, sugar solution and coating of wires, ice flow, synovial liquid, grease, apple sauces, tomato ketchup, gels, ketchup, paints, and ink are also classified as non-Newtonian fluids. Out of these, the thixotropic fluid is a shear rate fluid that extradites a diminishes in liquid viscosity across time at a steady shear rate. Hayat et al. (1) illustrated the magnetic field aspects in thixotropic nanofluid flow across a stretching sheet. Features of thixotropic nanoliquid flow subject to mixed convection under the impact of the stratification mechanism are revealed by Hayat et al. (2). Joule heating aspects in mixed convection flow of thixotropic nanofluid across a flat sheet is analyzed by Hayat et al. (3).

Nanofluids have attracted the attention of many investigators in recent years due to the excellent improvements in heat transfer enhancement. When nanometre-size particles (<100nm) (i.e., titanium dioxide, carbides, silver, and metals, etc) are immersed in a regular fluid, the heat transfer efficiency from coolants is improved. The research of the flow and thermal expansion within the same concentric nanofluid containing annulus, acquire consideration as it has various environmental and engineering applications including automobile thermal management, heat exchange, and energy storage, cooling of electronics appliances, and molecular biology. Magnetic nanomaterials have been utilized to replace with radioactive technetium to examine the growth of cancer including blood vessels. Nanofibers and nanomaterials play a vital role in the manufacture and design of novel structures for bone and tissue repair. In addition, the use of nanofluids in the field of pharmaceuticals for imaging and sensing is increasing. Further nanomaterials have been introduced into the packaging of food processing to estimate the ambient environment around the food keeping it safe and protected from bacterial contamination. Choi and Eastman (4) have introduced the idea of enhancing the thermal efficiency of base fluids via nanoparticles. Buongiorno (5) investigated the heat convective transport phenomenon of nanomaterial by considering Brownian diffusion and thermophoretic characteristics. Buongiorno model flow over a permeable and substantially extended surface is scrutinized by Alblawi et al. (6). Chemical reactions and heat generation/absorption in the boundary layer flow of Carreau nanofluid configured by a non-linearly stretching surface through a porous medium is illustrated by Eid et al. (7). Ahmad et al. (8) examined the three-dimensional second-grade nanofluid flow due to thermophoresis and Brownian motion behaviours. As-

ma et al. (9) demonstrated the MHD 3D nanofluid flow from a rotating disk. The 3D flow of MHD nanofluids through a non-linear surface with nanoparticles is illustrated by Hayat et al. (10). Hayat et al. (11) examined the 3D Carreau fluid flow in the occurrence of nanomaterials formed by a nonlinearly extensible surface. In view of the growing demand for current technologies and the industrial stages, attention has been paid to enhance the reach of nanofluid flow through the changed geometries (12). The heat transfer in the Maxwell nanofluid flow through the solar amplification is inspected by Khan et al. (13). More research executed in the field of nanofluids can be seen in attempts (14–22). Furthermore, magnetized nanoliquid is a unique category of fluid which possessed the characteristics of nanoparticles and magnet. Magnetic nanofluids are used for filtration, magnetoreception, and separation. Furthermore, magnetic nanofluid has commonly used in several fields such as hyperthermia treatment, imaging, and sensing, targeted drug delivery, optical modulators, and scanning, etc. (29). The crucial significance of the magnetic field in micropolar fluid flow with nanoparticles is addressed by Hsiao (24). Sheikholeslami and Rokni (25) reported the magnetic field aspects in the presence of nanoliquid via melting mechanisms.

When the swimming microorganisms are concentrated in the higher portion of the fluid, bioconvection arises owing to the unbalanced dens nature of microorganisms. During this phenomenon, bioconvection build-up and the microorganism travels from the top fluid portion to the bottom fluid zone due to the massive difference in density. Bioconvection happens as micro-organisms, which are thicker than water, swim forward onto the median. Hassan et al. (26) evaluated the numerical solution for nanofluid flow by revolving disk with microorganisms' slips. Khan et al. (27) examined the bioconvection movement of nanofluid throughout the stretched sheet which is assumed to be oscillatory. Tlili et al. (28) examined the inspiration of second-order slip and activation energy on Oldroyd-B nanofluid flow with bioconvection. The thermal conduction mechanism of the MHD Williamson nanofluid flow in the presence of the motile gyrostatic micro-organism is scrutinized by Hassan et al. (29). Hassan et al. (30) analyzed the bioconvection flow of modified second-grade nanoliquids consisting of nanomaterials and microorganisms. Wang et al. (31) illustrated the effectiveness of Prandtl bioconvective thermally magnetized tangent hyperbolic nanofluids with gyrotactic motile microorganisms. Khan et al. (32) examined the bioconvection of couple stress nanomaterial subject to activation energy and Wu's slip. Many researchers have recently contributed to bioconvection effects by utilizing different fluids (33-37).

The prime aim of this communication is to examine the bio-convection flow of magnetized thixotropic nanofluid involving gyrotactic motile microorganisms. The thixotropic model is more perfect and has novel characteristics. The governing equations are tackled numerically by utilizing the bvp4c scheme with the help of computational commercial MATLAB software. The behaviors of flow controlling

parameters against temperature distribution, the concentration of nanoparticles, and rescaled motile microorganisms are graphically examined.

2 Mathematical Statement

Here we intend to elaborate the model of 2D magneto-thixotropic nanofluid flow within a swimming gyrotactic motile microorganisms across a variable ticked surface. The mechanisms of stratified and convective conditions with bioconvection on magneto-thixotropic nanofluid are accounted. We chose Cartesian coordinates in x and y- ways (see Fig. 1). The stretching velocity is $U_w(x) = U_0(x+b)^n$. The system of the current model in the absence of a porous medium is given below (38).

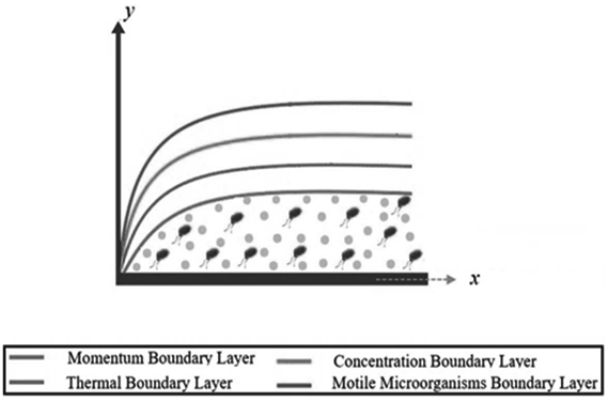

Fig. 1: Physical sketch of the model.

$$\partial_x u + \partial_y v = 0, \tag{1}$$

$$\left.\begin{aligned} u\partial_x u + v\partial_y u = v\partial_{yy}u - \tfrac{\sigma B_0^2 u}{\rho_f}(x+b)^{n-1} - \tfrac{6R_1}{\rho_f}\left(\partial_y u\right)^2\partial_{yy}u \\ -\tfrac{4R_2}{\rho_f}\begin{bmatrix} \left(\partial_y u\right)\left(\partial_{yy}u\right)\left(u\partial_{xy}u + v\partial_{yy}u\right) \\ +\left(\partial_y u\right)^2\begin{pmatrix} u\partial_{yy}u + v\partial_{yy}u \\ +\partial_y y\partial_{xy}u + \partial_y v\partial_{yy}u \end{pmatrix} \end{bmatrix} \\ +\tfrac{g^*}{\rho_f}\begin{bmatrix} \left(1-C_f\right)\rho_f\beta^{**}(T-T_\infty) \\ -\left(\rho_p-\rho_f\right)(C-C_\infty) \\ -(N-N_\infty)\gamma\left(\rho_m-\rho_f\right) \end{bmatrix} \end{aligned}\right\}, \tag{2}$$

$$\left.\begin{aligned} u\partial_x T + v\partial_y T = \alpha^*\partial_{yy}T + \tau\left\{D_B\partial_y C\partial_y T + \frac{D_T}{T_\infty}\left(\partial_y T\right)^2\right\} + \frac{\mu}{(\rho C)_f}\left(\partial_y u\right)^2 \\ -\frac{2\mu R_1}{(\rho c)_f}\left(\partial_y u\right)^4 + \frac{4\mu R_2}{(\rho c)_f}\left[u\partial_{xy}u + v\partial_{xy}u\right]\left(\partial_y u\right)^3 \\ +\frac{16\sigma^* T_\infty^3}{3k^*(\rho c)_f}\partial_{yy}T + \frac{Q(x)}{(\rho c)_f}(T - T_\infty) + \frac{\sigma B_0^2}{(\rho c)_f}(x+b)^{n-1}u^2 \end{aligned}\right\}, \tag{3}$$

$$u\partial_x C + v\partial_y C = D_B\partial_{yy}C + \frac{D_T}{T_\infty}\partial_{yy}T - Kr^2(C - C_\infty)\left(\frac{T}{T_\infty}\right)^n \exp\left(-\frac{E_a}{K_1 T}\right), \tag{4}$$

$$u\partial_x N + v\partial_y N + \frac{\left[\partial_y(N\partial_y C)\right]bW_c}{(C_f - C_\infty)} = D_m\partial_y\left(\partial_y N\right), \tag{5}$$

The associated boundary conditions are

$$\left.\begin{aligned} u = U_w(x) = U_0(x+b)^n, v = 0 - k\partial_y T = h_f\left(T_f - T\right), -D_B\partial_y C = h_g\left(C_f - C\right) \\ -D_m\partial_y N = h_m\left(N_f - N\right), at\ y = A_1(x+b)^{0.5(1-n)} \end{aligned}\right\}, \tag{6}$$

$$\left.\begin{aligned} u \to 0, v \to 0, T \to T_\infty = T_0 + d_1 x, C \to C_\infty = C_0 + d_2 x, \\ N \to N_\infty = N_0 + d_3 x\ at\ y \to \infty \end{aligned}\right\}, \tag{7}$$

where,

$$\left.\begin{aligned} Q(x) = Q_0(x+b)^{n-1}, T_f = T_0 + a_1 x, C_f = C_0 + a_2 x, N_f = N_0 + a_3 x \\ h_f = h_f^*(x+b)^{0.5(n-1)}, h_g = h_g^*(x+b)^{0.5(n-1)}, h_n = h_n^*(x+b)^{0.5(n-1)} \end{aligned}\right\}, \tag{8}$$

in which u and v stand for components of velocity in x- and y- axis correspondingly, B_0 for strength of magnetic field, σ for electrical conductivity, $U_w(x) = U_0(x+b)^n$ for stretching velocity, R_1 and R_2 for material constants, $(\rho c)_f$ and $(\rho c)_p$ for fluid specific heat and nanoparticles specific heat respectively, ρ_f for density of base fluid, α^* for thermal diffusivity, D_B for coefficient of Brownian motion, D_T for coefficient of thermophoresis diffusion, $Q(x)$ for non-uniform heat generation/absorption coefficient, n for velocity power index, $\left(\frac{T}{T_\infty}\right)^{n_1}\exp\left(-\frac{E_a}{K_1 T}\right)$ for modified Arrhenius function, E_a for activation energy, n_1 for fitted rate constant, σ^* for Stefan–Boltzmann constant, k^* for mean absorption coefficient, ρ_p for fluid density, ρ_m for density of motile microorganism, T for temperature of nanoparticles, C for nanoparticles volume fraction, N for microorganisms concentration, T_∞ for ambient temperature, C_∞ and N_∞ for ambient volumetric nanoparticles concentration and ambient microorganisms field, W_c for maximum cell speed of gyrotactic motile microorganisms and D_m for microorganisms diffusivity. Considering (1):

$$\left.\begin{array}{c}\zeta = y\sqrt{\frac{n+1}{2\nu}}U_0(x+b)^{n-1}, \psi = \sqrt{\left(\frac{2}{n+1}\right)\nu U_0(x+b)^{n+1}}\,F(\zeta)\\ T = \Theta(\zeta)\left(T_f - T_0\right) + T_\infty, C = \varphi(\zeta)\left(C_f - C_0\right) + C_\infty,\\ N = \varpi(\zeta)\left(N_f - N_0\right) + N_\infty\end{array}\right\}. \tag{9}$$

where ψ stands for stream function, ζ for dimensionless variable and U_0 for reference velocity. By employing the above transformations, the governing system is reduced to the following expressions:

$$\left.\begin{array}{c}F''' + FF'' + \frac{(n+1)}{2}K_1F''^2F'''' - \frac{(n-1)}{2}K_2\left(\begin{array}{c}\frac{(n+1)}{2}FF''^2F'''' - \frac{(5n-3)}{2}F'F''^2F'''\\ -\frac{(3n-1)}{2}F''^4 + \frac{(n+1)}{2}FF''F''''^2\end{array}\right)\\ -\frac{2}{n+1}M^2(F') + \frac{2}{n+1}\lambda(\theta - Nr\phi - Nc\chi) = 0\end{array}\right\}, \tag{10}$$

$$\left.\begin{array}{c}\left(1+\frac{4}{3}Rd\right)\Theta'' + PrF\Theta' - \frac{2}{n+1}PrF'\Theta + \Pr\left(Nb\Theta'\varphi' + Nt\,\Theta'^2\right) + \frac{(n+1)}{2}PrEcF''^2\\ + \frac{n+1}{6}K_1PrEcF''^4 + K_2\Pr^{Ec}\left\{\frac{(n+1)}{2}F'F''^4 - \frac{(3n-1)}{2}FF''^3F'''\right\} + \frac{(n+1)}{2}PrEcMF'^2\\ + \frac{2}{n+1}(Pr\delta\theta - PrS_1F') = 0\end{array}\right\}, \tag{11}$$

$$\left.\begin{array}{c}\varphi'' + PrLe(F\varphi') + \frac{Nt}{Nb}\Theta'' - \frac{2}{n+1}PrLe(S_2F' + F'\varphi)\\ -PrLe\sigma^*(1+\delta_0\Theta)^{n_1}\exp\left(-\frac{E_1}{1+\delta_0\Theta}\right)\varphi = 0\end{array}\right\}, \tag{12}$$

$$\varpi'' + LbF\varpi' - Pe[\varphi''(\varpi + \delta_1) + \varpi'\varphi'] = 0, \tag{13}$$

$$\left.\begin{array}{c}F(\alpha) = \alpha\frac{(1-n)}{1+n}, F'(\alpha) = 1, \Theta'(\alpha) = -\alpha_1\left(1 - S_1 - \Theta(\alpha)\right),\\ \varphi'(\alpha) = -\alpha_2\left(1 - S_2 - \varphi(\alpha)\right), \varpi'(\alpha) = -\alpha_3\left(1 - S_3 - \varpi(\alpha)\right),\\ F' \to 0, \Theta \to 0, \varphi \to 0, \varpi \to 0\ as\ \zeta \to \infty\end{array}\right\}. \tag{14}$$

Using $F(\zeta) = f(\zeta - \alpha) = f(\zeta), \Theta(\zeta) = \theta(\zeta - \alpha) = \theta(\zeta)$ and $\varphi(\zeta) = \phi(\zeta - \alpha) = \phi(\zeta), \varpi(\zeta) = \chi(\zeta - \alpha) = \chi(\zeta)$, in expressions (10)-(14), we have

$$f''' + ff'' + \frac{(n+1)}{2}K_1f''^2f''' - \frac{(n+1)}{2}K_2\left(\begin{array}{c}\frac{(n+1)}{2}ff''^2f'''' - \frac{5n-3}{2}f'f''^2f'''\\ -\frac{(3n-1)}{2}f''^4 + \frac{(n+1)}{2}ff''f''''^2\end{array}\right), \tag{15}$$

$$\left.\begin{array}{c}\left(1+\frac{4}{3}Rd\right)\theta'' + Prf\theta' - \frac{2}{n+1}Prf\theta' - \frac{2}{n+1}Prf'\theta + \Pr\left(Nb\theta'\phi' + Nt\theta'^2\right)\\ + \frac{(n+1)}{2}PrEcf''^2 + \frac{n+1}{6}K_1PrEcf''^4 + K_2PrEc\left\{\frac{n+1}{2}f'f''^4 - \frac{3n-1}{2}ff''^3f'''\right\}\\ \frac{n+1}{2}PrEcMf'^2 + \frac{2}{n+1}(Pr\delta\theta - PrS_1f') = 0\end{array}\right\}, \tag{16}$$

$$\left.\begin{aligned}\phi'' + PrLe(f\phi') + \frac{Nt}{Nb}\theta'' - \frac{2}{n+1}PrLe(S_2 f' + f'\phi)\\ -PrLe\sigma^*(1+\delta_0\theta)^{n_1}\exp\left(-\frac{E_1}{1+\delta_0\theta}\right)\phi = 0\end{aligned}\right\}, \tag{17}$$

$$\chi'' + Lbf\chi' - Pe[\phi''(\chi+\delta_1) + \chi'\phi'] = 0, \tag{18}$$

$$\left.\begin{aligned}f(0) = \alpha\frac{1-n}{1+n}, f'(0) = 1, \theta'(0) = -\alpha_1\big(1 - S_1 - \theta(0)\big),\\ \phi'(0) = -\alpha_2\big(1 - S_2 - \phi(0)\big), \chi'(0) = -\alpha_3\big(1 - S_3 - \chi(0)\big),\\ f' \to 0, \theta \to 0, \phi \to 0, \chi \to 0 \; as \; \zeta \to \infty\end{aligned}\right\}, \tag{19}$$

Here $K_1 \& K_2$ stand for material parameters of thixotropic liquid, Pr for Prandtl number, λ for mixed convection parameter, Nr for Buoyancy ratio parameter, Nc for bioconvection Rayleigh number, M for magnetic parameter, Rd for thermal radiation parameter, α for velocity slip parameter, Nt for thermophoresis number, Nb for Brownian motion parameter, τ for heat capacity ratio, Le for Lewis number, E_1 for activation energy, δ for heat generation parameter, α^* for thermal diffusivity, σ^* for chemical reaction parameter, δ_0 for temperature difference parameter, δ_1 for microorganisms difference parameter, S_1 for the thermally stratified parameter, S_2 for the solutal stratified variable, S_3 for microorganisms stratification variable, α_1 for Biot number, α_2 for solutal Biot number, α_3 for stratification Biot number and δ_1 for motile microorganism differences parameter. Such parameters are stated below:

$$\left.\begin{aligned}K_1 = -\frac{6R_1U_0^3(x+b)^{3n-1}}{\rho_f\nu^2}, K_2 = \frac{4R_2U_0^4(x+b)^{4n-2}}{\rho_f\nu^2}, Pr = \frac{\nu}{\alpha}, \lambda = \frac{g^*\beta^{**}(T_f-T_0)(1-C_f)}{U_0^2(x+b)^{2n-1}\rho_f},\\ Nr = \frac{(\rho_p-\rho_f)(C_f-C_0)}{\beta^{**}(1-C_f)(T_f-T_0)}, Nc = \frac{\gamma(\rho_m-\rho_f)(N_f-N_0)}{\beta^{**}(T_f-T_0)(1-C_f)}, M = \frac{\sigma B_0^2}{\rho_f U_0}, Rd = \frac{4\sigma^*T_\infty^3}{kk^*},\\ Ec = \frac{U_W^2}{C_f(T_f-T_\infty)}, Le = \frac{\alpha}{D_B}, Nt = \frac{\tau D_T(T_f-T_0)}{T_\infty\nu}, Nb = \frac{\tau D_B(C_f-C_0)}{\nu}, \tau = \frac{(\rho c)_p}{(\rho c)_f},\\ E_1 = \frac{E_a}{kT_\infty}, \delta = \frac{Q_0}{U_0(\rho c)_f}, \alpha^* = \frac{k}{(\rho c)_f}, \sigma^* = \frac{Kr^2}{a}, \delta_0 = \frac{T_W-T_\infty}{T_\infty}, \delta_1 = \frac{N_\infty}{N_f-N_\infty},\\ S_1 = \frac{d_1}{a_1}, S_2 = \frac{d_2}{a_2}, S_3 = \frac{d_3}{a_3}, \alpha_1 = \frac{h_f^*}{k}\sqrt{\frac{2\nu}{(n+1)U_0}}, \alpha_2 = \frac{h_g^*}{D_B}\sqrt{\frac{2\nu}{(n+1)U_0}},\\ \alpha_3 = \frac{h_n^*}{D_m}\sqrt{\frac{2\nu}{(n+1)U_0}}, \alpha = A_1\sqrt{\left(\frac{(n+1)}{2}\right)\left(\frac{U_0}{\nu}\right)}\end{aligned}\right\}. \tag{20}$$

The physical engineering quantities of interest such as skin friction coefficient C_f, local Nusselt number Nu , local Sherwood number Sh and local rescaled of motile microorganism's density number Nn are expressed by

$$C_f = \frac{2\tau_\omega}{\rho u_\omega^2}, Nu = \frac{(x+b)q_\omega}{k(T_f-T_\omega)}, Sh = \frac{(x+b)q_m}{D_B(C_f-C_\infty)}, Nn = \frac{(x+b)q_n}{D_m(N_f-N_\infty)}, \tag{21}$$

where,

$$\left.\begin{aligned}\tau_\omega = \left[\left(\mu - 2R_1\left(\partial_y u\right)^2\right)\partial_y u\right]\Big|_{y=A_1(x+b)^{0.5(1-n)}}, q_\omega = -k\left(\partial_y T\right)\Big|_{y=A_1(x+b)^{0.5(1-n)}}\\ q_m = -D_B\left(\partial_y C\right)\Big|_{y=A_1(x+b)^{0.5(1-n)}}, q_n = -D_m\partial_y N\Big|_{y=A_1(x+b)^{0.5(1-n)}}\end{aligned}\right\}, \tag{22}$$

By using (21) and (22), we get

$$C_{f_x}Re^{0.5} = \sqrt{\frac{(n+1)}{2}}\left[f''(0) + \frac{(n+1)}{2}K_1\left(f''(0)\right)^3\right], \tag{23}$$

$$Nu_xRe^{-0.5} = -\sqrt{\frac{(n+1)}{2}}\theta'(0), \tag{24}$$

$$Sh_xRe^{-0.5} = -\sqrt{\frac{(n+1)}{2}}\phi'(0), \tag{25}$$

$$Nn_xRe^{-0.5} = -\sqrt{\frac{(n+1)}{2}}\chi'(0). \tag{26}$$

In which $Re = \frac{U_0(x+b)^{n+1}}{\nu}$ stands for local Reynolds number, C_{f_x} for dimensionless skin friction, Nu_x for dimensionless local Nusselt number, Sh_x for dimensionless local Sherwood number and Nn_x for dimensionless local motile microorganisms' number.

3 Numerical Procedure

The solution of a coupled nonlinear system (15)–(18) with dimensionless restrictions (19) is not possible due to its nonlinearity. Various governing numerical and analytical techniques are available for solving this system. Here numerical computations for the velocity field, temperature distribution, concentration field, and microorganism's concentration are calculated by employing shooting technique via bvp4c solver under computational commercial software MATLAB. The bvp4c solver has been employed here for the calculation of the boundary value problem. Bvp4c is a finite difference collocation code that employs the interesting methodology 3-stages Lobatto-IIIa formula. This is a collocation method and the polynomial collocation gives C_1 -continuous result that is regularly specific to the 4th-order in the interval, where the function is integrated. The bvp4c is much harder to solve than initial boundary value problems and any other solver fails even with good guesses. The bvp4c scheme solves the nonlinear system of first-order ordinary differential equation. The bvp4c solves ODE's by using analytical conductions. Mesh choice and error manage are depended upon the residual of the incessant explanation. The process is repeated until results are obtained within tolerance 10^{-6}. Before starting

the simulation, firstly we convert higher-order systems into first-order problems such as follow:

$$f = p, \frac{df}{d\zeta} = p_1, \frac{d^2f}{d\zeta^2} = p_2, \frac{d^3f}{d\zeta^3} = p_3, \frac{d^4f}{d\zeta^4} = p_3', \theta = p_4, \frac{d\theta}{d\zeta} = p_5, \frac{d^2\theta}{d\zeta^2} = p_5', \phi = p_6,$$

$$\frac{df}{d\zeta} = p_7, \frac{d\phi}{d\zeta} = p_7', \chi = p_8, \frac{d\chi}{d\zeta} = p_9, \frac{d^2\chi}{d\zeta^2} = p_9',$$

$$\left.\begin{aligned}
p_3' &= \frac{1}{\left(\frac{(n+1)^2}{4}K_2 pp_2^2\right)}\begin{pmatrix} p_3 + pp_2 + \frac{(n+1)}{2}K_1 p_2^2 p_3 \\ -\frac{(n+1)}{2}K_2\begin{pmatrix} -\frac{(5n-3)}{2}p_1 p_2^2 p_3 - \frac{(3n-1)}{2}p_2^4 \\ +\frac{(n+1)}{2}pp_2 p_3^2 \end{pmatrix} \\ -\frac{2}{n+1}M^2 p_1 - \frac{2\lambda}{n+1}(p_4 - Nrp_6 - Ncp_8) \end{pmatrix}, \\
p_5' &= \frac{1}{\left(1+\frac{4}{3}R\right)}\begin{bmatrix} -\Pr\left(pp_5 - \frac{2}{n+1}p_1 p_4 + Nbp_5 p_7 + Ntp_5^2\right) \\ -\frac{PrEc(n+1)}{2}(p_2^2 + Mp_1^1) - \frac{n+1}{6}K_1 PrEcp_2^4 \\ -K_2 PrEc\left\{\frac{(n+1)}{2}p_1 p_2^4 - \frac{(3n-1)}{2}pp_2^3 p_3\right\} \\ -\frac{2}{n+1}(Pr\delta p_4 - PrS_1 p_1) \end{bmatrix}, \\
p_7' &= \begin{Bmatrix} -Prpp_7 - \frac{Nt}{Nb}p_5' + \frac{2}{n+1}PrLe(S_2 p_1 + p_1 p_6) \\ +PrLe\sigma^*(1+\delta_0 p_4)^n \exp\left(-\frac{E_1}{1+\delta_0 pL_4}\right)p_6 \end{Bmatrix}, \\
p_9' &= -Lbpp_9 + Pe[p_7'(p_8 + \delta_1) + p_9 p_7], \\
p(0) &= \alpha\frac{(1-n)}{1+n}, p_1(0) = 1, p_5(0) = -\gamma_1\big(1 - S_1 - p_4(0)\big), \\
p_7(0) &= -\gamma_2\big(1 - S_2 - p_6(0)\big) \\
p_9(0) &= -\gamma_3\big(1 - S_3 - p_8(0)\big), at\ \zeta = 0 \\
p_1 &\to 0, p_4 \to 0, p_6 \to 0, p_8 \to 0\ as\ \zeta \to \infty.
\end{aligned}\right\} \quad (27)$$

4 Results and Discussion

The behaviors of different flow-regulating variables namely radiation parameter Rd, Eckert number Ec , Biot number α_1 , magnetic parameter M , mixed convection parameter λ , Lewis number Le , thermophoresis parameter Nt , Prandtl number Pr,

solutal nanoparticles Biot number α_2 , Brownian motion parameter Nb , bioconvection Lewis number Lb , stratification motile microorganism Biot number α_3 and Peclet number Pe on the volumetric concentration of nanoparticle ϕ , temperature distribution θ and motile microorganisms field χ are visualized in this section. The salient features of prominent parameters are captured in Figs. 2-18. Fig. 2 is the illustration of the radiation parameter Rd over the temperature distribution. The intense magnitude of the radiation parameter intensifies the temperature field. Physically, the dimensionless parameter refers to the relative effect of heat transfer conduction to thermal radiation transfer. The variation of Eckert number Ec over-temperature field θ is delineated by Fig. 3. The output reflects that intensified paces of Eckert number Ec give an improvement in the temperature field. The dimensionless parameter is the characteristic of continuum mechanics and the relation between kinetic energy and boundary layer enthalpy difference. The physical significance of the Prandtl number Pr over-temperature distribution θ is portrayed by Fig. 4. Prandtl number Pr is the computation of thermal distribution between fluid and medium. Hence the larger amount of heat transfer rate gives a reduction of temperature of nanofluid. The graphical illustration exhibits reduction in temperature coefficient when the Prandtl number Pr is intensified. To exhibit the variation of fluid temperature for larger paces of Biot number α_1 is plotted in Fig. 5. It is notified that Biot number α_1 is the reason for the incrimination of temperature θ for the larger variation. The significance of the magnetic parameter versus temperature field is illustrated by Fig. 6. The larger function of the magnetic parameter M enhances temperature distribution. The physical nature of the thermophoresis parameter Nt versus the temperature field θ is revealed by Fig. 7. Here noted that when the thermophoresis parameter Nt is enhanced as an outcome, the temperature profile θ also rises. The impact of the mixed convection parameter λ over temperature distribution θ is depicted through Fig. 8. A retarding impact of the temperature θ is analyzed for the privileged amount of mixed convection parameter. The physical nature of the thermophoresis parameter Nt over the concentration profile ϕ is displayed by Fig. 9. The dimensionless parameter gives a rising trend for the concentration profile as we intensify it. The larger estimations of the thermophoresis parameter Nt upsurge the concentration of nanomaterials. The ratio between thermal and mass diffusivities is defined by the Lewis number. The physical significance of Lewis number over the volumetric concentration of nanoparticles is portrayed in Fig. 10. It is observed that privileged values of Lewis number Le results in decay in the amount of concentration profile. Generally, the rate of mass transfer diminishes by an increment of Lewis number. The variation of fluid concentration ϕ for varying values of solutal nanoparticles Biot number α_2 is disclosing in Fig. 11. The higher magnitude of solutal nanoparticle Biot number α_2 raise the concentration field. The physical nature of this trend depicts that the concentration profile gives a rising behavior on a larger variation of solutal nanoparticle Biot number. To depict the inspiration of b , Brownian motion parameter versus volumetric nanoparticle field ϕ is graphed in Fig. 12.

The concentration profile ϕ shows a decreasing trend for the higher amount of Brownian motion parameter b . The higher estimations of Prandtl number Pr to observe the effect of concentration distribution ϕ is portrayed in Fig. 13. The sketched lines are evidence that the Prandtl number Pr is the reason for the decreasing concentration of nanoparticles. The significance of the mixed convection parameter λ over concentration distribution ϕ is delineated in Fig. 14. The observed result reveals that when we intensify the mixed convection parameter λ the amount of concentration field ϕ declines. Physically, mixed convection is the mechanism of collective forced and free convections. To observe the behavior of stratification motile microorganism Biot number over motile microorganism distribution, Fig. 15 is sketched. The observed information reveals that stratification motile microorganism Biot number α_3 rises the motile microorganisms χ. The motile particle inside the fluid to upsurges the rate of heat transfer from the fluid to the medium. The amount of motility distribution χ decreases in case of larger variation of Peclet number e . The larger amount of Peclet number Pe gives a retarding trend for the motility profile of nanofluid. The physical evidence of the above discussion is presented in Fig. 16. The significance of bioconvection Lewis number Lb against microorganism distribution χ is discussed in Fig. 17. The amount of motile microorganism distribution χ reduces on the rising magnitude of bioconvection Lewis number b . The amount of motility also decreases when we undergo with mixed convection parameter. The above statement is illustrated graphically in Fig. 18. The numerical results of involved parameters against local Nusselt number $-\theta'(0)$, local Sherwood number $-\phi'(0)$ and rescaled density number of microorganisms $-\chi'(0)$ are elaborated in this section. Table 1 delineates the impacts of $M, Nt, Nb, Pr, \lambda, S_1, Rd, Nr, Nc$ via the local Nusselt number $-\theta'(0)$. Here local Nusselt number $-\theta'(0)$ uprises for a higher amount of Brownian motion Nb and thermophoresis Nt parameters while the opposite inspiration for mixed convection parameter is watched. Table 2 summarizes the effects of $M, Nt, Nb, Pr, \lambda, S_2, Rd, Nr, Nc$ on local Sherwood number. Local Sherwood number increases for different variations of bioconvection Rayleigh number Nc and Buoyancy ratio parameter r . The significance of the rescaled microorganism's density number against $Lb, Pe, \lambda, Nr, Nc, S_3$ is presented in Table 3. The microorganism's concentration decreases for bioconvection Lewis and Peclet numbers.

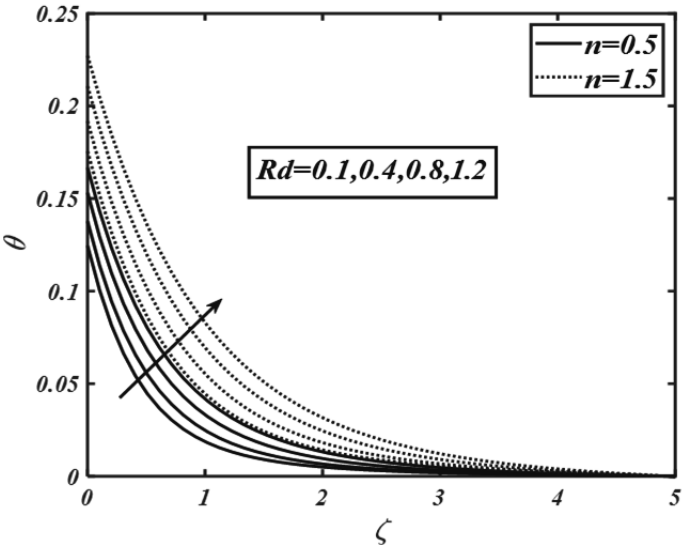

Fig. 2: Variation of Rd via θ.

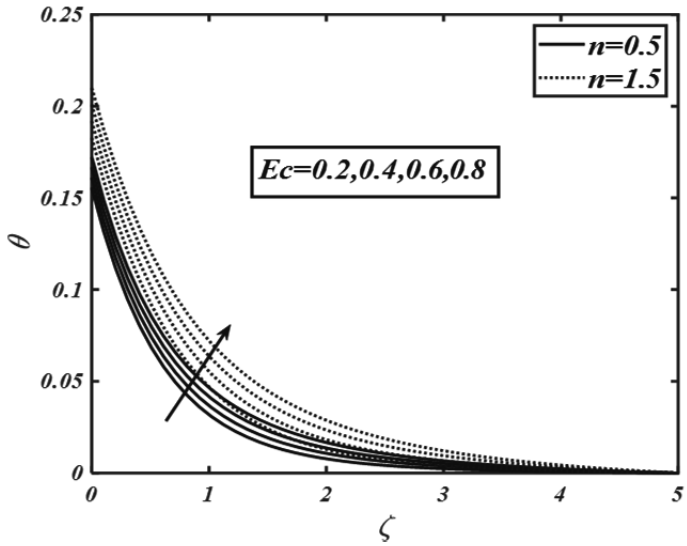

Fig. 3: Variation of Ec via θ.

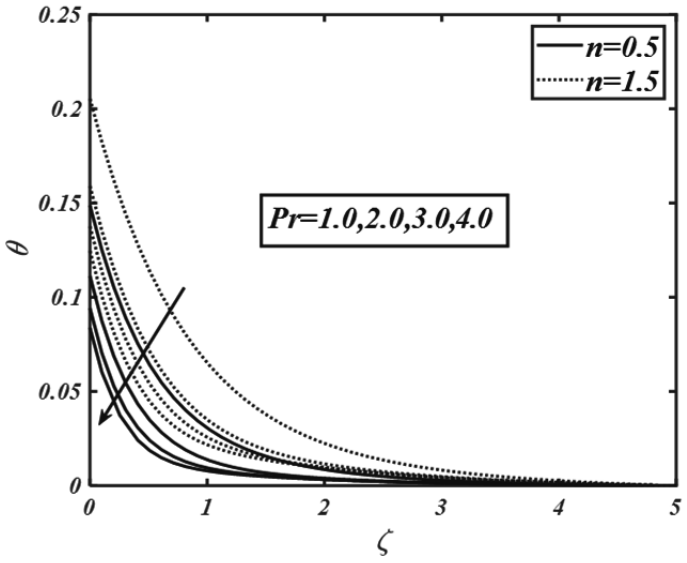

Fig. 4: Variation of Pr via θ.

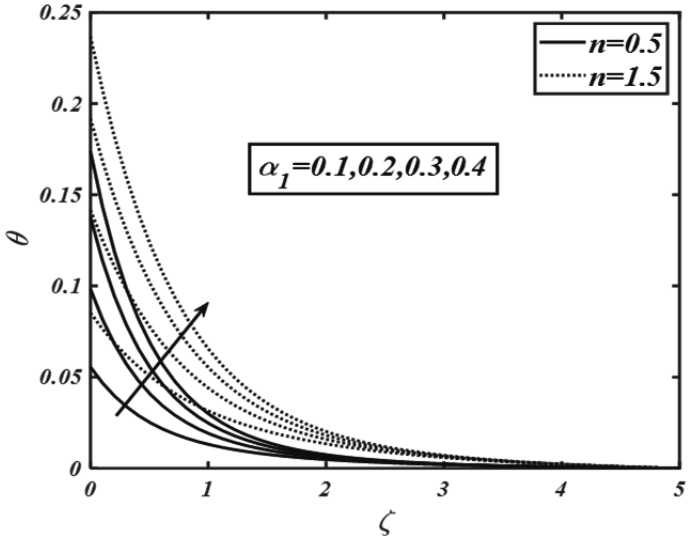

Fig. 5: Variation of α_1 via θ.

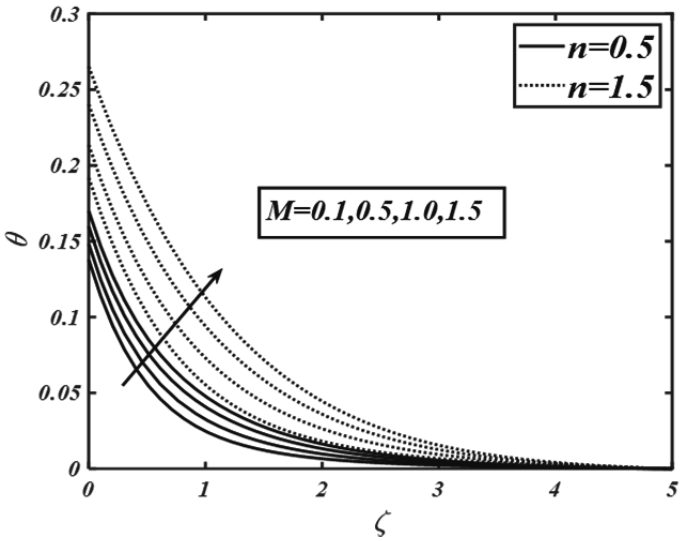

Fig. 6: Variation of M via θ.

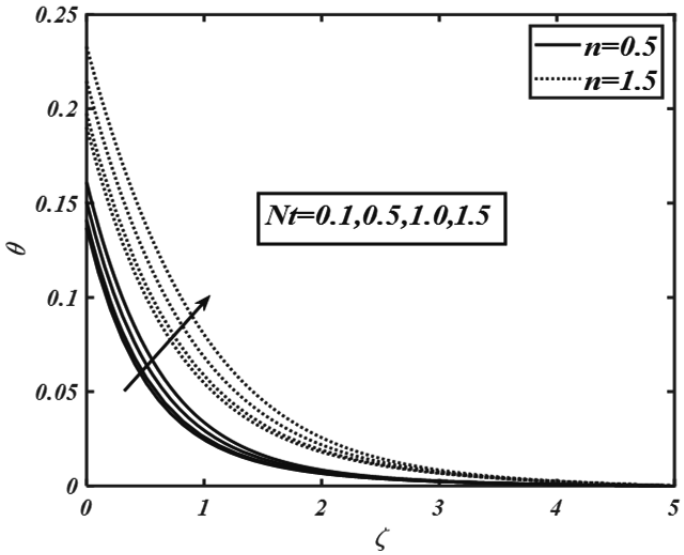

Fig. 7: Variation of Nt via θ.

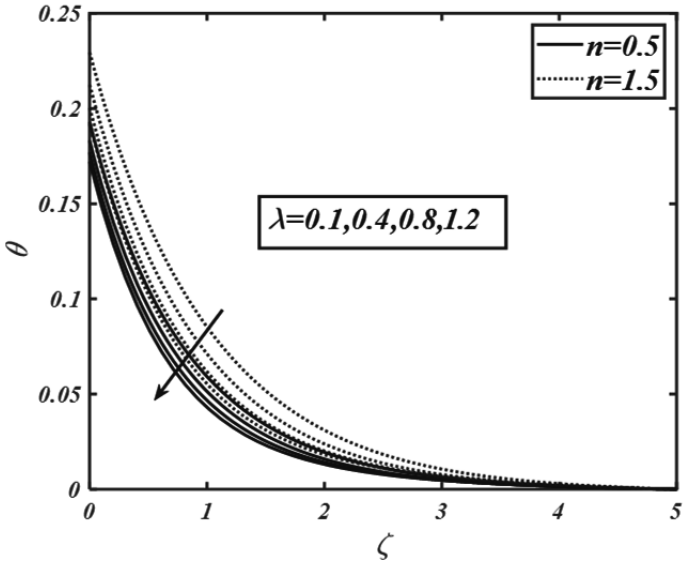

Fig. 8: Variation of λ via θ.

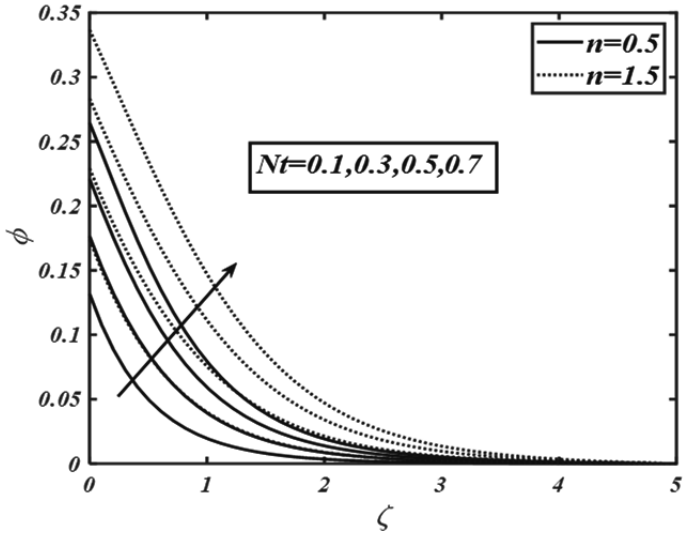

Fig. 9: Variation of Nt via ϕ.

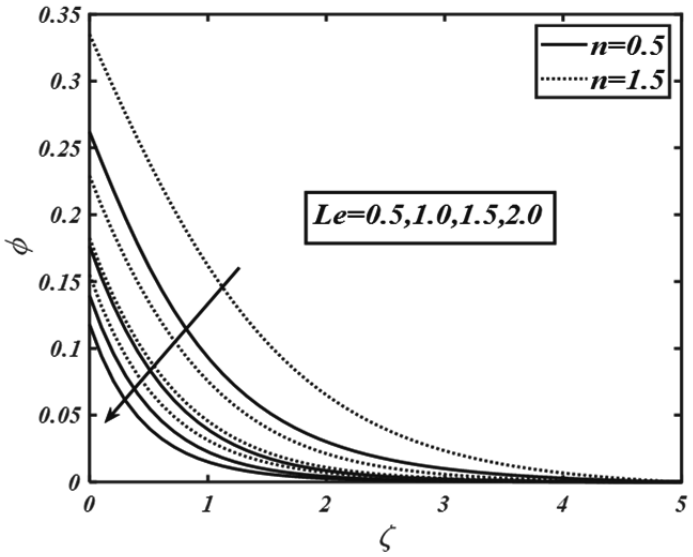

Fig. 10: Variation of Le via ϕ.

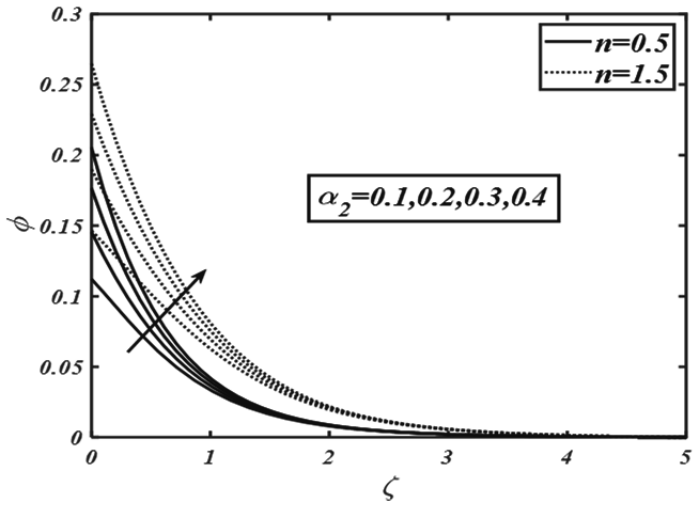

Fig. 11: Variation of α_2 via ϕ.

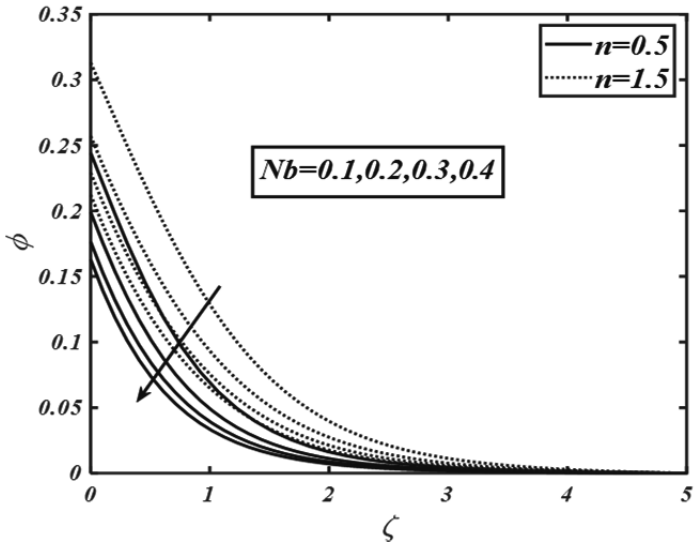

Fig. 12: Variation of Nb via ϕ.

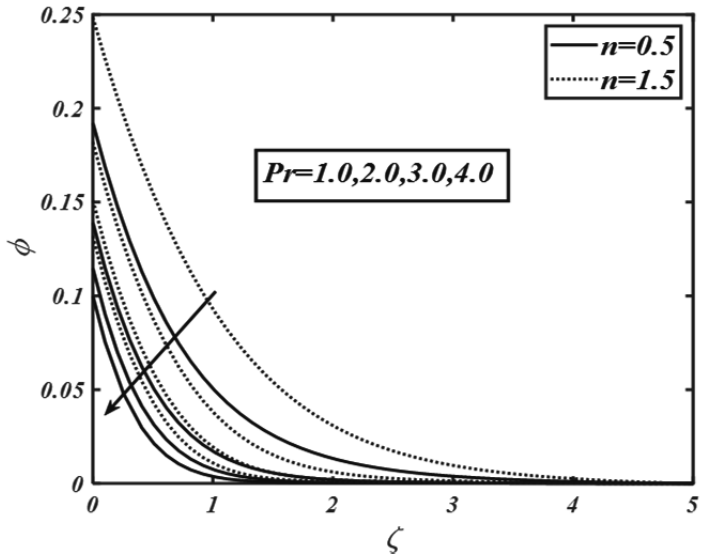

Fig. 13: Variation of Pr via ϕ.

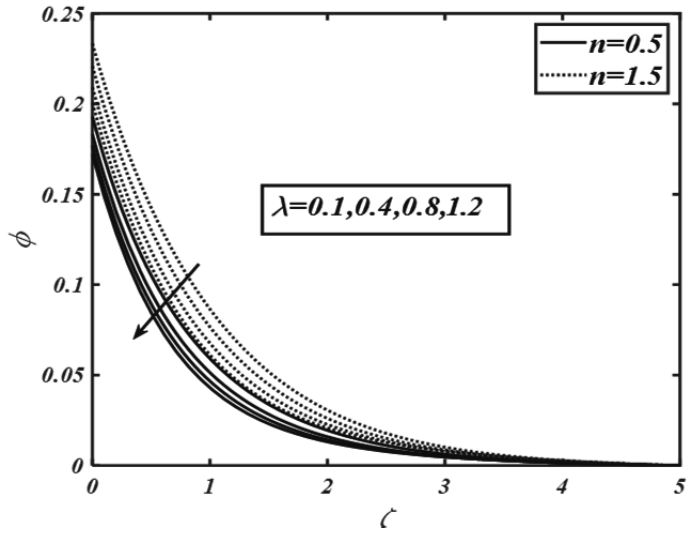

Fig. 14: Variation of λ via ϕ.

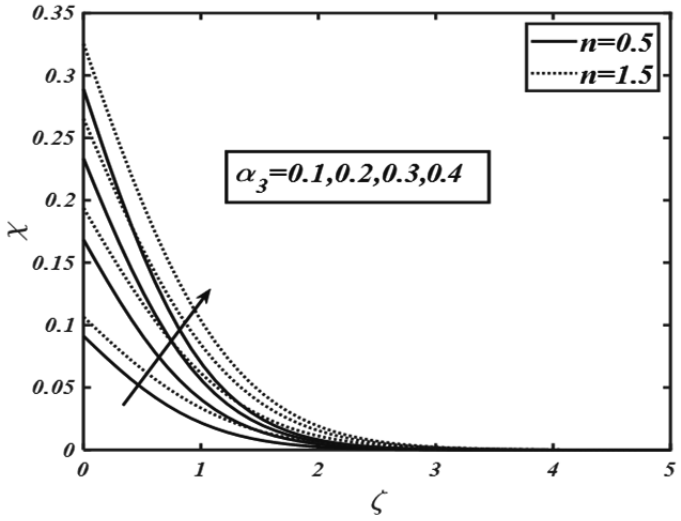

Fig. 15: Variation of α_3 via χ.

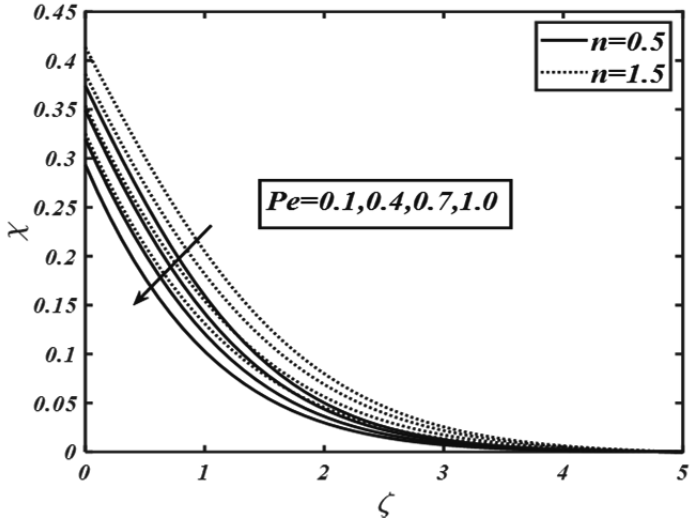

Fig. 16: Variation of Pe via χ.

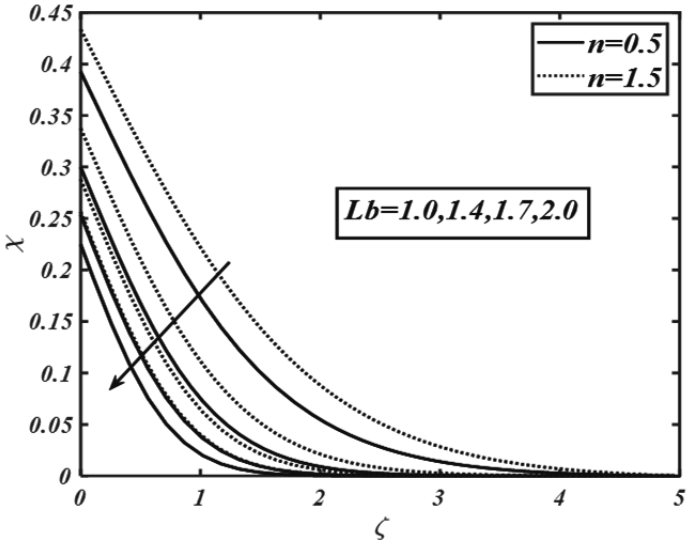

Fig. 17: Variation of Lb via χ.

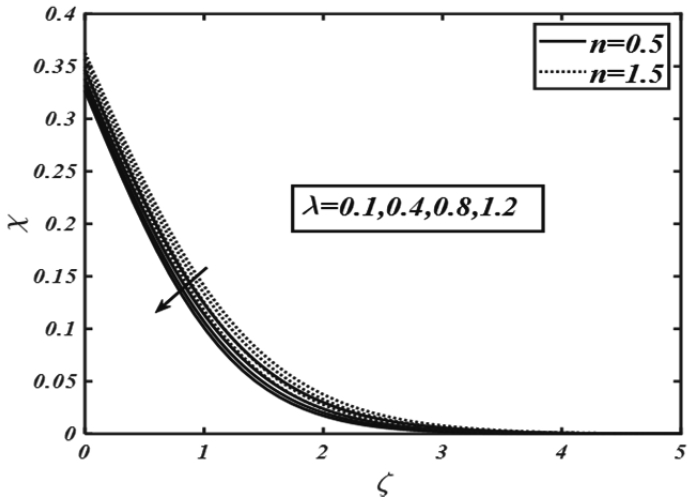

Fig. 18: Variation of λ via χ.

Tab. 1: Numerical data of local Nusselt number $-\theta'(0)$ against $M, Nt, Nb, Pr, \lambda, S_1, Rd, Nr, Nc$.

M	Nt	Nb	Pr	λ	S_1	Rd	Nr	Nc	$-\theta'(0)$	
									$n = 0.5$	$n = 1.5$
0.2	1.0	0.5	1.2	0.1	0.3	0.4	0.2	0.2	0.2579	0.2406
0.6									0.2542	0.2322
1.0									0.2509	0.2245
0.1	0.1	0.5	1.2	0.1	0.3	0.4	0.2	0.2	0.2352	0.2339
	0.6								0.2332	0.2319
	1.2								0.2308	0.2294
0.1	1.0	0.1	1.2	0.1	0.3	0.4	0.2	0.2	0.2329	0.2316
		0.6							0.2312	0.2299
		1.2							0.2290	0.2277
0.1	1.0	0.5	1.0	0.1	0.3	0.4	0.2	0.2	0.2264	0.2249
			2.0						0.2441	0.2432
			3.0						0.2521	0.2515
0.1	1.0	0.5	1.0	0.1	0.3	0.4	0.2	0.2	0.2305	0.2291

M	Nt	Nb	Pr	λ	S_1	Rd	Nr	Nc	$-\theta'(0)$	
									$n = 0.5$	$n = 1.5$
				0.6					0.2306	0.2293
				1.2					0.2307	0.2295
0.1	1.0	0.5	1.2	0.1	0.2	0.4	0.2	0.2	0.1671	0.1663
					0.4				0.2838	0.2816
					0.6				0.3678	0.3641
0.1	1.0	0.5	1.2	0.1	0.3	0.1	0.2	0.2	0.1838	0.1836
						0.5			0.1917	0.1876
						1.0			0.1956	0.1917
0.1	1.0	0.5	1.2	0.1	0.3	0.4	0.1	0.2	0.2304	0.2290
							1.0		0.2299	0.2288
							2.0		0.2191	0.2277
0.1	1.0	0.5	1.2	0.1	0.3	0.4	0.2	0.1	0.2304	0.2290
								1.0	0.2302	0.2288
								2.0	0.2300	0.2285

Tab. 2: Numerical data of local Sherwood number $-\phi'(0)$ against $M, Nt, Nb, Pr, \lambda, S_2, Rd, Nr, Nc$.

M	Nt	Nb	Pr	λ	S_2	Rd	Nr	Nc	$-\phi'(0)$	
									$n = 0.5$	$n = 1.5$
0.2	1.0	0.5	1.2	0.1	0.3	0.4	0.2	0.2	0.2644	0.2538
0.6									0.2646	0.2550
1.0									0.2648	0.2563
0.1	0.1	0.5	1.2	0.1	0.3	0.4	0.2	0.2	0.2380	0.2365
	0.6								0.2132	0.2105
	1.2								0.1850	0.1808
0.1	1.0	0.1	1.2	0.1	0.3	0.4	0.2	0.2	0.0074	0.0212

M	Nt	Nb	Pr	λ	S_2	Rd	Nr	Nc	$-\phi'(0)$	
									$n = 0.5$	$n = 1.5$
0.1	1.0	0.1	1.2	0.1	0.3	0.4	0.2	0.2	0.0074	0.0212
		0.6							0.2026	0.1993
		1.2							0.2334	0.2212
0.1	1.0	0.5	1.0	0.1	0.3	0.4	0.2	0.2	0.1843	0.1800
			2.0						0.2183	0.2160
			3.0						0.2338	0.2322
0.1	1.0	0.5	1.2	0.2	0.3	0.4	0.2	0.2	0.1908	0.1870
				0.6					0.1911	0.1875
				1.2					0.1913	0.1881
0.1	1.0	0.5	1.2	0.1	0.2	0.4	0.2	0.2	0.1358	0.1331
					0.4				0.2393	0.2338
					0.6				0.3208	0.3127
0.1	1.0	0.5	1.2	0.1	0.3	0.1	0.2	0.2	0.2152	0.2127
						0.5			0.2153	0.2129
						1.0			0.2155	0.2131
0.1	1.0	0.5	1.2	0.1	0.3	0.4	0.1	0.2	0.1907	0.1865
							1.0		0.1890	0.1848
							2.0		0.1895	0.1819
0.1	1.0	0.5	1.2	0.1	0.3	0.4	0.2	0.1	0.1908	0.1866
								1.0	0.1902	0.1860
								2.0	0.1895	0.1852

Tab. 3: Numerical data of density number of motile microorganisms $-\chi'(0)$ against $Lb, Pe, \lambda, Nr, Nc, S_3$.

Lb	Pe	λ	Nr	Nc	S_3	$-\chi'(0)$	
						$n = 0.5$	$n = 1.5$
0.6	0.1	0.1	0.2	0.2	0.3	0.1933	0.1899
1.2						0.2222	0.2201
1.8						0.2358	0.2343

Lb	Pe	λ	Nr	Nc	S_3	$-\chi'(0)$	
						$n = 0.5$	$n = 1.5$
1.0	0.2	0.1	0.2	0.2	0.3	0.1957	0.1924
	0.6					0.2040	0.2016
	1.2					0.2157	0.2134
1.0	0.1	0.2	0.2	0.2	0.3	0.2153	0.2124
		0.6				0.2154	0.2132
		1.2				0.2155	0.2133
1.0	0.1	0.1	0.1	0.2	0.3	0.2152	0.2127
			1.0			0.2146	0.2120
			2.0			0.2134	0.2109
1.0	0.1	0.1	0.2	0.2	0.3	0.2153	0.2128
				1.0		0.2151	0.2125
				2.0		0.2148	0.2122
1.0	0.1	0.1	0.2	0.2	0.2	0.1585	0.1572
					0.4	0.2623	0.2586
					0.6	0.3355	0.3295

5 Conclusions

In this research work, the bioconvection flow of magneto-thixotropic nanofluid with motile microorganisms is studied numerically. Moreover, salient features of mixed convection, Brownian motion, bioconvection Rayleigh number, activation energy, bioconvection Lewis number, buoyancy ratio parameter, and Peclet number are addressed. Both temperature field and volumetric concentration of nanoparticles depict decreasing trend for enhancing estimation of mixed convection parameter. The concentration profile declines for the higher magnitude of the Brownian motion parameter and Lewis number while the reverse scenario is witnessed for thermophoresis parameter and solutal Biot number. The inspiration of solutal Biot number and stratification rescaled microorganisms Biot number on concentration and temperature distribution is quite similar. Rescaled motile microorganism's concentration is enhanced by varying the magnitude of stratification rescaled microorganisms Biot number. The motile mi-

croorganism's field is diminished with enhancing variation of Peclet number, bioconvection Lewis number, and mixed convection parameter.

Bibliography

Hayat T, Qayyum S, Alsaedi A, Ahmad B. Modern aspects of nonlinear convection and magnetic field in flow of thixotropic nanofluid over a nonlinear stretching sheet with variable thickness. Physica B: Condensed Matter. 2018 May 15;537:267-76.

Hayat T, Waqas M, Khan MI, Alsaedi A. Analysis of thixotropic nanomaterial in a doubly stratified medium considering magnetic field effects. International Journal of Heat and Mass Transfer. 2016 Nov 1;102:1123-9.

Hayat T, Waqas M, Shehzad SA, Alsaedi A. A model of solar radiation and Joule heating in magnetohydrodynamic (MHD) convective flow of thixotropic nanofluid. Journal of Molecular Liquids. 2016 Mar 1;215:704-10.

Choi SUS, Eastman JA. Enhancing thermal conductivity of fluids with nanoparticles (No. ANL/MSD/CP-84938; CONF-951135-29). Argonne National Lab., IL (United States). 1995.

Buongiorno J. Convective transport in nanofluids. Journal of heat transfer, 2006; 128(3): 240-250.

Alblawi A, Malik MY, Nadeem S, Abbas N. Buongiorno's nanofluid model over a curved exponentially stretching surface. Processes. 2019 Oct;7(10):665.

Eid MR, Mahny KL, Dar A, Muhammad T. Numerical study for Carreau nanofluid flow over a convectively heated nonlinear stretching surface with chemically reactive species. Physica A: Statistical Mechanics and its Applications. 2020 Feb 15;540:123063.

Ahmad M, Muhammad T, Ahmad I, Aly S. Time-dependent 3D flow of viscoelastic nanofluid over an unsteady stretching surface. Physica A: Statistical Mechanics and its Applications. 2020 Aug 1;551:124004.

Asma M, Othman WA, Muhammad T, Mallawi F, Wong BR. Numerical study for magnetohydrodynamic flow of nanofluid due to a rotating disk with binary chemical reaction and Arrhenius activation energy. Symmetry. 2019 Oct;11(10):1282.

Hayat T, Aziz A, Muhammad T, Alsaedi A. Active and passive controls of 3D nanofluid flow by a convectively heated nonlinear stretching surface. Physica Scripta. 2019 Jun 3;94(8):085704.

Hayat T, Aziz A, Muhammad T, Alsaedi A. Numerical simulation for three-dimensional flow of Carreau nanofluid over a nonlinear stretching surface with convective heat and mass conditions. Journal of the Brazilian Society of Mechanical Sciences and Engineering. 2019 Jan 1;41(1):55.

Ahmed J, Khan M, Ahmad L. Transient thin-film spin-coating flow of chemically reactive and radiative Maxwell nanofluid over a rotating disk. Applied Physics A. 2019 Mar 1;125(3):161.

Khan M, Salahuddin T, Tanveer A, Malik MY, Hussain A. Change in internal energy of thermal diffusion stagnation point Maxwell nanofluid flow along with solar radiation and thermal conductivity. Chinese Journal of Chemical Engineering. 2019 Oct 1;27(10):2352-8.

Alamri SZ, Ellahi R, Shehzad N, Zeeshan A. Convective radiative plane Poiseuille flow of nanofluid through porous medium with slip: an application of Stefan blowing. Journal of Molecular Liquids. 2019 Jan 1;273:292-304.

Hussain A, Nadeem S. MHD oblique stagnation point flow of copper-water nanofluid with variable properties. Physica Scripta. 2019 Oct 2;94(12):125808.

Nadeem S, Abbas N. Effects of MHD on modified nanofluid model with variable viscosity in a porous medium. InNanofluid Flow in Porous Media 2019 May 7. IntechOpen.

Sheikholeslami M, Keramati H, Shafee A, Li Z, Alawad OA, Tlili I. Nanofluid MHD forced convection heat transfer around the elliptic obstacle inside a permeable lid drive 3D enclosure consider-

ing lattice Boltzmann method. Physica A: Statistical Mechanics and its Applications. 2019 Jun 1;523:87-104.

Nazari S, Ellahi R, Sarafraz MM, Safaei MR, Asgari A, Akbari OA. Numerical study on mixed convection of a non-Newtonian nanofluid with porous media in a two lid-driven square cavity. Journal of Thermal Analysis and Calorimetry. 2020 May;140(3):1121-45.

Ellahi R, Sait SM, Shehzad N, Mobin N. Numerical simulation and mathematical modeling of electro-osmotic Couette–Poiseuille flow of MHD power-law nanofluid with entropy generation. Symmetry. 2019 Aug;11(8):1038.

Tlili I, Hamadneh NN, Khan WA. Thermodynamic analysis of MHD heat and mass transfer of nanofluids past a static wedge with Navier slip and convective boundary conditions. Arabian Journal for Science and Engineering. 2019 Feb 12;44(2):1255-67.

Farhangmehr V, Moghadasi H, Asiaei S. A nanofluid MHD flow with heat and mass transfers over a sheet by nonlinear boundary conditions: Heat and mass transfers enhancement. Journal of Central South University. 2019 May;26(5):1205-17.

Khan M, Irfan M, Khan WA, Sajid M. Consequence of convective conditions for flow of Oldroyd-B nanofluid by a stretching cylinder. Journal of the Brazilian Society of Mechanical Sciences and Engineering. 2019 Mar 1;41(3):116.

Wu W, Wu Z, Yu T, Jiang C, Kim WS. Recent progress on magnetic iron oxide nanoparticles: synthesis, surface functional strategies and biomedical applications. Science and technology of advanced materials. 2015 Apr 28.

Hsiao KL. Micropolar nanofluid flow with MHD and viscous dissipation effects towards a stretching sheet with multimedia feature. International Journal of Heat and Mass Transfer. 2017 Sep 1;112:983-90.

Sheikholeslami M, Rokni HB. Melting heat transfer influence on nanofluid flow inside a cavity in existence of magnetic field. International Journal of Heat and Mass Transfer. 2017 Nov 1;114:517-26.

Waqas H, Shehzad SA, Khan SU, Imran M. Novel numerical computations on flow of nanoparticles in porous rotating disk with multiple slip effects and microorganisms. Journal of Nanofluids. 2019 Jul 1;8(7):1423-32.

Khan SU, Rauf A, Shehzad SA, Abbas Z, Javed T. Study of bioconvection flow in Oldroyd-B nanofluid with motile organisms and effective Prandtl approach. Physica A: Statistical Mechanics and its Applications. 2019 Aug 1;527:121179.

Tlili I, Waqas H, Almaneea A, Khan SU, Imran M. Activation energy and second order slip in bioconvection of Oldroyd-B nanofluid over a stretching cylinder: A proposed mathematical model. Processes. 2019 Dec;7(12):914.

Waqas H, Khan SU, Imran M, Bhatti MM. Thermally developed Falkner–Skan bioconvection flow of a magnetized nanofluid in the presence of a motile gyrotactic microorganism: Buongiorno's nanofluid model. Physica Scripta. 2019 Aug 27;94(11):115304.

Waqas H, Khan SU, Hassan M, Bhatti MM, Imran M. Analysis on the bioconvection flow of modified second-grade nanofluid containing gyrotactic microorganisms and nanoparticles. Journal of Molecular Liquids. 2019 Oct 1;291:111231.

Wang Y, Waqas H, Tahir M, Imran M, Jung CY. Effective Prandtl aspects on bio-convective thermally developed magnetized tangent hyperbolic nanoliquid with gyrotactic microorganisms and second order velocity slip. IEEE Access. 2019 Sep 11;7:130008-23.

Khan SU, Waqas H, Bhatti MM, Imran M. Bioconvection in the rheology of magnetized couple stress nanofluid featuring activation energy and Wu's slip. Journal of Non-Equilibrium Thermodynamics. 2020 Jan 28;45(1):81-95.

Khan M, Irfan M, Khan WA, Sajid M. Consequence of convective conditions for flow of Oldroyd-B nanofluid by a stretching cylinder. Journal of the Brazilian Society of Mechanical Sciences and Engineering. 2019 Mar 1;41(3):116.

Waqas H, Khan SU, Shehzad SA, Imran M. Radiative flow of Maxwell nanofluid containing gyrotactic microorganism and energy activation with convective Nield conditions. Heat Transfer—Asian Research. 2019 Jul;48(5):1663-87.

Khan MN, Nadeem S. Theoretical treatment of bio-convective Maxwell nanofluid over an exponentially stretching sheet. Canadian Journal of Physics. 2020;98(8):732-41.

Khan MI, Waqas M, Hayat T, Khan MI, Alsaedi A. Behavior of stratification phenomenon in flow of Maxwell nanomaterial with motile gyrotactic microorganisms in the presence of magnetic field. International Journal of Mechanical Sciences. 2017 Oct 1;131:426-34.

Waqas H, Khan SU, Tlili I, Awais M, Shadloo MS. Significance of bioconvective and thermally dissipation flow of viscoelastic nanoparticles with activation energy features: novel biofuels significance. Symmetry. 2020 Feb;12(2):214.

Waqas M, Dogonchi AS, Shehzad SA, Khan MI, Hayat T, Alsaedi A. Nonlinear convection and joule heating impacts in magneto-thixotropic nanofluid stratified flow by convectively heated variable thicked surface. Journal of Molecular Liquids. 2020 Feb 15;300:111945.

Nomenclature

Symbols	Definition
u, v	Components of velocity
M	Magnetic parameter
B_0	Magnetic field strength
U_0	Reference velocity
U_w	Stretching velocity
$(\rho c)_p$	Nanoparticle specific heat
$(\rho c)_f$	Fluid specific heat
R_1, R_2	Material constants
$Q(x)$	Non-uniform heat generation/absorption coefficient
Pr	Prandtl number
Ec	Eckert number
Nc	Bioconvection Rayleigh number
Nr	Buoyancy ratio parameter
Nb	Brownian motion parameter
Rd	Thermal radiation parameter
Nt	Thermophoresis parameter
E_1	Activation energy
Le	Lewis number
Pe	Peclet number
K_1, K_2	Material parameters of thixotropic liquid
Lb	Bioconvection Lewis number
S_1	Thermal stratified variable
S_2	Solutal stratified variable
S_3	Microorganism stratified variable
Re	Reynolds number
Nu	Local Nusselt number
Sh	Local Sherwood number
N_∞	Ambient fluid microorganisms
T_∞	Ambient fluid temperature
C_∞	Ambient fluid concentration
D_B	Coefficient of Brownian diffusion
D_m	Coefficient of microorganism's diffusion
D_T	Coefficient of thermophoresis diffusion
T_f	Hot fluid temperature
B	Chemotaxis constant
n_1	Fitted rate constant
n	Velocity power index
W_c	Cell swimming speed
C_f	Hot fluid concentration
N_f	Hot fluid rescaled density of microorganisms
f	Dimensionless velocity
k^*	Mean absorption coefficient
N	Microorganism field
E_a	Activation coefficient

Symbols	Definition
α_1	Thermal stratification Biot number
α_2	Solutal stratification Biot number
α_3	Microorganism stratification Biot number
α	Velocity slip parameter
σ	Electrical conductivity
σ^*	Chemical reaction parameter
σ^{**}	Stefan-Boltzmann constant
α^*	Thermal diffusivity
λ	Mixed convection parameter
δ_0	Temperature difference parameter
δ_1	Microorganism concentration difference parameter
δ	Heat generation parameter
τ	Heat capacity ratio
q_w	Thermal flux
q_m	Solutal flux
ϕ	Volumetric concentration
θ	Temperature distribution
χ	Microorganism concentration
g^*	Gravity
ρ_f	Density of fluid
ρ_m	Density of microorganisms
ρ_p	Density of nanoparticles
τ	Thermal diffusion coefficient
ν	Kinematic viscosity

Md Faisal Md Basir, S.A. Shehzad, A. Rauf

On the features of Stefan blowing magnetized flow of bioconvected nanofluid through slip conditions

On magnetized flow of bioconvected nanofluid

Abstract: The examinations of convection heat transportation in nanofluid flows have achieved the spatial attention of investigators from all over the globe due to their unique chemical and physical characteristics. This study has the main focus on Stefan blowing aspects in magnetized bio-convected nanofluid flow induced by the movement of the slippery moving sheet. The modeled expressions of the physical phenomenon are turned into dimensionless forms by the use of Lie group methodology. The Runge-Kutta-Fehlberg fourth and fifth-order numerical scheme is utilized to express the solutions of dimensionless expressions. The aspects of controlling constraints (chemical reaction, magnetic field, velocity slip, heat absorption and generation, thermal slip, zero mass diffusion, and Stefan blowing) on the transformed temperature, the local Nusselt number, velocity, the skin friction coefficient, concentration (nanoparticle volume-fraction), the local Sherwood number, motile microorganisms density, and the motile microorganisms density number are reported graphically. A good match is visualized between the present and already reported numerical data.

Keywords: Nanofluid; Lie group analysis; Bioconvection; Heat transport; Stefan blowing; Slip conditions.

1 Introduction

Fluid flow investigations via stretching surfaces are of immense interest among scientists due to its emerging industrial applications in chemical processes and engineering fields (1-5). Mainly fluid flow caused due to stretching surfaces has

Md Faisal Md Basir, Department of Mathematical Sciences, Faculty of Science, Universiti Teknologi Malaysia, 81310 UTM Johor Bahru, Johor, Malaysia, mfaisalmbasir@utm.my
S.A. Shehzad, Department of Mathematics, COMSATS University Islamabad, Sahiwal 57000, Pakistan.
A. Rauf, Department of Mathematics, COMSATS University Islamabad, Sahiwal 57000, Pakistan.

https://doi.org/10.1515/9783110696080-005

significance in the extrusion of polymers, plastic industry, paper production, chemical plants, power stations, petroleum industry, and cooling systems. In the above industrial applications, the main focus was to enhance heat transportation and energy generation. Several techniques have been implemented to enhance thermophysical characteristics but failed due to less energy generation. To get rid of such types of challenges, scientists developed a stable solution of heat generation by dispersing nanometre size particles uniformly in the base fluid, known as nanofluids (6), and have exceptional higher thermal characteristics. Nanofluids have useful features in microelectronics, power generation, hybrid engines, cooling towers, nuclear reactors, and chemical sectors. Furthermore, magnetized nanofluids find significance in drug delivery, cancer treatment, gastric medications, safer surgery, and tumor removal. Sheikholeslami et al. (7) discussed shape factor and Brownian movement impacts of alumina nanofluid in the permeable enclosure by CVFEM technique. Sheikholeslami (8) elucidated the impact of Darcy law in natural convective nanofluid flow under Lorentz forces impacts through the porous cavity. Hayat et al. (9) prescribed consequences of the homogeneous-heterogeneous phenomenon in magnetite-nanofluid flow through stretching surface of a non-linear kind. Gireesha et al. (10) computed solutions via the RKF method of the radiative, hybrid nanofluid model by adopting permeable moving longitudinal fin configuration. Khan et al. (11) developed solutions of the time-dependent viscoelastic micropolar flow of nanofluid subjected to the oscillatory stretching surface under heat/mass fluxes.

The expression “bioconvection” defines liquids microscopic convection that is created by density gradient. Bioconvection phenomenon arises due to the independent swimming of microorganisms using organism energy. The independent movement of motile organisms along fixed direction causes augmentation in base-liquid density. The attributes of the directional movement of various microorganisms’ species can recognize the process behind bioconvection systems. Various industrial appliances are manufactured due to microorganisms’ particles, such as ethanol, fertilizers, biofuel, bio-microsystems, and water plants. Furthermore, biodiesel and hydrogen gas, promising energy sources are processed by microorganisms. Raju et al. (12) numerically investigated the flow phenomenon of radiative, Casson fluid via moving wedge under the gyro-tactic microorganisms factor. They concluded that motile microorganisms can be used in the enhancement of the mass-heat transportation rate. Waqas et al. (13) studied magnetized nanomaterial flow of Oldroyd-B fluid through vertical surface under gyrotactic microorganisms and buoyancy forces impacts. They found that the parameter of motile density stratification declines the microorganism density field. Zaman and Gul (14) considered the bioconvective flow of Williamson nanofluid owing to vertical sheet accommodating gyrotactic microorganisms under Newtonian conditions. Khan et al. (15) analyzed activation energy influence in convective, magnetized flow thixotropic nanofluid subjected to vertical sheet in the presence of gyrotactic microorganisms using HAM. Naz et al. (16) discussed entropy generation in flow of Walters’ B fluid by adopting

horizontal cylinder configuration along with swimming microorganism. They scrutinized that heat flux may be increased by enhancement in the cell swimming motion of microorganisms.

In industrial processes, there arise situations (plastic sheet extrusion, glass blowing, and paper manufacturing), where combined heat-mass transportation processes take place between fluid flow and stretching surfaces. In addition, there exist circumstances, where massive mass diffusion from stretching surface to ambient can occur by evaporation like paper dying mechanism. Due to temperature dependency and moisture content of the wet paper surface, the species transfer can initiate a "blowing effect". Such blowing impact defined the idea of Stefan's theory (17, 18) for mass/species transfer. The species diffusion generates a fluid bulk motion and introduces additional fluid motion. Here it is important to explain that blowing occurs due to flux transfer of species from impermeable surfaces to ambient. As species transportation significantly depends upon fluid field and field of flow is affected by mass blowing, all these cause coupling between concentration and momentum fields. Fang and Jing (18) investigated the blowing impacts of mass transportation under flux conditions in viscous fluid flow subjected to the stretching plate. They found that coupled blowing impacts owing to mass transfer have significant outcomes on heat flux, flow field, and drag. Latiff et al. (19) discussed the influence of Stefan blowing in time-dependent viscous nanofluid flow subjected to stretchable rotating disk and revealed that local skin friction is enhanced by Stefan blowing. The impacts of Stefan blowing with partial slips under different flow configurations can be negotiated in Refs. (20-22).

2 Mathematical formulation

The boundary-driven magnetized flow of viscous nanomaterial flow generated by the movement of the sheet is assumed. A system of Cartesian-coordinates $(\bar{y}, \bar{x})$ is tackled where $\bar{y} -$ axis is adopted normal to surface and $\bar{x} -$ axis settled along with the sheet. We adopted the steady-state nanofluid flow having gyrotactic microorganisms. The suspension of nanoparticles is considered to be stable and microorganisms' swimming direction is free of nanoparticles. The motile microorganisms density N_w and temperature T_w are supposed at the wall of the boundary while C_∞, T_∞ and N_∞ are considered the ambient values. The nanofluid is considered to be diluted such that the instability of bioconvection by the augmentation of suspension's viscosity may be avoided. Here, the base-fluid is water to satisfy the physical conditions for the micro-organisms survival (Xu, 2015). The following field expressions demonstrated mass conservation, momentum conservation, energy conservation, nanoparticles conservation, and microorganisms conservation. The sheet is assumed by the multiple conditions of slip. The magnetic force of strength B_0^2 is

utilized in the positive direction of $\bar{x}-$ axis. Figure 1 represents the schematic flow chart of the problem (i) boundary-layer of momentum (ii) boundary-layer of thermal (iii) boundary-layer of nanoparticles volume-friction and (iv) boundary-layer of microorganisms. Hence, the model expressions are stated as:

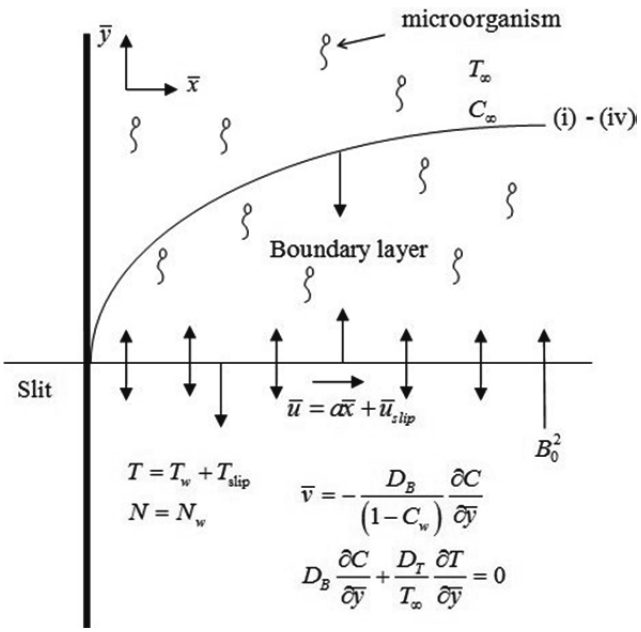

Fig. 1: Schematic flow chart of the model

Continuity expression

$$\frac{\partial \bar{v}}{\partial \bar{y}} + \frac{\partial \bar{u}}{\partial \bar{x}} = 0. \tag{1}$$

Momentum expression

$$\bar{v}\frac{\partial \bar{u}}{\partial \bar{y}} + \bar{u}\frac{\partial \bar{u}}{\partial \bar{x}} = -\frac{\sigma B_0^2}{\rho}\bar{u} + \upsilon\frac{\partial^2 \bar{u}}{\partial \bar{y}^2}. \tag{2}$$

Energy expression

$$\bar{v}\frac{\partial T}{\partial \bar{y}} + \bar{u}\frac{\partial T}{\partial \bar{x}} = \frac{Q_0}{\rho C_p}(T - T_\infty) + \alpha\frac{\partial^2 T}{\partial \bar{y}^2} + \tau\left(\frac{\partial T}{\partial \bar{y}}\right)^2\left(\frac{D_T}{T_\infty}\right) + \tau D_B\frac{\partial C}{\partial \bar{y}}\frac{\partial T}{\partial \bar{y}}. \tag{3}$$

Concentration expression

$$\bar{v}\frac{\partial C}{\partial \bar{y}} + \bar{u}\frac{\partial C}{\partial \bar{x}} = \left(\frac{D_T}{T_\infty}\right)\frac{\partial^2 T}{\partial \bar{y}^2} + D_B\frac{\partial^2 C}{\partial \bar{y}^2} - k_1(C - C_\infty). \tag{4}$$

Microorganisms expression

$$\bar{v}\frac{\partial C}{\partial \bar{y}} + \bar{u}\frac{\partial C}{\partial \bar{x}} = \left(\frac{D_T}{T_\infty}\right)\frac{\partial^2 T}{\partial \bar{y}^2} + D_B\frac{\partial^2 C}{\partial \bar{y}^2} - k_1(C - C_\infty). \tag{5}$$

The conditions at the boundary are (23):

$$\begin{gathered}\bar{v} = -\frac{D_B}{(1-C_w)}\frac{\partial C}{\partial \bar{y}}, \bar{u} = a\bar{x} + \bar{u}_{\text{slip}}, T = T_w + T_{\text{slip}},\\ \frac{\partial T}{\partial \bar{y}}\frac{D_T}{T_\infty} + D_B\frac{\partial C}{\partial \bar{y}} = 0, N = N_w \text{ at } \bar{y} = 0,\\ \bar{u} = 0, C \to C_\infty, T \to T_\infty, N \to 0 \text{ as } \bar{y} \to \infty\end{gathered} \tag{6}$$

in which $(\bar{v}, \bar{u})$ demonstrate the velocity components along $\bar{y} -$ and $\bar{x} -$ axes, υ the kinematic viscosity, σ the electric conductivity, ρ the liquid density, α the thermal diffusivity, c_p the specific heat capacitance, D_B the factor of Brownian diffusion, Q_0 the factor of variable heat absorption or generation, k_1 the rate of variable reaction, $\tau = \frac{(\rho c)_p}{(\rho c)_f}$ the heat capacities ratio, D_T the factor of thermophoresis movement, W_c the maximum speed of cell swimming, $\tilde{b}$ the chemotaxis constant, D_n the microorganism diffusivity, $\bar{u}_{\text{slip}} = N_1\frac{\partial \bar{u}}{\partial \bar{y}}$ the momentum slip constraint and $T_{\text{slip}} = D_1\frac{\partial T}{\partial \bar{y}}$ the temperature slip constraint.

3 Nondimensionalization of Model Expressions

The non-dimensional variables are implemented to elaborate the formulating expressions into dimensionless forms (24):

$$v = \frac{\bar{v}}{\sqrt{\upsilon a}}, y = \frac{\bar{y}}{\sqrt{\frac{\upsilon}{a}}}, u = \frac{\bar{u}}{\sqrt{\upsilon a}}, x = \frac{\bar{x}}{\sqrt{\frac{\upsilon}{a}}}, \ \phi = \frac{C - C_\infty}{C_\infty}, \theta = \frac{T - T_\infty}{T_w - T_\infty}, \chi = \frac{N}{N_w}, \tag{7}$$

Here, a is the positive constant. The stream function can be described as

$$v = -\frac{\partial \psi}{\partial x} \text{ and } u = \frac{\partial \psi}{\partial y}. \tag{8}$$

The number of expressions and number of independent variables is reduced with the help of stream function. The dimensionless momentum, temperature, nanoparticle volume fraction and microorganisms expressions have the below-mentioned forms:

$$\frac{\partial^2\psi}{\partial x\partial y}\frac{\partial\psi}{\partial y}-\frac{\partial^2\psi}{\partial y^2}\frac{\partial\psi}{\partial x}=-M\frac{\partial\psi}{\partial y}+\frac{\partial^3\psi}{\partial y^3}, \tag{9}$$

$$\frac{\partial\theta}{\partial x}\frac{\partial\psi}{\partial y}-\frac{\partial\theta}{\partial y}\frac{\partial\psi}{\partial x}=\frac{Q_0}{a\rho c_p}\theta+\frac{1}{Pr}\frac{\partial^2\theta}{\partial y^2}+\frac{Nb}{Pr}\frac{\partial\theta}{\partial y}\frac{\partial\phi}{\partial x}+\frac{Nt}{Pr}\left(\frac{\partial\theta}{\partial y}\right)^2 \tag{10}$$

$$\frac{\partial\phi}{\partial x}\frac{\partial\psi}{\partial y}-\frac{\partial\phi}{\partial y}\frac{\partial\psi}{\partial x}=\frac{1}{Pr\,Le}\frac{\partial^2\phi}{\partial y^2}+\frac{Nt}{Nb}\frac{1}{Pr\,Le}\frac{\partial^2\theta}{\partial y^2}-K_r\phi, \tag{11}$$

$$\frac{\partial\chi}{\partial x}\frac{\partial\psi}{\partial y}-\frac{\partial\chi}{\partial y}\frac{\partial\psi}{\partial x}+\frac{Pe}{Pr\,Lb}\left[\frac{\partial\chi}{\partial y}\frac{\partial\phi}{\partial y}+\chi\frac{\partial^2\phi}{\partial y^2}\right]=\frac{1}{Pr\,Lb}\frac{\partial^2\chi}{\partial y^2}, \tag{12}$$

and the boundary conditions have the following non-dimensional forms:

$$\left.\begin{aligned}\frac{\partial\psi}{\partial x}=\ \frac{C_\infty}{Pr\,Le(1-C_w)}\frac{\partial\phi}{\partial y},\frac{\partial\psi}{\partial y}=N_1\frac{1}{\left(\sqrt{\frac{v}{a}}\right)}\frac{\partial^2\psi}{\partial y^2}+\ x,\theta=D_1\frac{1}{\left(\sqrt{\frac{v}{a}}\right)}\frac{\partial\theta}{\partial y}+1\ ,\\ \mathrm{N}t\frac{\partial\theta}{\partial y}+Nb\frac{\partial\phi}{\partial y}=0,\chi=1\ \text{at}\ y=0,\\ \frac{\partial\psi}{\partial y}\to 0,\ \theta\to 0,\phi\to 0,\ \chi\to 0\ \text{as y}\to\infty\end{aligned}\right\} \tag{13}$$

Here, $M=\frac{B_0^2\sigma}{a\rho}$ the magnetic field constraint, $Nb=\frac{\tau D_B C_\infty}{\alpha}$ the Brownian movement constraint, $Pr=\frac{v}{\alpha}$ the Prandtl number, $Nt=\frac{\tau\Delta T D_T}{\alpha T_\infty}$ the constraint of sis,$Le=\frac{\alpha}{D_B}$ the Lewis number, $Lb=\frac{\alpha}{D_n}$ the bioconvected Lewis number, $K_r=\frac{k_1}{a}$ the chemical reaction constraint and $Pe=\frac{\tilde{b}W_c}{D_n}$ the Péclet number.

4 Applications of Scaling Group of Transformations

A transformation of scaling group is a special case of Lie group theory. The similarity solutions of expressions (9)-(13) are equal to computing the invariant solutions of these expressions. To compute the invariant solutions, one parametric scaling group of transformation is adopted as follows (25):

$$\Gamma: y^*=ye^{\varepsilon\alpha_2},x^*=xe^{\varepsilon\alpha_1},\psi^*=\psi e^{\varepsilon\alpha_3},\phi^*=\phi e^{\varepsilon\alpha_5},\theta^*=\theta e^{\varepsilon\alpha_4},\chi^*=\chi e^{\varepsilon\alpha_6}. \tag{14}$$

Here, ε notifies a parameter and $\alpha_i(i=1,2,\ldots,6)$ are the all arbitrary constant and all are not zero. The expressions (9)-(12) and conditions (13) in $(*)$ forms are:

$$\frac{\partial^2\psi^*}{\partial y^*\partial x^*}\frac{\partial\psi^*}{\partial y^*}-\frac{\partial^2\psi^*}{\partial y^{*2}}\frac{\partial\psi^*}{\partial x^*}=-M\frac{\partial\psi^*}{\partial y^*}+\frac{\partial^3\psi^*}{\partial y^{*3}}, \tag{15}$$

$$\frac{\partial \theta^*}{\partial x^*}\frac{\partial \psi^*}{\partial y^*} - \frac{\partial \theta^*}{\partial y^*}\frac{\partial \psi^*}{\partial x^*} = \frac{Q_0}{c_p a \rho}\theta^* + \frac{1}{Pr}\frac{\partial^2 \theta^*}{\partial y^{*2}} + \frac{Nb}{Pr}\frac{\partial \theta^*}{\partial y^*}\frac{\partial \phi^*}{\partial x^*} + \frac{Nt}{Pr}\left(\frac{\partial \theta^*}{\partial y^*}\right)^2 \tag{16}$$

$$\frac{\partial \phi^*}{\partial x^*}\frac{\partial \psi^*}{\partial y^*} - \frac{\partial \phi^*}{\partial y^*}\frac{\partial \psi^*}{\partial x^*} = \frac{1}{Pr\,Le}\frac{\partial^2 \phi^*}{\partial y^{*2}} - \frac{k_1}{a}\phi + \frac{1}{Pr\,Le}\frac{Nt}{Nb}\frac{\partial^2 \theta^*}{\partial y^{*2}}, \tag{17}$$

$$\frac{\partial \chi^*}{\partial x^*}\frac{\partial \psi^*}{\partial y^*} - \frac{\partial \chi^*}{\partial y^*}\frac{\partial \psi^*}{\partial x^*} + \frac{Pe}{Pr\,Lb}\left[\frac{\partial \chi^*}{\partial y^*}\frac{\partial \phi^*}{\partial y^*} + \chi^*\frac{\partial^2 \phi^*}{\partial y^{*2}}\right] = \frac{1}{Pr\,Lb}\frac{\partial^2 \chi^*}{\partial y^{*2}}, \tag{18}$$

with conditions:

$$\left.\begin{aligned} \frac{\partial \psi^*}{\partial x^*} = \frac{C_\infty}{Pr\,Le(1-C_w)}\frac{\partial \phi^*}{\partial y^*}, \frac{\partial \psi^*}{\partial y^*} = N_1\frac{1}{\left(\sqrt{\frac{v}{a}}\right)}\frac{\partial^2 \psi^*}{\partial y^{*2}} + x^*, \theta^* = D_1\frac{1}{\left(\sqrt{\frac{v}{a}}\right)}\frac{\partial \theta^*}{\partial y^*} + 1, \\ \mathrm{N}t\frac{\partial \theta^*}{\partial y^*} + Nb\frac{\partial \phi^*}{\partial y^*} = 0, \chi^* = 1 \text{ at } y = 0, \\ \frac{\partial \psi^*}{\partial y^*} \to 0,\ \theta^* \to 0, \phi^* \to 0,\ \chi^* \to 0 \text{ as y} \to \infty \end{aligned}\right\} \tag{19}$$

By the implementation of Equation (14) on Equations (15)-(19), the below relationship amongst the exponents is visualized in invariants if α_i's are following:

$$\alpha_1 = \alpha_3, \alpha_2 = \alpha_4 = \alpha_5 = \alpha_6 = 0. \tag{20}$$

Using Equation (20), transformations in Equation (14) become:

$$\Gamma: y^* = y, x^* = xe^{\varepsilon\alpha_1}, \psi^* = \psi e^{\varepsilon\alpha_1},\ \phi^* = \phi, \theta^* = \theta, \chi^* = \chi. \tag{21}$$

The expansion through Taylor's series in the power of ε, by the negligence of higher powers of ε yields:

$$\left.\begin{aligned} y^* = y(1+0), x^* = x(1+\varepsilon\alpha_1), \theta^* = \theta(1+0), \psi^* = \psi(1+\varepsilon\alpha_1), \\ \chi^* = \chi(1+0), \phi^* = \phi(1+0). \end{aligned}\right\} \tag{22}$$

The differential form of the equation in (22) is

$$\frac{d\psi}{\psi} = \frac{dx}{x}, \tag{23}$$

The following transformations are achieved through (23) by solving one by one:

$$\psi = xf(\eta)\eta = y, \phi = \phi(\eta), \theta = \theta(\eta), \chi = \chi(\eta), \tag{24}$$

here η the independent variable, $f(\eta), \phi(\eta), \theta(\eta)$, and$\chi = \chi(\eta)$ represent the dimensionless velocity, nanoparticles volume-friction, temperature and microorganisms

functions, respectively. With the inclusion of (24) into (15)-(19), the similarity transformed expressions are obtained in terms of ODEs as follows:

$$f''' - f'^2 + ff'' - Mf' = 0, \tag{25}$$

$$\theta'' + Nb\theta'\phi' + Pr\, f\, \theta' + Q\, Pr\, \theta + Nt\theta'^2 = 0, \tag{26}$$

$$\phi'' + \frac{Nt}{Nb}\theta'' + Le\, Pr\, f\, \phi' - x\, Kr\, Pr\, \phi = 0, \tag{27}$$

$$\chi'' - Pe(\phi'\chi' + \chi\phi'') + Lb\, Pr\, f\, \chi' = 0, \tag{28}$$

$$\left.\begin{array}{c} f'(0) = \varepsilon_a f'' + 1, f(0) = \frac{1}{LePr_b} \\ Nt\theta' + Nb\phi' = 0, \quad \chi(0) = 1, \text{at } \eta{=}0, \\ f' \to 0, \theta \to 0, \phi \to 0, \chi \to 0 \quad \text{as} \quad \eta \to \infty. \end{array}\right\} \tag{29}$$

Here, prime specifies the derivative with respect to η, $Q = \frac{Q_0}{a\rho c_p}$ the heat absorption or generation constraint, $\varepsilon_a = N_1 \frac{1}{\sqrt{\frac{v}{a}}}$ the momentum slip constraint, $s = \frac{C_\infty}{1-C_w}$ the Stefan blowing constraint and $\varepsilon_b = D_1 \frac{1}{\sqrt{\frac{v}{a}}}$ is the thermal slip constraint.

5 Physical Quantities

The practically interesting quantities here are the skin friction $C_{f_{\bar{x}}}$, Sherwood number $Sh_{\bar{x}}$, Nusselt number $Nu_{\bar{x}}$ and motile microorganisms density number $Nn_{\bar{x}}$ are defined as:

$$\left.\begin{array}{c} C_{f_{\bar{x}}} = \frac{\tau_w}{\bar{u}_w^2\rho}, Sh_{\bar{x}} = \frac{-q_m\bar{x}}{(C_w - C_\infty)D_B}, \\ Nu_{\bar{x}} = \frac{-q_w\bar{x}}{(T_w - T_\infty)k}, Nn_{\bar{x}} = \frac{-q_n\bar{x}}{N_w D_n}. \end{array}\right\}, \tag{30}$$

here τ_w, q_m, q_w and q_n denote the skin friction, surface mass diffusion, surface heat diffusion, and motile microorganism diffusion at the surface and described as:

$$\tau_w = \mu\left(\frac{\partial\bar{u}}{\partial\bar{y}}\right)_{\bar{y}=0}, q_m = -D_B\left(\frac{\partial C}{\partial\bar{y}}\right)_{\bar{y}=0}, q_w = -k\left(\frac{\partial T}{\partial\bar{y}}\right)_{\bar{y}=0}, \; q_n = -D_n\left(\frac{\partial N}{\partial\bar{y}}\right)_{\bar{y}=0}. \tag{31}$$

Substitute Equations (7), (24) and (31) into (30), obtained

$$f''(0) = Re_{\tilde{x}}^{1/2} C_f\,, \quad -\theta'(0) = Re_{\tilde{x}}^{-1/2} N u_{\tilde{x}},$$
$$-\frac{\phi'(0)}{\phi(0)} = Re_{\tilde{x}}^{-1/2} Sh\,, -\chi'(0) = Re_{\tilde{x}}^{-1/2} N n_{\tilde{x}} \tag{32}$$

$Re_{\tilde{x}}$ is the dimensional local Reynolds number.

6 Numerical Solution and Validation

The nonlinear system of partial differential model is converted into the model of ordinary differential expressions. The transformed system of expressions is tackled by the RKF45 order numerical technique by Maple 2015. To verify the correctness of the solution, the values of f"(0) are compared with (26-28) used the combination of variational iteration method (VIM) and the Padé approximation and Hayat et al., (28) employed the modified Adomian decomposition (MAD) method and the Padé approximation to solve the ODEs. The comparison is shown in Table 1.

Tab. 1: Comparison values of local skin friction factor $f''(0)$ for distinct M when $Pr = 6.8, \varepsilon_a = s = 0, Le = 1$.

M	Hayat *et al.*, (28) (MAD and the Padé approximation)	Xu & Lee (26,27) (VIM and the Padé approximation)	The present study (RK45)
0	-1.00000	-	-1.00000
1	-1.41421	-1.41421	-1.41421
5	-2.44948	-2.44948	-2.44949
10	-3.31662	-3.31662	-3.31662
50	-7.14142	-7.14142	-7.14143

7 Results and Discussion

The numerical results are denoted in the form of dimensionless velocity, temperature, nanoparticle volume fraction, and density of motile microorganism. The parameters that are focused on in this chapter are Stefan blowing, velocity slip, thermal slip, heat absorption/generation parameter, magnetic field parameter, and chemical reaction parameter on the dimensionless velocity, temperature, nanoparticle volume fraction, and density of motile microorganism profiles. The value of $Pr = 6.8, Nb = Nt = 0.1,\ Le = Pe = Lb = 1$ are fixed for every case in this problem.

Fig. 2(a-d) is developed to execute the behavior of momentum slip constraint ε_a and Stefan blowing constraint s on velocity $f'(\eta)$, temperature $\theta(\eta)$, nano-particles

volume fraction $\phi(\eta)$ and microorganisms density profile $\chi(\eta)$ by setting $\varepsilon_b = 0.1, Q = 0.1, M = 0.1$ and $K_r = 1$. Fig. 2a demonstrates that the larger ε_a and s values lead to the weaker velocity. The green lines represent the profile for $\varepsilon_a = 0$ and red lines are for the case when $\varepsilon_a = 1.5$. We revealed that the velocity is lower in presence of momentum slip constraint and higher in absence of slip constraint. The increment in Stefan constraint implies more fluid is injected or leaving the system that returns in the reduction of fluid velocity. From Fig. 2b, we found that the liquid temperature is retards by the increasing trend of momentum slip and Stefan blowing constraints. The lowest curve of temperature is achieved at $\varepsilon_a = 0$ and $s = -1$. This is due to the injected factor that reduces the temperature of the fluid. The curves of nanoparticles volume-fraction for distinct ε_a and s values are examined in Fig. 2c. Here, the curves of $\phi(\eta)$ demonstrate the fluctuation in the range $\eta(0,3)$ and is maximum at $\eta = 0.9$. The density of motile organisms profile $\chi(\eta)$ is weaker for the incrementing values of ε_a and s. The profile of $\chi(\eta)$ is higher in the presence of momentum slip constraint (see Fig. 2d). Fig. 3(a-c) reflects the behavior of temperature $\theta(\eta)$, nano-particles volume fraction $\phi(\eta)$ and microorganisms density profile $\chi(\eta)$ for the distinct thermal slip constraint ε_b and Stefan blowing constraint s when $\varepsilon_a = 0.1, Q = 0.1, M = 0.1\, and\, K_r = 1$. This Fig. describes that the temperature $\theta(\eta)$ and density of motile organisms profile $\chi(\eta)$ is decay for the higher ε_b and s values (see Fig. 3a and 3c). The involvement of thermal slip constraint is caused to the reduction in the profiles of $\theta(\eta)$ and $\chi(\eta)$. on contrary, the nanoparticle's volume-fraction is boosted in absence of thermal slip constraint (see Fig. 3b).

Features of Stefan blowing constraint s and magnetic constraint M on velocity $f'(\eta)$, temperature $\theta(\eta)$, nano-particles volume fraction $\phi(\eta)$ and microorganisms density profile $\chi(\eta)$ by fixing the values of $\varepsilon_a = 0.1, Q = 0.1, \varepsilon_b = 0.1\, and\, K_r = 1$ are disclosed in Fig. 4(a-d). We discussed both hydrodynamic and magnetohydrodynamic flow situations (here, $M = 0$ leads to hydrodynamic flow problem, and $M > 0$ is for the magnetohydrodynamic flow situation). The reducing trend in the velocity distribution is found for incrementing Stefan blowing and magnetic constraint (see Fig. 4a). The strong Lorentz force occurred due to a larger magnetic constraint that provides the resistance in fluid flowing due to which lower velocity distribution is achieved. On contrary, the temperature is boosted with the incrementing trend of magnetic constraint (see Fig. 4b). The resistance of the Lorentz force adds more heat in the fluid that returns in a higher temperature field. Fig. 4c addresses that the profile of $\phi(\eta)$ is improved by the increasing Stefan blowing constraint. From Fig. 4d, we noted that the profile of $\phi(\eta)$ is decreased with larger Stefan blowing constraint while improved for higher magnetic constraint. Fig. 5 discusses the chemical reaction constraint K_r and Stefan blowing constraint s on motile nanoparticles volume-fraction distribution $\phi(\eta)$ by putting $\varepsilon_a = 0.1, Q = 0.1, \varepsilon_b = 0.1$ and $M = 0.1$. The distribution curves of $\phi(\eta)$ are decaying for the enhancing chemical reaction constraints. By improving chemical reactive constraint corresponds to a larger reaction rate that leads to a reduction in $\phi(\eta)$ profile. The curves of $\phi(\eta)$ are higher in ab-

sence of a chemical reaction. The incrementing nature of Stefan blowing constraint s leads to a higher profile of $\phi(\eta)$.

Table 2 demonstrates the numerical data of $f"(0)$ for $s = -1$, $s = 1$ and distinct ε_a when $Q = Nb = \varepsilon_b = Nt = 0.1, Pr = 6.8, Le = K_r = Lb = Pe = 1$. The numeric values of $f"(0)$ are decreased by using higher ε_a values at $M = 1$ and $S = -1$. The increment in magnetic constraint leads to higher values of $f"(0)$. Further, $f"(0)$ values are larger in the case of positive Stefan blowing constraint as comparative negative Stefan blowing constraint. The values of $-\theta'(0)$ for distinct $\varepsilon_a, Q\ and\ s$ by taking $Nb = Nt = \varepsilon_b = M = 0.1, Pr = 6.8, Le = K_r = Lb = Pe = 1$ are computed in Table 3. The increasing trend of momentum slip constraint leads to decay in the values of $-\theta'(0)$. Further, the heat absorption case has higher values of $-\theta'(0)$ comparative to the values achieved in the case of the heat generation problem. The values of $-\theta'(0)$ are larger in positive Stefan blowing constraint values as compared to negative values of this constraint. Table 4 discloses the $-\phi'(0)/\phi(0)$ values by changing ε_a, K_r and s values when $Q = Nb = \varepsilon_b = M = Nt = 0.1, Pr = 6.8, Le = Lb = Pe = 1$. The higher $-\phi'(0)/\phi(0)$ values are achieved for higher chemical reaction constraint K_r values. Table 5 is provided to analyze the values of $-\chi'(0)$ for various ε_a, Pe and s values by fixing $Nb = \varepsilon_b = Nt = Q = M = 0.1, Pr = 6.8, K_r = Le = Lb = 1$. The increasing trend of Peclet number values leads to decay in the values of $-\chi'(0)$ for both $s = -1$ and $s = 1$ cases whereas these values are larger for positive values of s in comparison to negative values of s.

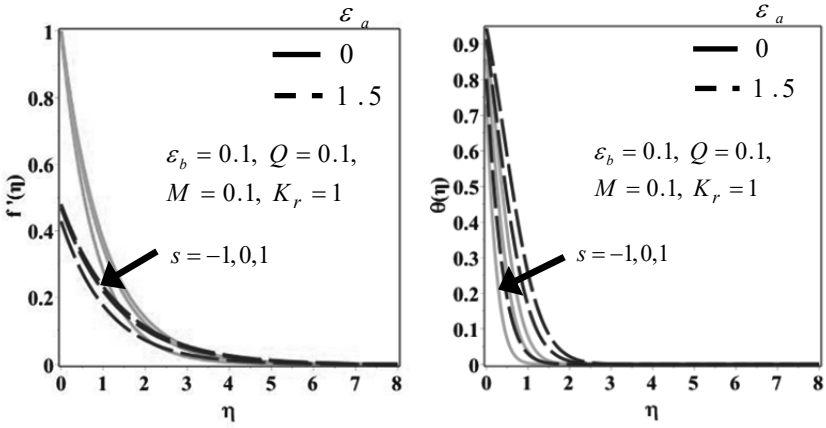

(a) Velocity **(b) Temperature**

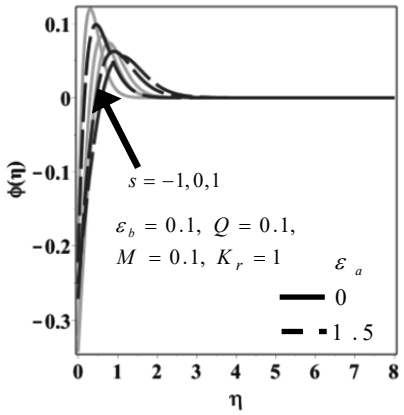

(b) Nanoparticle volume fraction

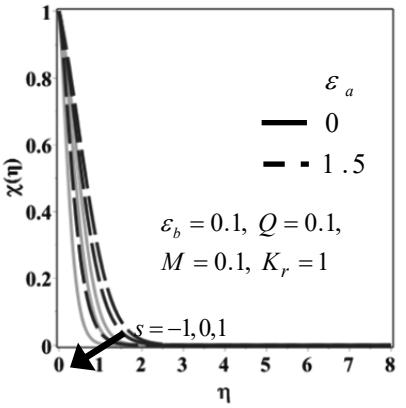

(d) Density of motile microorganism

Fig. 2: Effect of the Stefan blowing parameter and velocity slip parameter.

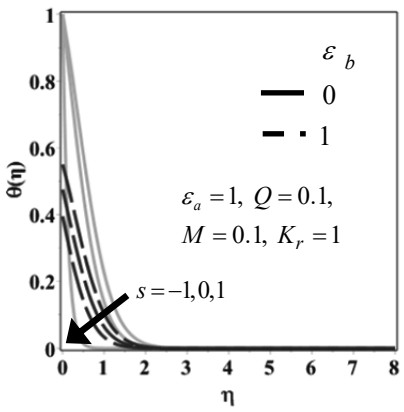

(a) Temperature

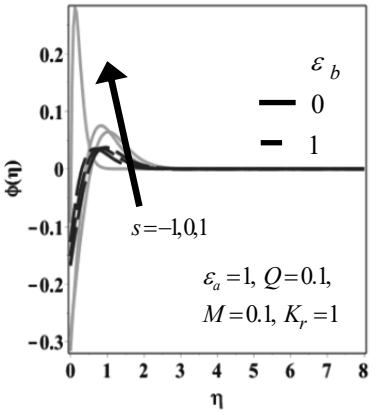

(b) Nanoparticle volume fraction

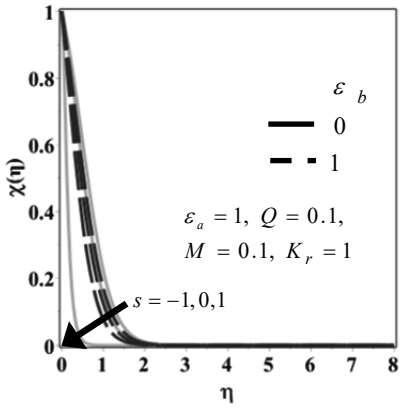

(b) Density of motile microorganism

Fig. 3: Effect of the Stefan blowing parameter and thermal slip parameter.

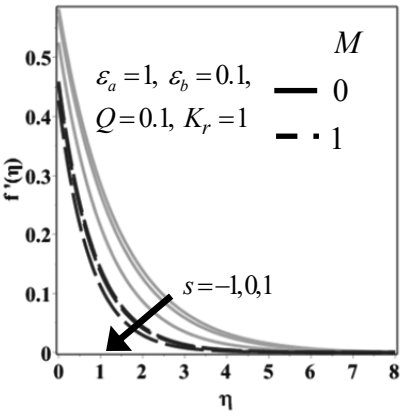

(a) Velocity

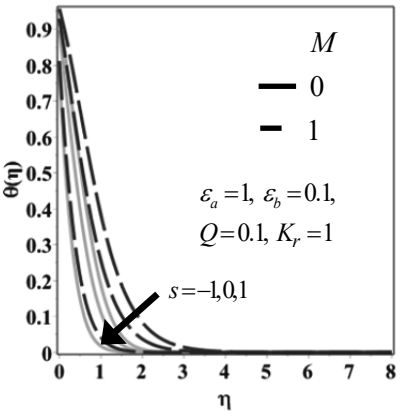

(b) Temperature

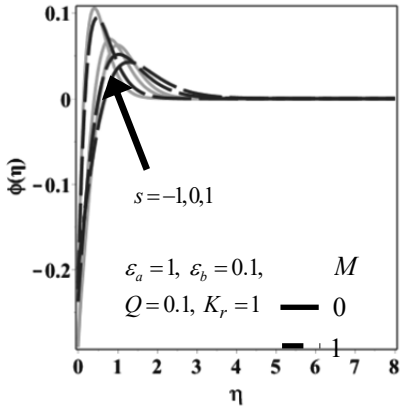

(b) Nanoparticle volume fraction

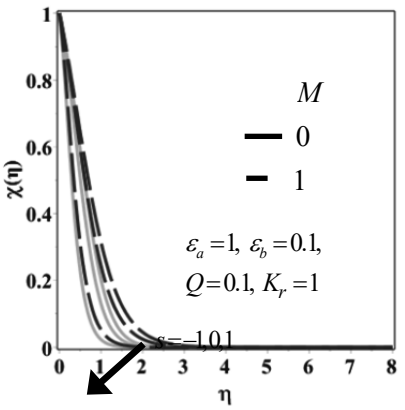

(d) Density of motile microorganism

Fig. 4: Effect of the Stefan blowing parameter and magnetic field parameter.

Tab. 2: Values of $f''(0)$ when $Q = Nb = \varepsilon_b = Nt = 0.1, Pr = 6.8, Le = K_r = Lb = Pe = 1$.

ε_a	$\boldsymbol{M = 1}$	$\boldsymbol{M = 2}$ $(\boldsymbol{s = -1})$	$\boldsymbol{M = 3}$	$\boldsymbol{M = 1}$	$\boldsymbol{M = 2}$ $(\boldsymbol{s = 1})$	$\boldsymbol{M = 3}$
0.2	-1.022812	-1.219705	-1.371720	-1.164740	-1.340662	-1.476817
0.3	-0.916102	-1.078515	-1.200030	-1.026205	-1.167942	-1.274305
0.4	-0.830971	-0.968010	-1.068005	-0.918925	-1.036358	-1.122211
0.5	-0.761245	-0.878920	-0.961465	-0.833079	-0.932435	-1.003438

Tab. 3: Values of $-\theta'(0)$ for distinct ε_a, Q and s by taking $Nb = Nt = \varepsilon_b = M = 0.1$,

$Pr = 6.8, Le = K_r = Lb = Pe = 1$.

ε_a	$\boldsymbol{Q = -0.2}$	$\boldsymbol{Q = -0.1}$ $(\boldsymbol{s = -1})$	$\boldsymbol{Q = 0.2}$	$\boldsymbol{Q = -0.2}$	$\boldsymbol{Q = -0.1}$ $(\boldsymbol{s = 1})$	$\boldsymbol{Q = 0.2}$
0	1.269743	1.174129	0.829555	3.013480	2.918678	2.560051
0.1	1.235234	1.135232	0.768610	2.945878	2.844020	2.449284
0.2	1.207109	1.103299	0.716617	2.891774	2.783753	2.355610
0.3	1.183502	1.076317	0.671043	2.846800	2.733269	2.273606

Tab. 4: Values of $-\phi'(0)/\phi(0)$ when $Q = Nb = \varepsilon_b = M = Nt = 0.1, Pr = 6.8$, and $Le = Lb = Pe = 1$.

ε_a	$K_r = 0.5$	$K_r = 1$ ($s = -1$)	$K_r = 1.5$	$K_r = 0.5$	$K_r = 1$ ($s = 1$)	$K_r = 1.5$
0	2.359787	2.783520	3.158370	15.423451	13.849742	13.144103
0.1	2.280925	2.711923	3.092505	14.623126	13.115701	12.477099
0.2	2.215792	2.652785	3.038089	13.965653	12.523684	11.943681
0.3	2.160265	2.602323	2.991607	13.406847	12.028187	11.500168

Tab. 5: Values of $-\chi'(0)$ when $Nb = \varepsilon_b = Nt = Q = M = 0.1, Pr = 6.8, K_r = Le = Lb = 1$.

ε_a	$Pe = 0.1$	$Pe = 0.5$ ($s = -1$)	$Pe = 1$	$Pe = 0.1$	$Pe = 0.5$ ($s = 1$)	$Pe = 1$
0	1.217637	0.982078	0.702772	3.624454	2.639706	1.421083
0.1	1.168324	0.943313	0.675831	3.462464	2.510564	1.332424
0.2	1.128216	0.912146	0.654719	3.332086	2.407561	1.263170
0.3	1.094601	0.886323	0.637689	3.222929	2.322010	1.206727

8 Conclusions

The Stefan blowing aspects in magneto bio-convected nanofluid flow over slippery moving sheets are exploited numerically. The computed numerical data is matched with already published numerical data and achieved an excellent agreement. The following conclusions are retracted from this analysis:

- The velocity of the fluid is reduced by improving the values of Stefan's blowing constraint.
- Temperature $\theta(\eta)$ is lower for hydrodynamic flow case and higher for magneto-hydrodymaic flow situation.
- The motile microorganisms density distribution curves are reduced by enhancing the thermal slip constraint.
- The values of $f"(0)$ are decaying in presence of momentum slip constraint ε_a.
- The increasing nature of chemical reaction constraint leads to larger $-\phi'(0)/\phi(0)$ values.
- The numeric values of $-\chi'(0)$ are higher for the positive Stefan blowing constraint and lower in the case of the negative Stefan blowing constraint.

Bibliography

Hayat T, Waqas M, Khan MI, Alsaedi A. Impacts of constructive and destructive chemical reactions in magnetohydrodynamic (MHD) flow of Jeffrey liquid due to nonlinear radially stretched surface. Journal of Molecular Liquids. 2017 Jan 1;225:302-10.

Sivakumar N, Prasad PD, Raju CS, Varma SV, Shehzad SA. Partial slip and dissipation on MHD radiative ferro-fluid over a non-linear permeable convectively heated stretching sheet. Results in physics. 2017 Jan 1;7:1940-9.

Thammanna GT, Kumar KG, Gireesha BJ, Ramesh GK, Prasannakumara BC. Three dimensional MHD flow of couple stress Casson fluid past an unsteady stretching surface with chemical reaction. Results in physics. 2017 Jan 1;7:4104-10.

Devi SA. Thermal radiation, viscous dissipation, ohmic dissipation and mass transfer effects on unsteady hydromagnetic flow over a stretching surface. Ain Shams Engineering Journal. 2018 Dec 1;9(4):1161-8.

Imtiaz M, Mabood F, Hayat T, Alsaedi A. Homogeneous-heterogeneous reactions in MHD radiative flow of second grade fluid due to a curved stretching surface. International Journal of Heat and Mass Transfer. 2019 Dec 1;145:118781.

Choi SUS. Enhancing thermal conductivity of fluids with nanoparticles, developments and applications of non-Newtonian flows, The American Society of Mechanical Engineers, 1995; 66: 99-105.

Sheikholeslami M, Shehzad SA, Li Z, Shafee A. Numerical modeling for alumina nanofluid magnetohydrodynamic convective heat transfer in a permeable medium using Darcy law. International Journal of Heat and Mass Transfer. 2018 Dec 1;127:614-22.

Sheikholeslami M. Application of Darcy law for nanofluid flow in a porous cavity under the impact of Lorentz forces. Journal of Molecular Liquids. 2018 Sep 15;266:495-503.

Hayat T, Rashid M, Alsaedi A. Three dimensional radiative flow of magnetite-nanofluid with homogeneous-heterogeneous reactions. Results in physics. 2018 Mar 1;8:268-75.

Gireesha BJ, Sowmya G, Khan MI, Öztop HF. Flow of hybrid nanofluid across a permeable longitudinal moving fin along with thermal radiation and natural convection. Computer methods and programs in biomedicine. 2020 Mar 1;185:105166.

Khan SU, Shehzad SA, Rauf A, Abbas Z. Thermally developed unsteady viscoelastic micropolar nanofluid with modified heat/mass fluxes: A generalized model. Physica A: Statistical Mechanics and its Applications. 2020 Jul 15;550:123986.

Raju CS, Hoque MM, Sivasankar T. Radiative flow of Casson fluid over a moving wedge filled with gyrotactic microorganisms. Advanced Powder Technology. 2017 Feb 1;28(2):575-83.

Waqas M, Hayat T, Shehzad SA, Alsaedi A. Transport of magnetohydrodynamic nanomaterial in a stratified medium considering gyrotactic microorganisms. Physica B: Condensed Matter. 2018 Jan 15;529:33-40.

Zaman S, Gul M. Magnetohydrodynamic bioconvective flow of Williamson nanofluid containing gyrotactic microorganisms subjected to thermal radiation and Newtonian conditions. Journal of theoretical biology. 2019 Oct 21;479:22-8.

Khan MI, Haq F, Khan SA, Hayat T, Khan MI. Development of thixotropic nanomaterial in fluid flow with gyrotactic microorganisms, activation energy, mixed convection. Computer methods and programs in biomedicine. 2020 Apr 1;187:105186.

Naz R, Tariq S, Alsulami H. Inquiry of entropy generation in stratified Walters' B nanofluid with swimming gyrotactic microorganisms. Alexandria Engineering Journal. 2020 Feb 1;59(1):247-61.

Nellis G, Klein S. Heat Transfer, Cambridge University Press, chapter 9, E23-25, 2008.

Lienhard JH, Lienhard VJH, A heat transfer textbook, 3rd edition, Cambridge, MA: Phlogiston Press, 662-633, 2005.

Fang T, Jing W. Flow, heat, and species transfer over a stretching plate considering coupled Stefan blowing effects from species transfer. Communications in Nonlinear Science and Numerical Simulation. 2014 Sep 1;19(9):3086-97.

Latiff NA, Uddin MJ, Ismail AM. Stefan blowing effect on bioconvective flow of nanofluid over a solid rotating stretchable disk. Propulsion and Power Research. 2016 Dec 1;5(4):267-78.

Uddin MJ, Alginahi Y, Bég OA, Kabir MN. Numerical solutions for gyrotactic bioconvection in nanofluid-saturated porous media with Stefan blowing and multiple slip effects. Computers & Mathematics with Applications. 2016 Nov 1;72(10):2562-81.

Zohra FT, Uddin MJ, Ismail AI, Bég OA, Kadir A. Anisotropic slip magneto-bioconvection flow from a rotating cone to a nanofluid with Stefan blowing effects. Chinese journal of physics. 2018 Feb 1;56(1):432-48.

Alamri SZ, Ellahi R, Shehzad N, Zeeshan A. Convective radiative plane Poiseuille flow of nanofluid through porous medium with slip: an application of Stefan blowing. Journal of Molecular Liquids. 2019 Jan 1;273:292-304.

Uddin MJ, Kabir MN, Bég OA. Computational investigation of Stefan blowing and multiple-slip effects on buoyancy-driven bioconvection nanofluid flow with microorganisms. International Journal of Heat and Mass Transfer. 2016 Apr 1;95:116-30.

Das K. Lie group analysis of stagnation-point flow of a nanofluid. Microfluidics and nanofluidics. 2013 Aug 1;15(2):267-74.

Ferdows M, Nabwey HA, Rashad AM, Uddin MJ, Alzahrani F. Boundary layer flow of a nanofluid past a horizontal flat plate in a Darcy porous medium: A Lie group approach. Proceedings of the Institution of Mechanical Engineers, Part C: Journal of Mechanical Engineering Science. 2020 Apr;234(8):1545-53.

Xu L, Lee EW. Variational iteration method for the magnetohydrodynamic flow over a nonlinear stretching sheet. InAbstract and Applied Analysis 2013 Jan 1 (Vol. 2013). Hindawi.

Xu H. Lie group analysis of a nanofluid bioconvection flow past a vertical flat surface with an outer power-law stream. Journal of Heat Transfer. 2015 Apr 1;137(4).

Hayat T, Hussain Q, Javed T. The modified decomposition method and Padé approximants for the MHD flow over a non-linear stretching sheet. Nonlinear Analysis: Real World Applications. 2009 Apr 1;10(2):966-73.

Mahesha Narayana, P. G. Siddheshwar, S. B. Ashoka

Computer-assisted successive linearization solution of the Darcy-Forchheimer-Brinkman flow through a rectangular channel

Darcy-Forchheimer-Brinkman flow

Abstract: Numerical solution of nonlinear differential equations forms an integral part of modeling and simulation in recent times. The nonlinear Darcy-Forchheimer-Brinkman (DFB) model has been extensively used in frontier areas like petroleum engineering, hydrogeology, reactor engineering, biology, medicine, and so on. This well-celebrated model has been chosen as a representative problem to highlight the utility and significance of the computer-assisted successive linearization method (SLM) that in general can be applied to nonlinear boundary value problems (BVPs). The study aims to solve the BVP of the fully developed DFB flow through the sparsely packed porous medium using computer-assisted SLM and investigate its accuracy and robustness. The SLM involves successively linearizing the nonlinear differential equations and starting with an initial solution solve the resultant iterative system of linearized BVPs using the spectral collocation method. The present method, in general, has a quadratic rate of convergence and not sensitive to the initial solution unlike other numerical methods like the shooting method. It is found that the governing parameters have the least effect on the method which means that method convergences even for large values of parameters. Further, SLM is successful in capturing boundary and inertia effects in DFB flow.

Keywords: Darcy-Forchheimer-Brinkman model; Rectangular channel; Successive linearization method.

Mahesha Narayana, Department of Mathematics, The University of the West Indies, Mona Campus, Kingston 7, Jamaica, narayanamahesha@gmail.com
P. G. Siddheshwar, Department of Mathematics, Bangalore University, Bengaluru-560 056.
S. B. Ashoka, Department of Computer Science (PG), Maharanis Science College for Women, Bengaluru, Karnataka 560001, India.

https://doi.org/10.1515/9783110696080-006

1 Introduction

Practical applications of porous media flows are quite evident in the present era and span over a wide range of disciples such as those mentioned in the abstract of the chapter. Comprehensive reviews on flow through porous media have been recorded in the books / edited books/review articles by Ingham and Pop (1, 2), Vafai (3), Nield and Bejan (4), Masuoka et al. (5), Rudraiah et al. (6), and Vadasz (7). As mentioned earlier the primary objective of the chapter is to highlight the implementation and effectiveness of computer-assisted SLM to nonlinear BVPs. Vowing to its practical relevance the DFB flow equation has opted as a representative BVP in order to detail on SLM and its effectiveness.

In view of the aforementioned facts, we present brief literature on DFB flow which takes into account boundary and inertia effects. The nonlinear DFB flow model, based on linear Brinkman drag and the super-linear form drag takes care of high flow rate and permeability in porous media which were not accounted for in the classical Darcys law. In literature, the latter drag is associated with either the name Forchheimer (8) or Ergun (9). The name of Forchheimer is mostly used in comparison to that of Ergun. Works of Skjetne and Auriault (10), and Calmidi and Mahajan (11) consider nonlinear effects on the flow through porous media. Khaled and Vafai (12) also point out to non-linear effect in modeling flow and heat transfer in biological tissues. Vafai and Kim (13), and Nield et al. (14) investigated forced convective flows in rectangular channels embedded with porous medium. In relation to Darcy drag and shear drag due to viscosity, the flows through the porous medium are modeled using two viscosities, namely, the actual fluid viscosity and the effective viscosity. The study of Givler and Altobelli (15) is devoted to the determination of effective viscosity for the DFB flow model by means of experiments. A numerical study of the natural convection in a vertical porous cavity was presented by Lauriat and Prasad (16). Other studies that consider the boundary and inertia effects on flow and heat transfer in porous medium include Poulikakos and Renken (17), Parang and Keyhany (18), and Hooman (19, 20).

Two-point nonlinear BVPs have been tackled either numerically or analytically. Finite difference/element methods, shooting method, collocation methods, variational methods of Galerkin and Rayleigh-Ritz, and other methods capture the numerical solution of the BVPs. Approximate analytical solutions of BVPs could be constructed in the form of infinite series using methods like homotopy methods (homotopy analysis method - HAM (21, 22), homotopy perturbation method – HPM (23, 24)), variational iteration method - VIM (25, 26, 27), Adomian decomposition method - ADM (28, 29), differential transform method - DTM (30, 31) and so on. Successive linearization method - SLM is a recently developed method (see (32, 33, 34, 35) and references therein) that fits into the category of semi-analytic / semi-numerical methods can effectively be used in solving two-point nonlinear BVPs.

In line with the objective of the chapter, we revisit the DFB equation with the intention to put the implementation of computer-assisted SLM and its effectiveness into the spotlight. Application of SLM requires the two-point nonlinear BVPs to be linearized successively giving rise to an iterative system of linear differential equations which is in general not tractable analytically. The pseudo-spectral method based on Chebyshev polynomials is then used to solve the iterative system. In what follows we first derive the Darcy – Forchheimer – Brinkman equation for flow through rectangular channel embedded with porous media and detail on the implementation of the computer-assisted SLM.

2 Darcy – Forchheimer – Brinkman Flow Through Rectangular Channel

The physical system, as shown in Figure 1, consists of a highly percolative medium of an infinite horizontal extent bounded by impermeable walls $x = \pm b/2$ and $z = \pm d/2$. The flow is driven by a constant pressure gradient in the axial direction (along y – axis). The fully-developed DFB flow in the rectangular channel filled with the porous medium can be described using the following equation of motion:

$$\tilde{\mu}\left(\frac{d^2v}{dx^2}+\frac{d^2v}{dz^2}\right)-\frac{\mu}{K}v-\frac{\rho\, C_F}{\sqrt{K}}v^2=\frac{dp}{dy}, \tag{1}$$

where ρ is the density of the fluid, $v(x,z)$ is the velocity, $p(y)$ is the pressure in the y – direction, μ is the usual dynamic viscosity of the fluid, $\tilde{\mu}$ is the effective viscosity due to the presence of solid matrix, K is the permeability of the porous medium and C_F is the dimensionless quadratic drag coefficient. We have chosen to use two viscosities in the above equation as this is in keeping with the current modeling trend. The following 'no-slip' boundary conditions are imposed on equation (1):

$$\left.\begin{aligned} v=0 \quad &\text{on} \quad x=\pm\frac{b}{2},\ \forall z\in\left[-\frac{d}{2},\frac{d}{2}\right],\\ v=0 \quad &\text{on} \quad z=\pm\frac{d}{2},\ \forall x\in\left[-\frac{b}{2},\frac{b}{2}\right]\end{aligned}\right\}. \tag{2}$$

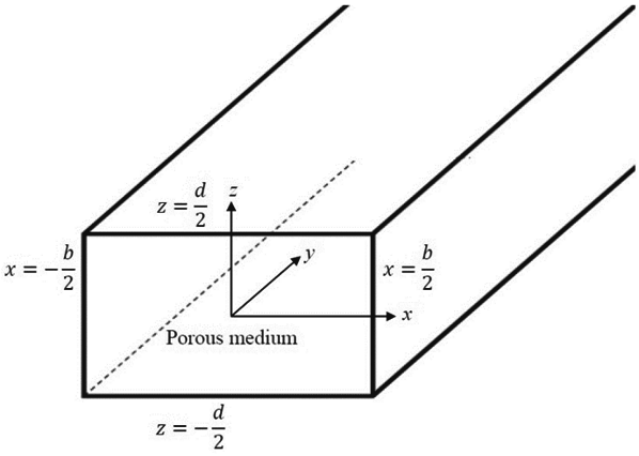

Fig. 1: Schematic of the rectangular porous channel.

We now non-dimensionalize equation (1) using the new variables defined as follows:

$$x^* = \frac{x}{b},\ y^* = \frac{y}{d},\ z^* = \frac{z}{d},\ p^* = \frac{p}{\mu v_0/d},\ v^* = \frac{v}{\left(-v_0 \frac{dp^*}{dy^*}\right)}, \tag{3}$$

where v_0 is a characteristic velocity. Substituting equation (3) into equations (1) and (2) and dropping asterisks for simplicity, we obtain the following BVP involving a second-order differential equation:

$$\Lambda\left(\frac{1}{A^2}\frac{d^2v}{dx^2} + \frac{d^2v}{dz^2}\right) - \sigma^2 v - Fv^2 = -1, \tag{4}$$

where $\Lambda = \tilde{\mu}/\mu$ is the viscosity ratio,

$$Re = \frac{-v_0 d}{\frac{\mu}{\rho}} \frac{dp^*}{dy^*} \text{ is the Reynolds number,}$$

$$\sigma = \frac{d}{\sqrt{K}} \text{ is the porous parameter,}$$

$$F = C_F Re\sigma \text{ is the Forchheimer number,}$$

$$A = \frac{b}{d} \text{ is the aspect ratio of the cross-section of the channel.}$$

The boundary conditions in (2), on using (3) and dropping asterisks, take the form

$$\left.\begin{aligned} v = 0 \ \text{ on } \ x = \pm\tfrac{1}{2}, \ \forall z \in \left[-\tfrac{1}{2}, \tfrac{1}{2}\right], \\ v = 0 \ \text{ on } \ z = \pm\tfrac{1}{2}, \ \forall x \in \left[-\tfrac{1}{2}, \tfrac{1}{2}\right] \end{aligned}\right\}. \tag{5}$$

If we assume that the depth of the cross-section d is sufficiently smaller than the breadth b, i.e., $d \ll b$ or $A \gg 1$ then the first term of equation (3) will be negligibly small and the flow velocity v will be a function of z alone, that is

$$\frac{1}{A^2}\frac{\partial^2 v}{\partial x^2} \ll 1, v = v(z).$$

Under these approximations, equations (3) and (4) reduce to the following BVP

$$\Lambda\frac{d^2 v}{dz^2} - \sigma^2 v - Fv^2 = -1 \tag{6}$$

$$v = 0 \text{ at } z = \pm\frac{1}{2} \tag{7}$$

Equations (6) and (7) form a two-point BVP involving a nonlinear ordinary differential equation whereas equations (4) and (5) represent a BVP involving a nonlinear partial differential equation. The latter problem will be dealt within a future study while the former problem is considered in the present study. Having derived the BVP for the flow problem we now present the implementation of SLM for the same.

3 Successive Linearization Method (SLM)

Consider the BVP defined by equations (6) and (7). Equation (6) can be decomposed into linear and nonlinear parts as follows

$$\mathcal{L}(v) + \mathcal{N}(v) + 1 = 0, \tag{8}$$

where

$$\mathcal{L}(v) = \Lambda\frac{d^2 v}{dz^2} - \sigma^2 v.$$

is the linear part of equation (6) and

$$\mathcal{N}(v) = -Fv^2.$$

is the nonlinear part of the equation (6). Let $v_0(z)$ be a solution of the linear differential equation

$$\mathcal{L}(v) + 1 = 0$$

that takes care of boundary conditions

$$v\left(\pm\frac{1}{2}\right) = 0.$$

In general, it is not necessary that such a function satisfy the linear differential equation but it has to satisfy the boundary conditions. Using $v_0(z)$, the solution of linear part, as an initial solution we construct the solution of nonlinear equation (8) as follows. The solution of equation (8) can be assumed in the form

$$v(z) = v_0(z) + v_1(z), \tag{9}$$

where $v_1(z)$ can be regarded as the pointwise error. Substituting equation (9) into (8) we get

$$\mathcal{L}(v_0 + v_1) + \mathcal{N}(v_0 + v_1) = 0,$$

and expanding nonlinear term about $v = v_0$ we obtain:

$$\mathcal{L}(v_0) + \mathcal{L}(v_1) + \mathcal{N}(v_0) + \frac{1}{1!}\left(\frac{d\mathcal{N}}{dv}\right)\Big|_{v=v_0} v_1 + \frac{1}{2!}\left(\frac{d^2\mathcal{N}}{dv^2}\right)\Big|_{v=v_0} v_1^2 + \cdots = 0. \tag{10}$$

Neglecting nonlinear terms in v_1, in equation (10), we get

$$\mathcal{L}(v_1) + \frac{1}{1!}\left(\frac{d\mathcal{N}}{dv}\right)\Big|_{v=v_0} v_1 = -[\mathcal{L}(v_0) + \mathcal{N}(v_0)].$$

On simplification we get

$$\Lambda\frac{d^2v_1}{dz^2} - (\sigma^2 + 2Fv_0)v_1 = Fv_0^2, \tag{11}$$

where v_1 satisfies homogeneous boundary conditions

$$v_1\left(\pm\frac{1}{2}\right) = 0.$$

Since the nonlinear terms in equation (10) are neglected, v_1 will not be an exact solution and there will be still some error involved in the assumed solution (9). Hence one can refine the solution (9) by taking

$$v(z) = v_0(z) + v_1(z) + v_2(z), \tag{12}$$

where $v_2(z)$ can be regarded as the pointwise error at the second iteration. Substituting equation (12) into (8) and expanding the nonlinear term in Taylor series about $v = v_0 + v_1$, we get the following linear differential equation on simplification:

$$\Lambda \frac{d^2 v_2}{dz^2} - (\sigma^2 + 2F \sum_{m=0}^{1} v_m)\, v_2 = F v_1^2, \tag{13}$$

The correction function $v_2(z)$ satisfies the homogeneous boundary condition

$$v_2\left(\pm\frac{1}{2}\right) = 0.$$

Assuming that the first $n-1$ corrections to the initial solution are available then the n^{th} correction to the solution form the linear differential equation

$$\Lambda \frac{d^2 v_n}{dz^2} - (\sigma^2 + 2F \sum_{m=0}^{n-1} v_m)\, v_n = F v_{n-1}^2. \tag{14}$$

The solution at this stage can be written as

$$v(z) = v_0(z) + v_1(z) + v_2(z) + \cdots + v_n(z) = \sum_{m=0}^{n} v_m. \tag{15}$$

It is to be noted that the linear differential equations, in general, for the n^{th} correction v_n, namely, equations (14) can be solved analytically, if possible. In cases where analytical solutions cannot be found, one has to revert to numerical methods. In the present chapter, we adopt Chebyshevs spectral method to solve the linearized equations for the corrections v_n,$n \geq 1$. To this end, we rewrite equation (14) as

$$\Lambda \frac{d^2 v_n}{dz^2} - a_{n-1} v_n = b_{n-1}. \tag{16}$$

where

$$a_{n-1} = \sigma^2 + 2F \sum_{m=0}^{n-1} v_m,$$

$$b_{n-1} = F v_{n-1}^2.$$

The successive corrections for the initial solution must satisfy trivial boundary conditions, namely,

$$v_n\left(\pm\frac{1}{2}\right) = 0. \tag{17}$$

To solve the linearized BVPs (16) – (17), we use the pseudo-spectral method that uses Chebyshev polynomials. Chebyshev-Gauss-Lobatto collocation points are used in the discretization of the solution domain.

$$z_j = \cos\left(\frac{\pi j}{N}\right), j = 0,1,2,\ldots,N. \tag{18}$$

The collocation points z_j are the points of extrema of the Chebyshev polynomial $T_N(z) = cos(N\, cos^{-1}(z))$ of degree N. It so happens that the domain of interest of the present problem is $\left[-\frac{1}{2},\frac{1}{2}\right]$ but the Chebyshev polynomials are defined on the interval [– 1,1]. Hence, in general, one has to transform the given interval $[a,b]$ to the computational domain [– 1,1] through the following linear transformation:

$$z = \left(\frac{b-a}{2}\right)\xi + \left(\frac{b+a}{2}\right).$$

In the present case, the interval $\left[-\frac{1}{2},\frac{1}{2}\right]$ is transformed to $\left[-1,1\right]$ be defining

$$\xi = 2z. \tag{19}$$

The Chebyshev spectral method in its original form uses a linear combination of Chebyshev polynomials to express the unknown variable and its derivatives but we use the pseudo-spectral version which uses the Chebyshev differentiation matrix $\mathcal{D}$ to express the derivatives of the unknown variable (see, Canuto et al. (36), Trefethen (37), Weideman and Reddy (38), Motsa and Animasaun, (39, 40)). The derivative of the unknown variable v_n at the collocation points can be written, using the differentiation matrix, as follows:

$$\frac{dv_n}{dz} = \sum_{k=0}^{N} D_{jk}\, v_n(\xi_k) = \mathbf{D}\mathbf{v}_n, j = 0,1,2,\ldots,N \tag{20}$$

where $\mathbf{D} = 2\mathcal{D}$ and $\mathbf{v}_\mathrm{n}$ is the vector that consists of values of v_n at the collocation points ξ_j as the entries. In this chapter we adopt the method proposed by Trefethen (37) to calculate the differentiation matrix using the MATLAB cheb.m script file.

The entries of matrix $\mathcal{D}$ are given by

$$\mathcal{D}_{ij} = \begin{cases} \frac{2N^2+1}{6}, & \text{for } i = j = 0, \\ \frac{-\xi_j}{2\left(1-\xi_j^2\right)}, & \text{for } 1 \le i = j \le N-1, \\ \frac{c_i}{c_j}\frac{(-1)^{i+j}}{\xi_i-\xi_j}, & \text{for } 1 \le i \ne j \le N-1, \\ -\frac{2N^2+1}{6}, & \text{for } i = j = N, \end{cases} \tag{21}$$

where

$$c_i = \begin{cases} 2, & \text{for } i = 0 \text{ or } i = N, \\ 1, & \text{for } 1 \le i \le N-1, \end{cases}$$

and $\mathcal{D}_{ij}$ denote entries of matrix $\mathcal{D}$. Substituting equations (18) - (21) in equation (16) we obtain the following linear matrix system

$$\begin{bmatrix} 1 & 0 & \cdots & 0 & 0 \\ & & D^2 - diag(a_{n-1}) & & \\ 0 & 0 & \cdots & 0 & 1 \end{bmatrix} \begin{bmatrix} v_n(\xi_0) \\ v_n(\xi_1) \\ \vdots \\ v_n(\xi_{N-1}) \\ v_n(\xi_N) \end{bmatrix} = \begin{bmatrix} 0 \\ b_{n-1}(\xi_1) \\ \vdots \\ b_{n-1}(\xi_{N-1}) \\ 0 \end{bmatrix}. \tag{22}$$

The matrix system (22) can be put in a compact form as

$$\mathbf{A}_{n-1}\mathbf{v}_n = \mathbf{b}_{n-1}, \tag{23}$$

where $\mathbf{v}_n = [v_n(\xi_0)\ v_n(\xi_1)\ \ldots\ v_n(\xi_{N-1})\ v_n(\xi_N)]^T$ is the solution vector, $\mathbf{A}_{n-1}$ and $\mathbf{b}_{n-1}$ are respectively the coefficient matrix and the constant vector. It must be noted that the boundary conditions (17) have been enforced on the linear system (23). The iterative procedure can be initiated with an initial approximation $v_0(z)$ and correction functions $v_n(z)$ for $n = 1,2,3, \ldots$ can be obtained using the following equation:

$$\mathbf{v}_n = \mathbf{A}_{n-1}^{-1}\mathbf{b}_{n-1}. \tag{24}$$

So far, we have seen the implementation of the SLM; in what follows we present results that establish the accuracy and robustness of SLM.

4 Results and Discussion

The chapter analyses the utility of computer-assisted SLM to solve BVP arising from DFB flow through a rectangular channel filled with sparsely packed porous medium. We first start by establishing the effectiveness of SLM, in terms of, measures like rate of convergence, sensitivity to the initial solution, dependency on the parameter values and time complexity, and so on, with respect to the BVP.

The rate of convergence of SLM is examined using the ratio of l_2 norms of errors at the successive iterations. To this end, we define the rate of convergence in the following way. Suppose $v^*(z)$ is the true solution and

$$v_n^*(z) = \sum_{m=0}^{n} v_m(z)$$

is the approximate solution at n^{th} iteration or n^{th} order. The error at the n^{th} iteration is the l_2 norm defined as

$$\epsilon_n = \|v_n^* - v^*\|_2 = \left(\sum_{j=0}^{N}\left[v_n^*(z_j) - v^*(z_j)\right]^2\right)^{\frac{1}{2}}.$$

An iterative scheme is said to converge at a rate p if

$$\lim_{n\to\infty}\frac{\|v_{n+1}^* - v^*\|}{\|v_n^* - v^*\|_2^p} = M,$$

where M is a positive finite constant. The above definition is equivalent to saying that the error at the $(n+1)^{th}$ iteration is proportional to the p^{th} power of error at the n^{th} iteration

$$\epsilon_{n+1} \propto \epsilon_n^p \Leftrightarrow \epsilon_{n+1} = M\epsilon_n^p.$$

From the above expression, the rate of convergence p can be calculated from

$$\log\left(\frac{\epsilon_{n+2}}{\epsilon_{n+1}}\right) = p\log\left(\frac{\epsilon_{n+1}}{\epsilon_n}\right),$$

where $\epsilon_{n+2}, \epsilon_{n+1}$ and ϵ_n are the l_2 norms computed using three consecutive iterations.

We shall first establish that SLM has a faster rate of convergence by actually computing the rate of convergence p from the above expression. The values of rate of convergence p are tabulated in Table 1 for different choices of the initial solution with σ = 1, $F = 0.05$, and $\Lambda = 1$. It can be easily seen that $p \approx 2$, which establishes the fact that the present iterative method has a quadratic convergence irrespective of the choice of the initial solution. Here we have presented the results pertaining to 2-norm. But it has been verified that the convergence rate remains quadratic for any choice of norm. Further, the values of the physical parameters present in the governing equations do not alter the convergence rate. These facts indicate that the SLM has a quadratic rate of convergence that is independent of the choice of the norm and the value of the parameter.

The missing value of p corresponding to the first row of Table 1 is due to the fact that in the first iteration the solution overshoots $v_0(z)$ thereby producing a spurious value for p. Similarly, the missing values in the second and third row of Table 1 are due to the fact the convergence has been achieved at the respective iterations meaning the error is almost zero. In this situation, if we take the quotient of the two consecutive errors it would lead to an indeterminate form for p. Thus, whenever the initial solution $v_0(z)$ tries to converge to the true solution $v^*(z)$, it always converges at a quadratic rate.

Tab. 1: Values of convergence parameter p at various iterations with $\sigma = 1, F = 0.05$, and $\Lambda = 1$.

Initial Solution	$p = \frac{\log\left(\frac{\epsilon_{n+2}}{\epsilon_{n+1}}\right)}{\log\left(\frac{\epsilon_{n+1}}{\epsilon_n}\right)}$		
	$n = 0$	$n = 1$	$n = 2$
$v_0(z) = \frac{1}{2} - \lvert z \rvert$	-	2.006467	1.993099
$v_0(z) = \frac{1}{4} - z^2$	1.989436	2.001950	-
$v_0(z) = \frac{1}{\sigma^2}\left[1 - \frac{\cosh\left(\frac{\sigma}{\sqrt{\Lambda}}z\right)}{\cosh\left(\frac{\sigma}{2\sqrt{\Lambda}}\right)}\right]$	1.867407	-	-

The implementation of SLM needs an initial guess to the actual solution. This initial solution can be selected to satisfy the boundary conditions of the given BVP (in the spirit of a Galerkin procedure). The successive iterates of this initial solution will have to satisfy homogeneous boundary conditions. Figures 2, 3 and 4 show the sensitivity of SLM to the initial solutions chosen. Respective numerical values of the solutions are tabulated in Tables 2, 3, and 4. Figure 2 shows velocity profiles and Table 2 respective numerical values at chosen nodes, for various orders (iterations) of SLM with a non-smooth, very bad initial solution $v_0(z) = 1/2 - |z|$. We observe that even with this poor choice of initial solution the convergence is achieved at the third iteration itself. From Figure 3 and Table 3 we see that the convergence is obtained at the second iteration itself with a smooth parabolic initial velocity profile given by $v_0(z) = 1/4 - z^2$. Even though the second initial solution is smooth it is nowhere near the actual solution. Finally, with the help of Figure 4 and Table 4 one can observe that the convergence is achieved at the first iteration itself with a very good initial estimate

$$v_0(z) = \frac{1}{\sigma^2}\left[1 - \frac{cosh\left(\frac{\sigma}{\sqrt{\Lambda}}z\right)}{cosh\left(\frac{\sigma}{2\sqrt{\Lambda}}\right)}\right]$$

considered for the velocity profile. These facts suggest that the successive linearization is not sensitive to the initial solution chosen unlike the shooting method (see Mahesha (41) and Abel et al. (42) for details on the shooting method). The convergence is achieved even if the initial solution is non-smooth and very poor, but takes a few more iteration for the same. Thus, the SLM is acceptable since it can produce convergent results even with poor initial guesses for the solution.

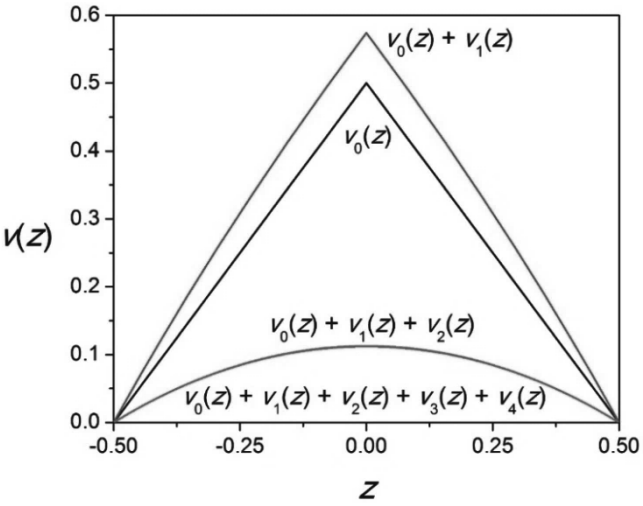

Fig. 2: Velocity profiles at various orders of SLM with an initial solution $v_0(z) = 1/2 - |z|$ and $\sigma = 1,\ F = 0.05, \Lambda = 1$.

Tab. 2: Numerical values of velocity at selected nodes at various orders of SLM with an initial solution $v_0(z) = 1/2 - |z|$ and $\sigma = 1,\ F = 0.05, \Lambda = 1$.

z	$v(z) = \sum_{m=0}^{n} v_m(z)$				
	$n = 0$	$n = 1$	$n = 2$	$n = 3$	$n = 4$
-0.5000	0.0000	0.0000	0.0000	0.0000	0.0000
-0.4755	0.0245	0.0326	0.0110	0.0110	0.0110
-0.4045	0.0955	0.1242	0.0398	0.0396	0.0396
-0.2939	0.2061	0.2581	0.0749	0.0746	0.0746
-0.1545	0.3455	0.4141	0.1030	0.1025	0.1025
0.0000	0.5000	0.5741	0.1137	0.1131	0.1131
0.1545	0.3455	0.4141	0.1030	0.1025	0.1025
0.2939	0.2061	0.2581	0.0749	0.0746	0.0746
0.4045	0.0955	0.1242	0.0398	0.0396	0.0396
0.4755	0.0245	0.0326	0.0110	0.0110	0.0110
0.5000	0.0000	0.0000	0.0000	0.0000	0.0000

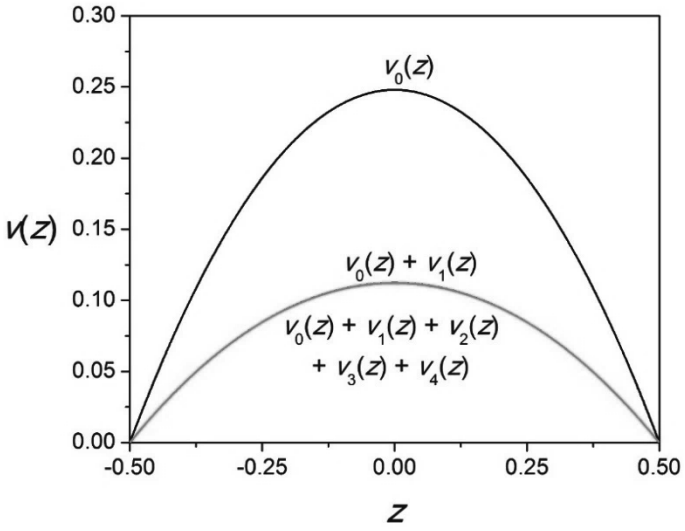

Fig. 3: Velocity profiles at various orders of SLM with an initial solution $v_0(z) = 1/4 - z^2$ and $\sigma = 1, F = 0.05, \Lambda = 1$.

Tab. 3: Numerical values of velocity at selected nodes at various orders of SLM with initial solution $v_0(z) = 1/4 - z^2$ *and* $\sigma = 1, F = 0.05, \Lambda = 1$.

z	$v(z) = \sum_{m=0}^{n} v_m(z)$				
	$n = 0$	$n = 1$	$n = 2$	$n = 3$	$n = 4$
-0.5000	0.0000	0.0000	0.0000	0.0000	0.0000
-0.4755	0.0239	0.0110	0.0110	0.0110	0.0110
-0.4045	0.0864	0.0396	0.0396	0.0396	0.0396
-0.2939	0.1639	0.0746	0.0746	0.0746	0.0746
-0.1545	0.2261	0.1026	0.1025	0.1025	0.1025
0.0000	0.2500	0.1132	0.1131	0.1131	0.1131
0.1545	0.2261	0.1026	0.1025	0.1025	0.1025
0.2939	0.1639	0.0746	0.0746	0.0746	0.0746
0.4045	0.0864	0.0396	0.0396	0.0396	0.0396
0.4755	0.0239	0.0110	0.0110	0.0110	0.0110
0.5000	0.0000	0.0000	0.0000	0.0000	0.0000

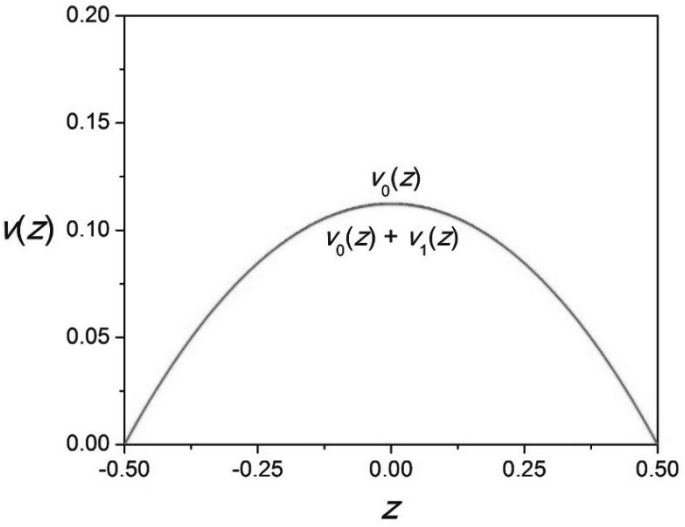

Fig. 4: Velocity profiles at various orders of SLM with an initial solution $v_0(z) = \frac{1}{\sigma^2}\left[1-\frac{cosh\left(\frac{\sigma}{\sqrt{\Lambda}}z\right)}{cosh\left(\frac{\sigma}{2\sqrt{\Lambda}}\right)}\right]$ and $\sigma = 1, F = 0.05, \Lambda = 1$.

Tab. 4: Numerical values of velocity at selected nodes at various orders of SLM with an initial solution $v_0(z) = \frac{1}{\sigma^2}\left[1-\frac{cosh\left(\frac{\sigma}{\sqrt{\Lambda}}z\right)}{cosh\left(\frac{\sigma}{2\sqrt{\Lambda}}\right)}\right]$ and $\sigma = 1, F = 0.05, \Lambda = 1$.

z	$v(z) = \sum_{m=0}^{n} v_m(z)$				
	$n = 0$	$n = 1$	$n = 2$	$n = 3$	$n = 4$
-0.5000	0.0000	0.0000	0.0000	0.0000	0.0000
-0.4755	0.0110	0.0110	0.0110	0.0110	0.0110
-0.4045	0.0396	0.0396	0.0396	0.0396	0.0396
-0.2939	0.0746	0.0746	0.0746	0.0746	0.0746
-0.1545	0.1026	0.1025	0.1025	0.1025	0.1025
0.0000	0.1132	0.1131	0.1131	0.1131	0.1131
0.1545	0.1026	0.1025	0.1025	0.1025	0.1025
0.2939	0.0746	0.0746	0.0746	0.0746	0.0746
0.4045	0.0396	0.0396	0.0396	0.0396	0.0396
0.4755	0.0110	0.0110	0.0110	0.0110	0.0110
0.5000	0.0000	0.0000	0.0000	0.0000	0.0000

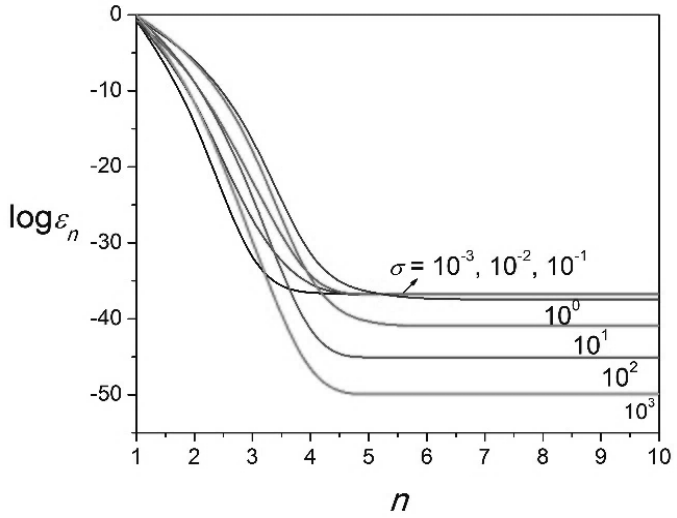

(a)

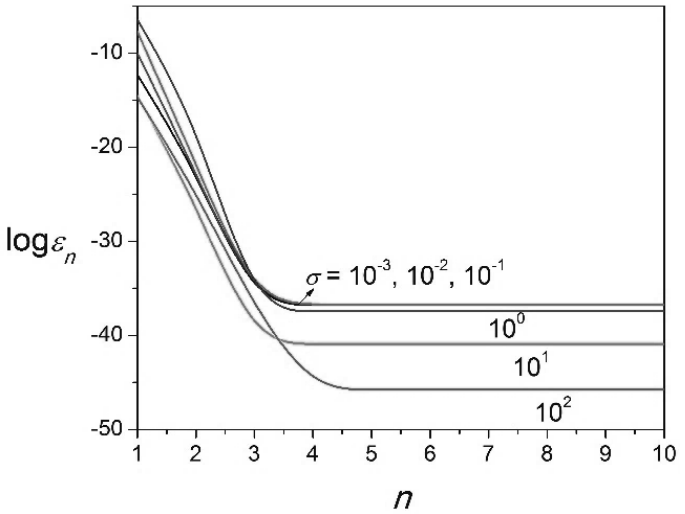

(b)

Fig. 5: Error plots for different values of σ with $F = 0.05, \Lambda = 1$ and initial solutions (a) $v_0(z) = 1/4 - z^2$ and (b) $v_0(z) = \frac{1}{\sigma^2}\left[1 - \frac{cosh\left(\frac{\sigma}{\sqrt{\Lambda}}z\right)}{cosh\left(\frac{\sigma}{2\sqrt{\Lambda}}\right)}\right]$.

Figures 5 –7 show the parameter dependency of the SLM for various physical parameters like porous parameter σ, quadratic drag coefficient F and Brinkman number Λ. Figures 5 (a) and (b) show the error plots for various values of porous parameter σ for two different initial velocities $v_0(z) = 1/4 - z^2$ and

$$v_0(z) = \frac{1}{\sigma^2}\left[1 - \frac{cosh\left(\frac{\sigma}{\sqrt{\Lambda}}z\right)}{cosh\left(\frac{\sigma}{2\sqrt{\Lambda}}\right)}\right],$$

respectively. From figure 5(a) we see that the initial solution $v_0(z) = 1/4 - z^2$ possess an error of almost unit order at the first iteration and convergence is achieved at almost the fifth iteration even for large values of σ. From figure 5(b) we see that the initial solution

$$v_0(z) = \frac{1}{\sigma^2}\left[1 - \frac{cosh\left(\frac{\sigma}{\sqrt{\Lambda}}z\right)}{cosh\left(\frac{\sigma}{2\sqrt{\Lambda}}\right)}\right]$$

is almost near to the actual solution and in this case, the convergence is achieved at almost the fourth iteration even for large values of σ. It needs to be mentioned here that the computations also capture plug-flow velocity profiles for large values of σ.

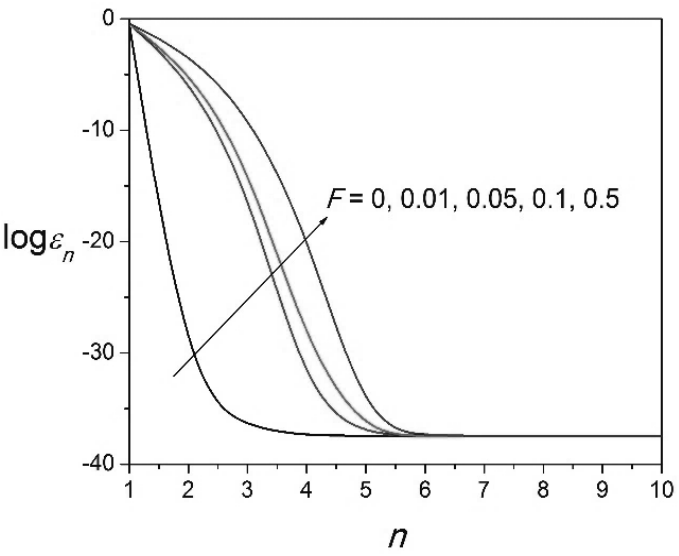

(a)

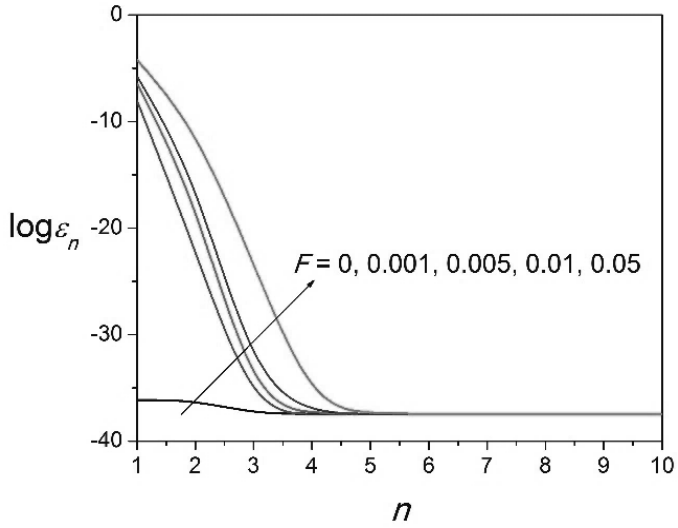

(b)

Fig. 6: Error plots for different values of F with $\sigma = 1, \Lambda = 1$ and initial solutions (a) $v_0(z) = 1/4 - z^2$ and (b) $v_0(z) = \frac{1}{\sigma^2}\left[1 - \frac{cosh\left(\frac{\sigma}{\sqrt{\Lambda}}z\right)}{cosh\left(\frac{\sigma}{2\sqrt{\Lambda}}\right)}\right]$.

Figures 6 (a) and (b) show the error plots for various values of Forchheimer number F with initial velocities $v_0(z) = 1/4 - z^2$ and $v_0(z) = \frac{1}{\sigma^2}\left[1 - \frac{cosh\left(\frac{\sigma}{\sqrt{\Lambda}}z\right)}{cosh\left(\frac{\sigma}{2\sqrt{\Lambda}}\right)}\right]$, respectively. When $F = 0$, the nonlinear BVP reduces to linear BVP as a result of the solution converging at the third iteration itself as can be seen from figures 6 (a) and (b). From figure 6 (a) it is clear that when the initial solution was chosen is $v_0(z) = 1/4 - z^2$ the convergence is achieved at sixth iteration for large values of F, whereas in the case of the initial solution $v_0(z) = \frac{1}{\sigma^2}\left[1 - \frac{cosh\left(\frac{\sigma}{\sqrt{\Lambda}}z\right)}{cosh\left(\frac{\sigma}{2\sqrt{\Lambda}}\right)}\right]$ the convergence is achieved at the fifth iteration as shown in figure 6 (b). The quadratic drag coefficient present in the nonlinear term of the governing BVP forces few more iterations to be taken in order to achieve convergence to the actual solution for large values of F.

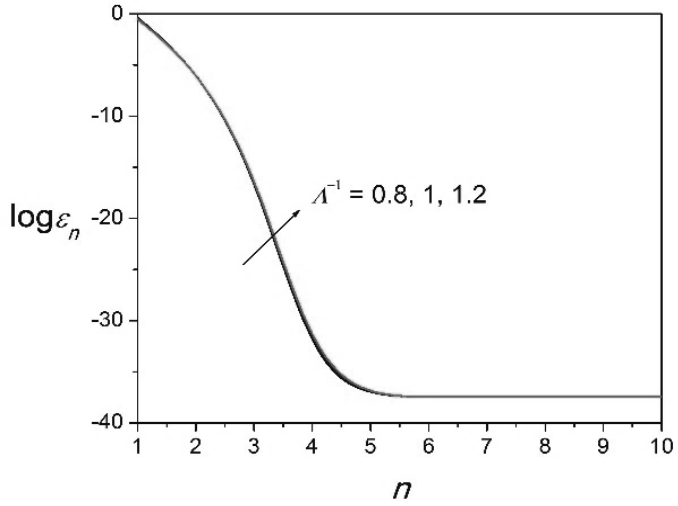

(a)

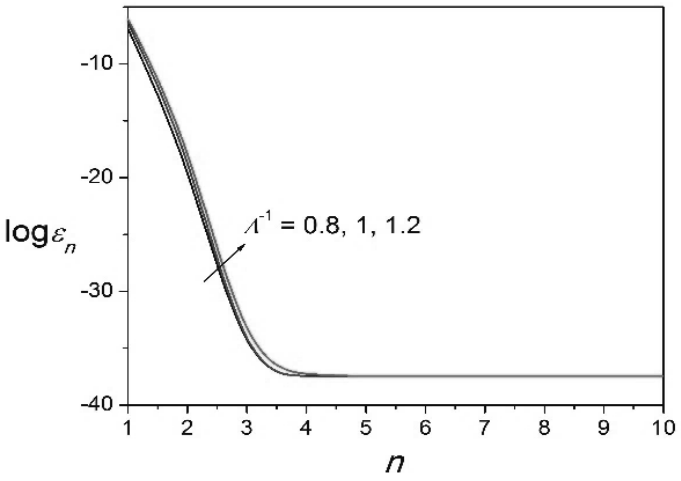

(b)

Fig. 7: Error plots for different values of Λ with $\sigma = 1, F = 0.05$ and initial solutions (a) $v_0(z) = 1/4 - z^2$ and (b) $v_0(z) = \frac{1}{\sigma^2}\left[1 - \frac{cosh\left(\frac{\sigma}{\sqrt{\Lambda}}z\right)}{cosh\left(\frac{\sigma}{2\sqrt{\Lambda}}\right)}\right]$.

Figures 7 (a) and (b) show the error plots for various values of viscosity ratio, Λ, for initial velocities $v_0(z) = 1/4 - z^2$ and

$$v_0(z) = \frac{1}{\sigma^2}\left[1 - \frac{cosh\left(\frac{\sigma}{\sqrt{\Lambda}}z\right)}{cosh\left(\frac{\sigma}{2\sqrt{\Lambda}}\right)}\right],$$

respectively. It should be noted from equation (6) that the Brinkman number appears with the viscous shear term that is not important in the major part of the flow where velocity is governed by the algebraic equation

$$Fv^2 + \sigma^2 v - 1 = 0,$$

This implies that the Brinkman number will not have any effect on the convergence of the solution. The same fact is reiterated in figures 7 (a) and (b). The convergence is achieved at the fifth iteration for the initial solution $v_0(z) = 1/4 - z^2$ and at the fourth iteration in case of the initial solution

$$v_0(z) = \frac{1}{\sigma^2}\left[1 - \frac{cosh\left(\frac{\sigma}{\sqrt{\Lambda}}z\right)}{cosh\left(\frac{\sigma}{2\sqrt{\Lambda}}\right)}\right]$$

as shown in figures 7 (a) and (b) respectively.

5 Scope for Future Research

The previous section points out the salient features of the SLM such as its accelerated convergence, insensitivity towards the initial solution, and stability against large parameter values. These facts render SLM a powerful technique designed to solve nonlinear BVPs. As future research work, the solution regime of SLM can be expanded for the following problems which are frequently encountered in mathematical modeling of many real-world situations:

- Non-linear BVPs involving partial differential equations
- Boundary eigenvalue problems
- Stiff differential equations and chaotic systems

6 Concluding Remarks

The chapter was aimed at highlighting the implementation and effectiveness of computer-assisted SLM. A fully developed DFB flow through the sparsely packed porous medium was chosen as a representative problem for this purpose. The pseudo-spectral method based on Chebyshev polynomials was used to solve the linearized BVPs. The following are some of the findings:

- The method of successive linearization has a quadratic rate of convergence.
- The method does not, in general, depend on the kind of initial solution chosen. Even with a very bad guess to the solution the convergence is guaranteed.
- The method is also not sensitive to the parameter values chosen. It would only need fewer additional iteration to arrive at the convergence. This is, in general, not true with conventional methods.
- The present method also captures boundary and inertial effects effectively.

Bibliography

Ingham DB, Pop I. Transport phenomena in porous media. Pergamon. Oxford. 1998.
Ingham DB, Pop I. Transport phenomena in porous media III (Vol. 3). Elsevier. 2005.
Vafai K. Handbook of porous media. Crc Press. 2015.
Nield DA, Bejan A. Convection in porous media (Vol. 3). New York: Springer. 2006.
Rudraiah N, Siddheshwar PG, Masuoka T. Nonlinear convection in porous media: A Review. Journal of Porous Media. 2003;6(1):1-32.
Rudraiah N, Siddheshwar PG, Pal D, Vortmeyer D. Non-Darcy effects on transient dispersion in porous media. American Society of Mechanical Engineers. Heat Transfer Division. (Publication) HTD. 1988;96:623-8.
Vadász P, Editor. Emerging topics in heat and mass transfer in porous media: From bioengineering and microelectronics to nanotechnology. Springer Science & Business Media; 2008 Apr 9.
Forchheimer P. Wasserbewegung durch boden. Z. Ver. Deutsch, Ing.. 1901;45:1782-8.
Ergun S. Fluid flow through packed columns. Chem. Eng. Prog. 1952;48:89-94.
Skjetne E, Auriault JL. New insights on steady, non-linear flow in porous media. European Journal of Mechanics-B/Fluids. 1999 Jan 1;18(1):131-45.
Calmidi VV, Mahajan RL. Forced convection in high porosity metal foams. J. Heat Transfer. 2000 Aug 1;122(3):557-65.
Khaled AR, Vafai K. The role of porous media in modeling flow and heat transfer in biological tissues. International Journal of Heat and Mass Transfer. 2003 Dec 1;46(26):4989-5003.
Vafai K, Kim SJ. Forced convection in a channel filled with a porous medium: An exact solution. ASME J. Heat Transfer. 1989 Nov 1;111(4):1103-6.
Nield DA, Junqueira SL, Lage JL. Forced convection in a fluid-saturated porous-medium channel with isothermal or isoflux boundaries. Journal of Fluid Mechanics. 1996 Sep;322:201-14.
Givler RC, Altobelli SA. A determination of the effective viscosity for the Brinkman–Forchheimer flow model. Journal of Fluid Mechanics. 1994 Jan;258:355-70.
Lauriat G, Prasad V. Natural convection in a vertical porous cavity: a numerical study for Brinkman-extended Darcy formulation. Journal of Heat Transfer. 1987; 109: 295-330.
Poulikakos D, Renken K. Forced convection in a channel filled with porous medium, including the effects of flow inertia, variable porosity, and Brinkman friction. ASME J. Heat Trans. 1987; 109: 880-8.
Vafai K, Tien CL. Boundary and inertia effects on flow and heat transfer in porous media. International Journal of Heat and Mass Transfer. 1981 Feb 1;24(2):195-203.
Hooman, K. (2008). A perturbation solution for forced convection in a porous-saturated duct. Journal of Computational and Applied Mathematics. 211(1), 57-66.
Hooman K, Gurgenci H. A theoretical analysis of forced convection in a porous-saturated circular tube: Brinkman–Forchheimer model. Transport in Porous Media. 2007; 69(3): 289-300.

Liao S. Beyond perturbation: introduction to the homotopy analysis method. CRC press. 2003.
Liao S. Homotopy analysis method in nonlinear differential equations Beijing: Higher education press. 2012; 153-165.
He JH. A coupling method of a homotopy technique and a perturbation technique for non-linear problems. International journal of non-linear mechanics, 2000; 35(1): 37-43.
He JH. Homotopy perturbation method for solving boundary value problems. Physics Letters A, 2006; 350(1-2): 87-8.
He JH, Wu XH. Variational iteration method: new development and applications. Computers & Mathematics with Applications. 2007 Oct 1;54(7-8):881-94.
He JH. Variational iteration method for autonomous ordinary differential systems. Applied Mathematics and Computation. 2000 Sep 11;114(2-3):115-23.
He JH. Variational iteration method–a kind of non-linear analytical technique: some examples. International Journal of Non-linear Mechanics. 1999 Jul 1;34(4):699-708.
Adomian G. Nonlinear stochastic differential equations. Journal of Mathematical Analysis and Applications. 1976 Aug 1;55(2):441-52.
Adomian G. A review of the decomposition method and some recent results for nonlinear equations. Computers & Mathematics with Applications. 1991 Jan 1;21(5):101-27.
Zhou JK. Differential transformation and its applications for electrical circuits. 1986.
Jang MJ, Chen CL, Liy YC. On solving the initial-value problems using the differential transformation method. Applied Mathematics and Computation. 2000 Oct 27;115(2-3):145-60.
Motsa SS, Sibanda P, Shateyi S. On a new quasi-linearization method for systems of nonlinear boundary value problems. Mathematical Methods in the Applied Sciences. 2011 Jul 30;34(11):1406-13.
Motsa SS, Sibanda P. A linearisation method for non-linear singular boundary value problems. Computers & Mathematics with Applications. 2012 Apr 1;63(7):1197-203.
Motsa SS. A new algorithm for solving nonlinear boundary value problems arising in heat transfer. International Journal of Modeling, Simulation, and Scientific Computing. 2011 Sep;2(03):355-73.
Narayana M, Khidir AA, Sibanda P, Murthy PV. Soret effect on the natural convection from a vertical plate in a thermally stratified porous medium saturated with non-Newtonian liquid. Journal of Heat Transfer. 2013 Mar 1;135(3).
Canuto C, Hussaini MY, Quarteroni A, Zang TA. Spectral Approximation. In Spectral Methods in Fluid Dynamics 1988 (pp. 31-75). Springer, Berlin, Heidelberg.
Trefethen LN. Spectral methods in MATLAB. Society for industrial and applied mathematics; 2000 Jan 1.
Weideman JA, Reddy SC. A MATLAB differentiation matrix suite. ACM Transactions on Mathematical Software (TOMS). 2000 Dec 1;26(4):465-519.
Motsa SS, Animasaun IL. Unsteady Boundary Layer Flow over a Vertical Surface due to Impulsive and Buoyancy in the Presence of Thermal-Diffusion and Diffusion-Thermo using Bivariate Spectral Relaxation Method. Journal of Applied Fluid Mechanics. 2016 Nov 1;9(5).
Motsa SS, Animasaun IL. Paired quasi-linearization analysis of heat transfer in unsteady mixed convection nanofluid containing both nanoparticles and gyrotactic microorganisms due to impulsive motion. Journal of Heat Transfer. 2016 Nov 1;138(11).
Mahesha, N. Solutions of Some Boundary Value Problems Arising in the Flow, Heat and Mass Transfer Due to a Linear/Non-linear Stretching Surface. Ph. D. Thesis. Gulbarga University (India). 2010.
Abel MS, Siddheshwar PG, Mahesha N. Numerical solution of the momentum and heat transfer equations for a hydromagnetic flow due to a stretching sheet of a non-uniform property micropolar liquid. Applied Mathematics and Computation. 2011 Feb 15;217(12):5895-909.

V. Ramachandramurthy, D. Uma, N. Kavitha

Linear and non-linear instability analysis of the onset of magnetoconvection in couple-stress fluids with thermorheological effect

Onset of magnetoconvection in couple-stress fluids

Abstract: The Rayleigh-Benard situation for the couple stress fluid with thermorheological effect in the presence of applied magnetic field is studied using both linear and non-linear stability analysis. This problem discusses the three important aspects that concern the mechanism of the control of convection namely suspended particles, applied magnetic field, and variable viscosity. It is found that the thermo-rheological parameter, Chandrasekhar number, and the couple-stress parameter influence the onset of convection. The effect of the thermo-rheological parameter is to destabilize the system whereas the couple-stress parameter and Chandrasekhar number stabilize the same. The generalized Lorenz's model has essentially coupled non-autonomous first-order differential equations and is solved numerically using the Runge-Kutta method to measure the heat transport. The effect of increasing these parameters influence the heat transfer. It is found that an effect of increasing thermo-rheological parameter enhances heat transfer whereas an increasing value of the couple-stress parameter and Chandrasekhar number diminishes the same. This problem has possible applications in the context of the magnetic field.

Keywords: Rayleigh-Benard convection; Boussinesq Stokes suspension; Boussinesq approximation; Magnetoconvection; Lorenz model; Lie group analysis.

1 Introduction

In many practical situations, most of the fluids are not so pure, which may contain suspended particles like polymeric suspensions, liquid crystals, etc. Suspended

V. Ramachandramurthy, Department of Mathematics, Ramaiah Institute of Technology, Bengaluru-560 054, India, vramachanramoorty@yahoo.co.in
D. Uma, Department of MCA, PES Institute of Technology, Bengaluru-560 085, India.
N. Kavitha, Department of Mathematics, Ramaiah Institute of Technology, Bengaluru-560 054, India.

https://doi.org/10.1515/9783110696080-007

particles play a very important role in the analysis of fluid. Due to the presence of suspended particles, there is a large stabilizing/destabilizing effect on the thermal convection of the fluids. As the growing importance of non-Newtonian fluids in modern science and industries, investigations on fluids with suspension are desirable. Many researchers have made significant contributions considering industrially important fluids like polymeric suspensions, chemicals, paints, also with possible applications related to solidifications of liquid crystals, pharmaceutical, food, and beverage as well as refrigeration and so on. Convection in the fluid layer with the variation of viscosity has drawn considerable attention in the present years due to its applications in various areas such as terrestrial planets, heat transfer, and so on. Hence the variable viscosity problems in Rayleigh-Benard convection have received considerable attention from many researchers (see Platten and Legros (1), Gebhart et al. (2), Siddheshwar and Pranesh (3), Siddheshwar (4) and references therein). When the viscosity varies significantly with temperature is called 'Thermorheological effect'. In many engineering and geophysical problems, viscosity strongly depends on temperature. The thermo-rheological effect which is generally in a polynomial or exponential form is approximated by Taylor series approximation, which has been investigated by Torrance and Turcotte (5), Busse and Frick (6), Stengel et al. (7), Severin and Herwig (8) and so on. The experimental work on convection in fluids with the Thermorheological effect has been studied by Somerscales and Dougherty (10). Siddheshwar and Stephan Titus (11) made a detailed non-linear analysis on Rayleigh-Benard convection for the Newtonian fluid in the presence of a heat source using the Ginzburg-Landau model. The investigations as mentioned above dealt with the Rayleigh-Benard convection in Newtonian fluids.

Some of the recent investigations concerning the effect of the magnetic field are discussed below: Rajagopal et al. (12) have studied the non-linear stability analysis of Rayleigh-Benard convection considering rotational modulation and magnetic field using the Ginzburg Landau model. They discussed the impact of various parameters in detail. The Rayleigh-Benard convection in a square enclosure filled with viscoplastic fluid has been investigated by Hassan and Manabendra (18), numerically as well as experimentally. A local nonlinear stability analysis using an eight-mode expansion is performed in arriving at the coupled amplitude equations for Rayleigh-Benard-Brinkman convection (RBBC) in the presence of LTNE effects by Siddheshwar and Kanchana (21). Siddheshwar and Siddabasappa (22) studied the effect of local thermal non-equilibrium (LTNE) on the onset of Brinkman Benard convection and heat transport is investigated. Wakif et al. (23) recently investigated the convection mechanism in a Newtonian nanofluid layer with spatially uniform and non-uniform heating in Sinusoidal spatial form. They have used Buongiorno's mathematical model to study the effect of control parameters and discussed the results for different boundary conditions. Wakif et al. (24) also discussed the effect of an external magnetic field on the onset of convection in nanofluids and is examined numerically using the same two phases mathematical model. Wakif et al. (25)

also considered both single-phase and two-phase nanofluid models for the investigation of Cu-water nanofluids. They studied the combined effects of thermal radiation and a uniform transverse magnetic field. Wakif et al. (26) examined the electroconvection in a dielectric nanofluid under the influence of perpendicularly applied alternating electric field assuming Newtonian rheological behavior of nanofluid considering thermoplastic and Brownian diffusions confined between two parallel plate electrodes. They found that the obtained analytical solutions agree well with the available know values for the limiting case of dielectric fluids. Wakif et al. (27) studied the onset of nanofluid convection in the presence of applied magnetic field numerically based on the non-homogeneous Buongiorno's mathematical model. In their study, they used the latest experimental correlations and powerful analytical models for expressing the thermophysical properties of some electrically conducting nanofluids. They considered three types of nanofluids including copper-water, silver-water, and gold-water, and analyzed the various pertinent parameters on the critical stability parameters such as critical Rayleigh number and wave number. Wakif et al. (28) analyzed numerically the effect of an externally applied magnetic field and an imposed negative temperature gradient on the onset of natural convection in a thin horizontal layer of alumina-water nanofluid for various sizes of spherical alumina nanoparticles and volumetric fractions. They have shown graphically the thermo-hydrodynamic stability of the nanofluidic system and the critical cell size of convection cells in terms of the critical thermal Rayleigh and wave numbers for the various values of the magnetic Chandrasekhar number, the volumetric fraction, and the diameter of alumina nanoparticles.

The present paper aims in analyzing the effect of Boussinesq-Stokes suspension and variable viscosity for the fluid with Rayleigh-Benard convection in the presence of applied magnetic fields both linearly and non-linearly.

2 Mathematical formulation

Consider a Boussinesq electrically conducting fluid that fills a thin horizontal layer of finite depth d extending to infinity in the two horizontal directions x and z, with an imposed traverse uniform magnetic field H_0 in the vertical z - direction, situated between stress free electrically conducting boundaries. The fluid is originally isothermal and at rest. At some time $t = 0$, heat is applied in an arbitrary manner with respect to time but uniformly with respect to the lower boundary surface. Let $\Delta T > 0$ be the temperature difference between the lower and upper surfaces with the lower boundary at the greater temperature than the upper boundary. Subjected to the Oberbeek-Boussinesq approximations, the equations which governs the physical model of the problem involving electrically conducting couple stress fluid are:

$$\nabla . q = 0, \tag{1}$$

$$\nabla . H = 0, \tag{2}$$

$$\rho_0 \left[\frac{\partial q}{\partial t} + (\boldsymbol{q} . \nabla)\boldsymbol{q}\right] = \left.\begin{array}{c} -\nabla p - \rho(T) g \hat{k} + \nabla\left(\mu_f(T)[\nabla \boldsymbol{q} + \nabla \boldsymbol{q}^T]\right) \\ +\mu_m^2 (\boldsymbol{H} . \nabla)\boldsymbol{H} - \mu' \nabla^4 \boldsymbol{q} \end{array}\right\}, \tag{3}$$

$$\frac{\partial T}{\partial t} + (\boldsymbol{q} . \nabla) T = \chi \nabla^2 T, \tag{4}$$

$$\frac{\partial \boldsymbol{H}}{\partial t} + (\boldsymbol{q} . \nabla)\boldsymbol{H} = (\boldsymbol{H} . \nabla)\boldsymbol{q} + \nu_m \nabla^2 \boldsymbol{H}, \tag{5}$$

$$\rho = \rho_0 (1 - \beta (T - T_0)), \tag{6}$$

$$\mu_f(T) = \mu_0 e^{-\delta (T - T_0)}, \tag{7}$$

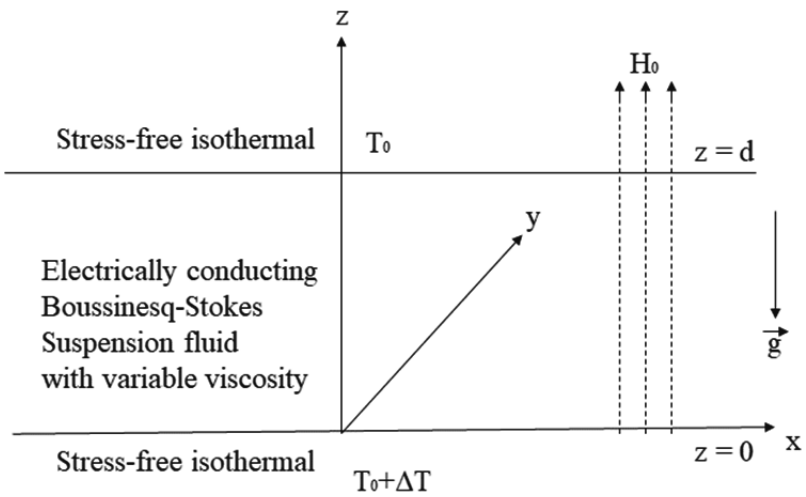

Fig. 1: Physical model of the problem

Assuming the components of velocity $\boldsymbol{q}$, temperature T, density ρ and viscosity μ in the basic state as $\boldsymbol{q}_b, T_b(z), \rho_b(z)$ and μ_{f_b}, the solutions obtained in the quiescent state of the form:

$$\left.\begin{aligned} \boldsymbol{q} = (0,0), T_b = T_0 + \Delta T f\left(\frac{z}{d}\right) \\ \rho_b\left(\frac{z}{d}\right) = \rho_0\left[1 - \beta\Delta T f\left(\frac{z}{d}\right)\right] \\ p_b\left(\frac{z}{d}\right) = -\int \rho_b\left(\frac{z}{d}\right) g d\left(\frac{z}{d}\right) + c_1 \end{aligned}\right\}, \tag{8}$$

We now superimpose the finite-amplitude perturbations for the basic state and obtain,

$$\left.\begin{aligned} \boldsymbol{q} = \boldsymbol{q}_b + \boldsymbol{q}', T = T_b(Z) + T', \rho = \rho_b(Z) + \rho' \\ p = p_b(Z) + p', \boldsymbol{H} = \boldsymbol{H}_b(Z) + \boldsymbol{H}', \mu = \mu_b(Z) + \mu' \end{aligned}\right\}, \tag{9}$$

where the prime denotes a perturbed quantity. Substituting Eqn. (9) in the governing equations, we get the following component equations:

$$\nabla . \boldsymbol{q}' = 0, \tag{10}$$

$$\nabla . \boldsymbol{H}' = 0, \tag{11}$$

$$\left.\begin{aligned} \rho_0\left[\frac{\partial q'}{\partial t} + (\boldsymbol{q}' . \nabla)\boldsymbol{q}'\right] = -\nabla q' - \rho'(T) g\hat{k} + \nabla\left(\mu_f(T)\left[\nabla \boldsymbol{q}' + \nabla \boldsymbol{q}'^T\right]\right) \\ +\mu_m^2 (\boldsymbol{H}' . \nabla)\boldsymbol{H}' + \mu_m H_b \frac{\partial \boldsymbol{H}}{\partial z} - \mu' \nabla^4 \boldsymbol{q}' \end{aligned}\right\}, \tag{12}$$

$$\frac{\partial T'}{\partial t} + (\boldsymbol{q}' . \nabla) T' + w' \frac{\partial T_b}{\partial z} = \chi \nabla^2 T', \tag{13}$$

$$\frac{\partial \boldsymbol{H}'}{\partial t} + (\boldsymbol{q}' . \nabla)\boldsymbol{H}' - (\boldsymbol{H}' . \nabla)\boldsymbol{q}' - H_b \frac{\partial w'}{\partial z} = \nu_m \nabla^2 \boldsymbol{H}', \tag{14}$$

$$\rho' = -\rho_0 \beta T', \tag{15}$$

In the view of analyzing the fluid, we consider only two-dimensional disturbances, hence we introduce the magnetic potential ϕ' and the stream function ψ' as

$$\left.\begin{aligned} u' = -\frac{\partial \psi'}{\partial Z}, w' = \frac{\partial \psi'}{\partial X}, \\ H_x' = -\frac{\partial \phi'}{\partial Z}, H_z' = -\frac{\partial \phi'}{\partial X} \end{aligned}\right\}, \tag{16}$$

The classical procedure of operating curl for the eq. (12) helps in eliminating the pressure p and transforming the above system of equations to dimensionless equations using the scaling mentioned below,

$$(X, Z) = \left(\frac{x}{d}, \frac{z}{d}\right), \psi = \frac{\psi'}{\chi}, \theta = \frac{T'}{\Delta T}, \Phi = \frac{\phi}{d H_b}, \tag{17}$$

We obtain the non-dimensional governing equations as

$$\frac{1}{Pr}\left(\frac{\partial}{\partial\tau}(\nabla^2\psi)+J(\psi,\nabla^2\psi)\right)=R_E\frac{\partial\Theta}{\partial X}-C\nabla^6\psi+QP_m\left(\frac{\partial(\nabla^2\Phi)}{\partial Z}+J(\Phi,\nabla^2\Phi)\right)+\mu_{f_b}\nabla^4\psi+\frac{\partial\mu_{f_b}}{\partial Z}\frac{\partial}{\partial Z}(\nabla^2\psi), \tag{18}$$

$$\left(\frac{\partial}{\partial\tau}-\nabla^2\right)\Theta=\frac{\partial\psi}{\partial X}+J(\psi,\Theta), \tag{19}$$

$$\left(\frac{\partial}{\partial\tau}-p_m\nabla^2\right)\Phi=\frac{\partial\psi}{\partial Z}+J(\psi,\Phi), \tag{20}$$

where, $\mu_{f_b}=\mu_0 e^{-V(1-Z)}$ and $\frac{\partial\mu_{f_b}}{\partial Z}=\mu_0 V e^{-V(1-Z)}$ both will be expressed as Half-range Fourier cosine series in the interval (0,1), also the Jacobian $J(F_1,H_1)=\frac{\partial F_1}{\partial X}\frac{\partial H_1}{\partial Z}-\frac{\partial F_1}{\partial Z}\frac{\partial H_1}{\partial X}$ and the Laplacian operator $\nabla^2=\frac{\partial^2}{\partial X^2}+\frac{\partial^2}{\partial Z^2}$.

The dimensionless parameter appeared in the equations (18), (19) and (20) are

$$Pr=\frac{\mu}{\rho_0\chi}\text{ (Prandtl Number)},$$

$$Pm=\frac{\nu_m}{\chi}\text{ (Magnetic Prandtl number)},$$

$$R_E=\frac{\beta\rho_0 g d^3\Delta T}{\mu_0\chi}\text{ (External Rayleigh number)},$$

$$Q=\frac{\mu_m^2\sigma H_0^2 d^2}{\mu}\text{ (Chandrasekhar number)},$$

$$C=\frac{\mu'}{\mu d^2}\text{ (Couple stress parameter)}.$$

The boundary conditions for the present problem on velocity, temperature, and magnetic potential are

$$\begin{matrix}\psi=\nabla^2\psi=\Theta=D\Phi=0\ at\ z=0\\ \psi=\nabla^2\psi=\Theta=D\Phi=0\ at\ z=1\end{matrix}\text{,} \tag{21}$$

Using (21), the solutions of dimensionless equations (18), (19), and (20) are obtained.

2.1 Linear Theory

To perform the linear analysis we consider the equations (18), (19), and (20) in linearized form along with the stress-free and isothermal boundary conditions (21). Which means that it is essential to neglect the Jacobian's i.e $J(\Psi,\nabla^2\Psi), J(\Phi,\nabla^2\Phi), J(\Psi,\Theta)$ and $J(\Psi,\Phi)$ in Eqs. (18), (19) and (20). The neglect of

the Jacobian's is essential to eradicate the products of amplitudes in the equations to obtain a linearized equation for the study of linear theory.

The solution of linear versions of these equations are assumed to be periodic waves (see Chandrasekhar (29)) in the form

$$\left.\begin{aligned}\psi(X,Z,\tau) &= \psi_0 \sin(\pi\alpha X)\sin(\pi Z)\\ \Theta(X,Z,\tau) &= \Theta_0 \sin(\pi\alpha X)\sin(\pi Z)\\ \Phi(X,Z,\tau) &= \Phi_0 \sin(\pi\alpha X)\cos(\pi Z)\end{aligned}\right\}, \tag{22}$$

then

$$R_{E_c} = \frac{\eta_1^2\left(Q\pi^2 + C\eta_1^6 + \frac{\eta_1^4}{2}(1-2\pi^2)a_2 - a_0\right)}{\pi^2\alpha^2}, \tag{23}$$

where, $\eta_1 = \pi^2(1+\alpha^2)$, $a_0 = 2\int_0^1 \mu_{f_b} dZ$ and $a_2 = 2\int_0^1 \mu_{f_b}\cos 2\pi\, Z dZ$ are the Fourier Cosine coefficients and $\pi\alpha$ the horizontal wave number. The quantities Ψ_0, Θ_0 and Φ_0 are the amplitudes of the magnetic potential, stream function, and temperature respectively.

Clearly, Ψ, Θ, and Φ considered in Eq. (22) satisfies the boundary conditions (21). Now Substituting the trial functions assumed in the equations (22) in the linearized version of the dimensionless equations (18), (19), and (20), using the standard Galerkin procedure (i.e integrating the equations with respect to X and Z between $\left[0, \frac{2\pi}{\pi\alpha}\right]$ and $(0,1)$ respectively), we obtain the set of homogeneous equations in Ψ_0, Θ_0 and Φ_0. Hence the critical value of R_{E_c} as in equation (23) is obtained, which signifies the onset of convection.

The above discussion of linear theory helps in the study of convective mode analysis but it fails in understanding the effect of heat transfer. Now we extend the analysis to nonlinear theory, to understand the amount of heat transfer and the effect of suspended particles in the fluid.

2.2 Nonlinear Theory

The representation of a minimal double Fourier series for the stream function Ψ, temperature Θ and the magnetic potential Φ which defines the finite-amplitude convection in the fluid is given by

$$\left.\begin{aligned}\psi(X,Z,\tau) &= A(\tau)\sin(\pi\alpha X)\sin(\pi Z)\\ \Theta(X,Z,\tau) &= B(\tau)\cos(\pi\alpha X)\sin(\pi Z) - D(\tau)\sin(2\pi Z)\\ \Phi(X,Z,\tau) &= E(\tau)\sin(\pi\alpha X)\cos(\pi Z) - F(\tau)\sin(2\pi\alpha X)\end{aligned}\right\}, \tag{24}$$

where A, B, D, E and F are the amplitudes to be determined from the dynamics of the system. Then substitute the Eq. (24) into the dimensionless Eqs. (18), (19), and (20)

and proceeding using the standard Galerkin procedure, we obtain the following nonlinear autonomous system of differential equations:

$$\frac{dA}{d\tau_1} = \left[(C\eta_1^2 + C_1)A + C_2 B - \frac{PmQ\pi}{\eta_1^2}E - PmQ\left(4\pi^4\alpha^3 - \frac{2\pi^2\alpha\eta_1^2}{\eta_1^4}\right)EF\right], \tag{25}$$

$$\frac{dB}{d\tau_1} = \frac{1}{\eta_1^2}[\pi\alpha A - \eta_1^2 B - \pi^2\alpha AD], \tag{26}$$

$$\frac{dD}{d\tau_1} = \frac{1}{\eta_1^2}\left[\frac{\pi^2\alpha}{2}AB - 4\pi^2 D\right], \tag{27}$$

$$\frac{dE}{d\tau_1} = \frac{1}{\eta_1^2}[\pi A - p_m\eta_1^2 E + \pi^2\alpha AF], \tag{28}$$

$$\frac{dF}{d\tau_1} = \frac{1}{\eta_1^2}[-\pi^2\alpha AE - 4\pi^2\alpha^2 p_m F], \tag{29}$$

where $C_1 = \mathrm{Pr}\left[\left(\frac{\eta_1^2 - 2\pi^2}{2\eta_1^2}\right)a_2 - \frac{a_0}{2}\right]$, $C_2 = \frac{Pr\pi\alpha R_E}{\eta_1^4}$ and $\tau_1 = \eta_1^2\tau$.

The above system of non-linear differential equations is difficult to be solved using the analytical procedure for the general time-dependent variable. So these equations have been solved using a numerical method like Runge-Kutta Fehlberg45 with the help of Mathematica 9.0 software.

3 Heat Transport

The amount of transfer of heat is very important in the study of convection in Boussinesq Stokes suspension fluids, as convection sets in with the increase of the temperature gradient across the layer of fluid, which can be identified by its effect on the heat transport.

The horizontally averaged Nusselt number Nu, for the stationary mode of magnetoconvection, is given by

$$Nu\,(\tau) = \frac{\left[\frac{\alpha_c}{2}\left(\int_{X=0}^{2/\alpha}(1-Z+\Theta)_Z dX\right)\right]_{Z=0}}{\left[\frac{\alpha_c}{2}\left(\int_{X=0}^{2/\alpha}(1-Z)_Z dX\right)\right]_{Z=0}}, \tag{30}$$

Substituting the Eq. (24b) in Eq. (30), the Nusselt number $Nu(\tau)$ expression is obtained as:

$$Nu(\tau) = 1 + \frac{2}{\left(\frac{\pi^2\alpha^2 R_{E_c}}{\eta^6}\right)}D(\tau). \tag{31}$$

4 Results and discussions

A study is made on Rayleigh-Benard convection in a weakly conducting fluid layer under the influence of temperature-dependent viscosity and suspended particles in the presence of the applied vertical magnetic field. These parameters have appeared in the form of thermorheological parameter V, couple stress parameter C, and the Chandrasekhar number Q. A linear and non-linear stability analysis is performed in the problem with these constraints. The effects of electrical conductivity and magnetic field come through the parameters P_m and Q. The effect of these parameters on the onset of stability and heat transfer are discussed in detail.

The linear stability analysis clearly explains the parameter influence on the eigenvalue of the problem whereas quantification of heat transport is analyzed through the non-linear theory

4.1 Linear theory

Some of the important highlights of linear stability analysis are

1. deriving the expression for the half range Fourier series for basic nonuniform temperature gradient and the basic viscosity over the interval (0, 1),
2. obtaining an expression for the eigenvalue, critical Rayleigh number R_{E_C} for the stationary convection using the Galerkin technique,
3. plotting Neutral stability curve (Rayleigh – wave number graphs) in order to analyze convective instability.

The figures from (2) to (4) are the plots of external Rayleigh number R_E verses wave number α, for the different combinations of Q, V and C. It can be observed that both R_{E_c} and α_c increases with the increasing values of Q which shows the stabilizing effect of the magnetic field. But it is apparent that the increasing values of C increases R_{E_c} and decreases the values of α_c. From these linear plots, we can clearly found that the system is more stable in the presence of suspended particles than the magnetic field. Also, these figures clearly, demonstrate an effect of Thermorheological parameter V which shows the destabilizing effect in the system due to the presence of variable viscosity V.

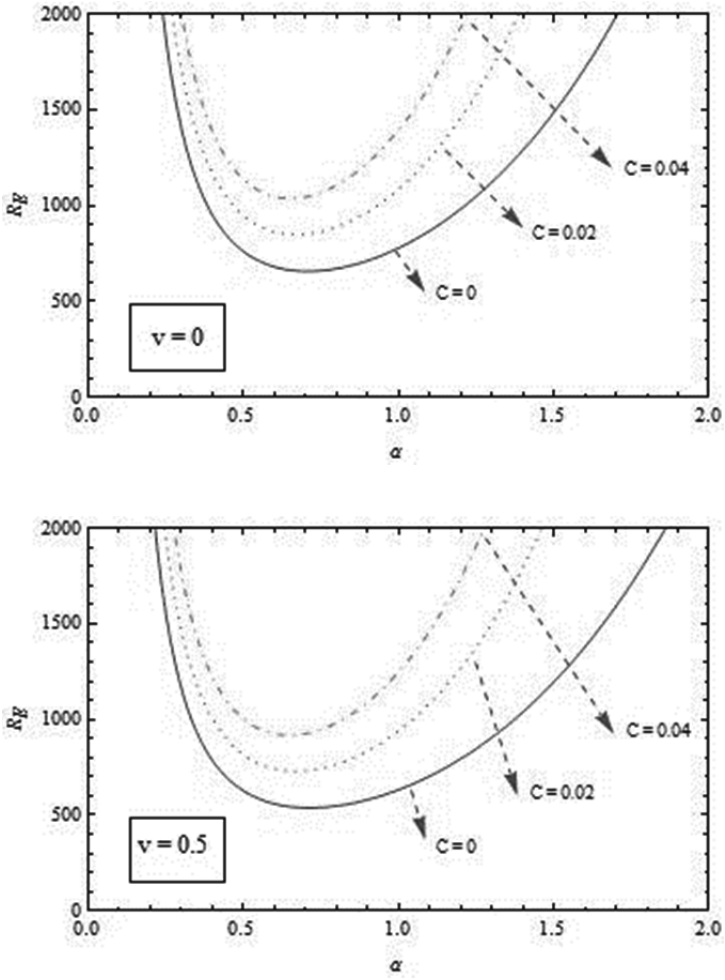

Fig. 2: Plot of R_{E_c} vs. α_c for $Q = 0$.

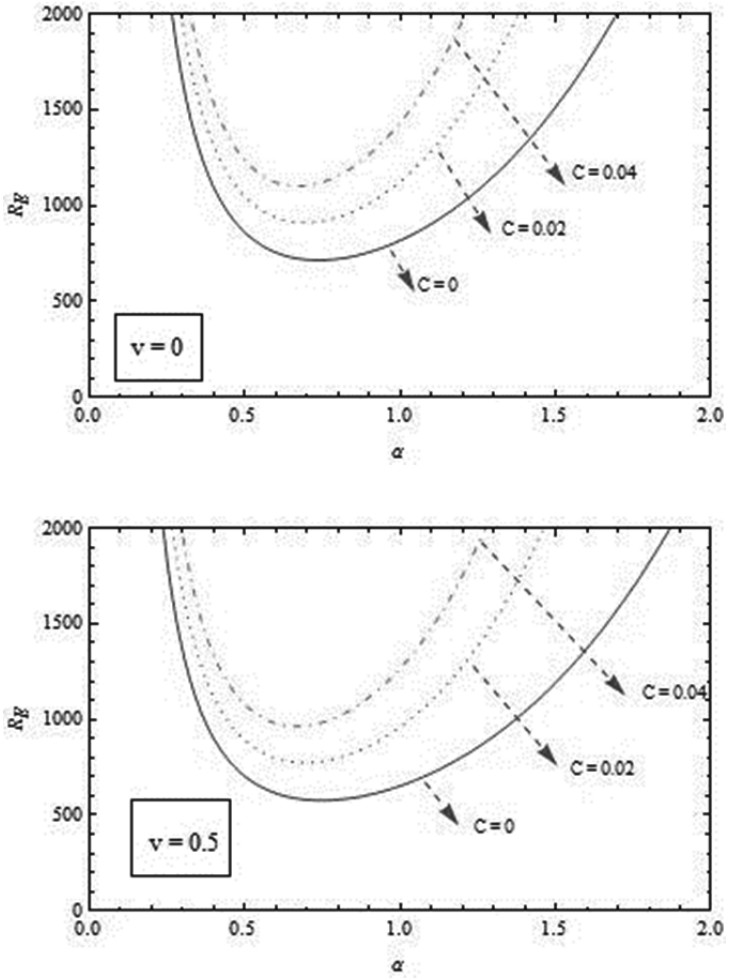

Fig. 32: Plot of R_{E_c} vs. α_c for $Q = 2$.

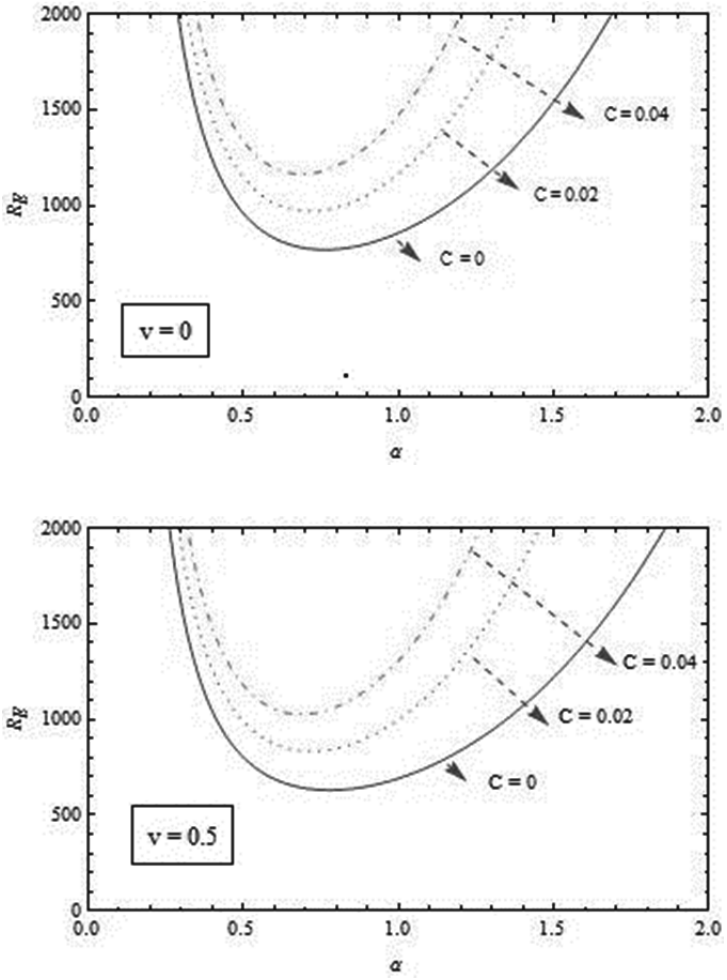

Fig. 4: Plot of R_{E_c} vs. α_c for $Q = 4$.

4.2 Non-linear theory

Some of the important highlights of non-linear stability analysis are

- Finite amplitude analysis is employed through double Fourier series representation for the magnetic potential Φ, stream function Ψ and the temperature Θ,
- The non-linear system of equations is obtained in the form of a generalized Lorenz model,
- Quantification of heat transport is analyzed through Nusselt number for the stationary mode of magnetoconvection in the Boussinesq Stokes suspension fluid.

– Plotting of Nusselt number variation concerning time to study the individual effects of the parameters involved.

Before we start on the discussion of the results, we note that the Lorenz model of the problem is numerically solved by employing Runge-Kutta Fehlberg 45 method with the adaptive step size. In order to carry out the numerical integration of the coupled system, we have used the initial conditions $A(0) = B(0) = D(0) = E(0) = F(0) = 5$, but dynamic of the system will remain same even for the random initial values. Due to the suspended particles being present in the carrier liquid, the Prandtl number of the couple-stress liquids is more than that of the Newtonian carrier liquid. Hence, we have taken the value of the Prandtl number as $Pr = 10$ and is maintained throughout the discussion.

We have dealt with the non-linear stability analysis in the present problem. Figures from (5) to (7) shows the plots of Nusselt number Nu versus time τ for different values of Q, C, V and for the fixed value of $Pr = 10$. The individual effects of the magnetic field suspended particles, and temperature-dependent viscosity can be observed from each of the Nusselt number plots. Figure 5 (both(a) and (b)) highlights the effect of variable viscosity in the absence of magnetic field Q. The Nusselt number Nu increases with increasing values of V indicate the convective contribution to heat transport which has been clearly shown in the figure (5) by comparing the points $C1, C2$, and $C3$ from figure 5 (a and b).

The influence of the magnetic field Q can be observed from the plots 5 and 6. From figures 5(a) and 6(a) we can notice the diminishing effect of heat transport due to the enhancement of the magnetic field, the same can be observed through points $C1, C2,$ and $C3$. Hence the increase of Q corresponds to a decrease in Nusselt number Nu. From all the above plots it is clear that Nu decreases with the increasing values of Q and C. Due to the presence of suspended particles in the fluid viscosity increases, so more heating is required to make the system unstable which resulting in stabilizing effect of C.

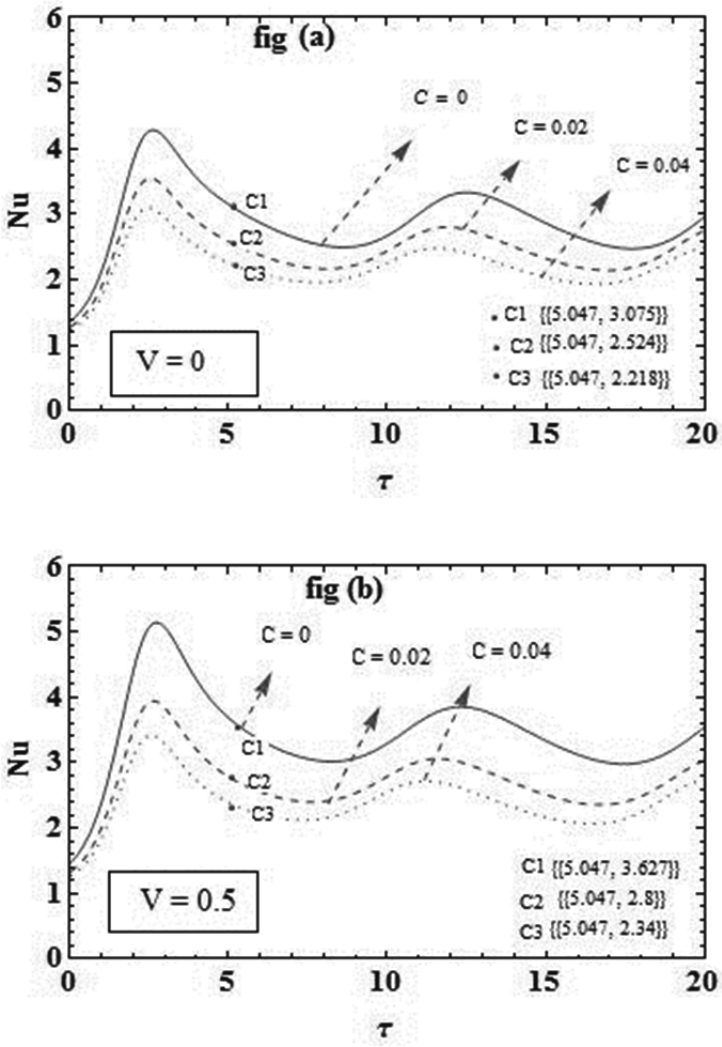

Fig. 5: Nusselt number Nu variation plot with τ for $Q = 0, Pr = 10$.

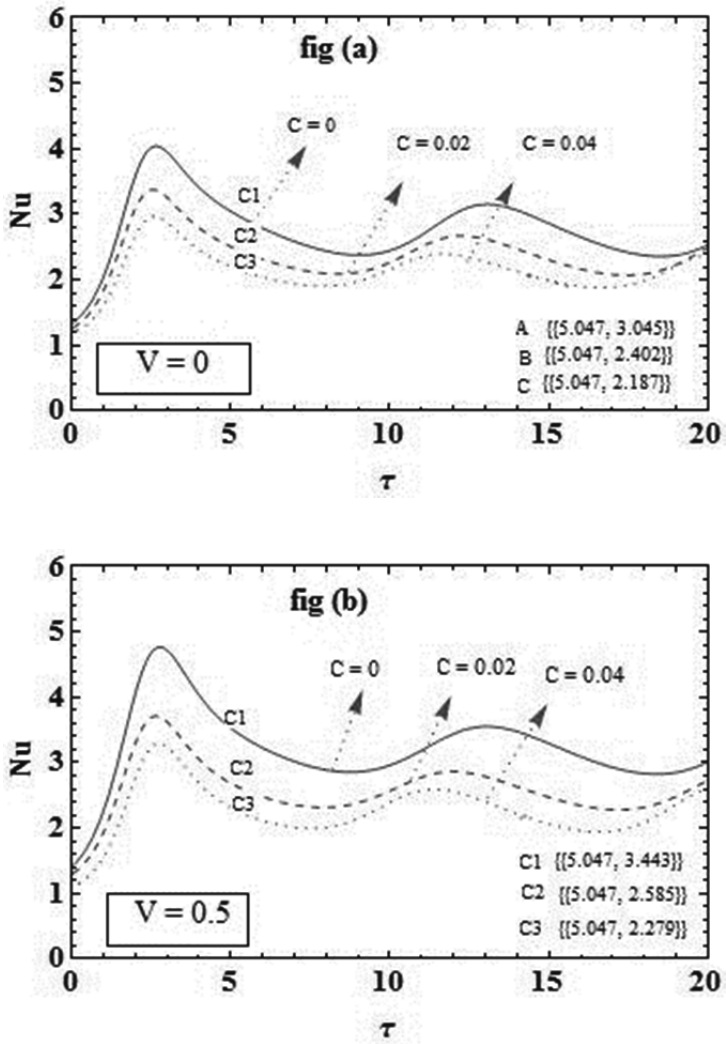

Fig. 6: Nusselt number Nu variation plot with τ for $Q = 2, Pr = 10$.

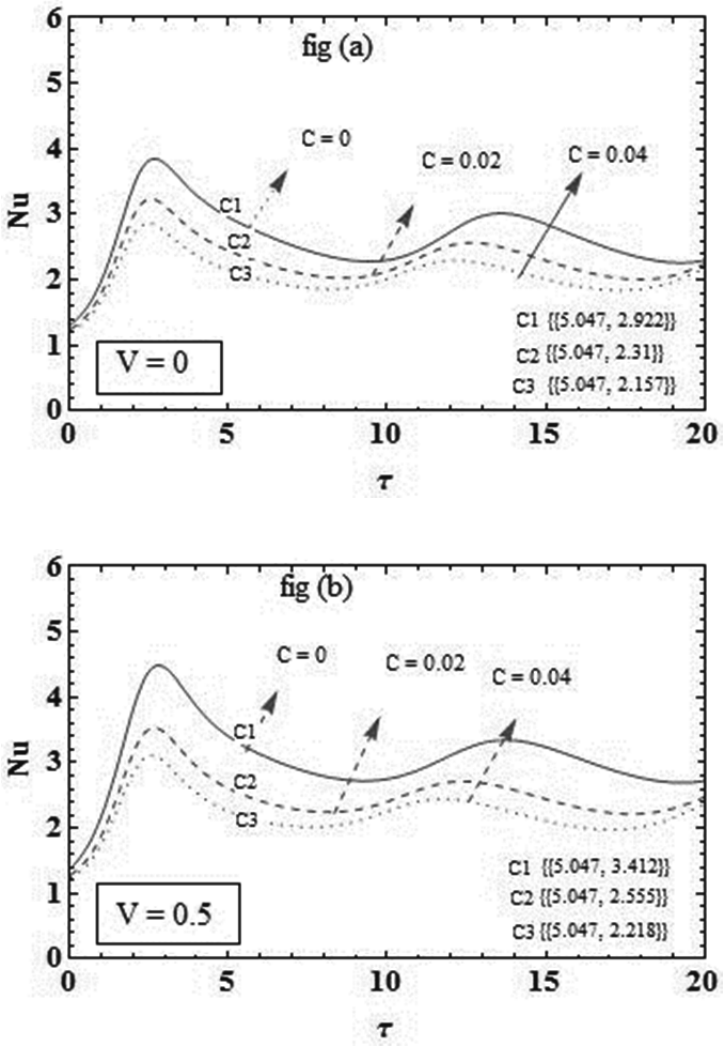

Fig. 7: Nusselt number Nu variation plot with τ for $Q = 4, Pr = 10$.

5 Conclusion

- The effect of the magnetic field and suspended particles is to stabilize the system.
- The effect of variable viscosity destabilizes the system
- Both R_{E_c} and $\pi\alpha_c$ decreases as V increases in the absence of C.
- R_{E_c} increases and $\pi\alpha_c$ decreases as C increases

- Nu increases with increasing values of V indicate the convective contribution to heat transport.
- The Nusselt number decreases with an increase in Q and C.
- Couple stress effect due to suspended particles is more dominant than the magnetic field effect on the onset of convection.

Acknowledgments

The first and third authors are grateful to the principal and management of Ramaiah Institute of Technology, Bengaluru. Whereas the second author is grateful to the management of PES university for the encouragement of research activities.

Bibliography

Platten JK, Legros JC. Convection in liquids, Springer Verlag, Berlin, 1984.

Gebhart Y, Jaluria RL, Mahajan, Sammakia B. Buoyancy induced flows and transport, Hemisphere Publishing Corporation, Reference edition, 1988.

Siddheshwar PG, Pranesh S. Magnetoconvection in fluids with suspended particles under 1g and μg. Aerospace Science and Technology. 2002 Feb 1;6(2):105-14.

Siddheshwar PG. Thermorheological effect on magnetoconvection in weak electrically conducting fluids under 1g or μg. Pramana. 2004 Jan;62(1):61-8.

Torrance KE, Turcotte DL. Thermal convection with large viscosity variations. Journal of Fluid Mechanics. 1971 May;47(1):113-25.

Busse FH, Frick H. Square-pattern convection in fluids with strongly temperature-dependent viscosity. Journal of fluid mechanics. 1985 Jan;150:451-65.

Stengel KC, Oliver DS, Booker JR. Onset of convection in a variable-viscosity fluid. Journal of Fluid Mechanics. 1982 Jul; 120:411-31.

Severin J, Herwig H. Onset of convection in the Rayleigh-Bénard flow with temperature dependent viscosity: An asymptotic approach. Zeitschrift für angewandte Mathematik und Physik ZAMP. 1999 May;50(3):375-86.

Riahi N. Nonlinear convection in a horizontal layer with an internal heat source. Journal of the Physical Society of Japan. 1984 Dec;53(12):4169-78.

Somerscales EF, Dougherty TS. Observed flow patterns at the initiation of convection in a horizontal liquid layer heated from below. Journal of Fluid Mechanics. 1970 Jul;42(4):755-68.

Siddheshwar PG, Stephen Titus P. Nonlinear Rayleigh–Bénard convection with variable heat source. Journal of heat transfer. 2013 Dec 1;135(12).

Rajagopal R, Jacob SE, Sangeetha George K. A Non-Linear Stability Analysis of Rayleigh Bènard Magnetoconvection of a Couple Stress Fluid in the Presence of Rotational Modulation. International Journal of Mathematics Trends and Technology (IJMTT). 2018;54(6):477-84.

Siddheshwar PG. Thermorheological effect on magnetoconvection in weak electrically conducting fluids under 1g or μg. Pramana. 2004 Jan;62(1):61-8.

Siddheshwar PG, Pranesh S. An analytical study of linear and non-linear convection in Boussinesq–Stokes suspensions. International journal of non-linear mechanics. 2004 Jan 1;39(1):165-72.

Siddheshwar PG, Ramachandramurthy V, Uma D. Rayleigh–Bénard and Marangoni magnetoconvection in Newtonian liquid with thermorheological effects. International journal of engineering science. 2011 Oct 1;49(10):1078-94.

Sharma V, Sharma S. Thermosolutal convection in micro polar fluids in hydromagnetic in porous medium, Indian Journal of pure and applied mechanics 2004.

Sharma RC, Sharma M. Effect of suspended particles on couple-stress fluid heated from below in the presence of rotation and magnetic field, Indian Journal of pure and applied mathematics, 2004; 35(8): 973.

Hassan MA, Pathak M, Khan MK. Rayleigh–benard convection in Herschel–Bulkley fluid. Journal of Non-Newtonian Fluid Mechanics. 2015 Dec 1;226:32-45.

Sekhar GN, Jayalatha G, Prakash R. Thermal convection in variable viscosity ferromagnetic liquids with heat source. International Journal of Applied and Computational Mathematics. 2017 Dec;3(4):3539-59.

Maruthamanikandan S, Thomas NM, Mathew S. Thermorheological and magnetorheological effects on Marangoni-ferroconvection with internal heat generation, J. Physics Conf. Series, 2018; 1139, 012024.

Siddheshwar PG, Vanishree RK, Kanchana C. Study of Rayleigh-Benard Brinkman convection using LTNE model and coupled, real Ginzburg-Landau equations, International scholarly and scientific research and innovation, 2017; 11(6).

Siddheshwar PG, Siddabasappa C. Linear and weakly nonlinear stability analysis of two-dimensional, steady Brinkman Benard convection using local thermal non-equilibrium model, J. Transport on porous media, 2017; 120: 605631,

Wakif A, Boulahia Z, Sehaqui R. Numerical study of the onset of convection in a Newtonian nanofluid layer with spatially uniform and non uniform internal heating. Journal of Nanofluids. 2017 Feb 1;6(1):136-48.

Wakif A, Boulahia Z, Sehaqui R. Numerical analysis of the onset of longitudinal convective rolls in a porous medium saturated by an electrically conducting nanofluid in the presence of an external magnetic field. Results in physics. 2017 Jan 1;7:2134-52.

Wakif A, Boulahia Z, Mishra SR, Rashidi MM, Sehaqui R. Influence of a uniform transverse magnetic field on the thermo-hydrodynamic stability in water-based nanofluids with metallic nanoparticles using the generalized Buongiorno's mathematical model. The European Physical Journal Plus. 2018 May 1;133(5):181.

Wakif A, Boulahia Z, Sehaqui R. Numerical analysis of the onset of longitudinal convective rolls in a porous medium saturated by an electrically conducting nanofluid in the presence of an external magnetic field. Results in physics. 2017 Jan 1;7:2134-52.

Wakif A, Boulahia Z, Ali F, Eid MR, Sehaqui R. Numerical analysis of the unsteady natural convection MHD Couette nanofluid flow in the presence of thermal radiation using single and two-phase nanofluid models for Cu–water nanofluids. International Journal of Applied and Computational Mathematics. 2018 Jun;4(3):1-27.

Wakif A, Boulahia Z, Amine A, Animasaun IL, Afridi MI, Qasimd M, Sehaqui R. Magneto-convection of alumina-water nanofluid within thin horizontal layers using the revised generalized Buongiorno's model. Frontiers in Heat and Mass Transfer (FHMT). 2018 Dec 5;12.

Chandrasekhar S, ydrodynamic and Hydromagnetic Stability, Oxford University Press, Oxford, 1961.

Nomenclature

Symbol	Definition
d	Depth of the fluid layer (m)
g	Acceleration due to gravity ($g = 9.8\ ms^{-2}$)
H_0	Magnetic field
p	Pressure (Pa)
$\boldsymbol{q}$	Velocity components of u, v, w (ms^{-1})
Pr	Prandtl number
Pm	Magnetic Prandtl number
Q	Chandrasekhar number
C	Couple stress parameter
R_E	External Rayleigh number
Nu	Nusselt number
T	Temperature (K)
t	Time (s)
ΔT	Temperature difference between the walls
Greek Symbols	
$\pi\alpha$	Wave number
μ	Dynamic viscosity (Pas)
μ'	Couple-stress viscosity
μ_m	Magnetic permeability
β	Thermal expansion coefficient (K^{-1})
χ	Constant thermal diffusivity
ρ	Density ($kg\ m^{-3}$)
ψ	Perturbed stream function
ϕ	Magnetic potential
Φ	Perturbed magnetic potential
Θ	Perturbed temperature
Other symbols	
x, y, z	Cartesian coordinates (m)
$\hat{\imath}$	Unit vector normal in x- direction
$\hat{k}$	Unit vector normal in z- direction
∇^2	Laplacian operator

J. Meghana, S. Pranesh

Two-component convection in micropolar fluid under time-dependent boundary concentration

Concentration modulation on DDC in a micropolar fluid

Abstract: The effect of imposed boundary concentration modulation on the onset of convection, heat, and mass transfer in two-component convection in a micropolar fluid is studied. In linear theory, using the perturbation method an expression for the Rayleigh number and the correction Rayleigh number is obtained as a function of micropolar fluid parameters, frequency, and amplitude. The effect of various parameters on heat and mass transport is studied by deriving the Ginzburg Landau equation from the sixth order Lorenz equations. It is found that by increasing the coupling parameter N_1, heat transfer decreases and mass transfer increases.

Keywords: Concentration modulation; Double diffusive convection; Micropolar fluid; Nusselt number; Sherwood number.

1 Introduction

Two Component Convection (Double Diffusive Convection-DDC) is gaining more importance because of its physical and engineering applications in astrophysics, oceanography, chemical engineering, food processing, solidification of molten alloys and crystal growth. Convection driven by difference in density due to the temperature and concentration gradient between the upper and lower plate is called as DDC. The theory of DDC was proposed by Turner (1, 2).

Rudraiah and Siddheshwar (3) examined the effect of cross-diffusion in a fluid with saturated porous medium and they found that by choosing the appropriate sign and magnitude of cross diffusion parameters it is possible to get diffusive and finger-instabilities in DDC. Motivated by this Malashetty and Bharati (4) did similar work in a Maxwell fluid. Capone and Luca (5) made a comprehensive report on effect of magnetic field on DDC in a porous medium. All the above-mentioned works deal with theory of DDC in the presence of porous medium.

Micropolar fluids belong to a class of non-Newtonian fluids which consists of a vis-

J. Meghana, Research Scholar, Department of Mathematics, CHRIST (Deemed to be University), Bangalore, India, meghana.j@res.christuniversity.in
S. Pranesh, Department of Mathematics, CHRIST (Deemed to be University), Bangalore, India.

https://doi.org/10.1515/9783110696080-008

cous medium and a randomly oriented suspended particles. Eringen (6) introduced micropolar fluid theory which has a lot of industrial applications. The complete information on the micropolar fluid theory and its applications can be found in the book Lukasazewicz (7). The Eringen micropolar fluid model can be used to study complicated fluids like animal blood, oil, paints, polymeric fluid, and certain biological fluids.

Sharma and Sharma (8) examined DDC in a micropolar fluid in presence of the magnetic field. They found that the solutal parameters and magnetic field stabilize the system. Pranesh and Arun (9) studied the effect of non-uniform concentration gradient on the onset of DDC using the Galerkin method. They found that by choosing non-uniform concentration gradient onset of DDC can be controlled. Pranesh and Sameena (10) investigated linear and non-linear analyses of DDC in presence of the electric field. They have analyzed the effect of various micropolar fluid parameters on the onset of DDC and heat and mass transfer. They concluded that an increase in the concentration of suspended particles increases the Rayleigh number and also it increases heat and mass transport.

Another important class of problems deals with the control of convection by modulating one of the parameters. Venezian (11) was the first to consider the periodic modulation and studied its effect on the onset of convection. Motivated by Venezian work Malashetty and Basavaraja (12), Bhadauria (13), Siddheshwar et al. (14), Bhadauria and Kiran (15), Bhadauria et al. (16), Pranesh and Arun (17), Pranesh and Thriveni (18) studied DDC under different types of modulating parameters. They have concluded that the onset of DDC, heat, and mass transfer can be controlled by varying the frequency and amplitude of modulation.

Concentration modulation is of great importance in material sciences and chemical laboratories. Vinod et al. (19) studied the effects of mass transfer under the concentration/gravity modulation by deriving Ginzburg Landau Equation. Vinod (20) used Ginzburg–Landau equation to investigate the effect of the Coriolis force on mass transfer in a couple-stress fluid with concentration modulation. Ansa et al. (21) were first to examine the effect of time-dependent concentration on the onset of Solutal Rayleigh-Bénard Convection in a micropolar fluid. They have concluded that out-of-phase modulation is most stable. The literature pertaining to concentration modulation on DDC in micropolar fluids is missing despite its practical importance in many technical problems.

Thus, in the present chapter we study the effect of concentration modulation on heat and mass transfer in micropolar fluid on DDC.

2 Mathematical Formulation

The incompressible micropolar fluid is considered between two parallel plates which are at a distance d from each other. The temperature and concentration gradient are maintained by heating and salting from below (see Figure 1).

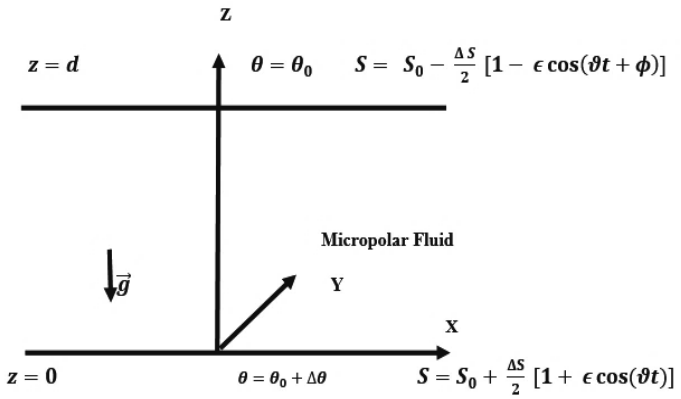

Fig. 1: Physical configuration.

The continuity equation, conservation of linear momentum, angular momentum, energy, solute concentration, and equation of state are (10, 21, 22):

$$\nabla.\vec{V} = 0, \tag{1}$$

$$\rho_0\left[\frac{\partial\vec{V}}{\partial t} + (\vec{V}\cdot\nabla)\vec{V}\right] = -\nabla p - \rho g\hat{k} + (2\zeta + \eta)\nabla^2\vec{V} + \zeta\nabla\times\vec{\omega}, \tag{2}$$

$$\rho_0 I\left[\frac{\partial\vec{\omega}}{\partial t} + (\vec{V}\cdot\nabla)\vec{\omega}\right] = (\lambda' + \eta')\nabla(\nabla\cdot\vec{\omega}) + \eta'\nabla^2\vec{\omega} + \zeta(\nabla\times\vec{V} - 2\vec{\omega}), \tag{3}$$

$$\frac{\partial\theta}{\partial t} + (\vec{V}\cdot\nabla)\theta = \frac{\beta}{\rho_0 C_v}(\nabla\times\vec{\omega})\cdot\nabla\theta + \chi\nabla^2\theta, \tag{4}$$

$$\frac{\partial S}{\partial t} + (\vec{V}\cdot\nabla)S = \chi_s\nabla^2 S \tag{5}$$

$$\rho = \rho_0[1 - \beta_t(\theta - \theta_0) + \beta_s(S - S_0)], \tag{6}$$

Time dependent concentration at the boundaries is considered as:

$$S(0,t) = S_0 + \frac{\Delta S}{2}[1 + \epsilon cos(\vartheta t)], \tag{7}$$

$$S(d,t) = S_0 - \frac{\Delta S}{2}[1 - \epsilon cos(\vartheta t + \phi)]. \tag{8}$$

We study two types of modulation in this paper namely: In-phase modulation (IPM) (ϕ=0) and Out-phase modulation (OPM) (ϕ= π).

The undisturbed state of the fluid is described by

$$\left.\begin{aligned} \overrightarrow{V_b} = (0,0,0), \overrightarrow{\omega_b} = (0,0,0), \theta = \theta_b(z), \\ \rho = \rho_b(z,t), S = S_b(z,t), p = p_b(z) \end{aligned}\right\}. \tag{9}$$

The basic state solutions are obtained by substituting equation (9) into equations (1)-(6):

$$\frac{\partial p_b}{\partial z} = -\rho_b g, \tag{10}$$

$$\frac{\partial^2 \theta_b}{\partial z^2} = 0, \tag{11}$$

$$\frac{\partial S_b}{\partial t} = \chi_s \nabla^2 S_b, \tag{12}$$

$$\rho_b = \rho_0[1 - \beta_t(\theta_b - \theta_0) + \beta_s(S_b - S_0)], \tag{13}$$

The solution of equations (11)-(12) that satisfy the boundary conditions are:

$$\theta_b = \theta_0 + \left(1 - \frac{z}{d}\right)\Delta\theta, \tag{14}$$

$$S_b = S_0 + \frac{\Delta S}{2}\left[1 - \frac{2z}{d}\right] + \epsilon Re\left[F(\lambda)e^{\frac{\lambda z}{d}} + F(-\lambda)e^{\frac{-\lambda z}{d}}\right]e^{-i\vartheta t} \tag{15}$$

where $\lambda = (1-i)\left(\frac{\vartheta d^2}{2\chi_s}\right)^{\left(\frac{1}{2}\right)}$, $F(\lambda) = \frac{\Delta S}{2}\left[\frac{e^{-i\phi} - e^{-\lambda}}{e^{\lambda} - e^{-\lambda}}\right]$ and Re stands for the real part.

The system is disturbed by a small quantity as defined below with primes indicating the disturbed quantity.

$$\left.\begin{aligned} \vec{V} = \overrightarrow{V_b} + \overrightarrow{V'}, \quad \vec{\omega} = \overrightarrow{\omega_b} + \overrightarrow{\omega'}, \quad p = p_b + p', \\ \rho = \rho_b + \rho', \quad \theta = \theta_b + \theta', \quad S = S_b + S' \end{aligned}\right\}, \tag{16}$$

Substituting equation (16) in equations (1)-(6) and using undisturbed state solution, eliminating the pressure, introducing the stream function in the form $u' = \frac{\partial \psi}{\partial z}$, $w' = -\frac{\partial \psi}{\partial x}$ and non-dimensionalizing by taking characteristic length as d, characteristic time as $\frac{d^2}{\chi}$, characteristic velocity as $\frac{\chi}{d}$, characteristic spin as $\frac{\chi}{d^2}$, characteristic temperature as $\Delta\theta$, and characteristic concentration as ΔS, we get the following dimensionless equation:

$$\frac{1}{Pr}\frac{\partial}{\partial t}(\nabla^2\psi) = -R\frac{\partial \theta}{\partial x} + R_s\frac{\partial S}{\partial x} + (1+N_1)\nabla^4\psi - N_1\nabla^2\omega_y + \frac{1}{Pr}J(\psi, \nabla^2\psi), \tag{17}$$

$$\frac{N_2}{Pr}\frac{\partial \omega_y}{\partial t} = N_1\nabla^2\psi - 2N_1\omega_y + N_3\nabla^2\omega_y + \frac{N_2}{Pr}J\big(\psi, \omega_y\big), \tag{18}$$

$$\frac{\partial \theta}{\partial t} = -\frac{\partial \psi}{\partial x} + \nabla^2\theta - N_5\frac{\partial \omega_y}{\partial x} + N_5 J\big(\omega_y, \theta\big) + J(\psi, \theta), \tag{19}$$

$$\frac{\partial S}{\partial t} = [-1 + \epsilon f]\frac{\partial \psi}{\partial x} + \Gamma\nabla^2 S + J(\psi, S), \tag{20}$$

where $f = Re\big[G(\lambda)e^{\lambda z} + G(-\lambda)e^{-\lambda z}\big]e^{-i\gamma t}$, $G(\lambda) = \frac{\lambda}{2}\left[\frac{e^{-i\phi} - e^{-\lambda}}{e^{\lambda} - e^{-\lambda}}\right]$, $\lambda = (1-i)\left(\frac{\gamma}{2}\right)^{\frac{1}{2}}$, $\gamma = \frac{\vartheta d^2}{\chi_s}$.

The non-dimensional parameters $Pr, R_s, R, N_1, N_2, N_3, N_5$ and Γ are as follows:

$$\left.\begin{array}{c} Pr = \frac{\zeta+\eta}{\rho_0\chi}, \quad R_s = \frac{\rho_0\beta_s g\Delta S d^3}{\chi(\zeta+\eta)}, \quad R = \frac{\rho_0\beta_t g\Delta\theta d^3}{\chi(\zeta+\eta)}, \quad N_1 = \frac{\zeta}{\zeta+\eta}, \\ N_2 = \frac{I}{d^2}, N_3 = \frac{\eta'}{(\zeta+\eta)d^2}, N_5 = \frac{\beta}{\rho_0 C_v d^2}, \Gamma = \frac{\chi_s}{\chi} \end{array}\right\}.$$

2.1 Linear Stability Analysis

Linearized versions of equations (17)-(20) are obtained by taking Jacobin equal to zero and eliminating S, θ and ω_y, we get:

$$\left.\begin{array}{l} \left\{\left(\frac{N_2}{Pr}\frac{\partial}{\partial t} + 2N_1 - N_3\nabla^2\right)\left(\frac{\partial}{\partial t} - \nabla^2\right)\left(\frac{\partial}{\partial t} - \Gamma\nabla^2\right)\left(\frac{1}{Pr}\frac{\partial}{\partial t} - (1+N_1)\nabla^2\right)\nabla^2\right. \\ \quad -\left(\frac{\partial}{\partial t} - \Gamma\nabla^2\right)\left(\frac{N_2}{Pr}\frac{\partial}{\partial t} + 2N_1 - N_3\nabla^2\right)R_s(-1+\epsilon f)\frac{\partial^2}{\partial x^2} \\ \quad \left.+\left(\frac{\partial}{\partial t} - \nabla^2\right)\left(\frac{\partial}{\partial t} - \Gamma\nabla^2\right)N_1^2\nabla^4\right\}\psi \\ = \left\{R\left(\frac{\partial}{\partial t} - \Gamma\nabla^2\right)\left[\left(\frac{N_2}{Pr}\frac{\partial}{\partial t} + 2N_1 - N_3\nabla^2\right)\frac{\partial^2}{\partial x^2} + N_1N_5\frac{\partial^2}{\partial x^2}(\nabla^2)\right]\right\}\psi \end{array}\right\}. \tag{21}$$

The boundary condition for solving equation (21) is in the form: see ((10, 21, 22))

$$\psi = \frac{\partial^2\psi}{\partial z^2} = \frac{\partial^4\psi}{\partial z^4} = \frac{\partial^6\psi}{\partial z^6} = \frac{\partial^8\psi}{\partial z^8} = 0 \qquad \text{at} \qquad z = 0, \quad z = 1. \tag{22}$$

Method of Solution

The equation (21) is solved by taking R and ψ in the series defined below,

$$(R, \psi) = (R_0, \psi_0) + \epsilon(R_1, \psi_1) + \epsilon^2(R_2, \psi_2) + \cdots \tag{23}$$

where R_0 represents Rayleigh number in the unmodulated case and $R_1, R_2,$ are correction to R_0.

Using equation (23) in equation (21) and comparing the corresponding powers of ϵ on both sides of resulting equation we get,

$$L\psi_0 = 0, \tag{24}$$

$$\left.\begin{aligned} L\psi_1 = \left[\left(\frac{N_2}{Pr}\frac{\partial}{\partial t} + 2N_1 - N_3\nabla^2\right)\left(\frac{\partial}{\partial t} - \nabla^2\right)\right] R_s f \frac{\partial^2\psi_0}{\partial x^2} + R_1\left(\frac{\partial}{\partial t} - \Gamma\nabla^2\right) \\ \left[\left(\frac{N_2}{Pr}\frac{\partial}{\partial t} + 2N_1 - N_3\nabla^2\right)\frac{\partial^2}{\partial x^2} + N_1N_5\frac{\partial^2}{\partial x^2}(\nabla^2)\right]\psi_0 \end{aligned}\right\}, \tag{25}$$

$$\left.\begin{aligned} L\psi_2 = \left[\left(\frac{\partial}{\partial t} - \Gamma\nabla^2\right)\left(\frac{N_2}{Pr}\frac{\partial}{\partial t} + 2N_1 - N_3\nabla^2\right)\frac{\partial^2}{\partial x^2} + N_1N_5\frac{\partial^2}{\partial x^2}(\nabla^2)\right] \\ (R_2\psi_0 + R_1\psi_1) + \left(\frac{N_2}{Pr}\frac{\partial}{\partial t} + 2N_1 - N_3\nabla^2\right)\left(\frac{\partial}{\partial t} - \nabla^2\right) R_s f \frac{\partial^2\psi_1}{\partial x^2} \end{aligned}\right\}. \tag{26}$$

where

$$\left.\begin{aligned} L = \left(\frac{N_2}{Pr}\frac{\partial}{\partial t} + 2N_1 - N_3\nabla^2\right)\left(\frac{\partial}{\partial t} - \nabla^2\right)\left(\frac{\partial}{\partial t} - \Gamma\nabla^2\right)\left(\frac{1}{Pr}\frac{\partial}{\partial t} - (1 + N_1)\nabla^2\right)\nabla^2 \\ + \left(\frac{N_2}{Pr}\frac{\partial}{\partial t} + 2N_1 - N_3\nabla^2\right)\left(\frac{\partial}{\partial t} - \nabla^2\right) R_s\frac{\partial^2}{\partial x^2} + \left(\frac{\partial}{\partial t} - \nabla^2\right)\left(\frac{\partial}{\partial t} - \Gamma\nabla^2\right) N_1^2\nabla^4 \\ -R_0\left(\frac{\partial}{\partial t} - \Gamma\nabla^2\right)\left[\left(\frac{N_2}{Pr}\frac{\partial}{\partial t} + 2N_1 - N_3\nabla^2\right)\frac{\partial^2}{\partial x^2} + N_1N_5\frac{\partial^2}{\partial x^2}(\nabla^2)\right] \end{aligned}\right\}, \tag{27}$$

Substituting $\psi_0 = sin(\pi\alpha x)sin(\pi z)$ in equation (24), we get R_0

$$R_0 = \frac{(2N_1 + N_3k^2)\left[-R_s\pi^2\alpha^2k^2 - (1+N_1)\Gamma k^8\right] + \Gamma k^8 N_1^2}{\Gamma k^2\pi^2\alpha^2[N_1N_5k^2 - (2N_1 + N_3k^2)]}. \tag{28}$$

The following limiting cases can be derived from equation (28) by keeping N_3, N_5 arbitrary and setting other parameters as shown in the table.

Parameters	Equation (28) reduces to
$N_1 = 0, R_s = 0$	Classical Bénard results
$N_1 = 0, R_s \neq 0$	Huppert and Turner (2)
$N_1 \neq 0, R_s = 0$	Siddheshwar and Pranesh (22)

Equation (25) using ψ_0 defined above reduces to

$$\left.\begin{aligned} L\psi_1 = -R_1\Gamma k^2\pi^2\alpha^2[2N_1 + N_3k^2 - N_1N_5k^2]\psi_0 \\ -(2N_1 + N_3k^2)R_sf\pi^2\alpha^2k^2\psi_0 \end{aligned}\right\}. \tag{29}$$

Following the analysis of Siddheshwar and Pranesh (22) we get $R_1 = R_3 = \cdots = 0$. The solution for ψ_1 is obtained by using Fourier series expansion for RHS of equation (29) and by inverting operator L.

$$\psi_1 = -R_s(2N_1 + N_3k^2)\pi^2\alpha^2k^2Re\sum\frac{B_n(\lambda)}{L(\gamma,n)}e^{-i\gamma t}sin(n\pi z), \tag{30}$$

where,

$$B_n(\lambda) = \frac{-2n\pi^2\lambda^2[e^{\lambda}-e^{-\lambda}+(-1)^n(e^{-\lambda-i\phi}-e^{\lambda-i\phi})]}{e^{\lambda}-e^{-\lambda}[\lambda^2+(n+1)^2\pi^2]},$$

$$L(\gamma,n) = Y_1 + iY_2,$$

$$\left.\begin{aligned} Y_1 = &\frac{-N_2\gamma^4k_n^2}{Pr^2} + \frac{N_2\gamma^2k_n^6\Gamma}{Pr} + \frac{N_2\gamma^2k_n^6\Gamma N_1}{Pr} + \frac{N_2\gamma^2k_n^6}{Pr} + \frac{N_2N_1\gamma^2k_n^6}{Pr} + \frac{N_2\gamma^2k_n^6\Gamma}{Pr^2} \\ &+2N_1\gamma^2k_n^4 + 2N_1^2\gamma^2k_n^4 + \frac{2N_1\gamma^2\Gamma k_n^4}{Pr} + \frac{2N_1\gamma^2k_n^4}{Pr} - 2N_1k_n^8\Gamma - 2N_1^2k_n^8\Gamma \\ &+N_3k_n^6\gamma^2 + N_3k_n^6\gamma^2N_1 + \frac{N_3k_n^6\gamma^2\Gamma}{Pr} + \frac{N_3k_n^6\gamma^2}{Pr} - N_3k_n^{10}\Gamma - N_3N_1k_n^{10}\Gamma \\ &+\frac{R_s\pi^2\alpha^2N_2\gamma^2}{Pr} - 2N_1k_n^2R_s\pi^2\alpha^2 - N_3k_n^4R_s\pi^2\alpha^2 - \gamma^2N_1^2k_n^4 + k_n^8\Gamma N_1^2 \\ &-\frac{R_0\gamma^2\pi^2\alpha^2N_2}{Pr} + 2N_1\pi^2\alpha^2\Gamma k_n^2R_0 + N_3k_n^4\Gamma R_0\pi^2\alpha^2 - \Gamma k_n^4R_0N_1N_5\pi^2\alpha^2 \end{aligned}\right\},$$

$$Y_2 = \left.\begin{aligned} &\frac{-N_2\gamma^3k_n^4}{Pr} - \frac{N_2\gamma^3N_1k_n^4}{Pr} - \frac{N_2\gamma^3k_n^4\Gamma}{Pr^2} - \frac{N_2\gamma^3k_n^4}{Pr^2} + \frac{N_2\gamma\Gamma k_n^8}{Pr} + \frac{N_2N_1\gamma k_n^8\Gamma}{Pr} \\ &-\frac{2N_1\gamma^3k_n^2}{Pr} + 2N_1\gamma\Gamma k_n^6 + 2N_1^2\gamma\Gamma k_n^6 + 2N_1\gamma k_n^6 + 2N_1^2\gamma k_n^6 + \frac{2N_1k_n^6\Gamma\gamma}{Pr} \\ &-\frac{N_3k_n^4\gamma^3}{Pr} + N_3k_n^8\gamma\Gamma + N_3N_1k_n^8\gamma\Gamma + N_3k_n^8\gamma + N_3N_1k_n^8\gamma + \frac{N_3k_n^8\Gamma\gamma}{Pr} \\ &+2N_1\gamma R_s\pi^2\alpha^2 + N_3k_n^2\gamma R_s\pi^2\alpha^2 + \frac{N_2k_n^2\gamma R_s\pi^2\alpha^2}{Pr} - \gamma\Gamma k_n^6N_1^2 - \gamma N_1^2k_n^6 \\ &-2R_0\gamma N_1\pi^2\alpha^2 - R_0\gamma N_3k_n^2\pi^2\alpha^2 + R_0\gamma N_1N_5\pi^2\alpha^2k_n^2 - \frac{\Gamma k_n^2R_0N_2\gamma\pi^2\alpha^2}{Pr} \end{aligned}\right\},$$

$$k_n^2 = (\pi^2\alpha^2 + n^2\pi^2).$$

The equation for ψ_2, then becomes

$$\left.\begin{aligned} L\psi_2 = R_2\Gamma k^2[N_1N_5k^2\pi^2\alpha^2 - \pi^2\alpha^2(2N_1 + N_3k^2)]\psi_0 \\ -R_s\pi^2\alpha^2 f\left(\frac{-N_2\gamma i}{Pr} + 2N_1 + N_3k_n^2\right)(-i\gamma + k_n^2)\psi_1 \end{aligned}\right\}, \tag{31}$$

The time-independent part of the RHS of equation (31) has to be orthogonal to sinπz in order to satisfy the solvability condition. We will not solve equation (31), but we use the solvability condition and get an expression for R_2 as:

$$R_2 = \frac{2R_s\left(\frac{-N_2i\gamma}{Pr} + 2N_1 + N_3k^2\right)(-i\gamma + k_n^2)}{\Gamma k^2[N_1N_5k^2 - (2N_1 + N_3k^2)]}\int_0^1 \overline{f\psi_1}\sin(\pi z)dz, \tag{32}$$

where overbar denotes the time average.

Using equation (29) and on simplifying we get an expression for critical correction Rayleigh number as,

$$R_{2c} = -\frac{R_S^2\pi^2\alpha^2(2N_1 + N_3k^2)}{2\Gamma[N_1N_5k^2 - (2N_1 + N_3k^2)]}\sum_{n=1}^{\infty}|B_n(\lambda)|^2|X_1|^2\left[\frac{L_1(\gamma,n) + L_1^*(\gamma,n)}{2|L_1|^2}\right], \tag{33}$$

where $X_1 = \left(2N_1 + N_3k_n^2 - i\,N_2\,\frac{\gamma}{Pr}\right)\,(-i\,\gamma\,+\,k_n^2)$, $L_1(\gamma,n) = A_1^*\,L(\gamma,n), X_1^*$ and $L_1(\gamma,n)^*$ are the conjugates of X_1 and $L_1(\gamma,n)$.

Minimum Solute Rayleigh Number for Convection:

The expression for R_{2c} in equation (33) represents a correction to critical Rayleigh number R_{0c} of order ϵ^2. R_{2c} is evaluated for in-phase and out of phase modulation with $B_n(\lambda)$.

Modulation		n
In-phase	$b_n = -\frac{4n\pi^2\lambda^2}{[\lambda^2+(n+1)^2\pi^2][\lambda^2+(n-1)^2\pi^2]}$	Even
	0	Odd
Out-phase	0	Even
	$b_n = -\frac{4n\pi^2\lambda^2}{[\lambda^2+(n+1)^2\pi^2][\lambda^2+(n-1)^2\pi^2]}$	Odd

2.2 Non-Linear Analysis

The non-linear analysis is performed by considering the Fourier series representation of ψ, $\omega_{y,}\theta$ and S to understand the amount of heat and mass transfer. The finite-amplitude convection of the truncated system is given by:

$$\psi(x,z,t) = A_1(t)\, sin(\pi\alpha x)\, sin(\pi z), \tag{34}$$

$$\omega_y(x,z,t) = A_2(t) sin(\pi\alpha x) sin(\pi z), \tag{35}$$

$$\theta(x,z,t) = A_3(t) cos(\pi\alpha x) sin(\pi z) + A_4(t) sin(2\pi z), \tag{36}$$

$$S(x,z,t) = A_5(t) cos(\pi\alpha x) sin(\pi z) + A_6(t) sin(2\pi z), \tag{37}$$

where A_1, A_2, A_3, A_4, A_5 and A_6 are obtained from the dynamics of the system. The x-the independent term is missing in functions ψ and ω_y due to the discount of the spontaneous generation of large-scale flow.

Using equations (34) – (37) into equations (17) – (20) we get the following system of equations.

$$\dot{A_1} = -\frac{R\pi\alpha Pr}{k^2}A_3 + \frac{R_s\pi\alpha Pr}{k^2}A_5 - (1+N_1)Prk^2A_1 - N_1PrA_2, \tag{38}$$

$$\dot{A_2} = \frac{-N_1Prk^2}{N_2}A_1 - \frac{2N_1Pr}{N_2}A_2 - \frac{N_3Prk^2}{N_2}A_2, \tag{39}$$

$$\dot{A_3} = -\pi\alpha A_1 - k^2A_3 - N_5\pi\alpha A_2 - \pi^2\alpha A_1A_4 - N_5\pi^2\alpha A_2A_4, \tag{40}$$

$$\dot{A_4} = -4\pi^2A_4 + \frac{N_5\pi^2\alpha}{2}A_2A_3 + \frac{\pi^2\alpha}{2}A_1A_3, \tag{41}$$

$$\dot{A_5} = (-1+\epsilon f)\pi\alpha A_1 - \Gamma k^2A_5 - \pi^2\alpha A_1A_6, \tag{42}$$

$$\dot{A_6} = -4\Gamma\pi^2A_4 + \frac{\pi^2\alpha}{2}A_1A_5, \tag{43}$$

where, over dot denotes time derivative.

The regular perturbation expansion given below is used in the equations (38)–(43):

$$\begin{pmatrix} A_1 \\ A_2 \\ A_3 \\ A_4 \\ A_5 \\ A_6 \\ R \end{pmatrix} = \begin{pmatrix} 0 \\ 0 \\ 0 \\ 0 \\ 0 \\ 0 \\ R_0 \end{pmatrix} + \delta \begin{pmatrix} A_{11} \\ A_{21} \\ A_{31} \\ A_{41} \\ A_{51} \\ A_{61} \\ R_1 \end{pmatrix} + \delta^2 \begin{pmatrix} A_{12} \\ A_{22} \\ A_{32} \\ A_{42} \\ A_{52} \\ A_{62} \\ R_2 \end{pmatrix} + \delta^3 \begin{pmatrix} A_{13} \\ A_{23} \\ A_{33} \\ A_{43} \\ A_{53} \\ A_{63} \\ R_3 \end{pmatrix} + \ldots \tag{44}$$

where $t = \delta^2 t, \epsilon = \delta^2 \epsilon_1$.

Let us now take

$$\mathcal{L} = \begin{pmatrix} -(1+N_1)Prk^2 & -N_1 Pr & \frac{-R_0 Pr\pi\alpha}{k^2} & 0 & \frac{R_S Pr\pi\alpha}{k^2} & 0 \\ -\frac{N_1}{N_2}Prk^2 & -\frac{Pr(2N_1+N_3k^2)}{N_2} & 0 & 0 & 0 & 0 \\ -\pi\,\alpha & -N_5\pi\alpha & -k^2 & 0 & 0 & 0 \\ 0 & 0 & 0 & -4\pi^2 & 0 & 0 \\ -\pi\,\alpha & 0 & 0 & 0 & -\Gamma k^2 & 0 \\ 0 & 0 & 0 & 0 & 0 & -4\Gamma\pi^2 \end{pmatrix}$$

$$Z_i = (A_{1i}, A_{2i}, A_{3i}, A_{4i}, A_{5i}, A_{6i})^T \qquad i = 1,2,3$$

Substituting equation (44) in equations (38)-(43) and on comparing the coefficients of δ, δ^2 and δ^3 on both sides, we get:

First-order system:

$$\mathcal{L}Z_1 = 0, \tag{45}$$

Second-order system:

$$\mathcal{L}Z_2 = (R_{21} \quad R_{22} \quad R_{23} \quad R_{24} \quad R_{25} \quad R_{26})^T, \tag{46}$$

Third-order system:

$$\mathcal{L}Z_3 = (R_{31} \quad R_{32} \quad R_{33} \quad R_{34} \quad R_{35} \quad R_{36})^T, \tag{47}$$

where,

$$R_{21} = \frac{R_1\pi\alpha Pr}{k^2}A_{31}, R_{22} = 0, R_{23} = \pi^2\alpha A_{11}A_{41} + N_5\pi^2\alpha A_{21}A_{41},$$

$$R_{24} = \frac{-N_5\pi^2\alpha}{2}A_{21}A_{31} - \frac{\pi^2\alpha}{2}A_{11}A_{31},\ R_{25} = \pi^2\alpha A_{11}A_{61},\ R_{26} = \frac{-\pi^2\alpha}{2}A_{11}A_{51},$$
$$R_{31} = \frac{dA_{11}}{dt} + \frac{R_1 Pr\pi\alpha}{k^2}A_{32} + \frac{R_2 Pr\pi\alpha}{k^2}A_{31},\ R_{32} = \frac{dA_{21}}{dt},$$

$$R_{33} = \frac{dA_{31}}{dt} + \pi^2\alpha(A_{11}A_{42} + A_{12}A_{41}) + N_5\pi^2\alpha(A_{22}A_{41} + A_{21}A_{42}),$$

$$R_{34} = \frac{dA_{41}}{dt} - \frac{\pi^2\alpha}{2}(A_{11}A_{32} + A_{12}A_{31}) - \frac{N_5\pi^2\alpha}{2}(A_{21}A_{32} + A_{22}A_{31}),$$

$$R_{35} = \frac{dA_{51}}{dt} - \epsilon_1 f\pi\alpha A_{11} + \pi^2\alpha[A_{11}A_{62} + A_{12}A_{61}],$$

$$R_{36} = \frac{dA_{61}}{dt} - \frac{\pi^2\alpha}{2}(A_{11}A_{52} + A_{12}A_{51}),$$

The solution of the first and second-order systems is given by:

$$Z_1^T = \left(A_{10} \quad \frac{-N_1k^2}{2N_1 + N_3k^2}A_{10} \quad \frac{-\pi\alpha}{k^2}A_{10} + \frac{N_1N_5\pi\alpha}{2N_1 + N_3k^2}A_{10} \quad 0 \quad \frac{-\pi\alpha}{\Gamma k^2}A_{10} \quad 0\right)^T$$

$$Z_2^T = \begin{pmatrix} A_{20} \\ \frac{-N_1k^2}{2N_1 + N_3k^2}A_{20} \\ \frac{N_1N_5\pi\alpha}{2N_1 + N_3k^2}A_{20} - \frac{\pi\alpha}{k^2}A_{20} \\ \frac{N_1N_5\pi\alpha^2}{4(2N_1 + N_3k^2)}A_{10}^2 - \frac{N_1^2N_5^2\pi\alpha^2k^2}{8(2N_1 + N_3k^2)^2}A_{10}^2 - \frac{\pi\alpha}{8k^2}A_{10}^2 \\ \frac{-\pi\alpha}{\Gamma k^2}A_{20} \\ \frac{\pi\alpha^2}{8\Gamma^2k^2}A_{10}^2 \end{pmatrix}$$

where A_{10} and A_{20} denotes the arbitrary functions of t and superscript T denotes transpose. Considering the Fredholm solvability condition of the form:

$$\sum_{j=1}^{6} R_{ij}\widehat{Z_1} = 0, \quad (i = 2,3) \tag{48}$$

where $\widehat{Z_1}$ refers to the solution of the adjoint system of equation (45). When $i = 2$ and $i = 3$ we get $R_1 = 0$ and Ginzburg-Landau equation in the form:

$$\frac{dA_{10}}{dt} + \frac{Q_2}{Q_1} A_{10} + \frac{Q_3}{Q_1} A_{10}^3 = 0, \tag{49}$$

where,

$$Q_1 = 1 + \frac{N_1^2 k^4}{(2N_1 + N_3 k^2)^2} + \frac{\pi^2 \alpha^2}{\Gamma^2 k^4} + \frac{\pi^2 \alpha^2}{k^4} - \frac{2N_1 N_5 \pi^2 \alpha^2}{k^2 (2N_1 + N_3 k^2)} + \frac{N_1^2 N_5^2 \pi^2 \alpha^2}{(2N_1 + N_3 k^2)^2},$$

$$Q_2 = \frac{-R_2 \pi^2 \alpha^2 Pr}{k^4} + \frac{R_2 \pi^2 \alpha^2 Pr N_1 N_5}{k^2 (2N_1 + N_3 k^2)} + \frac{\epsilon_1 f \pi^2 \alpha^2}{\Gamma k^2},$$

$$Q_3 = \left.\begin{aligned} &\frac{\pi^4 \alpha^4}{8k^4}\left(1 + \frac{1}{\Gamma^3}\right) - \frac{N_1 N_5 \pi^4 \alpha^4}{2k^2 (2N_1 + N_3 k^2)} + \frac{3N_1^2 N_5^2 \pi^4 \alpha^4}{4(2N_1 + N_3 k^2)^2} \\ &- \frac{N_1^3 N_5^3 \pi^4 \alpha^4 k^2}{2(2N_1 + N_3 k^2)^3} + \frac{N_1^4 N_5^4 \pi^4 \alpha^4 k^4}{8(2N_1 + N_3 k^2)^4} \end{aligned}\right\}.$$

Equation (49) is solved to get A_{10}.

Heat and Mass Transport at Lower Boundary

The expression for Nusselt number, Nu, and Sherwood number, Sh, which quantifies the amount of heat and mass transfer is given by

$$Nu = \frac{\left[\frac{k}{2\pi}\int_0^{\frac{2\pi}{k}} (1 - z + \theta)_z dx\right]_{z=0}}{\left[\frac{k}{2\pi}\int_0^{\frac{2\pi}{k}} (1 - z)_z dx\right]_{z=0}}, \tag{50}$$

$$Sh = \frac{\left[\frac{k}{2\pi}\int_0^{\frac{2\pi}{k}} (1 - z + S)_z dx\right]_{z=0}}{\left[\frac{k}{2\pi}\int_0^{\frac{2\pi}{k}} (1 - z)_z dx\right]_{z=0}}, \tag{51}$$

Using equation (36) and (37) in equations (50) and (51) we get

$$Nu = 1 - 2\pi A_4 = 1 - 2\pi\epsilon^2 \left[\frac{N_1 N_5 \pi \alpha^2}{4(2N_1 + N_3 k^2)} A_{10}^2 - \frac{N_1^2 N_5^2 \pi \alpha^2 k^2}{8(2N_1 + N_3 k^2)^2} A_{10}^2 - \frac{\pi \alpha}{8k^2} A_{10}^2\right], \tag{52}$$

$$Sh = 1 - 2\pi A_6 = 1 + \epsilon^2 \frac{2\pi^2 \alpha^2}{8k^2} A_{10}^2, \tag{53}$$

3 Results and Discussion

The effect of concentration modulation on DDC in a micropolar fluid is investigated using linear and non-linear analyses. It is clear from equation (7) and (8) that

concentration at the lower plate is higher than the concentration at the upper plate and also concentration profile explicitly depends on position and time. The expression for the critical Rayleigh number and the correction Rayleigh number is obtained as a function of $N_1, N_2, N_3, N_5, R_s, \Gamma$ and Pr using regular perturbation procedure. In the present analysis we have chosen moderate values of γ as γ is small, period of modulation is very large and as $\gamma \to \infty$ the modulation effects become zero.

The sign of R_{2c} characterizes the stability effect of modulation. The modulation stabilizes the system when $R_{2c} > 0$ and destabilizes the system when $R_{2c} < 0$. The effects of IPM and OPM on R_{2c} is studied in this paper. The result for linear analysis is depicted in figures (2)-(8).

Figures 2(a)-8(a) depicts the variation of R_{2c} with γ for different values of parameters $N_1, N_2, N_3, N_5, Pr, R_s$ and Γ for IPM. From these figures, we observe that when γ is very small $R_{2c} < 0$ indicating for a small frequency of modulation destabilizes the system, for moderate values $R_{2c} > 0$ indicating modulation effect is stabilizing and for large value $R_{2c} = 0$, thus the modulation disappears.

From figures 2(a)-8(a) following observations are made:

- Increase in N_1 increases R_{2c} negatively, when N_1 increases concentration of microparticles increases and this particle consumes more and more energy, therefore the onset of convection is advanced, Hence in IPM N_1 destabilizes the system.
- From equation (28) it is clear that R_{0c} is independent of N_2 but it appears in R_{2c} due to acceleration term, hence the effect of N_2 on R_{2c} is negligible.
- N_3 represents the couple stress in angular momentum conservation. As N_3 increases, R_{2c} decreases negatively and thereby stabilizes the system.
- Increase in N_5 increases the heat-induced into the system, thus for IPM in the general increase in N_5 increases R_{2c} negatively and destabilizes the system.
- Pr is the ratio of the viscous force and thermal force. Increase in Pr increases R_{2c} negatively and thereby destabilizes the system.
- Increase in solutal Rayleigh number increases, R_{2c} becomes negatively, therefore R_s destabilizes the system.
- Increase in diffusivity ratio increases R_{2c} negatively in general for IPM, therefore Γ stabilizes the system.

We now discuss the results obtained for OPM. Comparing the figures (2(b)) – (8(b)) respectively with figures (2(a)) – (8(a)), we found that $R_{2c} > 0$ for all values of γ, whereas in IPM $R_{2c} < 0$ in general. This is due to the fact that the concentration field in OPM has a linear gradient varying with time, so that Rayleigh number is subcritical during one-half cycle and in other half cycles. The effects of the parameters $N_1, N_2, N_3, N_5, Pr, R_s$ and Γ is reversed in OPM when compared to IPM. It is important to that note for small values of γ, N_3 and R_s have opposite effects.

We now discuss the results obtained for non-linear analysis. It is well-known fact that linear theory gives the condition for the onset of convection and it fails to

explain the heat and mass transfer. Therefore, the non-linear analysis is a must to explain the heat and mass transfer. Heat and Mass transfer in this paper are analyzed by computing Nusselt number, Nu and Sherwood number, Sh.

A non-linear analysis is studied by deriving the sixth order Lorenz model. The multimode method is used to convert the sixth order non-autonomous Lorenz model to an analytically solvable Ginzburg-Landau equation in terms of amplitude A_{10} and then obtained as an expression for Nusselt and Sherwood number as a function of amplitude A_{10}.

Figures (9(a)) -(15(a)) and figures (16(a)) -(22(a)) are the plots of Nu and Sh versus t for IPM. Figures (9(b)) -(15(b)) and figures (16(b)) -(22(b)) are the graphs of Nu and Sh, versus t for OPM. Figures (9(b)) -(22(b)) are oscillatory in nature because of OPM at both the boundaries. The following observations are made from figures (9)-(21) which is true for both IPM and OPM.

- Increase in N_1, decreases Nu and increases Sh. When N_1 increases, particle concentration increases thus decreases heat transfer and increases mass transfer.
- Effect of N_2 on Nu and Sh is not found, because N_2 does not affect R_c as explained earlier.
- Increase in N_3, decreases Sh and increases Nu, thus increases heat transfer and decreases mass transfer.
- Increase in N_5, decreases Nu and increases Sh, thus increases mass transfer and decreases heat transfer.
- Increase in R_s, Γ and Pr, increases the Nu and Sh number, thus the heat and mass transfer increases.

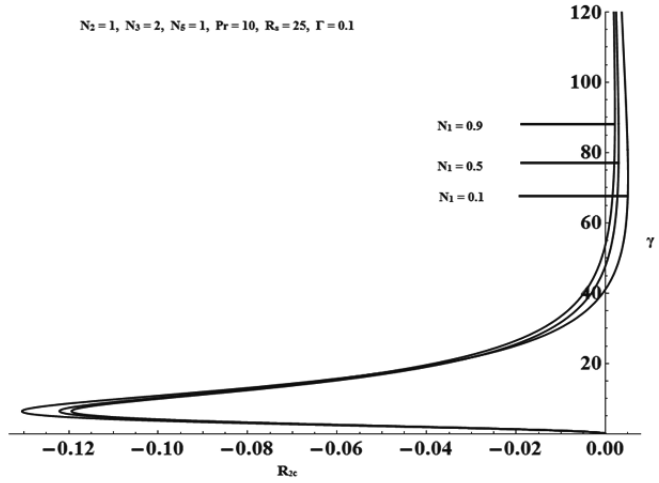

(a)

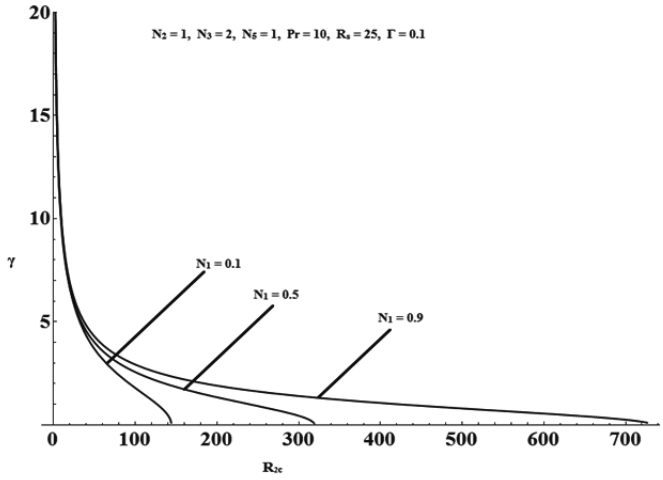

(b)

Fig. 2: Variation of R_{2c} with γ for different values of N_1 in (a) IPM and (b) OPM.

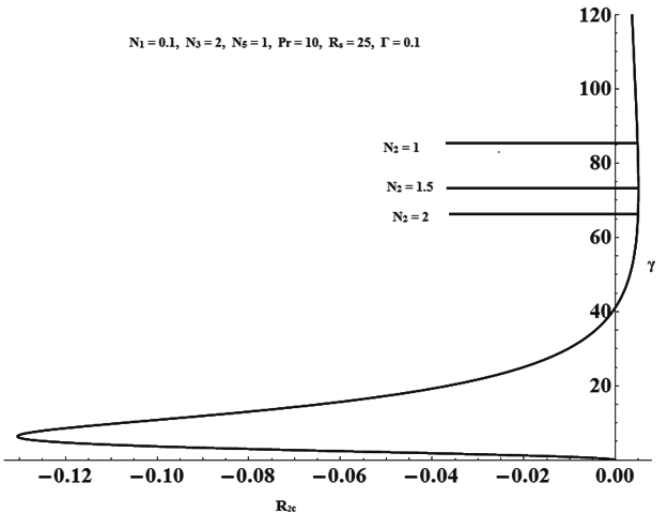

(a)

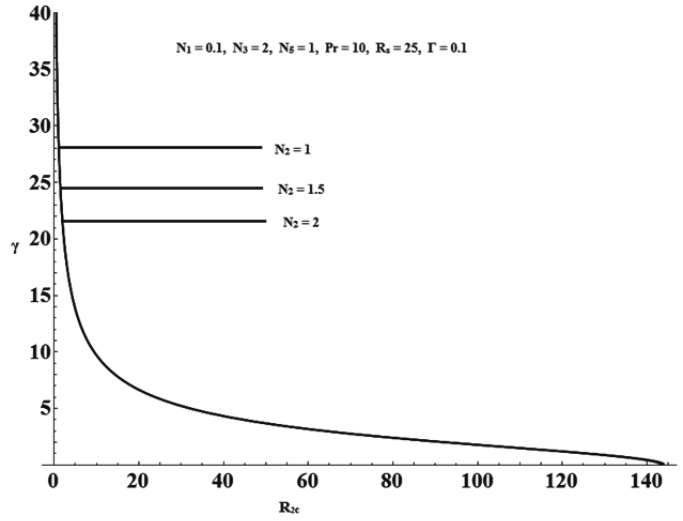

(b)

Fig. 3: Variation of R_{2c} with γ for different values of N_2 in (a) IPM and (b) OPM.

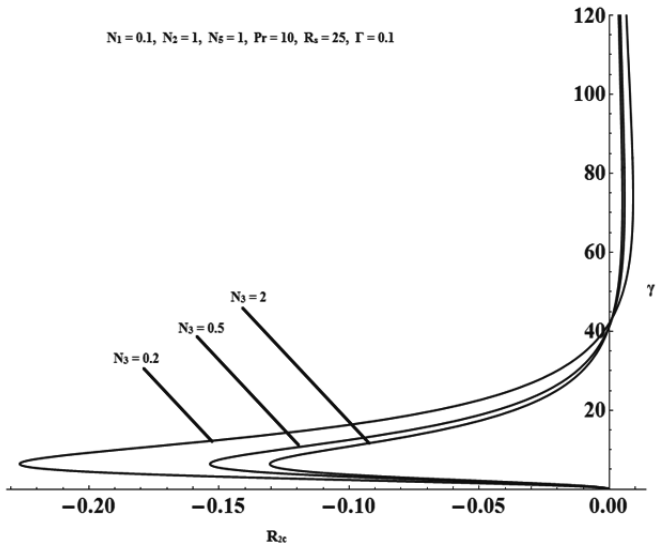

(a)

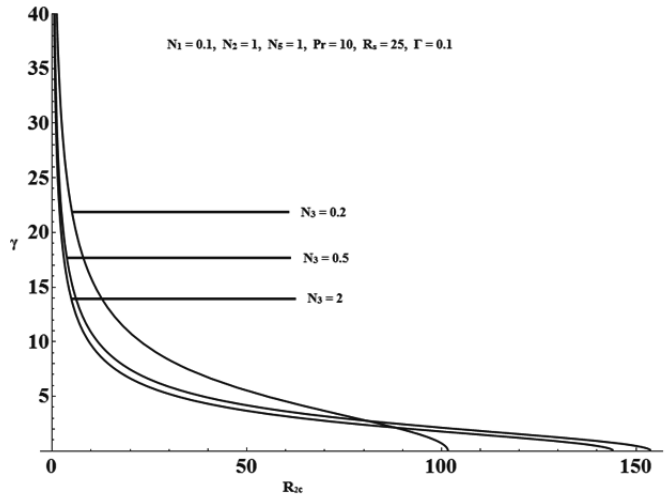

(b)

Fig. 4: Variation of R_{2c} with γ for different values of N_3 in (a) IPM and (b) OPM.

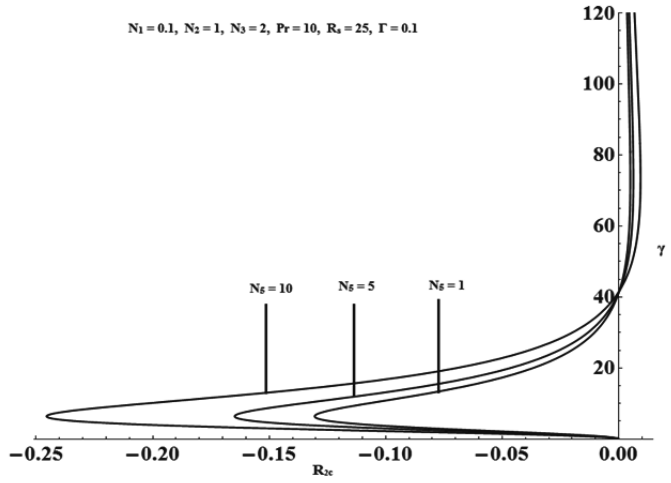

(a)

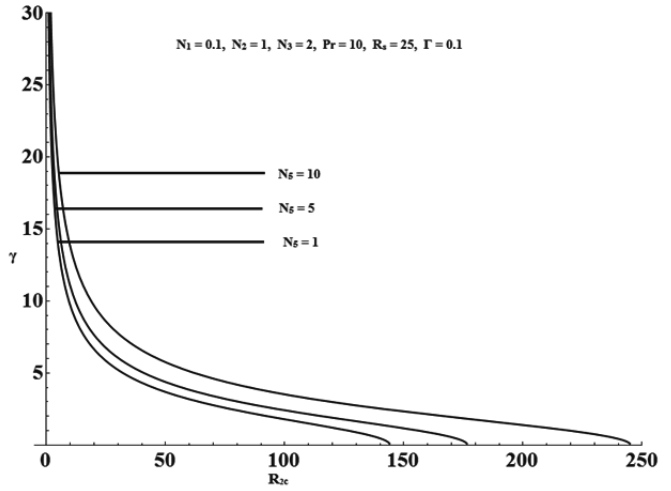

(b)

Fig. 5: Variation of R_{2c} with γ for different values of N_5 in (a) IPM and (b) OPM.

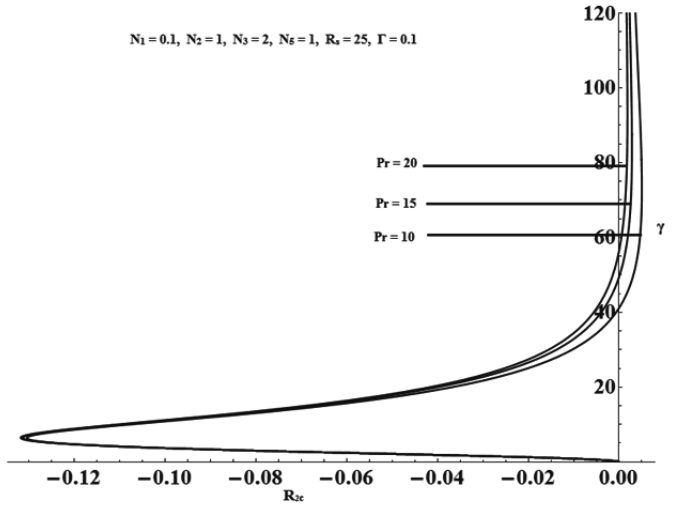

(a)

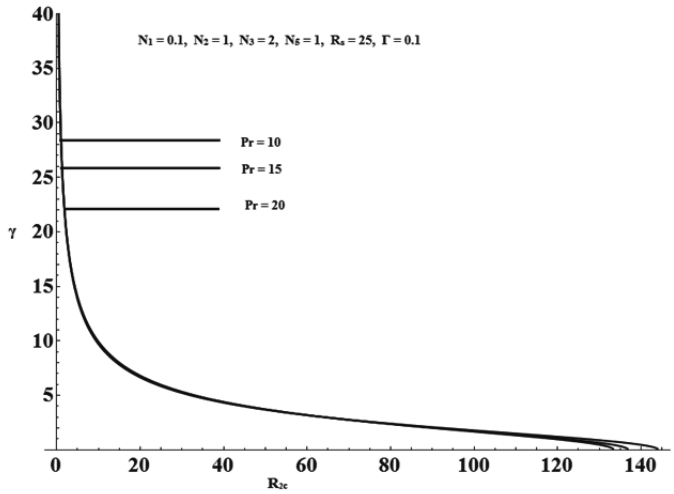

(b)

Fig. 6: Variation of R_{2c} with γ for different values of Pr in (a) IPM and (b) OPM.

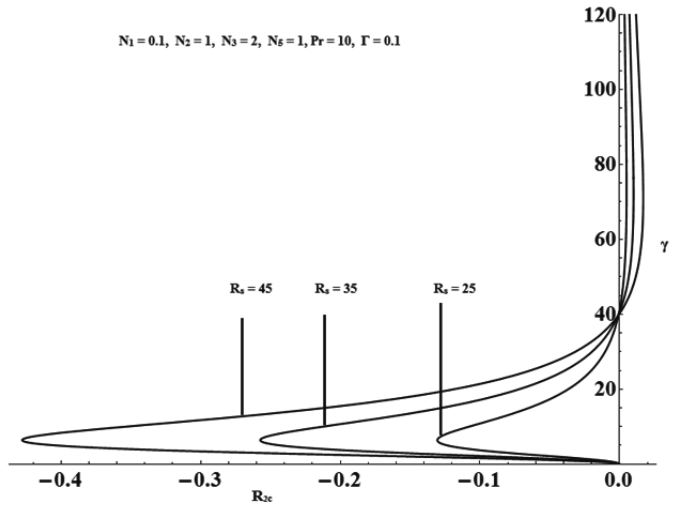

(a)

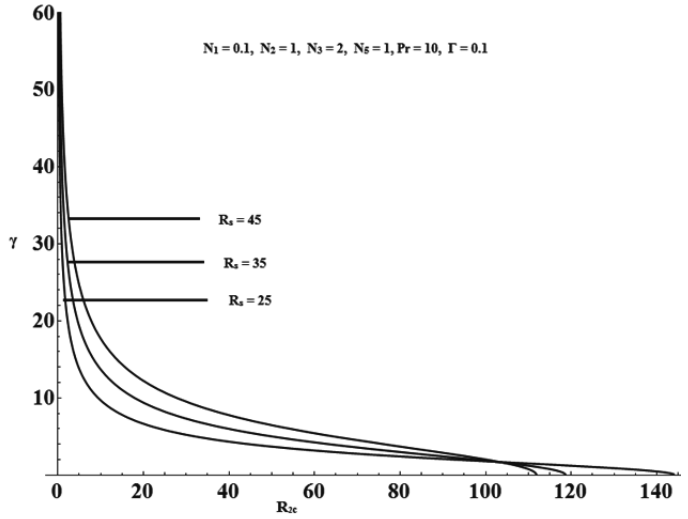

(b)

Fig. 7: Variation of R_{2c} with γ for different values of R_s in (a) IPM and (b) OPM.

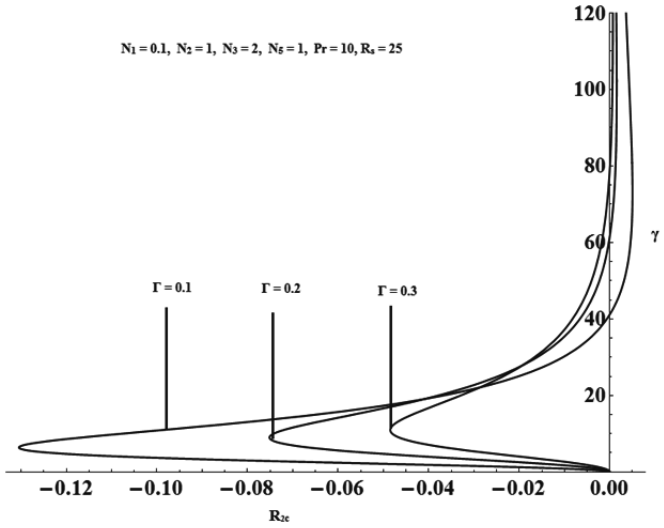

(a)

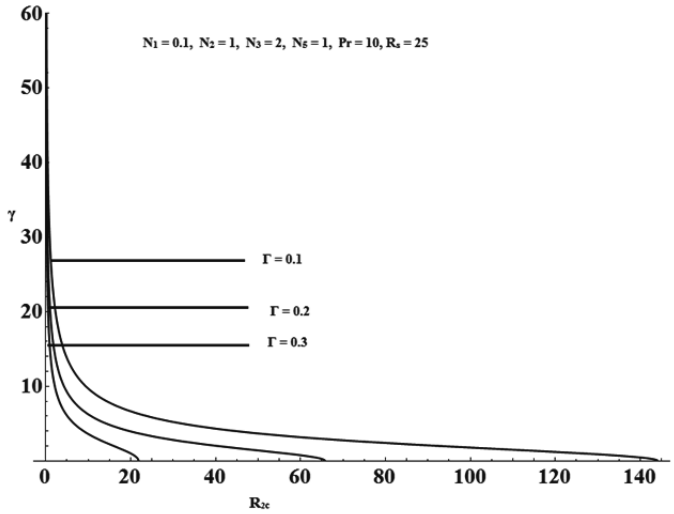

(b)

Fig. 8: Variation of R_{2c} with γ for different values of Γ in (a) IPM and (b) OPM.

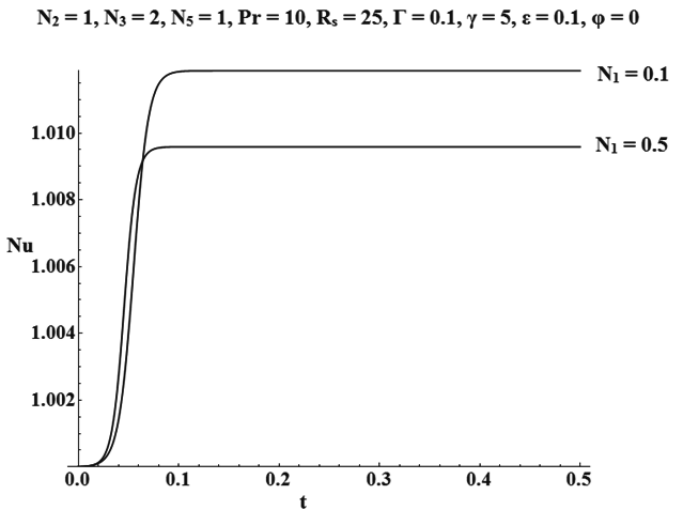

(a)

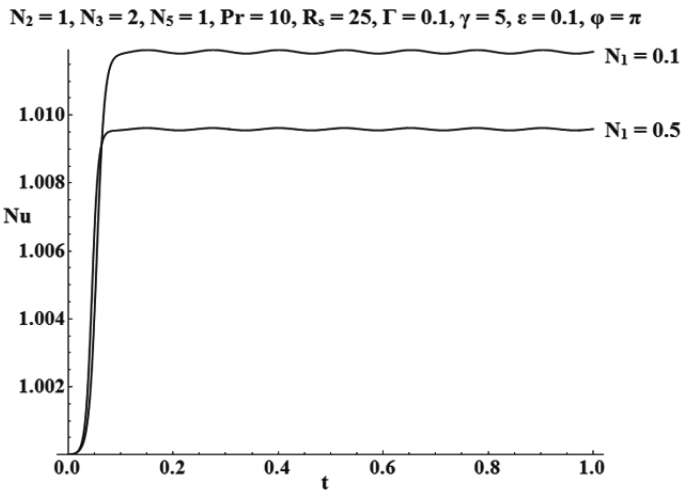

(b)

Fig. 9: Variation of Nu with t for different values of N_1 in (a) IPM and (b) OPM.

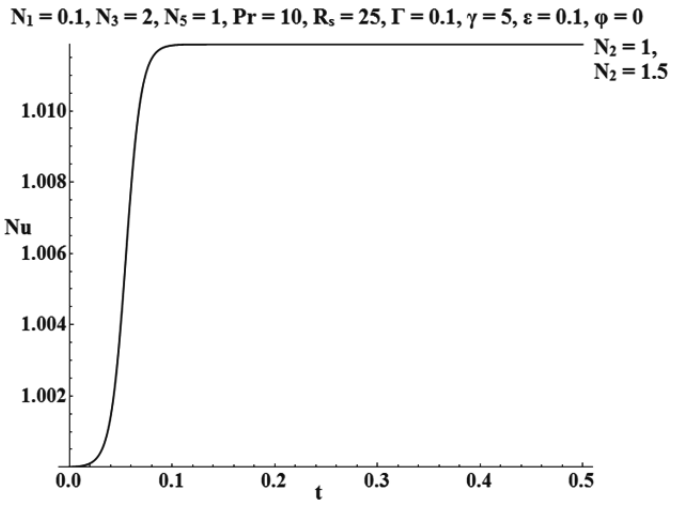

(a)

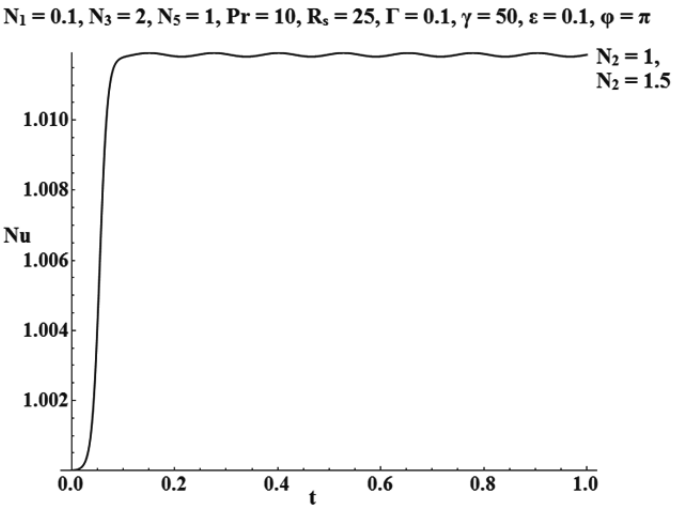

(b)

Fig. 10: Variation of Nu with t for different values of N_2 in (a) IPM and (b) OPM.

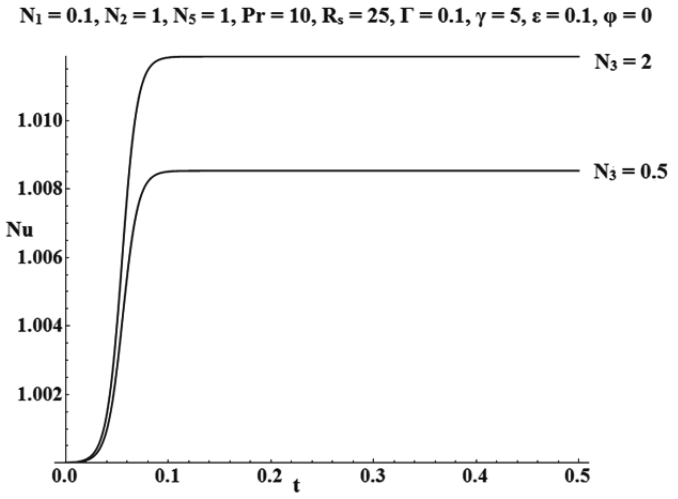

(a)

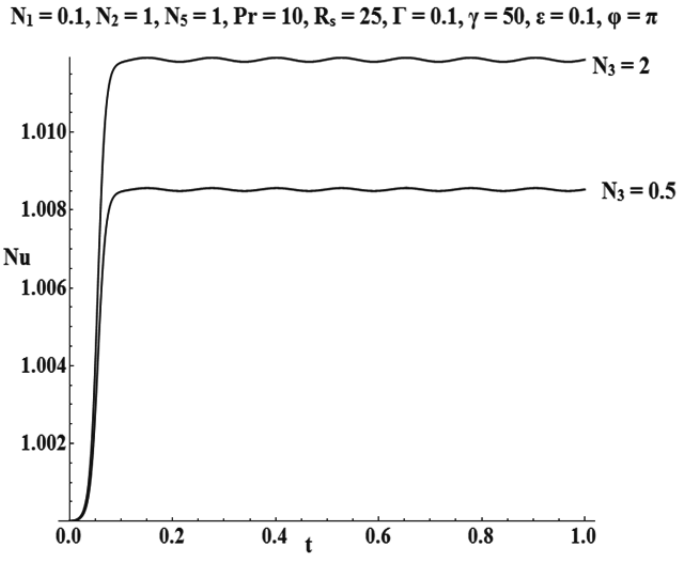

(b)

Fig. 11: Variation of Nu with t for different values of N_3 in (a) IPM and (b) OPM.

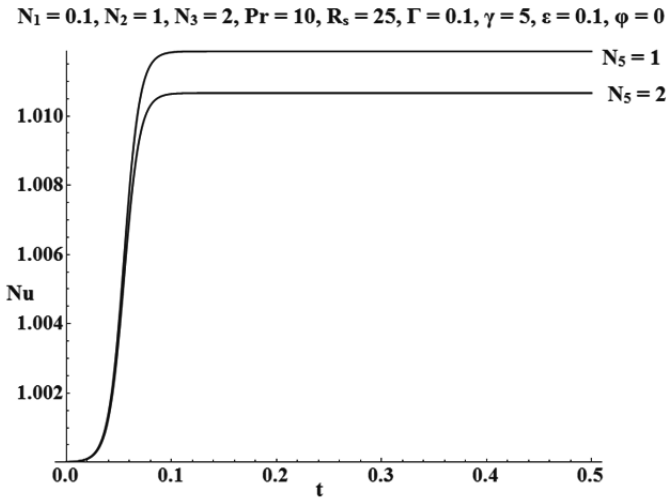

(a)

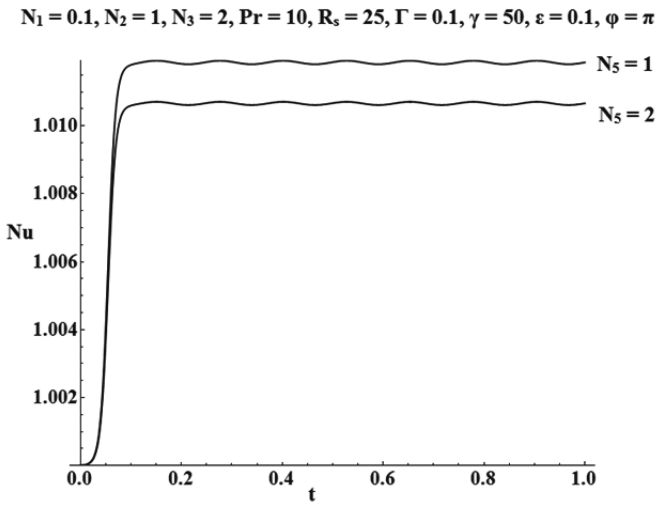

(b)

Fig. 12: Variation of Nu with t for different values of N_5 in (a) IPM and (b) OPM.

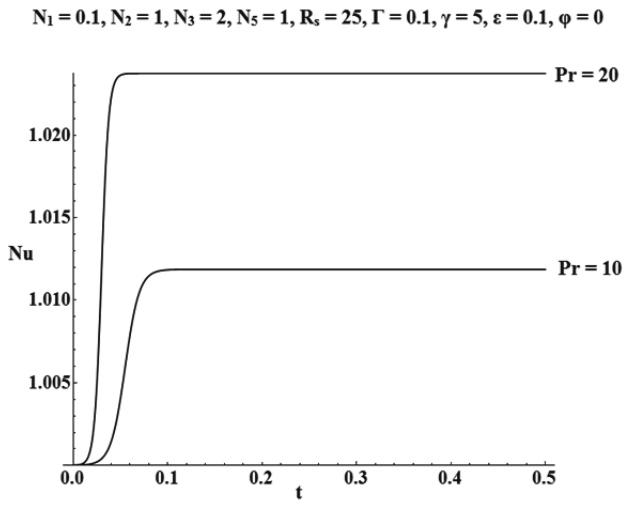

(a)

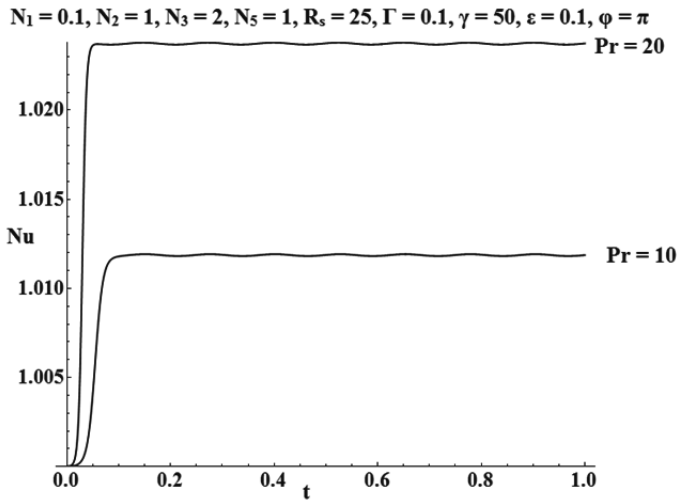

(b)

Fig. 13: Variation of Nu with t for different values of Pr in (a) IPM and (b) OPM.

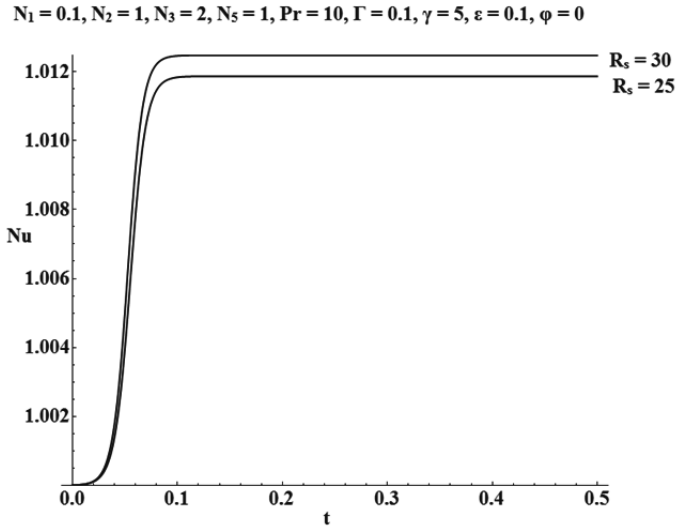

(a)

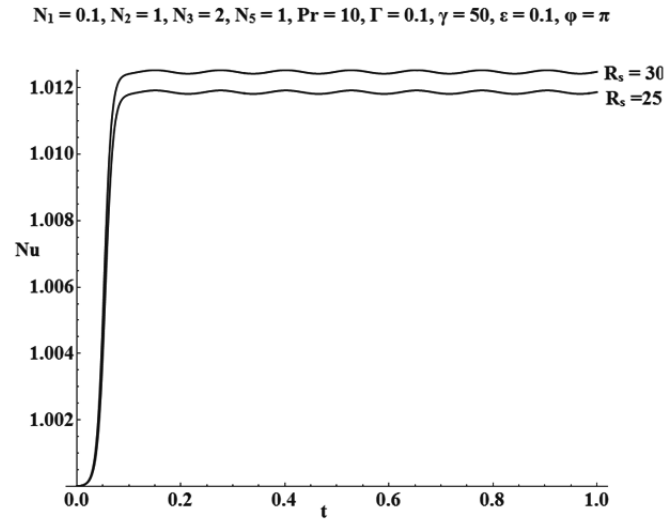

(b)

Fig. 14: Variation of Nu with t for different values of R_s in (a) IPM and (b) OPM.

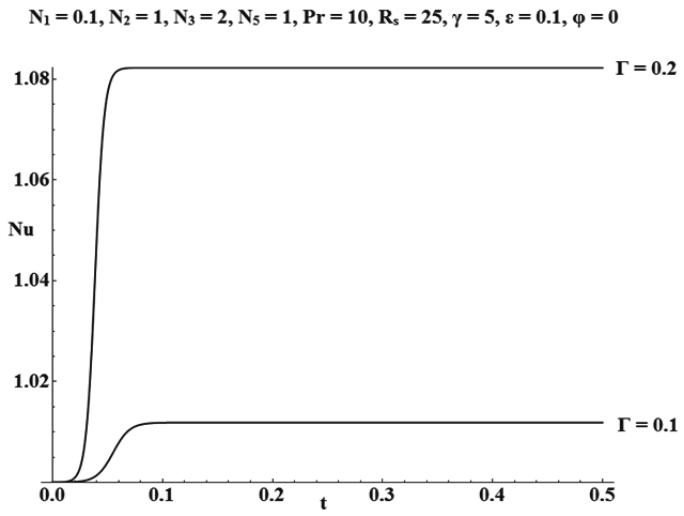

(a)

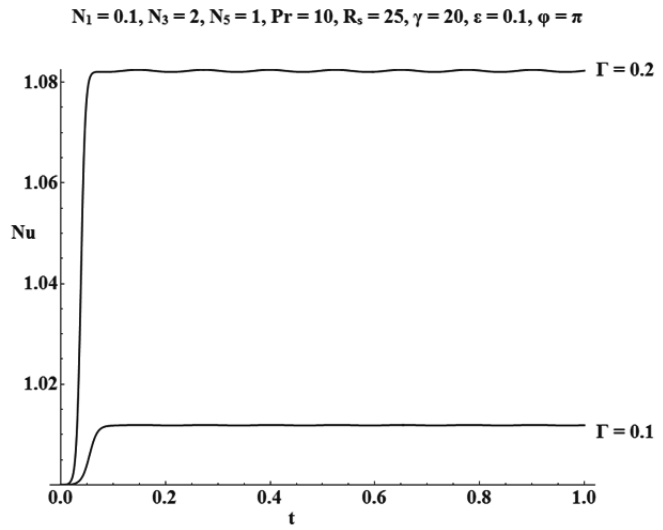

(b)

Fig. 15: Variation of Nu with t for different values of Γ in (a) IPM and (b) OPM.

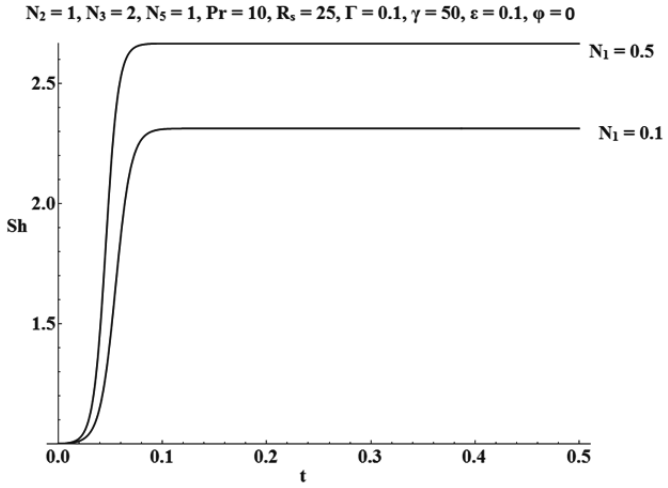

(a)

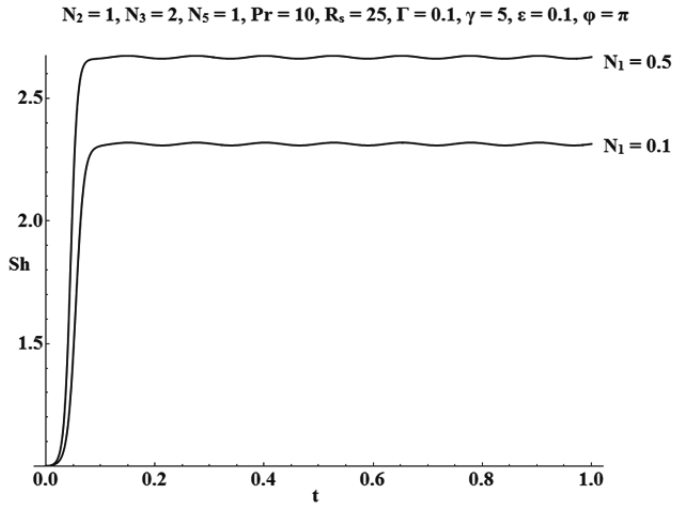

(b)

Fig. 16: Variation of Sh with t for different values of N_1 in (a) IPM and (b) OPM.

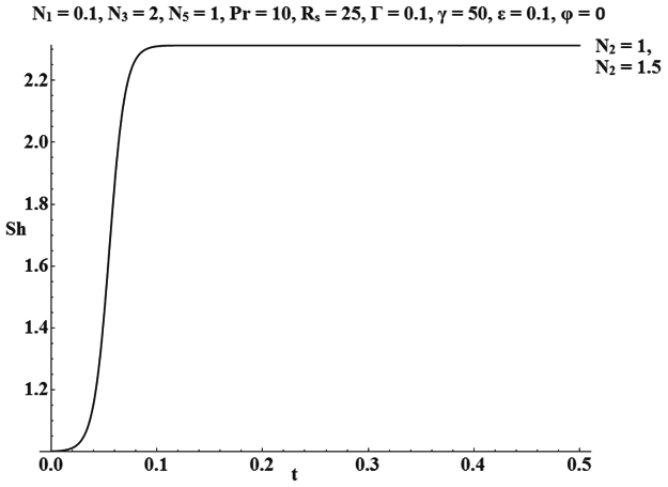

(a)

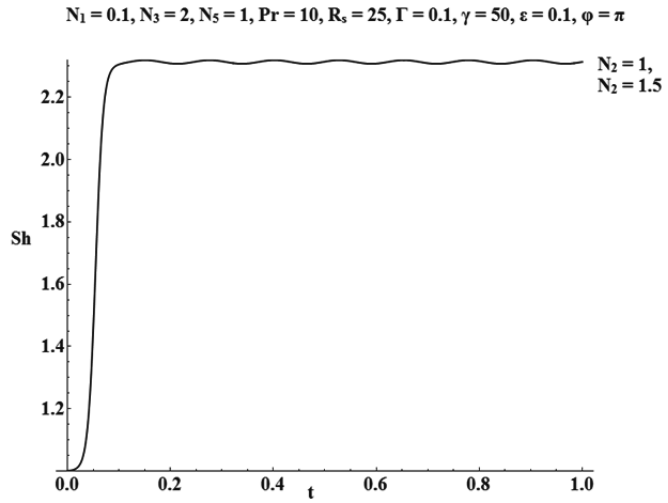

(b)

Fig. 17: Variation of Sh with t for different values of N_2 in (a) IPM and (b) OPM.

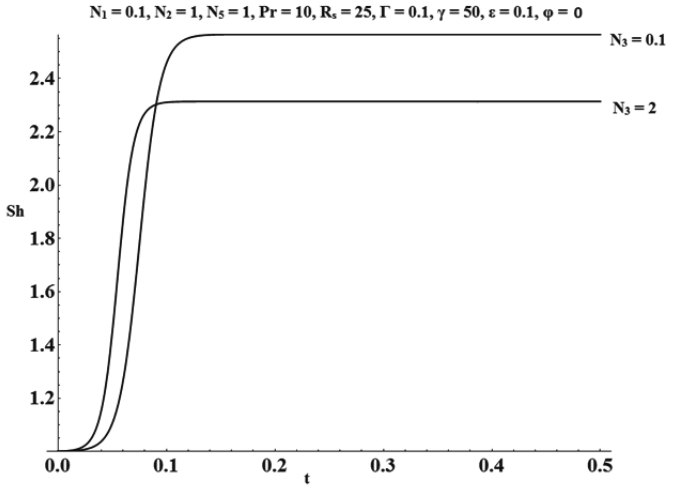

(a)

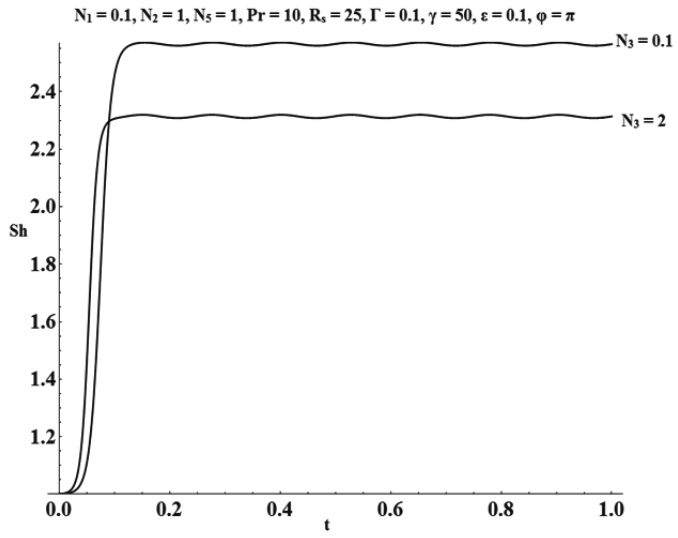

(b)

Fig. 18: Variation of Sh with t for different values of N_3 in (a) IPM and (b) OPM.

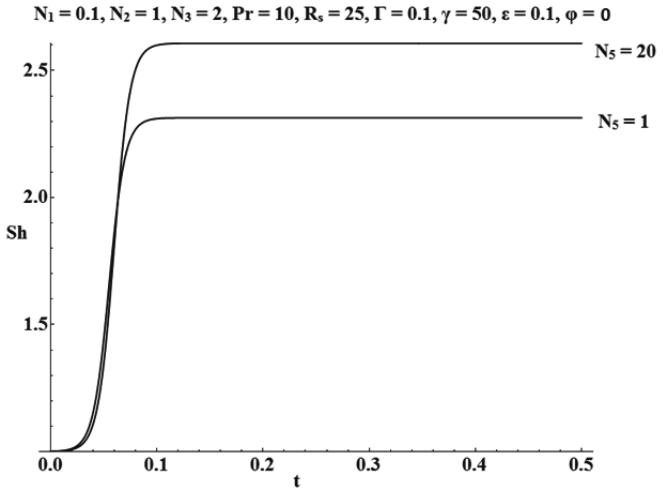

(a)

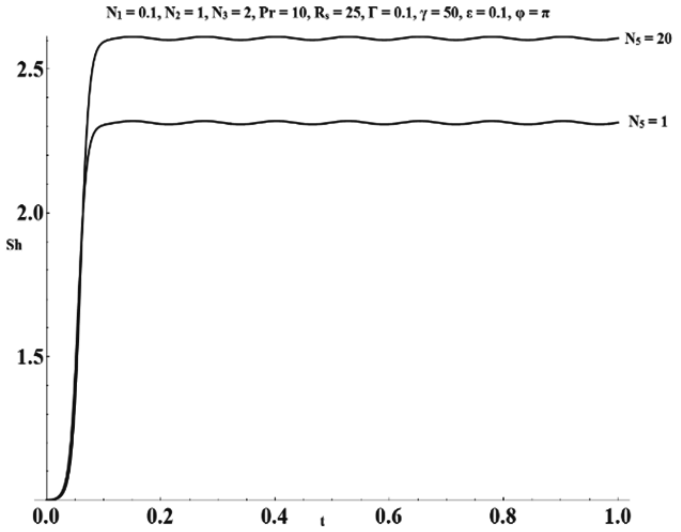

(b)

Fig. 19: Variation of Sh with t for different values of N_5 in (a) IPM and (b) OPM.

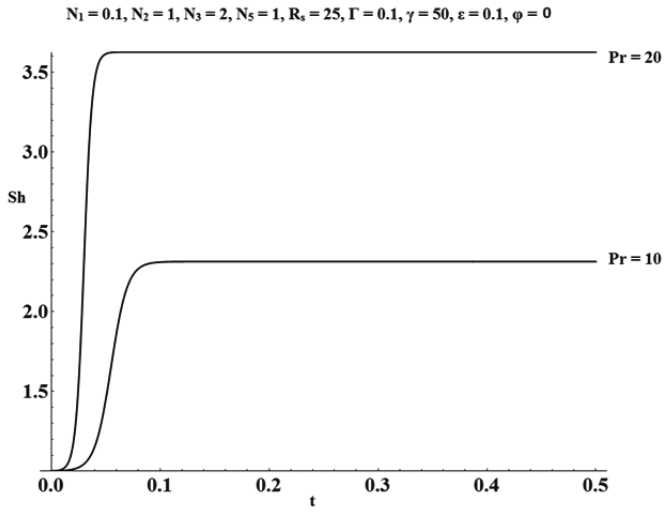

(a)

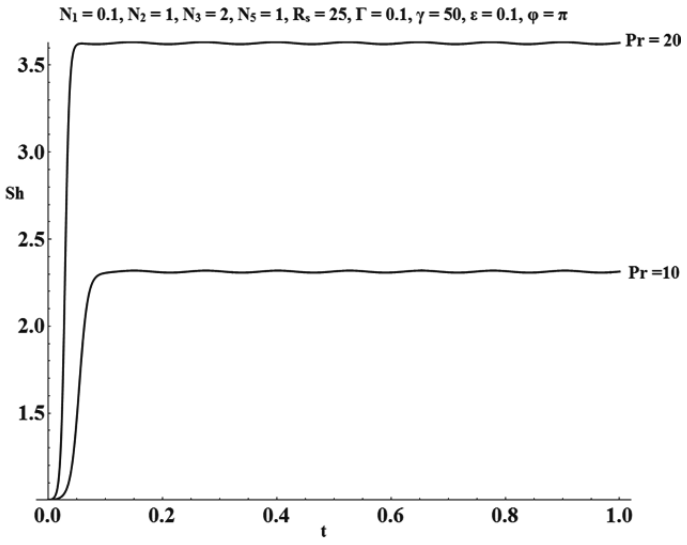

(b)

Fig. 20: Variation of Sh with t for different values of Pr in (a) IPM and (b) OPM.

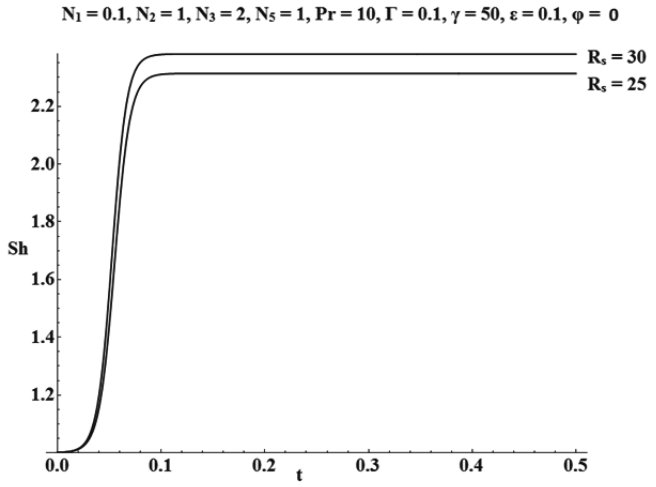

(a)

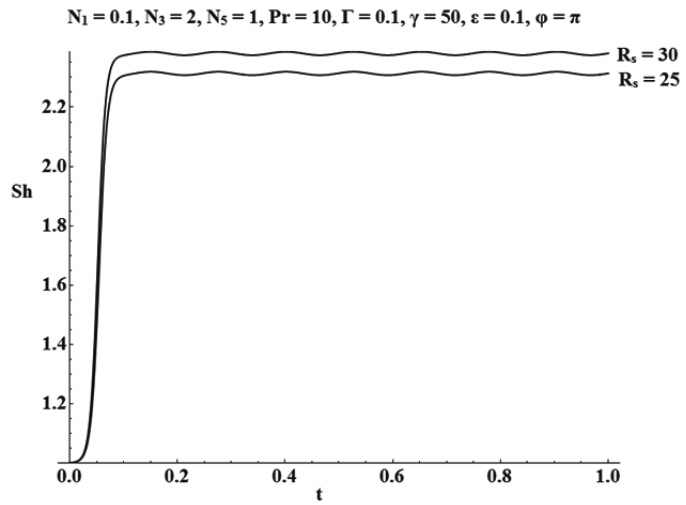

(b)

Fig. 21: Variation of Sh with t for different values of R_s in (a) IPM and (b) OPM.

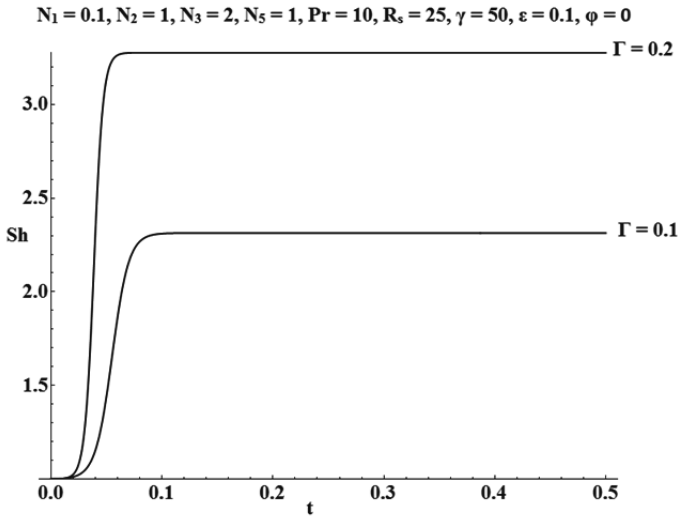

(a)

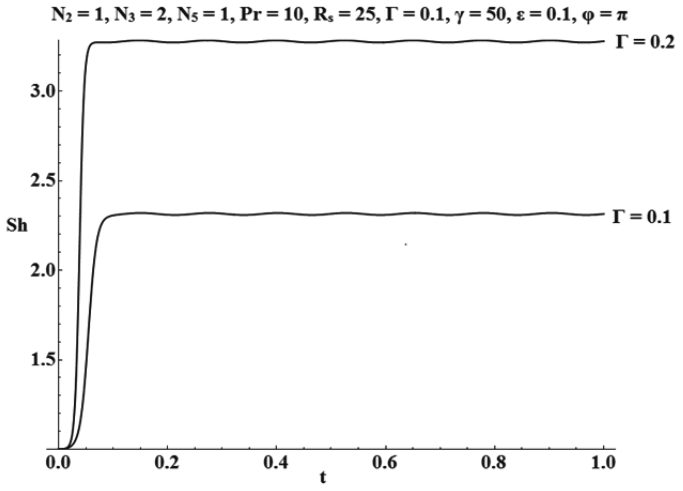

(b)

Fig. 22: Variation of Sh with t for different values of Γ in (a) IPM and (b) OPM.

4 Concluding Remarks

The effect of concentration modulation on DDC in the micropolar fluid is analyzed using linear and non-linear analysis. The following conclusions are made from the study.

- OPM is more stable than IPM i.e., $R_{OPM} > R_{IPM}$.
- The onset of convection in presence of concentration modulation can be delayed by adding micron-sized particles i.e., $R/_{N_1 \neq 0} > R/_{N_1 = 0}$.
- Effect of increase in N_1 decreases the heat transfer and increases mass transfer i.e., $Nu/_{N_1 \neq 0} < Nu/_{N_1 = 0}$ and $Sh/_{N_1 \neq 0} > Sh/_{N_1} = 0$.
- Effect of increase in N_3 increases heat transfer and decreases mass transfer i.e., $Nu/_{N_5 \neq 0} < Nu/_{N_5 = 0}$ and $Sh/_{N_5 \neq 0} > Sh/_{N_5 = 0}$.
- Effect of increase in N_5 decreases the heat transfer and increases mass transfer i.e, $Nu/_{N_5 \neq 0} < Nu/_{N_5 = 0}$ and $Sh/_{N_5 \neq 0} > Sh/_{N_5 = 0}$.
- Effect of increase in R_s and Γ increases heat transfer and mass transfer i.e., $Nu/_{R_s \neq 0} > Nu/_{R_s = 0}$, $Nu/_{\Gamma \neq 0} > Nu/_{\Gamma = 0}$, $Sh/_{R_s \neq 0} > Sh/_{R_s = 0}$ and $Sh/_{\Gamma \neq 0} > Sh/_{\Gamma = 0}$.

Acknowledgment

The authors are thankful to the Department of Mathematics, CHRIST (Deemed to be University), Bangalore for the support given to complete the paper.

Bibliography

Turner J. Double-diffusive phenomena. Annual Review of Fluid Mechanics, 1974; 6(1): 37-54.

Huppert HE, Turner JS. Double-diffusive convection. Journal of Fluid Mechanics, 1981; 106: 299-329.

Rudraiah N, Siddheshwar PG. A weak nonlinear stability analysis of double diffusive convection with cross-diffusion in a fluid-saturated porous medium. Heat and mass transfer, 1998; 33(4): 287-93.

Malashetty MS, Biradar BS. The onset of double diffusive convection in a binary Maxwell fluid saturated porous layer with cross-diffusion effects. Physics of Fluids, 2011; 23(6): 064109.

Capone F, De Luca R. Double diffusive convection in porous media under the action of a magnetic field. Ricerche di Matematica, 2019; 68(2): 469-83.

Eringen AC. Theory of micropolar fluids. Journal of Mathematics and Mechanics, 1966; 1-18.

Lukaszewicz G. Micropolar fluids: theory and applications. Springer Science & Business Media, 1999.

Sharma V, Kumar S. Thermosolutal convection of micropolar fluids in hydromagnetics. Czechoslovak Journal of Physics, 2000; 50(10): 1133-46.

Pranesh S, Narayanappa AK. Effect of non-uniform basic concentration gradient on the onset of double-diffusive convection in micropolar fluid. Applied Mathematics, 2012; 3(5): 417-24.

Pranesh S, Tarannum S. Linear and weakly non-linear stability analyses of double-diffusive electro-convection in a micropolar fluid. IOSR J. Math, 2015; 11(6), 1.
Venezian G. Effect of modulation on the onset of thermal convection. Journal of Fluid Mechanics, 1969; 35(2): 243-54.
Malashetty MS, Basavaraja D. Effect of thermal modulation on the onset of double diffusive convection in a horizontal fluid layer. International journal of thermal sciences, 2005; 44(4): 323-32.
Bhadauria BS. Double diffusive convection in a porous medium with modulated temperature on the boundaries. Transport in porous media, 2007; 70(2): 191-211.
Siddheshwar PG, Bhadauria BS, Srivastava A. An analytical study of nonlinear double-diffusive convection in a porous medium under temperature/gravity modulation. Transport in porous media, 2012; 91(2): 585-604.
Bhadauria BS, Kiran P. Weak nonlinear double diffusive magneto-convection in a Newtonian liquid under gravity modulation. Journal of Applied Fluid Mechanics, 2015; 8(4).
Bhadauria BS, Siddheshwar PG, Singh AK, Gupta VK. A local nonlinear stability analysis of modulated double diffusive stationary convection in a couple stress liquid. Journal of Applied Fluid Mechanics, 2016; 9(3): 1255-64.
Pranesh S, Arun NK. Study of heat transfer in a time dependent vertically oscillating micropolar liquid. Recent Trends in Fluid Mechanics, 2018; 5: 63–74.
Thriveni K, Pranesh S. Linear and non-linear analysis of solute-convection modulation in a couple stress fluid under temperature modulation. International Journal of Applied Engineering Research. 2018; 13(24): 16984–94.
Gupta VK, Kumar A, Singh AK. Analytical study of weakly nonlinear mass transfer in rotating fluid layer under time-periodic concentration/gravity modulation. International Journal of Non-Linear Mechanics. 2017 Dec 1;97:22-9.
Mathew A, Jagannath M, Pranesh S. Inphase and outphase concentration modulation on the onset of magneto-convection and mass transfer in weak electrically conducting micropolar fluids. InAIP Conference Proceedings 2019 Mar 8 (Vol. 2080, No. 1, p. 030012). AIP Publishing LLC.
Siddheshwar PG, Pranesh S. Effect of temperature/gravity modulation on the onset of magneto-convection in weak electrically conducting fluids with internal angular momentum. Journal of Magnetism and Magnetic materials. 1999 Feb 1;192(1):159-76.

Nomenclature

Symbols	Definition
d	Depth of the fluid
I	Moment of inertia
$\vec{g}$	Acceleration due to gravity
$\hat{k}$	Unit vector in the vertical direction
p	Pressure
S	Concentration
$\vec{V}$	Velocity
C_v	Specific heat at constant volume
N_1	Coupling parameter
N_2	Inertia parameter
N_3	Couple stress parameter
N_5	Micropolar heat conduction parameter
Nu	Nusselt number
Pr	Prandtl number
Sh	Sherwood number
R	Rayleigh number
R_s	Solutal Rayleigh number
Greek symbols	
β	Micropolar heat conduction coefficient
β_s	Coefficient of solutal expansion
β_t	Coefficient of thermal expansion
ϵ	Amplitude of modulation
ζ	Coupling viscosity coefficient
η	Shear kinematic viscosity coefficient
θ	Temperature
ϑ	Frequency of modulation
λ	Bulk kinematic viscosity coefficient
η'	Shear spin viscosity coefficient
λ'	Bulk spin viscosity coefficient
ρ	Density
ρ_0	Density at reference temperature
ϕ	Phase angle
χ	Thermal diffusivity
χ_s	Solutal diffusivity
$\vec{\omega}$	Angular velocity

Swaraj D. Lewis, Purushothama Chippar

A numerical study of metal hydride reactor embedded with helical coil heat exchanger

Hydrogen charging and discharging in a metal hydride reactor

Abstract: The critical challenge of heat management in a Metal Hydride (MH) reactor necessitates comprehensive research and development towards an effective heat transfer system to enhance its hydrogen charging and discharging rates. Several interesting strategies were reported in the literature to assist effective heat transport from and to the reactor. In this report, a comprehensive three-dimensional numerical model accounting for reaction kinetics and, heat and mass transfer is developed for hydrogen charging and discharging in a $LaNi_5$ based MH reactor. The model is compared with the experimental data, and the simulation results agree closely with the experimental data. A detailed parametric study is carried out to optimize the operating conditions of the reactor and the geometry of the Helical Coil Heat Exchanger (HCHX) to improve the hydrogen charging and discharging rates. The effect of essential parameters such as supply/exit pressures, Heat Transfer Fluid (HTF) temperature, and helical coil pitch/turns on the thermal performance and sorption rate of the MH bed are analyzed systematically. The hydrogen charging simulation results show that increasing the inlet hydrogen pressure and reducing the HTF temperature significantly improves the charging rate. From the HCHX design point of view, it is observed that increasing the number of coils turns benefits the hydrogen storage performance due to improved heat transfer from the MH bed to the helical coil. The influence of the exit pressure and the HTF temperature on the hydrogen discharge rate is also discussed in detail. The present study with multi-dimensional contours of temperature and hydrogen mass fraction will improve the fundamental knowledge of the MH reactor and shed light on the development of an effective heat exchanger.

Keywords: Heat transfer; Helical coil heat exchanger; Hydrogen storage; Metal hydride.

Swaraj D. Lewis, St. Joseph Engineering College (Affiliated to Visvesvaraya Technological University, Belagavi), Vamanjoor, Mangaluru, 575 028, India
Purushothama Chippar, St. Joseph Engineering College (Affiliated to Visvesvaraya Technological University, Belagavi), Vamanjoor, Mangaluru, 575 028, India, purushothama@sjec.ac.in

https://doi.org/10.1515/9783110696080-009

1 Introduction

The scarcity of fossil fuel availability and the promising candidacy of renewable resources as alternative energy has motivated researchers worldwide to research and develop its efficient utilization. Among the several alternative energy carriers, hydrogen is considered a high potential fuel because it is cleaner, highly efficient, and easy for domestic production, particularly for fuel cell applications. Apart from developing a hydrogen infrastructure, the main challenge is its storage and transportation. Among the several methods, solid-state storage or Metal Hydride (MH) based storage of hydrogen has received significant attention from researchers, and extensive research is underway in developing combinations of solid mediums (metal, alloy, and intermetallic compounds) to enhance its storage performance. It should be noted that heat management in the MH reactor plays a significant role in hydrogen charging and discharging rates. Therefore, optimization of the design and operation parameters of a heat exchanger is important.

Various heat transfer systems have been discussed in the literature and can be classified as heat exchanger method, methods to adjunct thermal conductivity, and latent heat storage. The internal heat exchangers are spiral tubes (1, 2), tube with fins (3-7), coiled tubes (8,9), helical coils (10-13), capillary tube bundles (14), double-layered annulus reactor (15-18), and heat pipes (19,20). The methods used to supplement operative thermal conductivity in a reactor are metal wire matrix (21), multilayer sheet structures (22), metal powder composite (23), metal foam (24, 25), and porous expanded graphite (26). Several studies devised the MH reactors with phase change materials (27-29). Demircan et al. (30) analyzed the effect of reactor geometry and operational parameters on heat transport, and subsequently, on hydrogen storage time in a $LaNi_5$ bed via experimental and theoretical studies. The study emphasized on delineating the hydrating time and heat transfer area in the bed. Wang et al. (31) developed a 3D numerical model to understand the coupled mass and heat transport during hydrogen charging in a $LaNi_5$ bed, and the results revealed that the flow of hydrogen provides extra cooling in the bed, in particular at the inlet during the early stages of the absorption process. However, Jemni et al. (32) on analyzing the heat transport by convection in an MH reactor, suggested that the convection effect can be neglected since the change in bed temperature was less than 1 percent. Burger et al. (33) developed a cylindrical reactor to test its hydrogen desorption performance with exit pressure above 1.7 bar, where both metal and complex hydrides were used and separated by a gas-permeable layer. The results showed that the use of metal hydride and complex hydride reduced the desorption time by a factor of 1.2 and a hydrogen desorption efficiency of 94%. Haneul et al. (34) developed a three-dimensional hydrogen desorption model to study desorption and the resultant mass and heat transfer in the reactor. The model was used to compare a simple cylindrical rector's desorption performance with a thin double-layered annu-

lus reactor. The thin double-layered annulus reactor showed even distribution of temperature and hydrogen mass fraction and superior desorption performance. Nam et al. (35) performed a study to probe the influence of reactor design and hydrogen feed pressure on absorption kinetics. Three shapes of MH reactors, i.e., cylindrical, square, and rectangular with a cooling water jacket, were used. The results revealed that the ratio of the exterior to the volume of the reactor dictated the absorption kinetics. Cho et al. (36) investigated the MH tank's dynamic response for varying operational conditions of a fuel cell by manipulating the reactor discharge valve. The study concluded that the circulation fluid temperature plays an important role in the discharge of hydrogen.

Anurag et al. (5) studied the absorption and desorption characteristics of a cylindrical MH reactor incorporated with an annular heat exchanger tube with circular copper fins by varying the supply pressure, coolant temperature, and velocity, and fin configurations. Mellouli et al. (25) analyzed the effects of various types of metal foam in the bed and its density and porosity on hydrogen storage. The results revealed that hydrogen storage improved with increasing density and decreased porosity of the metal foam. The presence of a concentric heat exchanger tube further improved the absorption kinetics. Visaria et al. (8,9) developed a helical coil with the objective of placing it in close proximity to metal powder in a 4 kg $Ti_{1.1}CrMn$ bed. The study emphasized that the metal powder's distance from the coiled tube and the coolant temperature played a significant role in the hydrating rate. In contrast, the effect of supply pressure was inferior. Askri et al. (37) studied the temperature distribution and storage of hydrogen in a bare reactor and a reactor with external fins with a concentric tube and fins attached to the concentric tube. The MH reactor, integrated with the concentric tube with fins showed the highest performance in hydrogen storage. Chippar et al. (38) studied the effect of using compartments in the MH bed, which facilitated fast heat removal and improved the sorption rate. The authors also studied an embossed plate heat exchanger embedded MH reactor for its hydrogen absorption rate and thermal performance (39). Wang et al. (10) investigated the influence of the helical coil's pitch and the convective heat transfer coefficient on the hydrating rate. The results revealed that faster charging times were achieved when the heat transfer coefficient was increased, and the charging was less sensitive to the coil's pitch when the metal foam was introduced in the bed. Dhaou et al. (1) experimentally demonstrated that fins in the spiral coil could significantly improve the charging time, and studied the influence of the geometry of fins and operating parameters on charging time.

The present study was conducted to investigate the charging and discharging behavior of hydrogen in a cylindrical MH reactor integrated with a Helical Coil Heat Exchanger (HCHX). A study was carried out on the effects of operating pressure, HTF temperature, and HCHX geometry on temperature distribution, and absorption and desorption kinetics in the MH reactor.

2 Numerical Model

The numerical model uses overall heat and mass balances with the following assumptions: (1) ideal gas law; (2) homogeneous porous metal bed; (3) local thermal equilibrium hypothesis between the fluid and solid phases, and (4) the physical properties are independent of pressure, concentration, and temperature.

Mass Balance

$$\frac{\partial \varepsilon \rho^g}{\partial t} + \nabla.(\rho^g u) = -\dot{m}, \tag{1}$$

The hydrogen density, ρ^g is expressed as below:

$$\rho^g = \frac{P^g M^g}{RT}. \tag{2}$$

For metal

$$\frac{(1-\varepsilon)\partial \rho^s}{\partial t} = \dot{m}. \tag{3}$$

In Equations (1) and (3), ε and $\dot{m}.$ indicate the MH bed porosity and sorption rate of hydrogen per unit volume, respectively. The value of $\dot{m}$ is calculated using the reaction kinetics of $LaNi_5$ as:

For absorption: $$\dot{m} = C_{\mathrm{a}} \exp\left(-\frac{E_a}{RT}\right) \cdot \ln\left(\frac{P^{\mathrm{g}}}{P_{\mathrm{eq}}}\right)(\rho^{\mathrm{s}}_{\mathrm{sat}} - \rho^{\mathrm{s}}) \tag{4}$$

For desorption: $$\dot{m} = -C_{\mathrm{d}} \exp\left(-\frac{E_d}{RT}\right) \cdot \ln\left(\frac{P^{\mathrm{g}} - P_{\mathrm{eq}}}{P_{\mathrm{eq}}}\right)(\rho^s - \rho^s_{emp}) \tag{5}$$

Where, P_{eq} represent the equilibrium pressure in the MH bed and can be expressed in terms of temperature and hydrogen to metal mass fraction (H/M ratio) as below (38,40):

$$P_{eq}(bar) = f\left(\frac{H}{M}\right) exp\left(\frac{\Delta H}{R_g}\left(\frac{1}{T} - \frac{1}{T_{ref}}\right)\right). \tag{6}$$

Here, $f\left(\frac{H}{M}\right)$ describes the equilibrium pressure at a given temperature as an H/M ratio function and is estimated using a polynomial equation expressed in Eq. (7).

The coefficients of the polynomial expression are determined from the experimental P-C-T data by (40).

For absorption: $$f\left(\frac{H}{M}\right)_{ref} = a_o + \sum_{n=1}^{9} a_n \left(\frac{H}{M}\right)^n. \quad (7)$$

$$\left.\begin{aligned} a_0 = -0.23691, a_1 = 16.963, a_2 = -38.94368, a_3 = 46.25223, \\ a_4 = -32.09352, a_5 = 13.7198, a_6 = -3.65573, a_7 = 0.59087, \\ a_8 = -0.05297 \text{ and } a_9 = 0.0020197 \end{aligned}\right\}.$$

For desorption: $$f\left(\frac{H}{M}\right)_{ref} = d_o + \sum_{n=1}^{9} d_n \left(\frac{H}{M}\right)^n. \quad (8)$$

$$\left.\begin{aligned} d_0 = -1.31878, d_1 = 18.41173, d_2 = -41.04133, d_3 = 49.50453, \\ d_4 = -35.54625, d_5 = 15.7913, d_6 = -4.36325, d_7 = 0.72797, \\ d_8 = -0.06701 \text{ and } d_9 = 0.0026098 \end{aligned}\right\}.$$

Momentum Balance

$$\frac{1}{\varepsilon}\frac{\partial \rho^g \vec{u}}{\partial t} + \frac{1}{\varepsilon^2}\nabla.(\rho^g \vec{u}\vec{u}) = -\nabla p + \nabla.\tau + S_u\,. \quad (9)$$

The source term in the above equation for the porous region is estimated by using Darcy's Law $S_u = \frac{-\mu}{k}\,\vec{u}$, while in the other regions, $S_u = 0$.

Heat Balance

The following energy equations are used in the porous and non-porous mediums.

Non-porous medium

$$\frac{\partial}{\partial t}(\rho^g E^g) + \nabla.\left(\vec{u}(\rho^g E^g + P)\right) = -\nabla(k^g \nabla T + \tau.\vec{u}). \quad (10)$$

Porous medium

$$\left.\begin{aligned} \frac{\partial(\varepsilon\rho^g E^g + (1-\varepsilon)\rho^s E^s)}{\partial t} + \nabla.\left(\vec{u}(\rho^g E^g + P)\right) = -\nabla\left(k_{eff}\nabla T + \tau.\vec{u}\right) \\ + \dot{m}\left[\Delta H + T\left(C_p^g - C_p^s\right)\right] \end{aligned}\right\}. \quad (11)$$

Where E_g and E_s are the total energy in the fluid and solid phases, respectively. The energy source during the hydrogen absorption/desorption is denoted by the second term of the RHS of Eq. (11). The effective thermal conductivity in the MH bed is calculated as the weighted porosity of the gas and metal powder.

$$k_{eff} = \varepsilon k_{h2} + (1 - \varepsilon)k_M. \tag{12}$$

The source terms of the conservation equations and properties of the MH bed were written as User Defined Functions (UDF) and compiled to a Computational Fluid Dynamics (CFD) commercial software package, ANSYS-FLUENT 17.2. The convergence criteria for density, velocity, and temperature calculations were set at 10^{-6}. The constant pressure was maintained at the inlet/outlet during hydrogen absorption and desorption. Table 1 lists the various physical properties and boundary conditions used in the simulations.

Tab. 1: Comparison boundary conditions and physical properties of $LaNi_5$ bed.

Description	Absorption	Ref.	Desorption	Ref.
Inlet/Exit temperature, $\boldsymbol{T, K}$	293.15			
Inlet/Exit pressure, P, bar	10		0.085	
Activation energy, $E_a, J\ mol^{-1}\ K^{-1}$	21179.6	(36)	22500	(40)
Heat of reaction, $\Delta H, J\ kg^{-1}$	1.54×10^7	(36)	1.54×10^7	(36)
Sorption rate coefficient, $C_a/C_d, s^{-1}$	59.187	(36)	9.57	(40)
Specific heat of hydrogen, $C_{P,H_2}, J\ mol^{-1}K^{-1}$	14,890	(36)	14,890	(36)
Specific heat of metal, $C_{P,M}, J\ mol^{-1}K^{-1}$	419	(36)	419	(36)
Thermal conductivity of hydrogen, $K_{H_2}, Wm^{-1}K^{-1}$	0.167	(41)	0.167	(41)
Thermal conductivity of metal, $K_M, Wm^{-1}K^{-1}$	1.5	(40)	1.5	(40)
Metal bed porosity, ϵ	0.5		0.5	
Hydrogen-free metal density, ρ_0^s, kgm^{-3}	8175	(20)		

3 Results and Discussion

3.1 Validation of the numerical model

The current MH model was validated against the experimental data given by Jemni et al. (40). A cylindrical MH reactor of 50 mm diameter, 80 mm height with 422 g of $LaNi_5$ metal powder was used. The temperature at the exterior of the cylinder was maintained at 293K, and the convective heat transfer coefficient was specified as 1652 $W\ m^{-2}K^{-1}$. The heat flux at the external wall of the cylinder was determined using the below equation:

$$k_{wall}\nabla \mathrm{T}_{wall} = h(T_{wall} - T_{\infty}). \tag{13}$$

Fig. 1 compares the experimental and predicted temperature at three monitoring points in the bed during the hydrogen charging and discharging processes. As shown in the figure, the simulation data closely matches the experimental results during the hydrogen absorption process. During the initial stages of charging, the temperature rises sharply to 341K from the initial temperature of 293K due to the abundant availability of free metallic sites, low equilibrium pressure, and faster hydrogen absorption. A constant temperature region after the peak point indicates a balance between the equilibrium pressure and free metallic sites. Further, the temperature gradually decreases with the retardation of absorption. For discharging, the bed's initial pressure is considered to be equal to the equilibrium pressure at the initial temperature and fully saturated state. Although the agreement at point A is reasonable, the predicted results closely agree at B and C with the experimental data. Moreover, the predicted results capture the key experimental trends during hydrogen desorption. Both the experimental and simulation results show a rapid decrease in bed temperature, indicating that heat consumption during desorption (endothermic reaction) is much more than the heat supplied at the walls. It should also be noted that desorption is driven by a strong pressure difference between the initial bed pressure and the vacuum pressure at the outlet (0.085 bar). After 160 s, the bed's temperature starts to increase, indicating that the heat supplied is in surplus to the heat consumed.

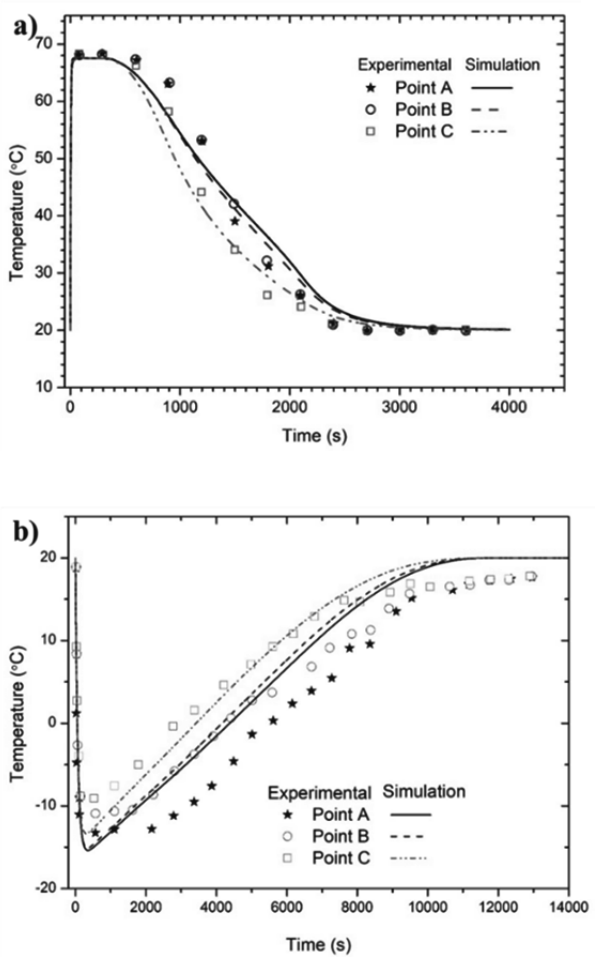

Fig. 1: Experimental and simulation temperature at monitoring locations (A, B, and C) in a cylindrical MH bed: during hydrogen (a) charging and (b) discharging processes.

3.2 Implementation of an MH model to an HCHX embedded MH reactor

A cylindrical MH reactor of 80 mm diameter and 100 mm height was filled with $LaNi_5$ to a height of 80 mm. The outer and inner diameters of the HCHX tube were 6 mm and 4.8 mm, respectively. The diameter and height of the HCHX were 30 mm and 85 mm, respectively. The flow rate of the HTF in the HCHX was fixed at 0.00046349 kg/s for all the simulations. The HTF flow rate was estimated based on the amount of heat generated in the MH bed and HTF temperature rise from the inlet

to outlet in the HCHX. The effects of the temperature of the HTF and supply/exit pressure on average bed temperature, temperature distribution, and absorption/desorption mass fraction were analyzed through several simulations. A mesh independence study was performed by checking the effects of mesh sizes on MH bed temperature to optimize the mesh attributes. Fig. 2 shows the computational domain and mesh configuration for the HCHX embedded MH reactor. The mesh sizes varied from coarse (200686 cells), medium (334072 cells), fine (455011 cells), and very fine (640670 cells). From Fig. 3, the bed temperature during hydrogen absorption with fine and very fine meshes closely matched and hence, geometry with fine mesh was considered for the simulations.

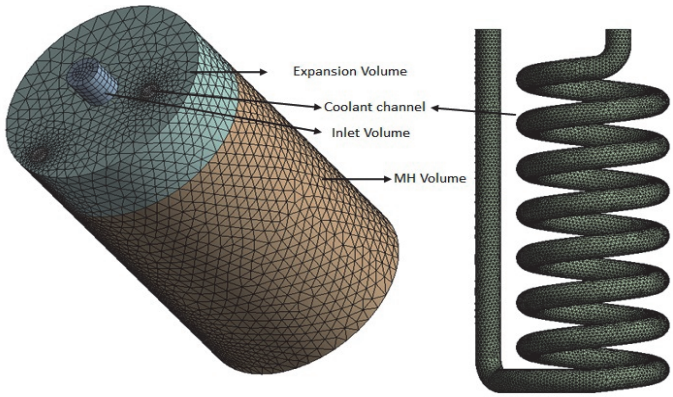

Fig. 2: Geometry and mesh of HCHX embedded MH reactor.

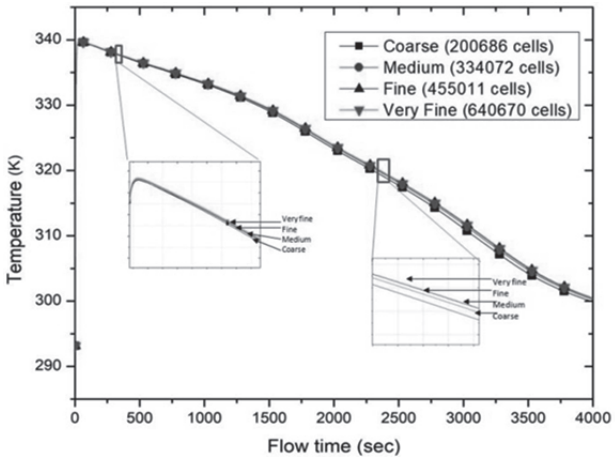

Fig. 3: Grid independence analysis for the MH reactor.

3.3 Hydrogen absorption

First, the simulations were carried out with varying the number of turns, i.e., 3, 5, and 7 in the HCHX to investigate its effect on bed temperature and hydrogen absorption. The results are presented in Fig.4. The inlet temperature of the HTF and hydrogen supply pressure were maintained at $20^{o}C$ and 10 bar, respectively. As shown in the figure, an increase in the coil turns enhances the heat transfer and hence, faster hydrogen storage. Comparing the three simulations, the time taken for charging 90% of saturation was 2550 s, 2000 s, and 1750 s with 3, 5, and 7 turns, respectively. However, the significance of the coil turns reduces when it is increased showing that heat transfer is limited by the low thermal conductivity of the metal hydride. The corresponding contours of temperature and H/M ratio at different intervals of time are presented in Fig. 5. During the initial stages of absorption, the bed temperature increases monotonically due to quick hydrogen absorption. As the absorption proceeds, the higher number of coils turns yields better heat transfer, uniformity in temperature distribution, and faster hydrogen absorption.

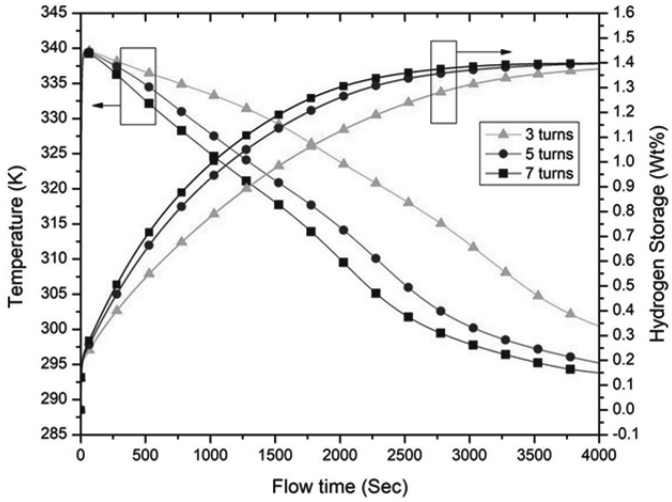

Fig. 4: Evolution curves of bed temperature and hydrogen storage under different numbers of coil turns in the HCHX for the absorption process.

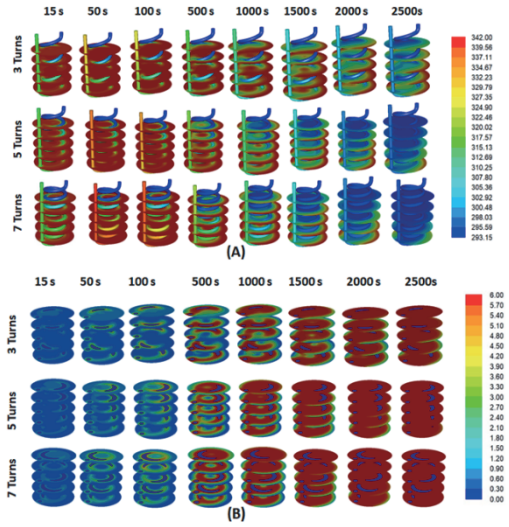

Fig. 5: Contours of local temperature in kelvin (A) and H/M ratio (B) under different numbers of coil turns in the HCHX for the hydrogen absorption process.

Fig. 6 presents the bed temperature, and H2 storage evolution curves plotted for different HTF inlet temperatures with hydrogen supply pressure of 10 bar and seven turns in the HCHX. It is evident that the HTF inlet temperature plays an important role in heat removal from the bed. The average temperature in the bed at 2000 s and the time taken for 90% of bed saturation are 294K and 1375 s, 310K and 1750 s, and 322K and 2375 s with HTF inlet temperatures 283.15 K, 293.15K and 303.15K, respectively. The corresponding distribution contours at different time intervals are presented in Fig. 7.

Figs. 8 and 9 present average bed temperature, hydrogen storage (wt%), and equilibrium pressure evolution in the bed for three different hydrogen supply pressures with HTF inlet temperature at $10^{o}C$ and seven turns in the HCHX. It is known that the difference in the supply inlet pressure and equilibrium pressure in the bed determines the rate of hydrating, and the higher the difference, the faster is the hydrating. As shown in the figures, an increase in the supply pressure enables faster hydrogen absorption and, consequently, a sharp increase in the bed temperature. The increase in bed temperature exponentially increases the equilibrium pressure. Therefore, the temperature in the bed and the equilibrium pressure decreases gradually as the absorption proceeds. Approximately around 1500 s, the temperature evolution trend for high supply pressure flips indicates faster retardation of hydrating in the bed. Concurrently, the equilibrium pressure increases slightly as it is a function of bed temperature and H/M ratio (see Eq. 6). Finally, when the bed is

entirely saturated and reaches HTF temperature, the equilibrium pressure settles around 4.4 bar.

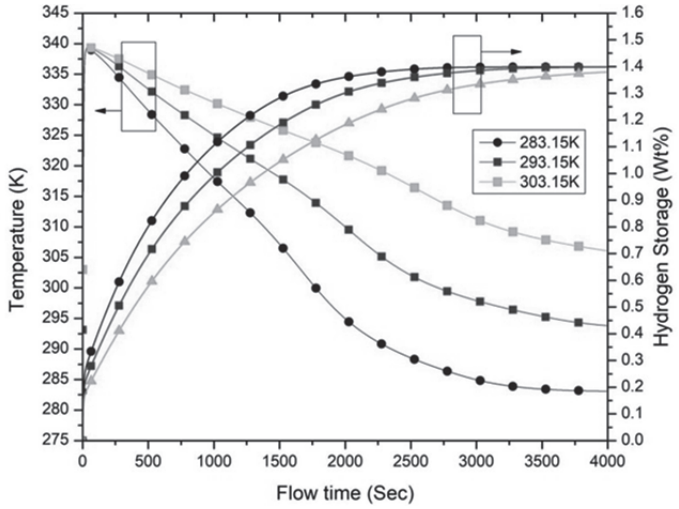

Fig. 6: Bed temperature and H_2 storage under different HTF inlet temperatures for hydrogen absorption process.

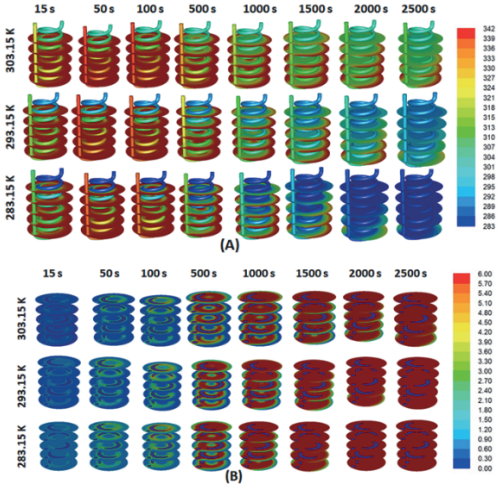

Fig. 7: Contours of temperature in kelvin (A) and H/M ratio (B) under different HTF inlet temperatures for hydrogen absorption process.

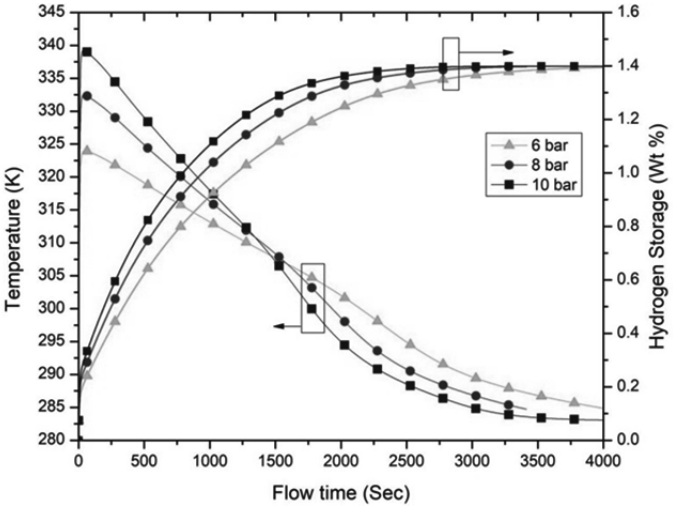

Fig. 8: Evolution of bed temperature and hydrogen storage under different supply pressures for hydrogen absorption process.

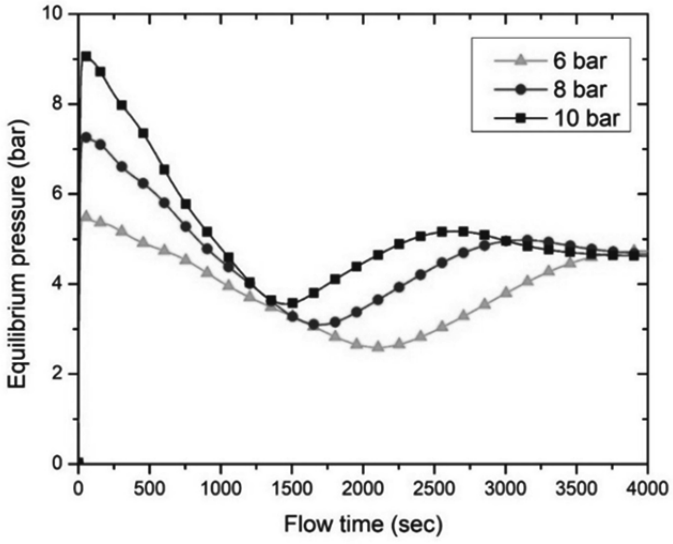

Fig. 9: Equilibrium pressure evolution curves under different supply pressures for hydrogen absorption process.

3.4 Hydrogen desorption

Next, the MH model was used to study the effect of HTF temperature and exit pressure on the hydrogen release rate. The effects of HTF temperature and exit pressure on average bed temperature, temperature distribution, and desorption rate were analyzed through several simulations. Fig. 10 shows the evolution of average bed temperature and hydrogen desorption in the MH reactor with different HTF temperatures. The reactor exit pressure was maintained at a vacuum 0.085 bar. The results showed that an increase in HTF temperature accelerated the desorption kinetics. This is because a significant increase in the reactor's equilibrium pressure and the difference between the developed equilibrium pressure and the exit pressure drives the reaction. At the initial stage of the desorption process, the heat consumption dominates the heat supplied by the HTF, and therefore, a sharp drop in temperature is observed, and a significant amount of hydrogen is released. Around 250 sec, the temperature of the reactor slowly starts to increase indicating effective heat supply by the HTF. The desorption retards at 3500 s, and the temperature in the reactor reaches that of the HTF. Fig. 11 shows the temperature distribution and H/M ratio at different cross-sections in the reactor at different time intervals. From the contours, it is clear that the increase in HTF temperature improves uniformity in the distribution of temperature and H/M ratio in the reactor.

Fig. 12 presents the advancement of temperature and hydrogen release in the reactor with different exit pressures, while the HTF temperature is maintained at 333K in the inlet. As predicted in the figure, the drop in bed temperature was large, with low vacuum pressure at the exit, indicating a large driving force for the desorption process. After a sharp drop, the temperature slowly increased, and around 1750 s, the bed temperature with low exit pressure increased faster than the high exit pressure cases. This was due to the fast release of hydrogen during the initial stages and early retardation of the hydrogen desorption reaction. The time required for 90% of hydrogen release from the reactor with 0.085 bar, 0.5 bar, and 1.01325 bar was 2000 s, 2300 s, and 2700 s, respectively. Fig. 13 shows the corresponding distribution of H/M distribution and temperature in the reactor. Similar to Fig. 12, for low exit pressure case, a sharp drop in temperature and faster release of hydrogen is observed during the initial stages. As time proceeds, the temperature increases sharply, indicating retardation of the desorption kinetics.

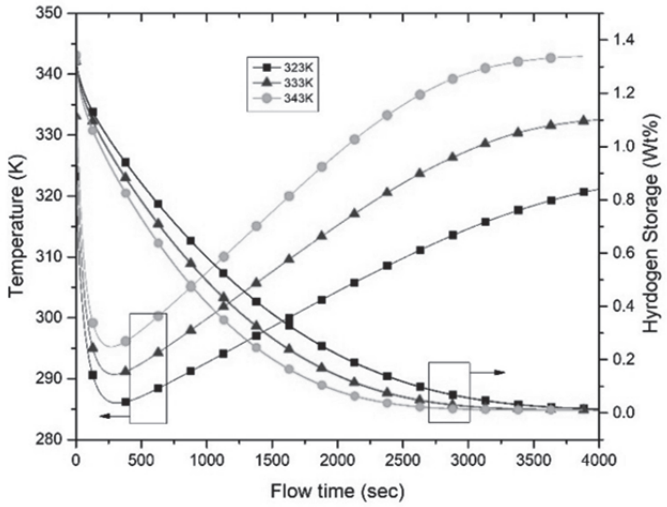

Fig. 10: MH bed temperature in kelvin and H_2 release evolution curves under different HTF temperatures for hydrogen desorption process.

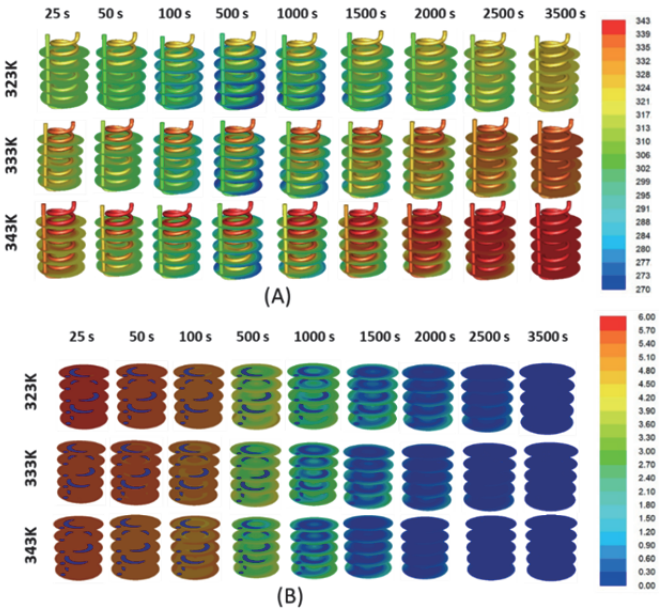

Fig. 11: Contours of local temperature in kelvin (A) and H/M ratio (B) distribution under different HTF temperatures for hydrogen desorption process.

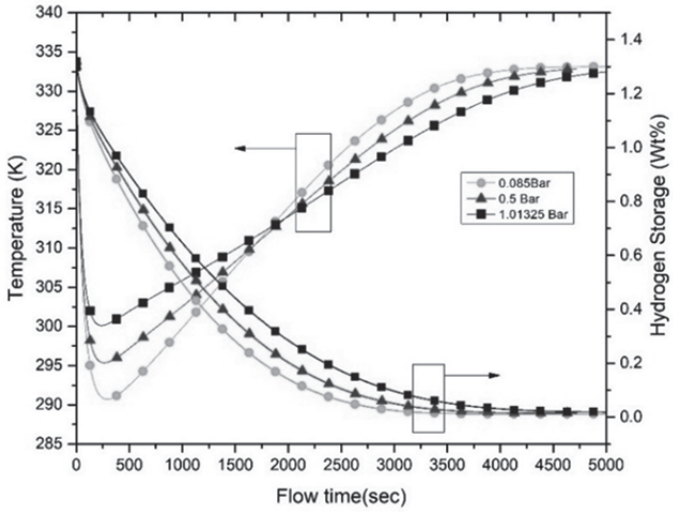

Fig. 12: Bed temperature in kelvin and H_2 release evolution curves under different exit pressures for hydrogen desorption process.

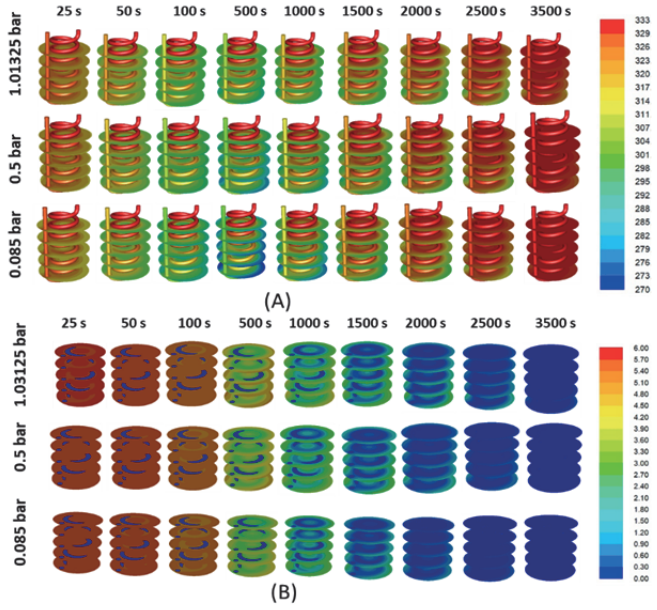

Fig. 13: Contours of temperature in kelvin (A) and H/M ratio (B) distribution under different exit pressures for hydrogen desorption process.

4 Concluding Remarks

The present study involves developing a comprehensive 3D model for hydrogen absorption/desorption in a $LaNi_5$ based reactor, and the validation of the model against the experimental results available in the literature. The predicted results are in close agreement with the experimental data. Further, the model is used to understand the influence of geometry and operational parameters of the HCHX on thermal performance and hydrogen storage in the $LaNi_5$ bed. The study reveals that the amount of hydrogen storage and heat transfer rate in the bed improves with the increase in the number of coils turns, but the extent of improvement diminishes with the increase in the number of coils turns. A significant improvement in heat transfer is observed by decreasing the HTF inlet temperature. Simulations by varying the hydrogen supply pressure show paramount changes in bed temperature during the initial stages of the hydrogen absorption process. Further, a detailed study was performed to understand the influence of HTF temperature and exit pressure on temperature distribution and hydrogen desorption rate. The increase in HTF temperature significantly improved the desorption rate and improved uniformity in the temperature and H/M ratio distribution in the reactor. The decrease in the exit pressure (vacuum pressure) had a similar effect on an increase in HTF temperature, as both increased the equilibrium pressure and enhanced the driving force for hydrogen desorption. The findings of this study can help in enhancing the understanding of hydrogen absorption/desorption processes in the MH bed and the influence of key parameters on hydrating/dehydriding kinetics.

Acknowledgment

This work is supported by the Vision Group on Science and Technology (VGST) – GRD 477, Department of Information Technology, Biotechnology and Science & Technology, Government of Karnataka.

Bibliography

Dhaou H, Souahlia A, Mellouli S, Askri F, Jemni A, Nasrallah SB. Experimental study of a metal hydride vessel based on a finned spiral heat exchanger. International Journal of Hydrogen Energy. 2010 Feb 1;35(4):1674-80.

Li H, Wang Y, He C, Chen X, Zhang Q, Zheng L, Yang F, Zhang Z. Design and performance simulation of the spiral mini-channel reactor during H2 absorption. International Journal of Hydrogen Energy. 2015 Oct 19;40(39):13490-505.

Souahlia A, Dhaou H, Askri F, Mellouli S, Jemni A, Nasrallah SB. Experimental study and characterization of metal hydride containers. international journal of hydrogen energy. 2011 Apr 1;36(8):4952-7.

Pourpoint TL, Velagapudi V, Mudawar I, Zheng Y, Fisher TS. Active cooling of a metal hydride system for hydrogen storage. International Journal of Heat and Mass Transfer. 2010 Mar 1;53(7-8):1326-32.

Singh A, Maiya MP, Murthy SS. Effects of heat exchanger design on the performance of a solid state hydrogen storage device. International Journal of Hydrogen Energy. 2015 Aug 17;40(31):9733-46.

Singh A, Maiya MP, Murthy SS. Experiments on solid state hydrogen storage device with a finned tube heat exchanger. International Journal of Hydrogen Energy. 2017 Jun 1;42(22):15226-35.

Nyamsi SN, Yang F, Zhang Z. An optimization study on the finned tube heat exchanger used in hydride hydrogen storage system–analytical method and numerical simulation. International Journal of Hydrogen Energy. 2012 Nov 1;37(21):16078-92.

Visaria M, Mudawar I. Coiled-tube heat exchanger for High-Pressure Metal Hydride hydrogen storage systems–Part 1. Experimental study. International journal of heat and mass transfer. 2012 Feb 1;55(5-6):1782-95.

Visaria M, Mudawar I. Coiled-tube heat exchanger for high-pressure metal hydride hydrogen storage systems–Part 2. Computational model. International journal of heat and mass transfer. 2012 Feb 1;55(5-6):1796-806.

Wang H, Prasad AK, Advani SG. Hydrogen storage system based on hydride materials incorporating a helical-coil heat exchanger. International journal of hydrogen energy. 2012 Oct 1;37(19):14292-9.

Wu Z, Yang F, Zhu L, Feng P, Zhang Z, Wang Y. Improvement in hydrogen desorption performances of magnesium based metal hydride reactor by incorporating helical coil heat exchanger. International Journal of Hydrogen Energy. 2016 Sep 28;41(36):16108-21.

Wu Z, Yang F, Zhang Z, Bao Z. Magnesium based metal hydride reactor incorporating helical coil heat exchanger: simulation study and optimal design. Applied energy. 2014 Oct 1;130:712-22.

Raju M, Kumar S. Optimization of heat exchanger designs in metal hydride based hydrogen storage systems. International Journal of Hydrogen Energy. 2012 Feb 1;37(3):2767-78.

Linder M, Mertz R, Laurien E. Experimental analysis of fast metal hydride reaction bed dynamics. International journal of hydrogen energy. 2010 Aug 1;35(16):8755-61.

Kang HG, Cho S, Lee MK, Yun SH, Chang MH, Chung H, Koo DS, Song KM, Kim D. Fabrication and test of thin double-layered annulus metal hydride bed. Fusion Engineering and Design. 2011 Oct 1;86(9-11):2196-9.

Yoo H, Ko J, Ju H. A numerical investigation of hydrogen absorption phenomena in thin double-layered annulus ZrCo beds. International journal of hydrogen energy. 2013 Jun 18;38(18):7697-703.

Kou H, Huang Z, Luo W, Sang G, Meng D, Luo D, Zhang G, Chen H, Zhou Y, Hu C. Experimental study on full-scale ZrCo and depleted uranium beds applied for fast recovery and delivery of hydrogen isotopes. Applied Energy. 2015 May 1;145:27-35.

Cui Y, Zeng X, Kou H, Ding J, Wang F. Numerical modeling of heat transfer during hydrogen absorption in thin double-layered annular ZrCo beds. Results in Physics. 2018 Jun 1;9:640-7.

Chung CA, Yang SW, Yang CY, Hsu CW, Chiu PY. Experimental study on the hydrogen charge and discharge rates of metal hydride tanks using heat pipes to enhance heat transfer. Applied energy. 2013 Mar 1;103:581-7.

Chung CA, Chen YZ, Chen YP, Chang MS. CFD investigation on performance enhancement of metal hydride hydrogen storage vessels using heat pipes. Applied Thermal Engineering. 2015 Dec 5;91:434-46.

Nagel M, Komazaki Y, Suda S. Effective thermal conductivity of a metal hydride bed augmented with a copper wire matrix. Journal of the Less Common Metals. 1986 Jun 2;120(1):35-43.

Suda S, Komazaki Y. The effective thermal conductivity of a metalhydride bed packed in a multiple-waved sheet metal structure. Journal of the Less Common Metals. 1991 Jan 1;172:1130-7.

Kim KJ, Lloyd G, Razani A, Feldman Jr KT. Development of LaNi5/Cu/Sn metal hydride powder composites. Powder technology. 1998 Sep 1;99(1):40-5.

Laurencelle F, Goyette J. Simulation of heat transfer in a metal hydride reactor with aluminium foam. International Journal of Hydrogen Energy. 2007 Sep 1;32(14):2957-64.

Mellouli S, Dhaou H, Askri F, Jemni A, Nasrallah SB. Hydrogen storage in metal hydride tanks equipped with metal foam heat exchanger. International Journal of Hydrogen Energy. 2009 Dec 1;34(23):9393-401.

Kim KJ, Montoya B, Razani A, Lee KH. Metal hydride compacts of improved thermal conductivity. International journal of hydrogen energy. 2001 Jun 1;26(6):609-13.

Mellouli S, Khedher NB, Askri F, Jemni A, Nasrallah SB. Numerical analysis of metal hydride tank with phase change material. Applied Thermal Engineering. 2015 Nov 5;90:674-82.

Mâad HB, Askri F, Virgone J, Nasrallah SB. Numerical study of high temperature metal-hydrogen reactor (Mg2Ni-H2) with heat reaction recovery using phase-change material during desorption. Applied Thermal Engineering. 2018 Jul 25;140:225-34.

Lewis SD, Chippar P. Analysis of Heat and Mass Transfer During Charging and Discharging in a Metal Hydride-Phase Change Material Reactor. Journal of Energy Storage. 2021 Jan 1;33:102108.

Demircan A, Demiralp M, Kaplan Y, Mat MD, Veziroglu TN. Experimental and theoretical analysis of hydrogen absorption in $LaNi_5-H_2$ reactors. International Journal of Hydrogen Energy. 2005 Oct 1;30(13-14):1437-46.

Wang Y, Adroher XC, Chen J, Yang XG, Miller T. Three-dimensional modeling of hydrogen sorption in metal hydride hydrogen storage beds. Journal of Power Sources. 2009 Dec 1;194(2):997-1006.

Jemni A, Nasrallah SB. Study of two-dimensional heat and mass transfer during absorption in a metal-hydrogen reactor. International Journal of Hydrogen Energy. 1995 Jan 1;20(1):43-52.

Bürger I, Luetto C, Linder M. Advanced reactor concept for complex hydrides: Hydrogen desorption at fuel cell relevant boundary conditions. International journal of hydrogen energy. 2014 May 5;39(14):7346-55.

Yoo H, Ko J, Yun SH, Chang MH, Kang HG, Kim W, Ju H. A numerical investigation of hydrogen desorption phenomena in ZrCo based hydrogen storage beds. International journal of hydrogen energy. 2013 May 10;38(14):6226-33.

Nam J, Ko J, Ju H. Three-dimensional modeling and simulation of hydrogen absorption in metal hydride hydrogen storage vessels. Applied energy. 2012 Jan 1;89(1):164-75.

Cho JH, Yu SS, Kim MY, Kang SG, Lee YD, Ahn KY, Ji HJ. Dynamic modeling and simulation of hydrogen supply capacity from a metal hydride tank. International journal of hydrogen energy. 2013 Jul 17;38(21):8813-28.

Askri F, Salah MB, Jemni A, Nasrallah SB. Optimization of hydrogen storage in metal-hydride tanks. International journal of hydrogen Energy. 2009 Jan 1;34(2):897-905.

Chippar P, Lewis SD, Rai S, Sircar A. Numerical investigation of hydrogen absorption in a stackable metal hydride reactor utilizing compartmentalization. International Journal of Hydrogen Energy. 2018 Apr 19;43(16):8007-17.

Lewis SD, Chippar P. Numerical investigation of hydrogen absorption in a metal hydride reactor with embedded embossed plate heat exchanger. Energy. 2020 Mar 1;194:116942.

Jemni A, Nasrallah SB, Lamloumi J. Experimental and theoretical study of ametal–hydrogen reactor. International Journal of Hydrogen Energy. 1999 Jul 1;24(7):631-44.

Mellouli S, Askri F, Dhaou H, Jemni A, Nasrallah SB. A study of the thermal behavior of a deformable metal-hydride bed. International journal of hydrogen energy. 2016 Jan 21;41(3):1711-24.

Nomenclature

Symbols	Definition
C	Sorption rate constant (s^{-1})
C_p	Specific hear ($J\ kg^{-1}K^{-1}$)
E	Activation energy (Jkg^{-1})
H/M	Hydrogen to metal atomic ratio
ΔH	Reaction heat of formation ($J\ kg^{-1}$)
M	Molecular weight ($kg\ mol^{-1}$)
P	Permeability (m^2)
R	Universal gas constant ($8.314\ J\ mol^{-1}K^{-1}$)
T	Temperature (K)
$\vec{u}$	Velocity vector ($ms^{-1}\ J\ mol^{-1}K^{-1}$)
Greek symbols	
ϵ	Porosity
ρ	Density (kgm^{-3})
k	Thermal conductivity ($Wm^{-1}K^{-1}$)
μ	Dynamic viscosity ($kgm^{-1}s^{-1}$)
Superscripts	
g	Gas phase
s	Solid phase
sat	Saturation value
Subscripts	
a	Absorption
d	Desorption
eq	Equilibrium
H_2	Hydrogen
M	Metal
MH	Metal hydride
ref	Reference value
0	Initial value
eff	Effective

B. Mahanthesh, T. V. Joseph, K. Thriveni

Dynamics of non-Newtonian nanoliquid with quadratic thermal convection

On quadratic thermal radiation

Abstract: In this chapter, the non-Newtonian nanoliquid (Jeffrey nanoliquid) flow driven by flexible surface exposed to quadratic thermal radiation and quadratic Boussinesq approximation is examined. The Brownian movement and thermophoretic characteristics are preserved. The influence of the inclined magnetic field, convective and second-order velocity slip boundary conditions are also accounted. The dimensionless distributions of velocity, temperature, nanoparticle concentration, and rate of heat transfer are simulated by solving the system of nonlinear differential equations utilizing the finite difference method (FDM). Besides, a statistical analysis is also performed to enhances the understanding of heat transport behavior. The surface and streamline plots are sketched to analyse various flow fields and heat transport. It is found that larger Deborah number, quadratic thermal radiation, temperature ratio, and nonlinear convection aspect due to concentration results in heat transport enhancement. The reduced multivariate model for the heat transport rate is obtained by eliminating the quadratic terms of thermophoretic and Brownian motion aspects. Further, the heat transport rate is found to be more sensitive to quadratic thermal radiation rather than the zig-zag motion of nanoparticles and thermophoretic characteristics.

Keywords: Convective and slip boundary conditions; Jeffery nanofluid; Quadratic thermal radiation; Quadratic Boussinesq approximation; Sensitivity analysis.

1 Introduction

Recently, many researchers have been fascinated by the investigation of non-Newtonian fluids due to its huge applications in the engineering and manufacturing process. The fluids which do not obeys Newton's law (i.e., rate of stress is not direct-

B. Mahanthesh, Department of Mathematics, CHRIST (Deemed to be University), Bengaluru-560029, India, mahanthesh.b@christuniversity.in
T.V. Joseph, Department of Mathematics, CHRIST (Deemed to be University), Bengaluru-560029, India.
K. Thriveni, Department of Mathematics, CHRIST (Deemed to be University), Bengaluru-560029, India.

https://doi.org/10.1515/9783110696080-010

ly proportional to the rate of strain) are known as non-Newtonian fluids. In comparison to Newtonian fluids, the constitutive equations of these fluids are very complicated. Consequently, the non-Newtonian governing equations are highly non-linear. The non-Newtonian fluids were classified into three types namely i) rate type of fluid model, ii) differential type of fluid model and iii) integral type of fluid model. Here the impact of relaxation and retardation time was signified by the rate type of fluid model. Jeffrey fluid is an example of a rate type model. Which has a linear viscoelastic characteristic and various applications in the polymer field. Among the non-Newtonian fluid models, the Jeffrey fluid model is the simplest and has the derivative of time instead of the convective derivative. In the case of the Jeffrey model, the constitutive relation of non-Newtonian fluids is described as

$$\boldsymbol{\tau} = -P\boldsymbol{I} + \frac{\mu}{(1+\lambda_1)}\left[\boldsymbol{R_1} + \lambda_2\left(\frac{\partial \boldsymbol{R_1}}{\partial t} + \nabla \cdot \boldsymbol{V}\right)\boldsymbol{R_1}\right]$$

here, P, τ and R_1 signifies the pressure, Cauchy stress tensor, and Rivlin-Ericken tensor ($R_1 = [\nabla V + \nabla V^t]$) respectively. The above model reduced to the Newtonian model when λ_1 and λ_2 are set to zero. There are two-time representations of the Jeffrey fluid model, specifically the retardation time and relaxation time. The idea of retardation was initially introduced by Jeffrey to examine the occurrence of wave propagation in the mantle of the earth and eventually in the explanation of the model of the Jeffrey temperature flux. Relaxation time defines the time used by the fluid to recover its primary equilibrium state from the deformed position. Of all these facts, Jeffrey's fluid model has received a lot of attention from scientists. A two-dimensional magnetized Jeffery fluid past an elongated plate was examined by Ahmad et al. (1). It was showed that the Deborah number is favorable for the velocity field. The 3D flow of non-Newtonian fluid over a bidirectional expanding surface was examined by Hayat et al. (2). Their results proved that heat transport rate augments for an increase in relaxation parameter. The heat transport characteristics of Jeffery fluid flow over a flexible surface exposed to the magnetic field and heat source aspect were discussed by Hayat et al. (3). Their results proved that the friction at the surface increases for ascending values of Deborah number. The laminar convective flow of non-Newtonian fluid over an elongated surface was analyzed by Kumar (4) and found that the increase in Deborah number augments the temperature field. Raju et al. (5) studied the heat and mass transport mechanisms between two parallel plates filled with Jeffery fluid. Their results showed that the magnetic Reynold's number declines the concentration profile.

On the other hand, nanofluids have received considerable attention for its practical applications. A nanofluid is composed of a mixture of non-metallic or metallic nanoparticles and conventional heat transfer fluids. Water, lubricants, bio-fluids, ethylene, and oil are some examples of common base fluids. The suspension of nanoparticles enriches the thermal characteristics of base liquids, as a result, it has

a wide range of applications in the heat exchanger, vehicle cooling, biomedicine, and nuclear reactor. The heat transport with nanoliquid can be modeled via two approaches namely i) single-phase model and ii) two-phase model (Buongiorno model). For the first time, Choi (6) demonstrated that the utilization of nanoliquids in the heat transfer mechanism is more efficient compare to conventional liquid. Later, Buongiorno (7) proposed a mathematical model for nanomaterials by accounting thermophoresis and Brownian motion effects. The significance of Jeffery nanofluid flow past a flexible plate subjected to the applied magnetic field was inspected by Nadeem et al. (8). Their findings proved that the heat transport rate reduces as the zig-zag motion of nanoparticles increases. Shahzad et al. (9) studied the MHD Jeffery nanoliquid flow and heat transport over an extending plate in the presence of Joule heating. Their results showed that an increase in Deborah's number advances the surface drag force. The heat and mass transport characteristics of MHD Jeffery nanoliquid past an extending curved surface were investigated by Saif et al. (10). Their results portrayed that the temperature profile enriches for the rise in thermophoretic aspect and hepatized motion of nanoparticles.

In many practical applications like nuclear power plants, hot rolling, heat storage systems, solar thermal systems, and electronic devices the temperature difference is quite large. In such cases, density of the fluid fluctuates nonlinearly with temperature/concentration. In fact, this fluctuation affects the flow and heat transport characteristics significantly. Therefore, it is recommended to use the quadratic density variation (quadratic Boussinesq approximation (QBA)) with temperature to examine the impact of buoyancy force in the flow system. Goren (11) established the quadratic-density-temperature variation as $\Delta\rho = -\rho\gamma(T - T_s)^2$ in the buoyancy term. Later, the natural convection between two plates by employing the linear and quadratic variation in density with temperature was examined by Vajravelu and Sastri (12) and it is given by

$$\Rightarrow \rho(T) = \rho(T_w) + \left(\frac{\partial\rho}{\partial T}\right)_w (T - T_w) + \frac{1}{2!}\left(\frac{\partial^2\rho}{\partial T^2}\right)_w (T - T_w)^2,$$

$$\Rightarrow \frac{\Delta\rho}{\rho} = -[\beta_0(T - T_w) + \beta_1(T - T_w)^2].$$

$$\text{where } \beta_0 = \left(\frac{\partial p}{\partial T}\right)_w \text{ and } \beta_1 = \frac{1}{2}\left(\frac{\partial^2 p}{\partial T^2}\right)_w.$$

Afterward, the radiative heat transport of Jeffery nanoliquid over an extending plate exposed to quadratic convection was studied by Kumar et al. (13). Their findings revealed that the heat transport rate is higher for the quadratic convection aspects. The impact of nonlinear thermal radiation on the non-Newtonian nanofluid flow over a vertical plate subjected to convective boundary conditions was investigated by Waqas et al. (14). Their results showed that the nonlinear radiation augments the

temperature field. Aforesaid studies on QBA have been examined by employing the Rosseland approximation for thermal radiation either in linear or own form, which is inconsistent with the QBA. To overcome this inconsistency Thriveni and Mahanthesh (15) proposed a new way to study the thermal radiation aspect when QBA present in the model. Their results proved that the combination of quadratic radiation and quadratic convection strengthens the friction factor. However, the studies related to the influence of the quadratic thermal convection and quadratic thermal radiation on the Jeffery nanofluid flow over a stretched surface are not available in the literature.

The main objective of the current investigation is to scrutinize the combined impact of quadratic convection and quadratic radiation on the Jeffery nanofluid flow over a plate subjected to convective and second-order velocity slip boundary conditions. The flow is configured in a vertical plate with the mechanism of the strength of the inclined magnetic field (B_0) through angle α. To the best of the author's knowledge, such a study has not been analysed yet. The highly nonlinear governing equations are treated numerically and the results are analysed through 3D surface plots and streamlines. Further, the heat transport rate is examined via response surface methodology and sensitivity analysis.

2 Mathematical Formulation

The non-transient, two-dimensional flow of Jeffrey nanoliquid on an elongated vertical plate is considered. By fixing the origin, the x-axis is taken along the plate and y-axis perpendicular to it. The plate is maintained at the temperature T_w and concentration C_w. Also, T_∞ and C_∞ signifies the ambient temperature and concentration respectively. The plate is elongated linearly in its plane with the velocity $u_w(x) = ax$, where the constant $a > 0$. The mechanisms of convective boundary condition, and second-order velocity slip are also taken into account. Due to the large temperature difference of the system, by following the work of Vajravelu and Sastri (12) the nonlinear (quadratic) Boussinesq approximation where density fluctuates quadratically with temperature is considered. Further to agree with this hypothesis a quadratic Rosseland approximation is accounted (see (15)). The impact of viscous heating, induced magnetism, and Joule heating are ignored. The governing equations for an incompressible, laminar flow of Jeffrey nanoliquid exposed to aforesaid assumptions are as follows (see Nadeem et al. (8), Waqas et al. (14) and Shahzadi et al. (17)):

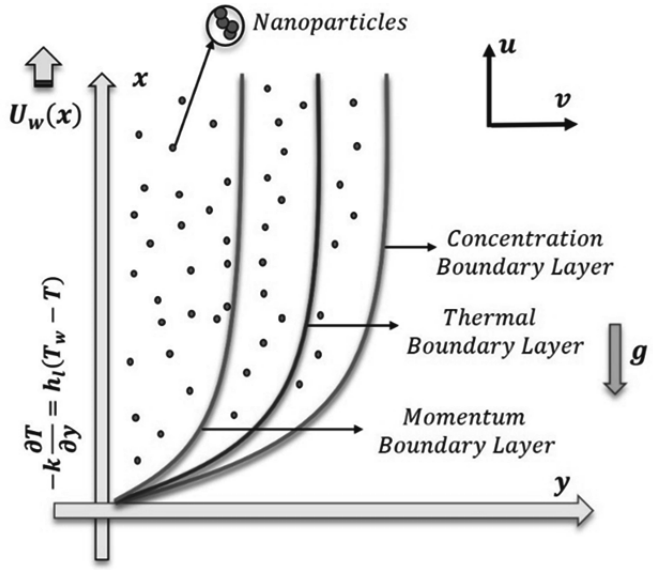

Fig. 1: Physical arrangement of the problem.

Conservation of Mass

$$\frac{\partial u}{\partial x} + \frac{\partial v}{\partial y} = 0, \tag{1}$$

Conservation of linear Momentum

$$\left.\begin{aligned} u\frac{\partial u}{\partial x} + v\frac{\partial u}{\partial y} = \frac{v}{1+\lambda}\left[\frac{\partial^2 u}{\partial y^2} + \lambda_1\left(u\frac{\partial^3 u}{\partial x \partial y^2} - \frac{\partial u}{\partial x}\frac{\partial^2 u}{\partial y^2} + \frac{\partial u}{\partial y}\frac{\partial^2 u}{\partial x \partial y} + v\frac{\partial^3 u}{\partial y^3}\right)\right] \\ +g[\beta_0(T - T_\infty) + \beta_1(T - T_\infty)^2 + \beta_2(C - C_\infty) + \beta_3(C - C_\infty)^2] \end{aligned}\right\}, \tag{2}$$

Conservation of Energy

$$u\frac{\partial T}{\partial x} + v\frac{\partial T}{\partial y} = \alpha\frac{\partial^2 T}{\partial y^2} + \tau\left[D_B\frac{\partial C}{\partial y}\frac{\partial T}{\partial y} + \frac{D_T}{T_\infty}\left(\frac{\partial T}{\partial y}\right)^2\right] - \frac{1}{\rho C_p}\frac{\partial q_r}{\partial y}, \tag{3}$$

Now, by following the Rosseland approximation for an optically dense media, the q_r is given by:

$$q_r = -\frac{4}{3k^*}\nabla(\sigma^* T^4). \tag{4}$$

where k^* – coefficient of mean absorption and σ^* -Stefan–Boltzmann constant.

As in Thriveni and Mahanthesh (15), expanding T^4 about T_w by using Taylor series and retaining up-to quadratic term yields:

$$T^4 \approx 3T_w^4 - 8TT_w^3 + 6T^2T_w^2. \tag{5}$$

Substituting Eqs. (4) and (5) in Eq. (3) one can have

$$\left.\begin{aligned} u\frac{\partial T}{\partial x} + v\frac{\partial T}{\partial y} = \alpha\frac{\partial^2 T}{\partial y^2} + \tau\left[D_B\frac{\partial C}{\partial y}\frac{\partial T}{\partial y} + \frac{D_T}{T_\infty}\left(\frac{\partial T}{\partial y}\right)^2\right] \\ + \frac{16\sigma^* T_\infty^2}{3k^*(\rho C_p)}\left[(3T - 2T_\infty)\frac{\partial^2 T}{\partial y^2} + 3\left(\frac{\partial T}{\partial y}\right)^2\right] \end{aligned}\right\}, \tag{6}$$

Concentration equation

$$u\frac{\partial C}{\partial x} + v\frac{\partial C}{\partial y} = D_B\frac{\partial C^2}{\partial y^2} + \frac{D_T}{T_\infty}\frac{\partial^2 T}{\partial y^2}, \tag{7}$$

Subjected to the boundary conditions (see Jagan et al. (18) and Ibrahim (19))

$$\left.\begin{aligned} \text{at } y = 0\text{: } u = u_w + u_{slip} = a_1 x + A\frac{\partial u}{\partial y} + B\frac{\partial^2 u}{\partial y^2},\ v = -v_w, \\ C = C_w, -k\frac{\partial T}{\partial y} = h_1(T_w - T), \\ \text{as } y \to \infty\text{: } u = 0,\ v = 0,\ C = C_\infty, T = T_\infty. \end{aligned}\right\} \tag{8}$$

where (u, v) are the velocity components along with the (x, y) directions respectively, ν- kinematic viscosity, λ- the ratio of relaxation to retardation time, g- acceleration due to gravity, β_0 & β_1- coefficients of thermal expansion, C- nanoparticles fraction, T- temperature, λ_1-retardation time, α- thermal diffusivity, ρ − density, D_B- Brownian diffusion coefficient, C_p- specific heat at constant pressure, D_T- thermophoretic diffusion coefficient, q_r- radiative heat flux, A & B- first and second-order velocity slip factor and h_1- convective heat transfer coefficient.

The local Nusselt number and Sherwood number at the plate are defined as (see (8)):

$$\left.\begin{aligned} Nu = \frac{xq_w}{\alpha(T_w - T_\infty)}, \\ Sh = \frac{xq_m}{D_B(C_w - C_\infty)}, \end{aligned}\right\} \tag{9}$$

here, $q_w = -k\left(\frac{\partial T}{\partial y}\right) + (q_r)_{(y=0)}$ is the total heat flux at the plate and q_m signifies the mass flux.

The similarity solutions of Eqs. (1)-(9) can be obtained by utilizing following suitable transformation (see (8)):

$$\left.\begin{aligned} \eta &= y\sqrt{\frac{u_w}{\nu x}}, \\ \psi &= \sqrt{a_1 \nu} x f(\eta), \\ \theta(\eta) &= \frac{(T-T_\infty)}{T_w - T_\infty}, \\ \phi(\eta) &= \frac{(C-C_\infty)}{C_w - C_\infty}. \end{aligned}\right\} \tag{10}$$

The where η corresponds to the similarity variable. ψ is the stream function and $v = -\frac{\partial \psi}{\partial x}, u = \frac{\partial \psi}{\partial y}$.

Plugging Eq. (10) in Eqs. (1), (2) & (6)-(9), Eq. (1) satisfies itself, and Eqs. (2), & (6)–(9) reduced to:

$$\left.\begin{aligned} &f''' + De\left(f''^2 - f f^{iv}\right) + (1+\lambda)\left(f f'' - f'^2\right) \\ &+(1+\lambda) Mc\{\theta + Qc_1\theta^2 + N(\phi + Qc_2\phi^2)\} = 0, \end{aligned}\right\} \tag{11}$$

$$\left(1 + \tfrac{4R_T}{3}\right)\theta'' + \Pr\left(f\theta' + Nb\phi'\theta' + Nt\theta'^2\right) + 4R_T(\theta_w - 1)\left(\theta\theta'' + \theta'^2\right) = 0, \tag{13}$$

$$\phi'' + \frac{Nt}{Nb}\theta'' + LePrf\phi' = 0, \tag{14}$$

$$\left.\begin{aligned} &\text{at } \eta = 0: f' = 1 + \epsilon_1 f'' + \epsilon f''', f = S, \theta' = -Bi(1-\theta), \phi = 1, \\ &\text{as } \eta \to \infty: \ f' \to 0, f'' \to 0, \theta \to 0, \phi \to 0. \end{aligned}\right\}. \tag{15}$$

$$\left.\begin{aligned} Nu_x Re_x^{-0.5} &= -\left(1 + \tfrac{4R_T}{3}(3(\theta_w - 1)\theta(0) + 1)\right)\theta'(0), \\ Sh_x Re_x^{-0.5} &= -\phi'(0). \end{aligned}\right\}, \tag{16}$$

Where $De = \lambda_1 a$ (Deborah number), $Mc = \frac{Gr}{Re_x^2}$ (mixed convection parameter), $Qc_1 = \frac{\beta_1(T_W - T_\infty)}{\beta_0}$ (nonlinear convection aspect due to temperature), $N = \frac{\beta_2(C_W - C_\infty)}{\beta_0(T_W - T_\infty)}$ (buoyancy ratio parameter), $Qc_2 = \frac{\beta_3(C_W - C_\infty)}{\beta_2}$ (nonlinear convection aspect due to concentration), $R_T = \frac{4\sigma^* T_\infty^3}{kk^*}$ (quadratic thermal radiation aspect), $Le = \frac{\alpha}{D_B}$ (Lewis number), $Pr = \frac{\nu}{\alpha}$ (Prandtl number), $Nt = \frac{(\rho C_p)_p D_T(T_W - T_\infty)}{\nu(\rho C_p)_p}$ (thermophoretic parameter), $\theta_w = \frac{T_w}{T_\infty}$ (temperature ratio parameter), $\epsilon_1 = A\sqrt{\frac{a}{\nu}}$ (first-order velocity slip aspect), $Nb = \frac{(\rho C_p)_p D_B(\phi_w - \phi_\infty)}{\nu(\rho C_p)_p}$ (Brownian movement aspect), $\epsilon_2 = \frac{Ba}{\nu}$ (second-order velocity slip aspect), $B_i = \frac{h_1}{k}\sqrt{\frac{\nu}{a}}$ (Biot number), $Re_x = \frac{u_w(x)x}{\nu}$ (local Reynolds number) and $S = \frac{v_w}{\sqrt{a\nu}}$ (suction/injection parameter).

3 Results and Discussion

The highly nonlinear differential Eqs. (11)–(13) exposed to the boundary conditions (14) are solved numerically by utilizing the Finite Difference Method (FDM) based on the bvp4c algorithm. The employed algorithm has been validated by comparing the computational values of local Nusselt number ($Re_x^{-0.5}Nu_x$) with Khan and Pop (16) and Nadeem et al. (8) for different values of Nt. The comparison shows an excellent association and hence it confirms the validity of the present numeric solutions (see Table 1).

Tab. 1: Values of $Re_x^{-0.5}Nu_x$ as compared with published data when $\lambda = De = Mc = N = R_T = S = \epsilon_1 = \epsilon_2 = 0$ for different values of Nt.

			$Re_x^{-0.5}Nu_x$
Nt	Khan and Pop (16)	Nadeem et al. (8) (fourth order Runge-Kutta-Fehlberg method)	Khan and Pop (16) (finite difference method-bvp4c)
0.1	0.9524	0.95247	0.95233
0.3	0.5201	0.52013	0.52009
0.5	0.3110	0.32110	0.32109

The influence of key parameters such as Deborah number De, the ratio of relaxation to retardation time λ, nonlinear convection parameter due to concentration Qc_2, mixed convection parameter Mc, nonlinear convection parameter due to temperature Qc_1, buoyancy force ratio N, Biot number Bi, suction/injection parameter S, first-order velocity slip ϵ_1, thermophoretic aspect Nt, quadratic thermal radiation R_T, Prandtl number Pr, Brownian motion aspect Nb and Lewis number Le on dimensionless profiles like velocity $f'(\eta)$, temperature $\theta(\eta)$, nanoparticles fraction $\phi(\eta)$, local Nusselt number $Re_x^{-0.5}Nu_x$ and local Sherwood number $Re_x^{-0.5}Sh_x$ is analyzed via graphical representations. Further, a statistical analysis like RSM and sensitivity analysis is performed to enhance the understanding of heat transport behavior. For numerical computation, the default values for the key parameters ($De = 0.4, \lambda = 0.5, Mc = 0.5, Qc\_1 = Qc\_2 = 0.3, N = 0.4, R\_T = 0.3, \theta\_w = 1.2, Nt = Nb = 0.3, Le = 0.5, Pr = 1.5, \epsilon\_1 = \epsilon\_2 = 0.1, Bi = 0.5$ and $S = 0.5$) has been carefully selected from standard sources, namely Kumar et al. (4) and Waqas and his collaborators (14).

3.1 Parametric analysis

Fig. 2 (a, b, c) is plotted to demonstrate the behavior of $f'(\eta), \theta(\eta)$ and $\phi(\eta)$ for change in the value of De when $\lambda = 0.1$ and $\lambda = 0.5$. The $f'(\eta)$ enhances with an increase in De. Physically this is due to an improvement in the retardation time, causing the reduction in viscous force. Further the magnitude of $f'(\eta)$ decreases for larger values of λ due to greater relaxation time. Besides the opposite trend is noticed in $\theta(\eta)$ and $\phi(\eta)$ for various values of De and λ. The impact of Mc and Qc_2 on $f'(\eta), \theta(\eta)$ and $\phi(\eta)$ is illustrated in Fig. 3 (a, b, c). Here, $f'(\eta)$ and $\theta(\eta)$ & $\phi(\eta)$ shows an increasing and decreasing nature for an ascending value of Mc respectively. This is because of the domination of the buoyancy force. $f'(\eta)$ advances for higher values of Qc_2. On the other hand, an increase in Qc_2, both $\theta(\eta)$ & $\phi(\eta)$ decreases. The effect of N and Qc_1 on $f'(\eta)$ is visualized in Fig. 4a. An increase in N and Qc_1, augments the $f'(\eta)$ and its associated boundary layer thickness. The magnitude of $\theta(\eta)$ & $\phi(\eta)$ reduces for greater values of N, as shown in Fig. 4b. The fluctuation in $f'(\eta), \theta(\eta)$ and $\phi(\eta)$ for different values of Bi and S is portrayed in Fig. 5 (a, b). Here, Bi has a favorable impact on $f'(\eta), \theta(\eta)$ and $\phi(\eta)$. The convective conditions are utilized as a key factor to control the improvement in the allied boundary layers. The coefficient of heat transport h_1 enhances with the rise in Bi as a result, heat energy is restored in liquid. On the other hand, an increase in suction aspect declines the allied boundary layer thickness as displayed in Fig. 5b. Because the suction aspect stabilizes the boundary layer growth. The $f'(\eta)$ decreases for the rise in ϵ_1 when $S = 0.5$ and $S = 0.6$ as illustrated in Fig. 6. The influence of R_T and Nt on the temperature field is depicted in Fig. 7. The $\theta(\eta)$ advances significantly for a higher value of R_T and Nt. The radiation mechanism generates additional heat into the liquid system, due to which temperature field boosts. Fig. 8 shows the significance of Nb and Pr on $\theta(\eta)$. The magnitude of temperature profile advances and reduces respectively for change in the value of Nb and Pr. Physically, the zig-zag motion of nanoparticles increased by rising the value of Nb. On the other hand, a reduction in the thermal diffusivity is noticed for greater values of the Prandtl number. The impact of Nb and Le on $\phi(\eta)$ is sketched in Fig. 9. Here the $\phi(\eta)$ is dwindling function of Nb and Le. This is because an increase in Le acts as an obstacle for the haphazard motion of nanoparticles. The effect of Nt and Pr on $\phi(\eta)$ is visualized in Fig. 10. The thermophoretic aspect and Prandtl number are favorable for concentration profile.

The 3D surface plots of the Nusselt number and Sherwood number for different values of key parameters involved in the study are presented in Figs. 11 and 12. From Fig. 11 it is inferred that the heat transport rate augments by increasing the values of De, Qc_2, R_T and θ_w. While it reduces for different values of λ, Nb, Nt and Qc_1. The mass transport rate reduces with an ascending value of Nt and λ as displayed in Fig. 12. The $Re_x^{-0.5} Sh_x$ is an enhances function of De, Nb, Qc_1, Qc_2, Pr, and Le. Besides, the streamlines are disclosed in Fig. 13 for numerous values of De when $\lambda = 0.5, Mc =$

$0.5, Qc\_1 = Qc\_2 = 0.3, N = 0.4, R\_T = 0.3, \theta\_w = 1.2, Nt = Nb = 0.3, Le = 0.5, Pr = 1.5, \epsilon\_1 = \epsilon\_2 = 0.1, Bi = 0.5$ and $S = 0.5$.

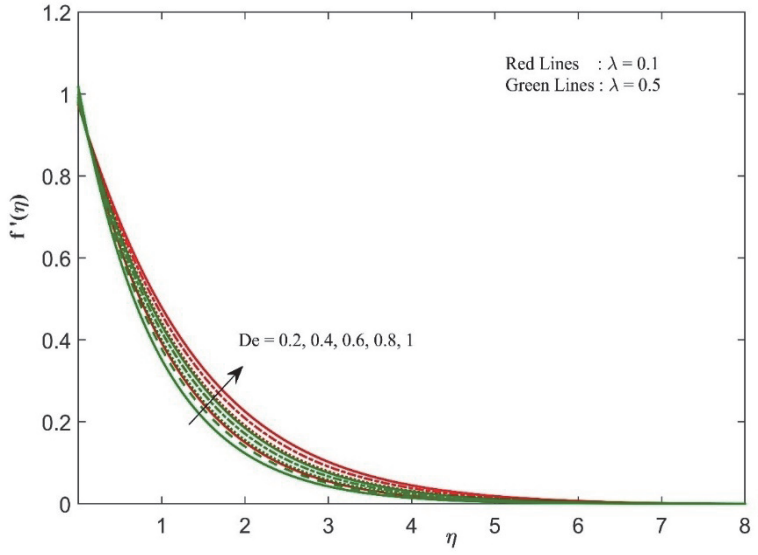

(a)

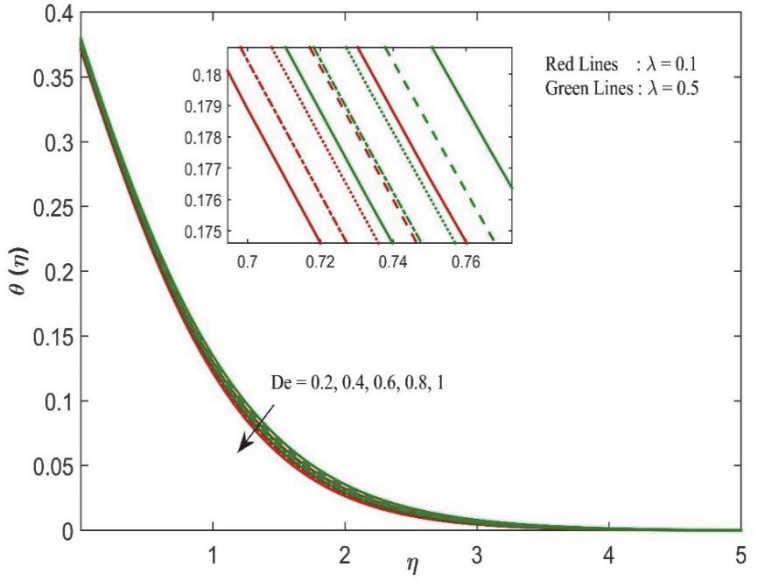

(b)

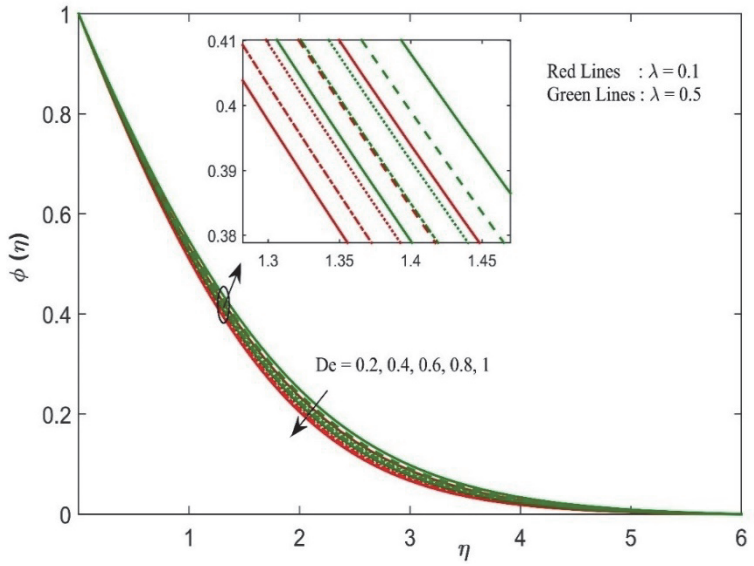

(c)

Fig. 2: Significance of De and λ on (a) $f'(\eta)$ (b) $\theta(\eta)$ and (c) $\phi(\eta)$.

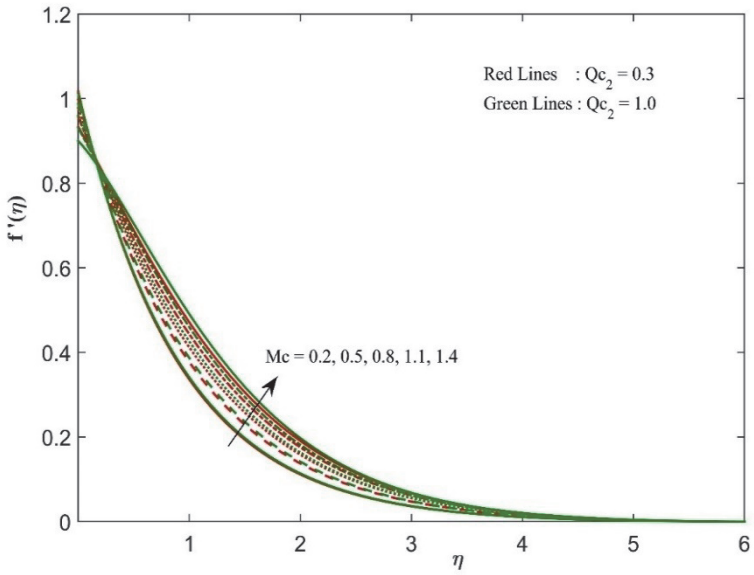

(a)

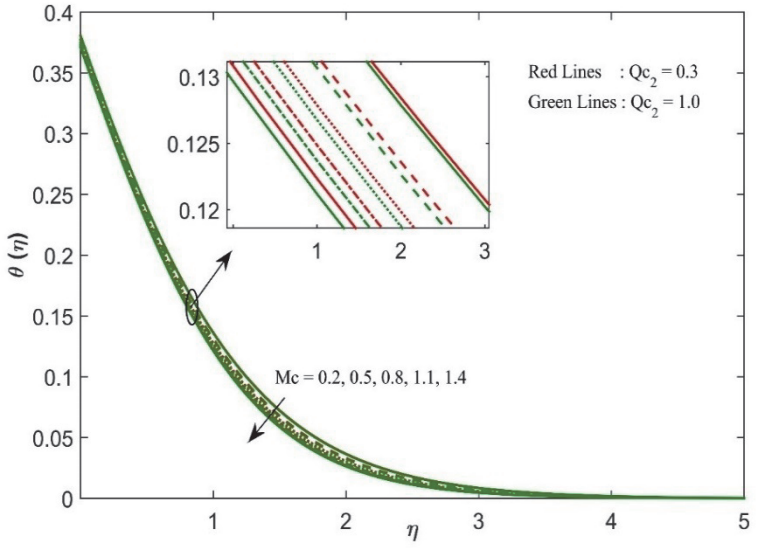

(b)

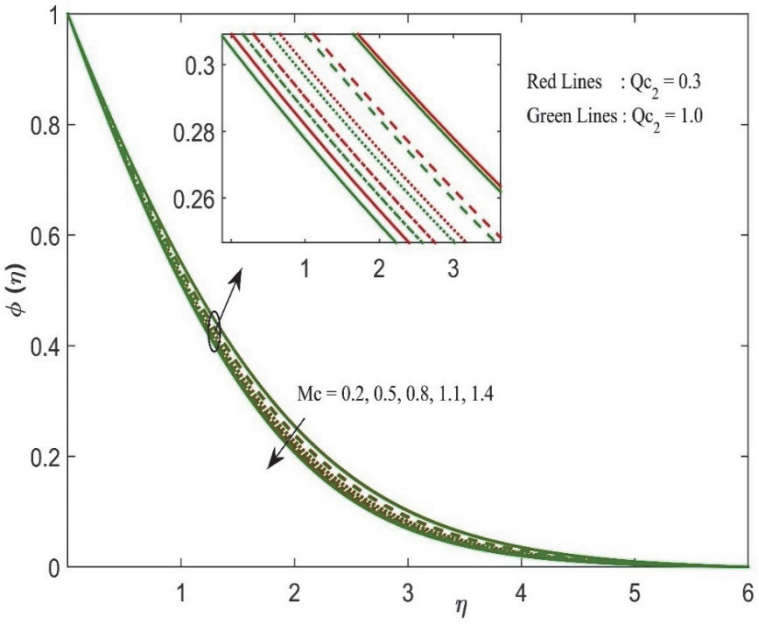

(c)

Fig. 3: Significance of Qc_2 and Mc on (a) $f'(\eta)$ (b) $\theta(\eta)$ and (c) $\phi(\eta)$.

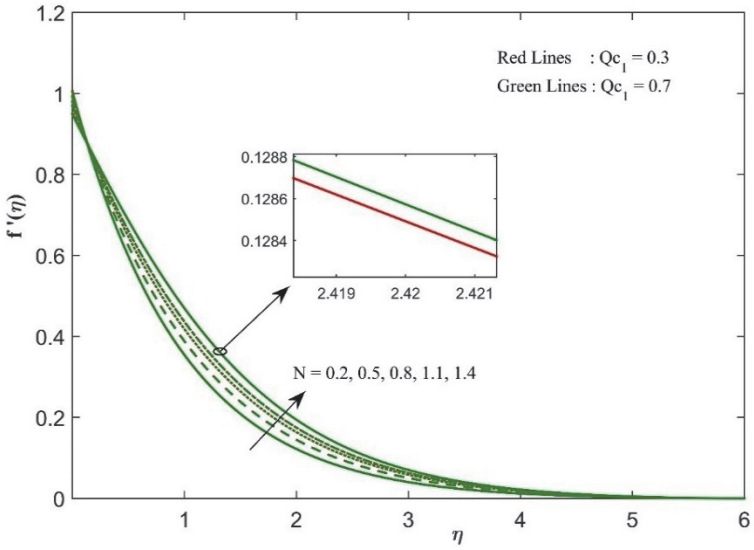

(a)

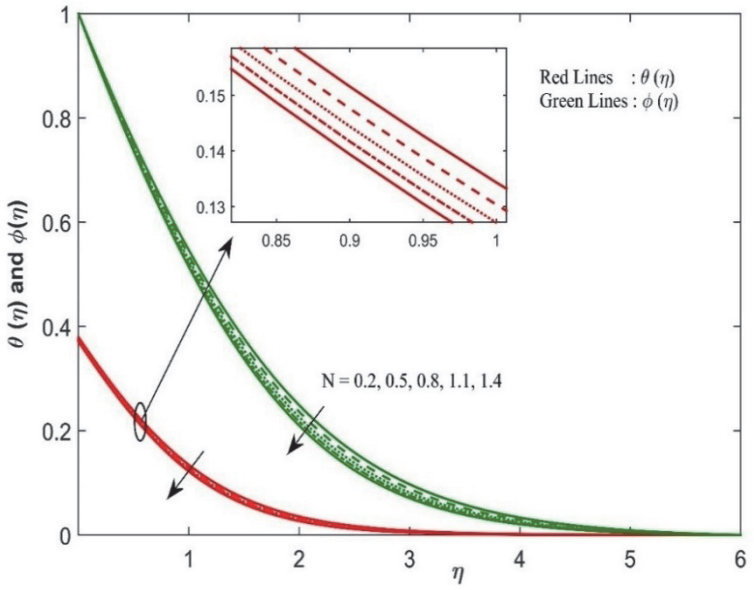

(b)

Fig. 4: Significance of N on (a) $f'(\eta)$ (b) $\theta(\eta)$ and (c) $\phi(\eta)$.

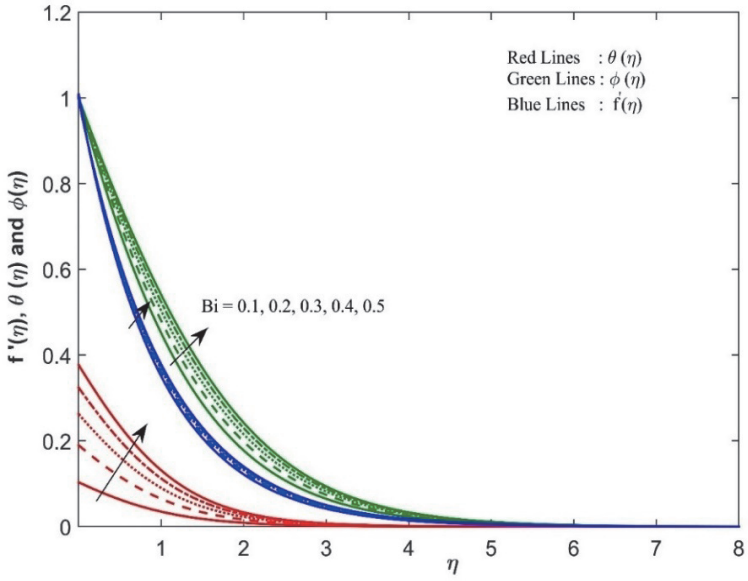

(a)

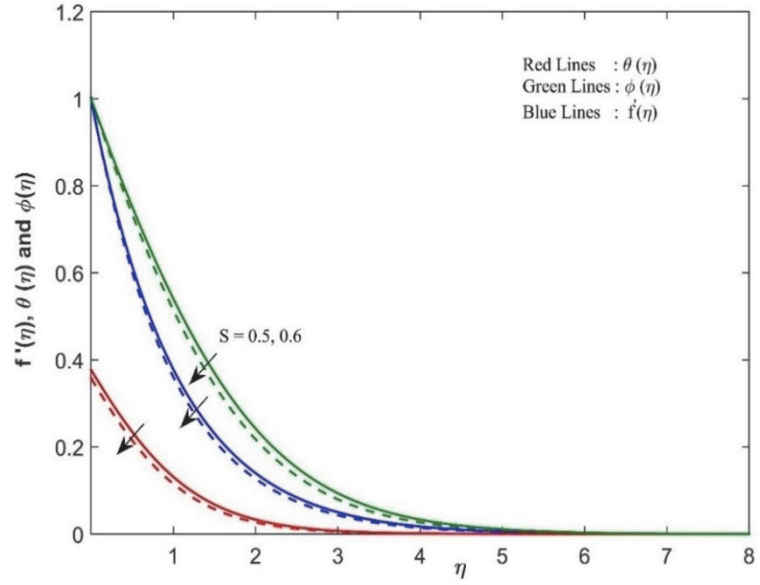

(b)

Fig. 5: The nature of $f'(\eta), \theta(\eta)$ and $\phi(\eta)$ for various values of (a) Bi and (b) S.

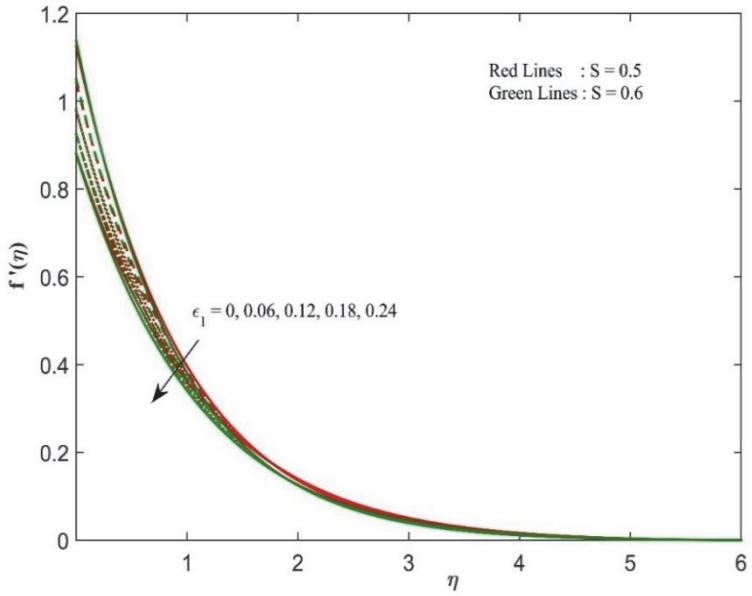

Fig. 6: Significance of ϵ_1 and S on $f'(\eta)$.

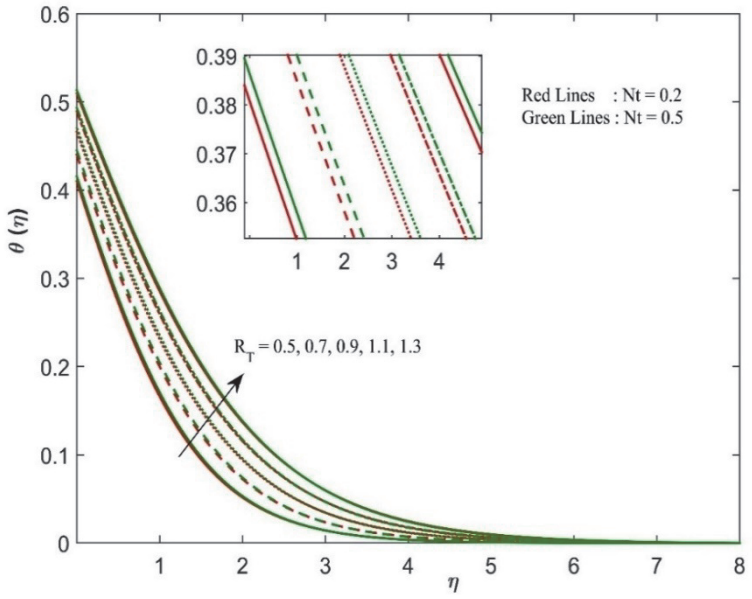

Fig. 7: Significance of R_T and Nt on $\theta(\eta)$.

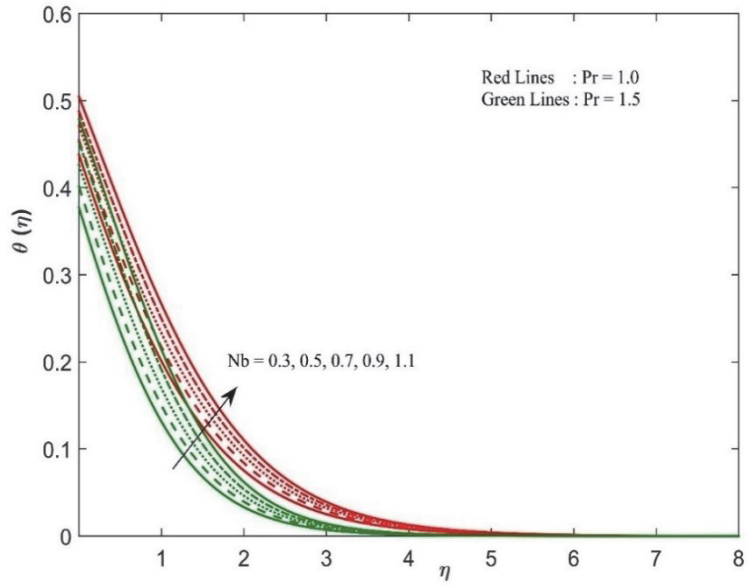

Fig. 8: Significance of Nb and Pr on $\theta(\eta)$.

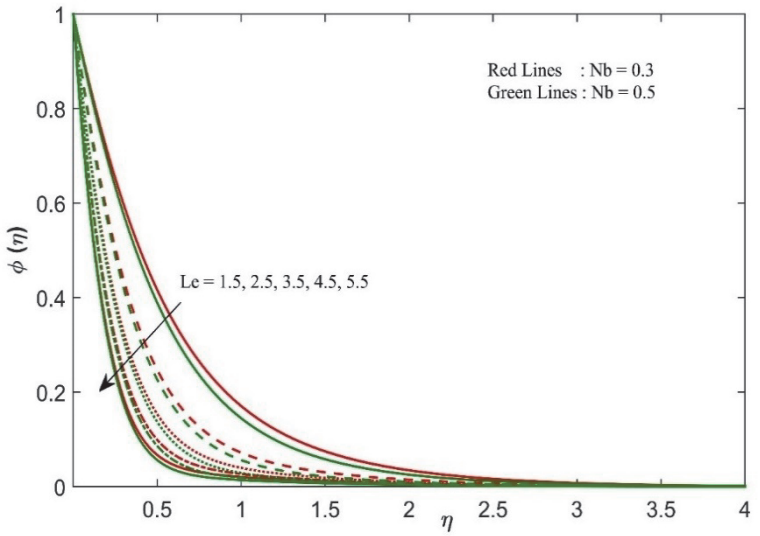

Fig. 9: Significance of Le and Nb on $\phi(\eta)$.

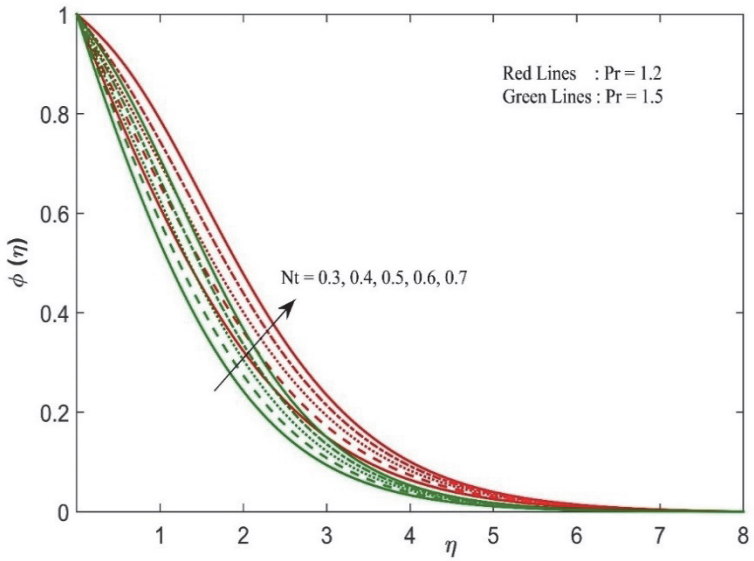

Fig. 10: Significance of Nt and Pr on $\phi(\eta)$.

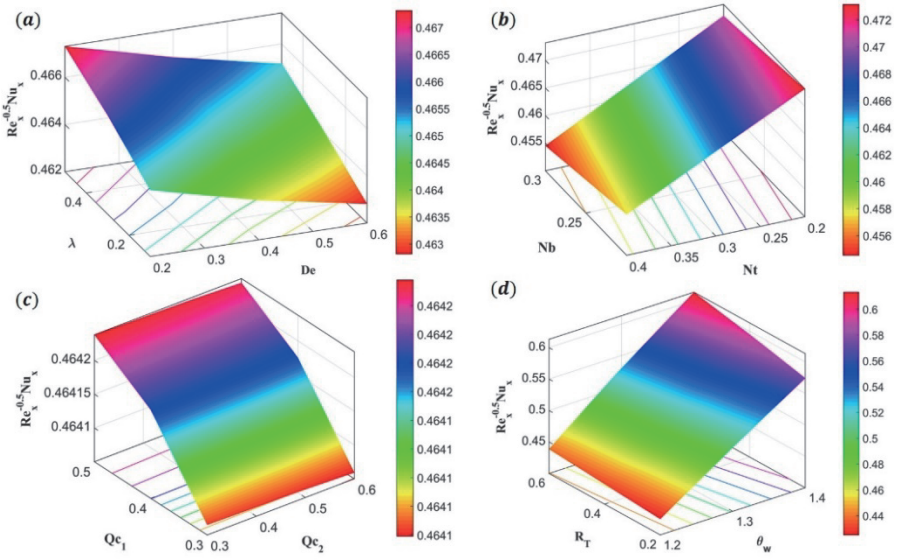

Fig. 11: Significance of (a) De & λ,(b) Nt & Nb,(c) Qc_1 & Qc_2 and (d) R_T & θ_w on $Re_x^{-0.5}Nu_x$.

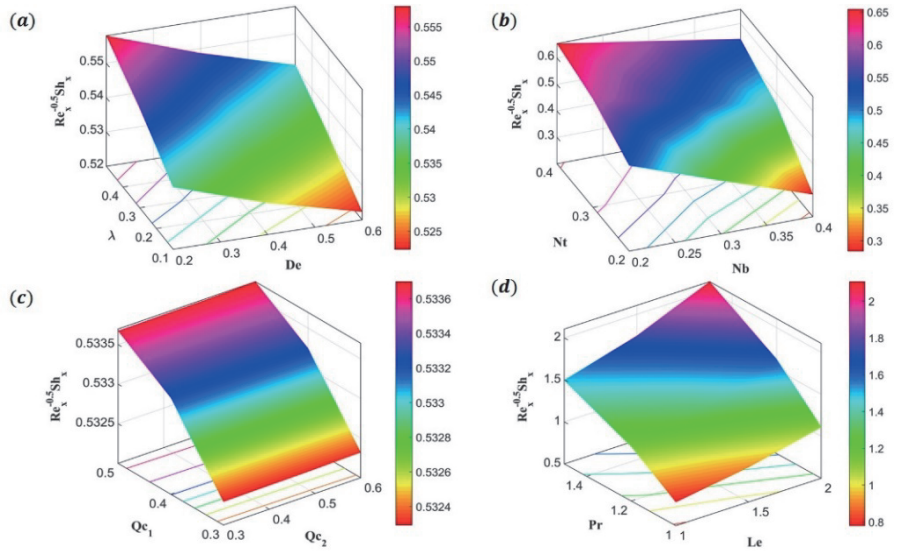

Fig. 12: Significance of (a) De & λ,(b) Nt & Nb,(c) Qc_1 & Qc_2 and (d) Pr & Le on $Re_x^{-0.5}Sh_x$.

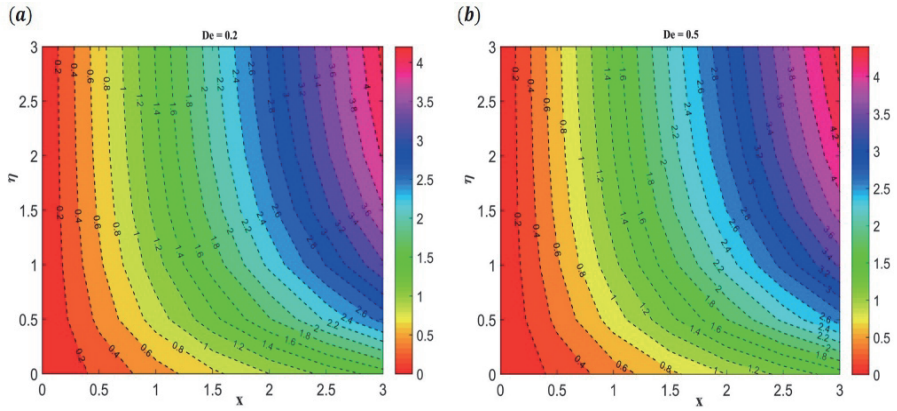

Fig. 13: Streamlines for various values of De.

3.2 Response Surface Methodology (RSM)

The correlation between the response variable and the key parameters is well explained by a hybrid mathematical-statistical technique known as RSM. The RSM is one of the powerful tools, which is used to optimize the response. In the current study the impact of three effective parameters Nt, Nb and R_T on the chosen response variable $Re_x^{-0.5}Nu_x$ is analyzed through the satistical RSM model. The range of three

key parameters at three levels (low (-1), middle (0), high (+1)) is considered as shown in Table 2.

Tab. 2: Range and levels of three key parameters.

Parameter	Symbol	Level		
		-1 (Low)	0 (Middle)	1 (High)
$0.2 \leq Nt \leq 0.6$	K_1	0.2	0.4	0.6
$0.2 \leq Nb \leq 0.6$	K_2	0.2	0.4	0.6
$0.3 \leq R_T \leq 0.7$	K_3	0.3	0.5	0.7

Further the statistical model having 20 runs for chosen three key parameters is taken into account and is tabulated in Table 3. On utilizing face-centered central composite design (CCF) the multivariate model for the current study is as follows:

$$\left.\begin{aligned} Nu_r = t_0 + t_1 Nt + t_2 Nb + t_3 R_T + t_{11} Nt^2 + t_{22} Nb^2 \\ + t_{33} R_T^2 + t_{12} Nt\, Nb + t_{13} Nt\, R_T + t_{23} Nb R_T \end{aligned}\right\}. \tag{17}$$

where t_0 is the intercept, t_i, t_{ii} and t_{ij} are respectively linear, quadratic, and interaction regression coefficients.

Tab. 3: Experimental design by using CCD.

Runs	Coded values			Real Values			Responses
	K_1	K_2	K_3	Nt	Nb	R_T	$Re_x^{-0.5} Nu_x$
1	-1	-1	-1	0.2	0.2	0.3	0.473264
2	1	-1	-1	0.6	0.2	0.3	0.468945
3	-1	1	-1	0.2	0.6	0.3	0.441119
4	1	1	-1	0.6	0.6	0.3	0.434120
5	-1	-1	1	0.2	0.2	0.7	0.619912
6	1	-1	1	0.6	0.2	0.7	0.615029
7	-1	1	1	0.2	0.6	0.7	0.581801
8	1	1	1	0.6	0.6	0.7	0.573258
9	-1	0	0	0.2	0.4	0.5	0.531208
10	1	0	0	0.6	0.4	0.5	0.524549
11	0	-1	0	0.4	0.2	0.5	0.546432

Runs	Coded values			Real Values			Responses
12	0	1	0	0.4	0.6	0.5	0.509557
13	0	0	-1	0.4	0.4	0.3	0.454537
14	0	0	1	0.4	0.4	0.7	0.597280
15	0	0	0	0.4	0.4	0.5	0.527939
16	0	0	0	0.4	0.4	0.5	0.527939
17	0	0	0	0.4	0.4	0.5	0.527939
18	0	0	0	0.4	0.4	0.5	0.527939
19	0	0	0	0.4	0.4	0.5	0.527939
20	0	0	0	0.4	0.4	0.5	0.527939

Tab. 4: ANOVA table for $Re_x^{-0.5}Nu_x$.

Source	Degrees of Freedom	Adjusted sum of squares	Adjusted mean Square	F-value	P-value	Coefficients
Model	**9**	0.054685	0.006076	214 898.40	0	(Constant) 0.527936
Linear	**3**	0.054639	0.018213	64 4145.05	0	
Nt	1	0.000099	0.000099	34 87.51	0	-0.003140
Nb	1	0.003376	0.003376	119 386.05	0	-0.018373
R_T	1	0.051164	0.051164	180 9561.59	0	0.071529
Square	**3**	0.000020	0.000007	238 .70	0	
Nt^2	1	0.000000	0.000000	0.2 5	0.630	-0.000050
Nb^2	1	0.000000	0.000000	0.4 1	0.536	0.000065
R_T^2	1	0.000011	0.000011	397 .00	05	-0.002020
Interaction	**3**	0.000026	0.000009	311 .45	0	

Source	Degrees of Freedom	Adjusted sum of squares	Adjusted mean Square	F-value	P-value	Coefficients
$Nt \times Nb$	1	0.000005	0.000005	177.67	0	-0.000792
$Nt \times R_T$	1	0.000001	0.000001	19.67	0	-0.000264
$Nb \times R_T$	1	0.000021	0.000021	737.02	0	-0.001614
Error	**10**	0.000000	0.000000			
Lack-of-Fit	5	0.000000	0.000000			
Pure Error	5	0.000000	0.000000			
Total	19	0.054686				
			R^2 = 100.00%			Adjusted R^2=100.00%

From Table 4 it is inferred that the greater value of R^2 (100%) for $Re_x^{-0.5}\, Nu_x$, exposed by the statistical analysis and test methods indicate that the obtained model is appropriate for calculating the values of $Re_x^{-0.5}Nu_x$. The terms in the model are said to be insignificant and are ignored from the model if their p-value > 0.05 and F-value < 1. Accordingly, the quadratic terms of Nt and Nb are ignored in Table 4. The reduced model for $Re_x^{-0.5}Nu_x$ by eliminating the insignificant terms in Table 4 is still significant and it is given by:

$$\left.\begin{aligned} Re_x^{-0.5}Nu_x = -0.003140Nt - 0.018373Nb + 0.071529R_T \\ -0.002020R_T^2 - 0.000792NtNb - 0.000264NtR_T \\ -0.001614NbR_T + 0.527936. \end{aligned}\right\}. \tag{18}$$

The residual plots obtained while designing the ANOVA is displayed in Fig. 14. Here the date is normal due to the appearance of all residues close to the straight line and the residual histogram follows the symmetrical distribution. From all these facts one can conclude that the modeled design is valid with a good fit.

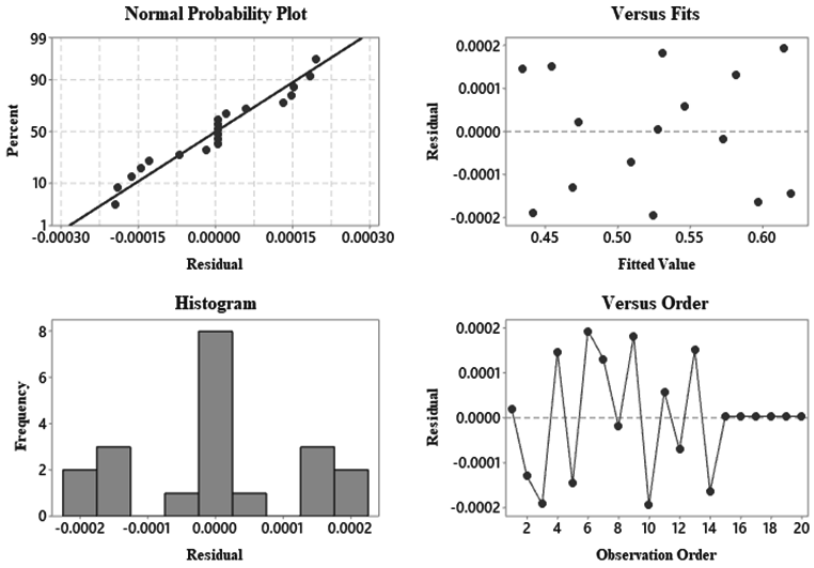

Fig. 14: Residual plots for $Re_x^{-0.5}Nu_x$.

3.3 Sensitivity Analysis

The partial derivatives of $Re_x^{-0.5}Nu_x$ with respect to Nt, Nb and R_T are referred to as the sensitivity of $Re_x^{-0.5}Nu_x$ to those key parameters. Mathematically, the partial derivatives of Eq. (17) with respect to Nt, Nb and R_T are calculated as follows:

$$\frac{\partial\left(Re_x^{-0.5}Nu_x\right)}{\partial Nt} = -0.003140 - 0.000792Nb - 0.000264R_T, \tag{19}$$

$$\frac{\partial\left(Re_x^{-0.5}Nu_x\right)}{\partial Nb} = -0.018373 - 0.000792Nt - 0.001614R_T, \tag{20}$$

$$\frac{\partial\left(Re_x^{-0.5}Nu_x\right)}{\partial R_T} = 0.071529 - 0.004040R_T - 0.000264Nt - 0.001614Nb. \tag{21}$$

Here the positive and negative bar chart of sensitivity shows that the value of $Re_x^{-0.5}Nu_x$ advances and decays respectively as the value of Nt, Nb and R_T increases. The numerical values are obtained for $Re_x^{-0.5}Nu_x$ with Nt at level 0, Nb & R_T with levels of $-1, 0, +1$ and are sketched in Fig. 15. The sensitivity of $Re_x^{-0.5}Nu_x$ to R_T is always positive whereas it is negative for Nt and Nb. The sensitivity of $Re_x^{-0.5}Nu_x$ to Nt enhances for change in values of R_T and Nb. As the value of R_T increases from -1 to +1 the sensitivity of $Re_x^{-0.5}Nu_x$ towards Nb augments. The sensitivity of $Re_x^{-0.5}Nu_x$ towards R_T decays for an ascending value of Nb and R_T. Finally, the heat transport rate is found to be more sensitive to R_T rather than Nt and Nb.

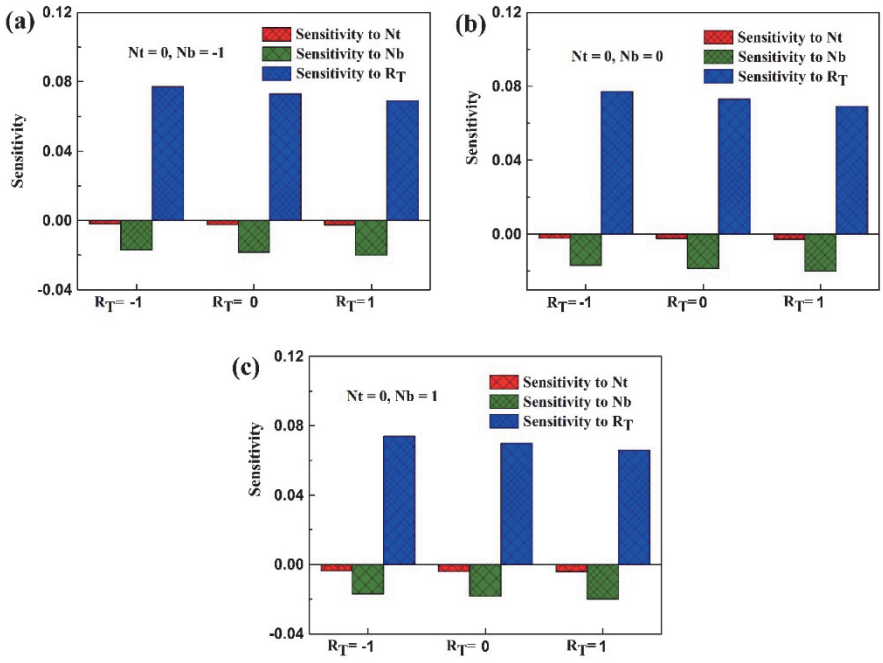

Fig. 15: Sensitivity analysis for $Re_x^{-0.5}Nu_x$.

4 Conclusion

The combined effect of quadratic thermal radiation and quadratic thermal convection on the Jeffrey nanoliquid flow over a flexible surface is investigated. In this study, the convective and second-order velocity slip boundary conditions were also considered. The highly nonlinear equations are solved numerically and validated with previously published data. The current research analysis reveals that:

- The velocity field enhances when Deborah number, nonlinear convection aspects, mixed convection, buoyancy ratio, and Biot number are augmented.
- An increment in the ratio of relaxation to retardation time, suction/injection, and first-order velocity slip aspects yield a lower velocity field.
- The ratio of relaxation to retardation time and Biot number corresponds to temperature and concentration profiles enhances while Deborah number, nonlinear convection aspects, mixed convection, buoyancy ratio, suction/injection, and Prandtl number reduces the temperature and concentration fields.
- Larger Deborah number, quadratic thermal radiation, temperature ratio, and nonlinear convection aspect due to concentration results heat transport enhancement.

- The local Nusselt number profile decreases when the ratio of relaxation to retardation time, thermophoretic aspect, nonlinear convection aspect due to temperature and hepatized motion of nanoparticles are augmented.
- An increasing ratio of relaxation to retardation time and thermophoretic aspect decreases the mass transport rate however it improves when Deborah number, nonlinear convection aspects, Prandtl number, Lewis number, and random motion of nanoparticles are increased.
- The reduced multivariate model for the heat transport rate is obtained by eliminating the quadratic terms of thermophoretic and Brownian motion aspects.
- The heat transport rate is found to be more sensitive to quadratic thermal radiation rather than the zig-zag motion of nanoparticles and the thermophoretic aspect.
- The sensitivity of the local Nusselt number to the quadratic thermal radiation remains positive.

Acknowledgment

The authors are grateful to the Management of CHRIST (Deemed to be University), Bangalore, India for the support through the Major Research Project (MRPDSC-1724).

Bibliography

Ahmad K, Hanouf Z, Ishak A. Mixed convection Jeffrey fluid flow over an exponentially stretching sheet with magnetohydrodynamic effect. AIP Advances. 2016 Mar 30;6(3):035024.

Hayat T, Muhammad T, Mustafa M, Alsaedi A. Three-dimensional flow of Jeffrey fluid with Cattaneo–Christov heat flux: an application to non-Fourier heat flux theory. Chinese Journal of Physics. 2017 Jun 1;55(3):1067-77.

Hayat T, Waqas M, Khan MI, Alsaedi A. Impacts of constructive and destructive chemical reactions in magnetohydrodynamic (MHD) flow of Jeffrey liquid due to nonlinear radially stretched surface. Journal of Molecular Liquids. 2017 Jan 1; 225:302-10.

Kumar M. Study of differential transform technique for transient hydromagnetic Jeffrey fluid flow from a stretching sheet. Nonlinear Engineering. 2020 Feb 7;9(1):145-55.

Raju A, Ojjela O. Numerical investigation of induced magnetic field and variable mass diffusivity on double stratified Jeffrey fluid flow with heat and mass flux boundary conditions. Heat Transfer. 2020.

Choi SUS, Eastman JA. Enhancing thermal conductivity of fluids with nanoparticles. Argonne National Lab., IL (United States); 1995 Oct 1.

Buongiorno, J. Convective transport in nanofluids. Journal of Heat Transfer, 2006 128, 240-250.

Nadeem S, Haq RU, Khan ZH. Numerical solution of non-Newtonian nanofluid flow over a stretching sheet. Applied Nanoscience. 2014 Jun;4(5):625-31.

Shahzad F, Sagheer M, Hussain S. Numerical simulation of magnetohydrodynamic Jeffrey nanofluid flow and heat transfer over a stretching sheet considering Joule heating and viscous dissipation. AIP Advances. 2018 Jun 20;8(6):065316.

Saif RS, Muhammad T, Sadia H, Ellahi R. Hydromagnetic flow of Jeffrey nanofluid due to a curved stretching surface. Physica A: Statistical Mechanics and its Applications. 2020 Aug 1;551:124060.

Goren SL. On free convection in water at 4 C. Chemical Engineering Science. 1966 Jun 1;21(6-7):515-8.

Vajravelu K, Sastri KS. Fully developed laminar free convection flow between two parallel vertical walls—I. International Journal of Heat and Mass Transfer. 1977 Jun 1;20(6):655-60.

Kumar PS, Mahanthesh B, Gireesha BJ, Shehzad SA. Quadratic convective flow of radiated nano-Jeffrey liquid subject to multiple convective conditions and Cattaneo-Christov double diffusion. Applied Mathematics and Mechanics. 2018 Sep;39(9):1311-26.

Waqas M, Shehzad SA, Hayat T, Khan MI, Alsaedi A. Simulation of magnetohydrodynamics and radiative heat transport in convectively heated stratified flow of Jeffrey nanofluid. Journal of Physics and Chemistry of Solids. 2019 Oct 1;133:45-51.

Thriveni K, Mahanthesh B. Optimization and sensitivity analysis of heat transport of hybrid nanoliquid in an annulus with quadratic Boussinesq approximation and quadratic thermal radiation. The European Physical Journal Plus. 2020 Jun;135(6):1-22.

Khan WA, Pop I. Boundary-layer flow of a nanofluid past a stretching sheet. International journal of heat and mass transfer. 2010 May 1;53(11-12):2477-83.

Shahzadi I, Kausar N. Doubly stratified non-Newtonian nanofluid flow featuring nonlinear convection. International Journal of Numerical Methods for Heat & Fluid Flow. 2020 Aug 6.

Jagan K, Sivasankaran S, Bhuvaneswari M, Rajan S. Effect of second order slip and non-linear thermal radiation on mixed convection flow of MHD Jeffrey nanofluid with double stratification under convective boundary condition. InIOP Conference Series: Materials Science and Engineering 2018 Jul 1 (Vol. 390, No. 1, p. 012081). IOP Publishing.

Ibrahim W. Magnetohydrodynamics (MHD) flow of a tangent hyperbolic fluid with nanoparticles past a stretching sheet with second order slip and convective boundary condition. Results in physics. 2017 Jan 1;7:3723-31.

List of contributors

P. G. Siddheshwar,
Department of Mathematics,
Bangalore University, Bangalore
India.

F. Mebarek-Oudina,
Department of Physics,
Faculty of Sciences, University of 20 aout 1955 - Skikda,
B.P 26 Road El-Hadaiek, Skikda 21000, Algeria.

A. Aissa,
Laboratoire de Physique Quantique de la Matiere et Modelisation Mathematique (LPQ3M),
Mascara University, Algeria.

Taseer Muhammad,
Department of Mathematics,
College of Sciences, King Khalid University, Abha
61413, Saudi Arabia.

Md Faisal Md Basir,
Department of Mathematical Sciences,
Faculty of Science, Universiti
Teknologi Malaysia, 81310 UTM Johor Bahru,
Johor, Malaysia.

Hassan Waqas,
Department of Mathematics,
Government College University Faisalabad, Layyah
Campus 31200, Pakistan.

S.A. Shehzad,
Department of Mathematics,
COMSATS University Islamabad, Sahiwal 57000,
Pakistan.

A. Rauf,
Department of Mathematics,
COMSATS University Islamabad, Sahiwal 57000,
Pakistan.

Mahesha Narayana,
Department of Mathematics,
The University of the West Indies, Mona
Campus, Kingston 7, Jamaica.

T.V. Joseph,
Department of Mathematics,
CHRIST (Deemed to be University),
Bangalore, India.

S. Pranesh,
Department of Mathematics,
CHRIST (Deemed to be University),
Bangalore, India.

B. Mahanthesh,
Department of Mathematics,
CHRIST (Deemed to be University),
Bangalore-29. India.

Swaraj D. Lewis,
St. Joseph Engineering College (Affiliated to Visvesvaraya Technological
University, Belagavi),
Vamanjoor, Mangaluru, 575 028, India.

Purushothama Chippar,
St. Joseph Engineering College (Affiliated to Visvesvaraya Technological
University, Belagavi),
Vamanjoor, Mangaluru, 575 028, India.

B. N. Shivakumar,
Department of Mathematics,
Bangalore University,
Jnana Bharathi Campus
Bengaluru-560 056, India.

S. B. Ashoka,
Department of Computer Science (PG),
Maharanis Science College for Women,
Bengaluru, Karnataka 560001, India.

V. Ramachandramurthy,
Department of Mathematics, Ramaiah Institute of Technology,
Bengaluru-560 054, India.

D. Uma,
Department of MCA,
PES Institute of Technology, Bengaluru-560 085,
India.

N. Kavitha,
Department of Mathematics,
Ramaiah Institute of Technology,
Bengaluru-560054, India.

J. Meghana,
Department of Mathematics,
CHRIST (Deemed to be University),
Bangalore, India.

K. Thriveni,
Department of Mathematics,
CHRIST (Deemed to be University),
Bangalore, India.

De Gruyter Series on the Applications of Mathematics in Engineering and Information Sciences

Already published in the series:

Volume 6: Distributed Denial of Service Attacks. Concepts, Mathematical and Cryptographic Solutions
Rajeev Singh, Mangey Ram (Eds.)
ISBN 978-3-11-061675-0, e-ISBN (PDF) 978-3-11-061975-1
e-ISBN (EPUB) 978-3-11-061985-0

Volume 5: Systems Reliability Engineering. Modeling and Performance Improvement
Amit Kumar, Mangey Ram (Eds.)
ISBN 978-3-11-060454-2, e-ISBN (PDF) 978-3-11-061737-5
e-ISBN (EPUB) 978-3-11-061754-2

Volume 4: Systems Performance Modeling
Adarsh Anand, Mangey Ram (Eds.)
ISBN 978-3-11-060450-4, e-ISBN (PDF) 978-3-11-061905-8
e-ISBN (EPUB) 978-3-11-060763-5

Volume 3: Computational Intelligence. Theoretical Advances and Advanced Applications
Dinesh C. S. Bisht, Mangey Ram (Eds.)
ISBN 978-3-11-065524-7, e-ISBN (PDF) 978-3-11-067135-3
e-ISBN (EPUB) 978-3-11-066833-9

Volume 2: Supply Chain Sustainability. Modeling and Innovative Research Frameworks
Sachin Kumar Mangla, Mangey Ram (Eds.)
ISBN 978-3-11-062556-1, e-ISBN (PDF) 978-3-11-062859-3,
e-ISBN (EPUB) 978-3-11-062568-4

Volume 1: Soft Computing. Techniques in Engineering Sciences
Mangey Ram, Suraj B. Singh (Eds.)
ISBN 978-3-11-062560-8, e-ISBN (PDF) 978-3-11-062861-6,
e-ISBN (EPUB) 978-3-11-062571-4

https://www.degruyter.com/view/serial/AMEIS-B